EAST EUROPEAN JOURNAL OF PHYSICS. 4. 590-600 (2025)
DOI:10.26565/2312-4334-2025-4-62 ISSN 2312-4334

INPUT CHARACTERISTICS OF ELECTRICALLY THIN DIPOLE WITH VARIABLE RADIUS ALONG ANTENNA LENGTH

Mikhail V. Nesterenko*, Oleksandr M. Dumin, Yurii V. Arkusha
V.N. Karazin Kharkiv National University, 4, Svobody Sq., Kharkiv, Ukraine, 61022
**Corresponding Author: mikhail.v.nesterenko@gmail.com*
Received July 1, 2025; revised November 5, 2025; accepted November 15, 2025

An approximate analytical solution to the problem of radiation (diffraction) of electromagnetic waves by dipole (monopole) with variable radius along antenna length is presented. The solution was carried out using generalized method of induced electromotive forces (EMF). An influence of the change of monopole radius upon input characteristics is numerically studied. Theoretical results are compared with the experimental data.
Keywords: *Dipole; Monopole; Variable radius; Input characteristics; Generalized method of induced EMF*
PACS: 02.70.Pt; 78.70Gq; 84.40.-x

An additional parameter for obtaining the given electrodynamic characteristics of cylindrical dipole (monopole) antennas can be the change of the radius of the cross-section of the dipole along its length. Such radiators can be located in free space (dipole), half-space (monopole), rectangular waveguide, resonator, on sphere etc. Suppose the radius of the dipole increases from the center of the antenna to its ends according to a linear law (biconical dipole, conical monopole). In that case, such an antenna resonates at a shorter geometric length and is more broadband than a dipole of constant radius. Starting from the classic publications of Schelkunoff [1], Tai [2], Woodward & Brown [3], Bevensee [4], antennas of this type have attracted the attention of many researchers. These can be symmetrical radiators excited by a point source [5], [6], [7], [8], [9], [10]; dipoles with asymmetrical arms [11], [12], antennas with asymmetrical arms and excitation [13], [14], [15], [16]; modified radiators with minor design changes compared to traditional designs [17], [18], [19], [20]; as well as passive scattering antenna elements [21], [22], [23], [24], [25]. However, all of them are devoted to calculating the characteristics of a radiating (scattering) dipole (monopole) with a linear law of the change of antenna radius.

In this paper, an approximate analytical solution to the problem of radiation (scattering) of electromagnetic waves by a dipole (monopole) with other laws of change of radius along antenna length (piecewise linear (diamond-shaped), Vivaldi type, combined trigonometric, circle, piecewise constant) is presented. The solution was carried out using the generalized method of induced electromotive forces (EMF) in accordance with the concept of "thin-wire approximation". The input characteristics of the antennas under consideration are analyzed in detail.

PROBLEM FORMULATION AND INTEGRAL EQUATION SOLUTION

Let the monopole of the L length and the variable radius $r(s)$, located in half-space, be excited by the electric field extraneous source $E_{0s}(s)$ (Fig. 1). The monochromatic fields and currents depend on time t as $e^{i\omega t}$ ($\omega = 2\pi f$ is the circular frequency, f is the frequency, measured in Hz). The monopole is electrically thin, if the following inequalities are performed:

$$kr(s) << 1,\ r(s) << 2L, \tag{1}$$

where $k = 2\pi/\lambda$, λ is the wavelength in free space.

The integral equation in the current $J(s)$ for the impedance boundary condition on the dipole surface acquires the form [6], [24]:

$$\left(\frac{\mathrm{d}^2}{\mathrm{d}s^2} + k^2\right)\int_{-L}^{L} J(s')\frac{e^{-ik\tilde{R}(s,s')}}{\tilde{R}(s,s')}\mathrm{d}s' = -\frac{i\omega}{\cos\psi}\left[E_{0s}(s) - z_i J(s)\right]. \tag{2}$$

Here $\tilde{R}(s,s') = \sqrt{(s-s')^2 + r^2(s)}$, s and s' are the local coordinates related to the dipole axis and surface, z_i is the distributed internal linear impedance, $J(\pm L) = 0$, $-L$ is the coordinate of the mirror image of the dipole relative to the infinite ideally conducting plane (for monopole). So, for example, for metal cylinders (σ is the metal conductivity, Δ^{o} is the skin layer thickness) under the condition $r >> \Delta^{\mathrm{o}}$, is determined by the relation $z_i = \dfrac{1+i}{2\pi r\sigma\Delta^{\mathrm{o}}}$. Despite the fact that

Cite as: M.V. Nesterenko, O.M. Dumin, Y.V. Arkusha, East Eur. J. Phys. 4, 590 (2025), https://doi.org/10.26565/2312-4334-2025-4-62

for real metals the values z_i are quite small, it is necessary to take this term into account. In this case, equation (2) is the Fredholm equation of the 2-nd kind and has a unique solution. Note also that at $r(s) = const = r_0$, equation (2) transforms into the equation in the current along an impedance dipole of constant radius with a quasi-one-dimensional core $\tilde{R}(s,s') = R(s,s') = \sqrt{(s-s')^2 + r_0^2}$.

The approximate analytical solution of the equation (2) can be obtained by the generalized method of induced EMF [13], [14]. Note that in [24] equation (2) for a symmetric biconical dipole is solved by means of the averaging method [26]. Using this method the approximating current distribution functions in expressions (3) were also found.

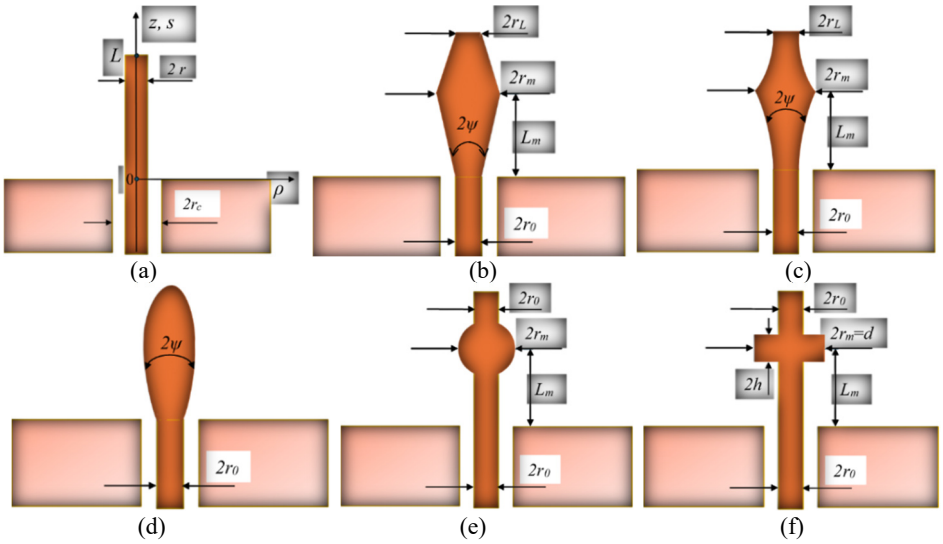

Figure 1. The problem geometry and corresponding notations: (a) - constant radius; (b) - (f) - variable radius

The dipole currents can be presented as product of the unknown complex amplitudes J_n and distribution functions $f_n(s)$ ($n = 0,1$) as

$$J(s) = J_0 f_0(s) + J_1 f_1(s); \quad f_n(\pm L) = 0. \tag{3}$$

Then the approximate solution to equation (2) can be obtained in the form ($m,n = 0,1$)

$$J(s) = -\frac{i\omega}{2k\cos\psi}\left[J_0 f_0(s) + J_1 f_1(s)\right], \tag{4}$$

where $J_0 = \dfrac{E_0 Z_{11}^{\Sigma} - E_1 Z_{01}^{\Sigma}}{Z_{00}^{\Sigma} Z_{11}^{\Sigma} - Z_{10}^{\Sigma} Z_{01}^{\Sigma}}$, $J_1 = \dfrac{E_1 Z_{00}^{\Sigma} - E_0 Z_{10}^{\Sigma}}{Z_{00}^{\Sigma} Z_{11}^{\Sigma} - Z_{10}^{\Sigma} Z_{01}^{\Sigma}}$,

$$Z_{mn} = \frac{1}{2k\cos\psi}\left\{-\frac{\mathrm{d}f_m(s)}{\mathrm{d}s}A_n(s)\Big|_{-L}^{L} + \int_{-L}^{L}\left[\frac{\mathrm{d}^2 f_m(s)}{\mathrm{d}s^2} + k^2 f_m(s)\right]A_n(s)\mathrm{d}s\right\}, \quad A_n(s) = \int_{-L}^{L} f_n(s')\frac{e^{-ik\tilde{R}(s,s')}}{\tilde{R}(s,s')}\mathrm{d}s', \tag{5a}$$

$$\tilde{Z}_{mn} = -\frac{i\omega}{2k\cos\psi}\int_{-L}^{L} f_m(s) f_n(s) z_i \,\mathrm{d}s, \quad Z_{mn}^{\Sigma} = Z_{mn} + \tilde{Z}_{mn}, \quad E_m = \int_{-L}^{L} f_m(s) E_{0s}(s)\mathrm{d}s. \tag{5b}$$

Let the dipole be excited in the point $s = 0$ by the voltage generator with amplitude V_0: $E_{0s}(s) = V_0\delta(s-0)$, where δ is the Dirac delta function. Let us choose the functions $f_{0,1}(s)$ according to [26] in the following form:

$$f_0(s) = \sin\tilde{k}(L - |s|), \quad f_1(s) = \cos\tilde{k}s - \cos\tilde{k}L, \tag{6}$$

where $\tilde{k} = k - \dfrac{iz_i[3/2 - r_0/(2r_m)]}{120\cos\psi\ln(2L/r_m)}$, r_0 and r_m are the radii of the dipole in points $s = 0$ and $s = L_m$ (Fig. 1). Note that the approximation of functions (6) adequately represents the real physical process if the dipole electrical lengths are small

$(2L/\lambda) \le 1.4$ [26]. Other approximating function [26] $f_2^s(s) = \cos(ks/2) - \cos(kL/2)$ is valid in the range $1.4 < (2L/\lambda) \le 2.5$.

The coefficients Z_{mn}^{Σ} in the formulas (4) can be obtained from expressions (5), (6):

$$Z_{0n} = \frac{\tilde{k}[A_n(L) - \cos\tilde{k}LA_n(0)]}{k\cos\psi} + \frac{k^2 - \tilde{k}^2}{2\cos\psi}\int_{-L}^{L} f_0(s)A_n(s)\mathrm{d}s,\ Z_{1n} = \frac{\tilde{k}\sin\tilde{k}LA_n(L)}{k\cos\psi} - \frac{1}{2k\cos\psi}\begin{bmatrix} k^2\cos\tilde{k}L\int_{-L}^{L} A_n(s)\mathrm{d}s \\ -(k^2-\tilde{k}^2)\int_{-L}^{L}\cos\tilde{k}sA_n(s)\mathrm{d}s \end{bmatrix}$$

$$\tilde{Z}_{00} = -\frac{i\omega\varepsilon_i(2\tilde{k}L - \sin 2\tilde{k}L)}{2k\tilde{k}\cos\psi},\ \tilde{Z}_{01} = \tilde{Z}_{10} = -\frac{i\omega\varepsilon_i[\tilde{k}L\sin\tilde{k}L - 2\cos\tilde{k}L(1-\cos\tilde{k}L)]}{k\tilde{k}\cos\psi},$$

$$\tilde{Z}_{11} = -\frac{i\omega\varepsilon_i[2\tilde{k}L - 3\sin 2\tilde{k}L + 4\tilde{k}L\cos^2\tilde{k}L]}{2k\tilde{k}\cos\psi},\ E_0 = \sin\tilde{k}L,\ E_1 = 1 - \cos\tilde{k}L.$$

The input impedance for monopole $Z_{in} = R_{in} + iX_{in}$ and admittance $Y_{in} = G_{in} + iB_{in}$ can be presented as

$$Z_{in}[\mathrm{Ohm}] = \frac{30i}{J_0 f_0(0) + J_1 f_1(0)},\qquad Y_{in}[\mathrm{mS}] = \frac{10^3}{Z_{in}} \tag{7}$$

Then, the module of reflection coefficient in the antenna feeder with the wave impedance W is equal to

$$|S_{11}| = \left|\frac{Z_{in} - \mathrm{W}}{Z_{in} + \mathrm{W}}\right|, \tag{8}$$

and the voltage standing wave ratio is determined by the formula $\mathrm{VSWR} = (1 + |S_{11}|)/(1 - |S_{11}|)$.

Note that for printed antennas of the type under consideration (piecewise linear (diamond-shaped), Vivaldi type, combined trigonometric, circle, piecewise constant), the solution to equation (2) is also valid, but it is necessary to make the replacement $r(s) = d(s)/4$ [26], where $d(s)$ is the antenna width.

NUMERICAL AND MEASURED RESULTS

Next we will consider radiators with the following geometric parameters [27]: r_0 =1.522 mm, r_c =3.5 mm, L =50.065 mm, $k\rho \to \infty$. Then the characteristic impedance of the feeder line is $\mathrm{W} = 60\ln(r_c/r_0)$ =50 Ohm. Fig. 2 shows the dependences of the real and imaginary parts of the input impedance of the regular and conical monopoles ($L_m = L$) on its electrical length at different angles ψ.

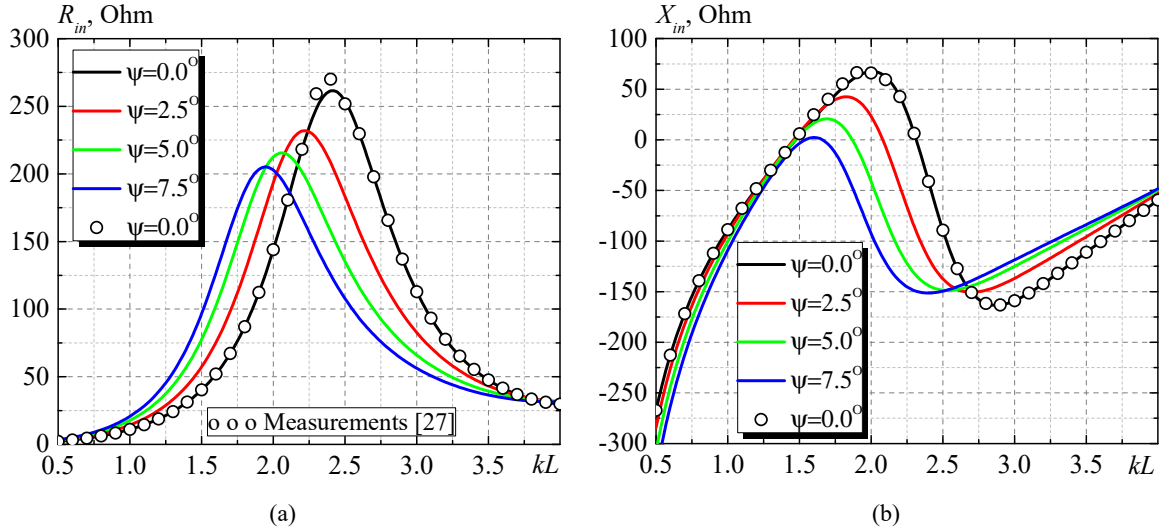

Figure 2. The dependences of the calculated (7) and measured [27] monopole input impedance on its electrical length at different angles ψ: (a) – real part R_{in}, (b) – imaginary part X_{in}

As can be seen, the agreement between the calculated and measured values $Z_{in}(kL)$ at $\psi = 0.0^{O}$ (regular monopole) is quite satisfactory, and with the increase of the angle ψ the impedance change trends to coincide with those measured in [3]. To satisfy inequalities (1), we will limit ourselves to the value $\psi = 7.5^{O}$ ($r_m = 8.038$ mm, $r_m / 2L = 0.08$).

1. Numerical results for piecewise linear law of $r(s)$

Fig. 3a shows the laws of change of radius along the monopole (Fig. 1b) determined by the following formula

$$r(s) = \begin{cases} r_0 + s\tan\psi, \text{ at } s \le \kappa L, \\ r_0 + [\kappa/(1-\kappa)](L-s)\tan\psi, \text{at } s \ge \kappa L, \end{cases} \tag{9}$$

where $\kappa = s_m / L$, and Fig. 3b shows the dependences of the reflection coefficient modulus $|S_{11}|$ in the feeder line corresponding to these laws. Fig. 3a also shows that curve $\kappa = 0.75$ has the longest path length on the surface of those presented there. Accordingly, this curve describes the resonance at the lowest frequency in Fig. 3b. However, the effect of this phenomenon on the resonance frequency is not always proportional to the increase in the path length. As for the minimum value of reflection observed for curve $\kappa = 0.25$, this can be explained by a relatively smooth bend at point L_m. It is also interesting that the shift of the resonant frequency in this case is proportional to the increase in the wave path along the dipole surface.

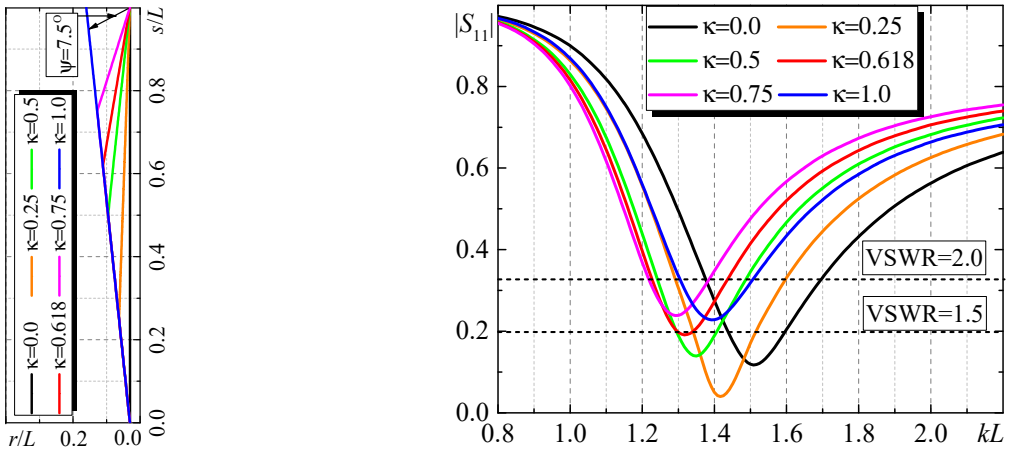

(a) (b)

Figure 3. The laws of change of radius along the monopole (a), the dependences of the reflection coefficient modulus $|S_{11}|$ in the feeder line from the electrical length of the monopole (b) at different positions of the maximum values of the radius and $\psi = 7.5^{O}$

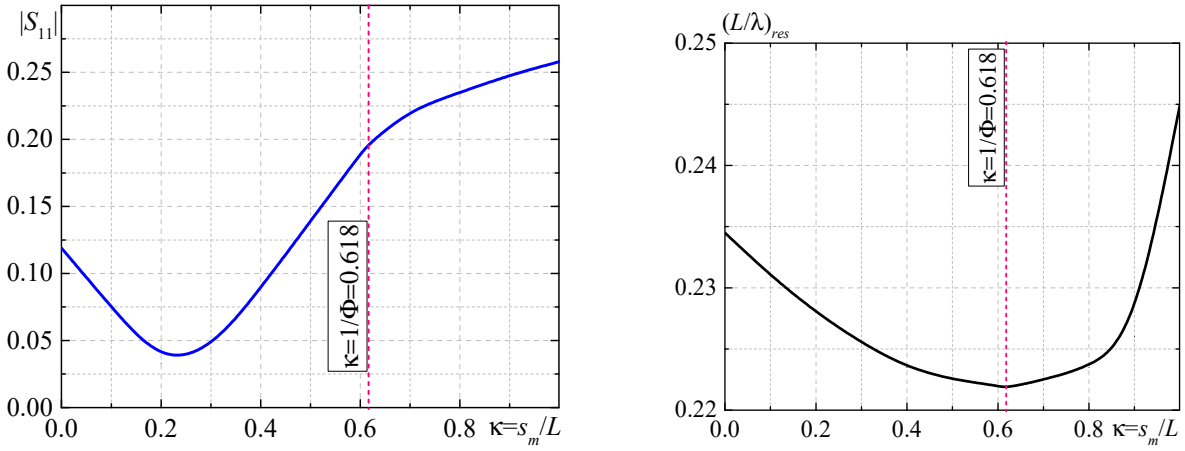

(a) (b)

Figure 4. The dependences of the reflection coefficient modulus $|S_{11}|$ on the coordinate of the point with the maximum radius along the length of the monopole (a), the dependences of the values of resonant "shortening" $(L/\lambda)_{res}$ on the coordinate of the point with the maximum radius along the length of the monopole at $\psi = 7.5^{O}$

Figs. 4 show the dependences of the reflection coefficient modulus $|S_{11}|$ and values of resonant "shortening" (the resonance condition is the fulfillment of equality $X_{in}=0$ when the sign X_{in} changes from negative to positive) $(L/\lambda)_{res}$ (compared to a tuned monopole, where $(L/\lambda)_{res}=0.25$) on the coordinate of the point with the maximum radius along the length of the monopole. In Figs. 4 the dotted line indicates the value $\kappa=0.618$ that is associated with the quantity $\kappa=1/\Phi$, where $\Phi=1.618$ is the so-called "golden ratio" [28]. As you can see, the value $\kappa\approx 0.618$ is a "inflection point" on both graphs. This can be explained by the fact that at this point the additional capacitance formed by the last segment of the monopole operates in an optimal way, which creates this shortening. Approximation of the function in Fig. 4a and the study of its derivatives indeed allow us to conclude that at $\kappa\approx 0.618$ there is an inflection point.

Placing the maximum values of the monopole radius at this point for different angles ψ (Fig. 5a) leads to an even better matching of the monopole with the feeder line (Fig. 5b).

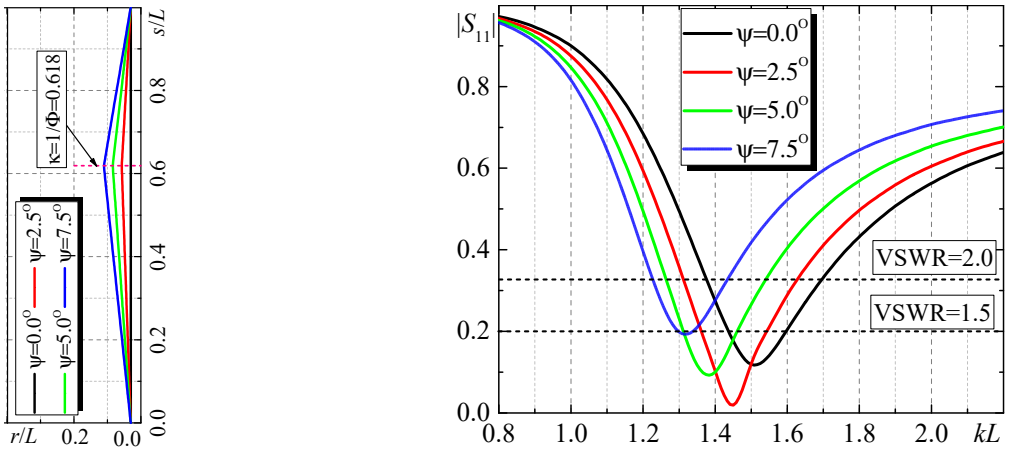

(a) (b)

Figure 5. The laws of change of radius along the monopole at $\kappa=0.618$ (a), the dependences of the reflection coefficient modulus $|S_{11}|$ in the feeder line from the electrical length of the monopole (b) for different ψ

2. Numerical results for Vivaldi type law of $r(s)$

Fig. 6a shows the laws of change in radius along the monopole, determined by the following formula (Vivaldi type antenna [29], Fig. 1c).

$$r(s)=\begin{cases} r_0+(1/\kappa)s\tan\psi e^{\beta(s/L-\kappa)}, \text{ at } s\le \kappa L, \\ r_0+[1/(1-\kappa)](L-s)\tan\psi e^{-\beta(s/L-\kappa)}, \text{at } s\ge \kappa L, \end{cases} \tag{10}$$

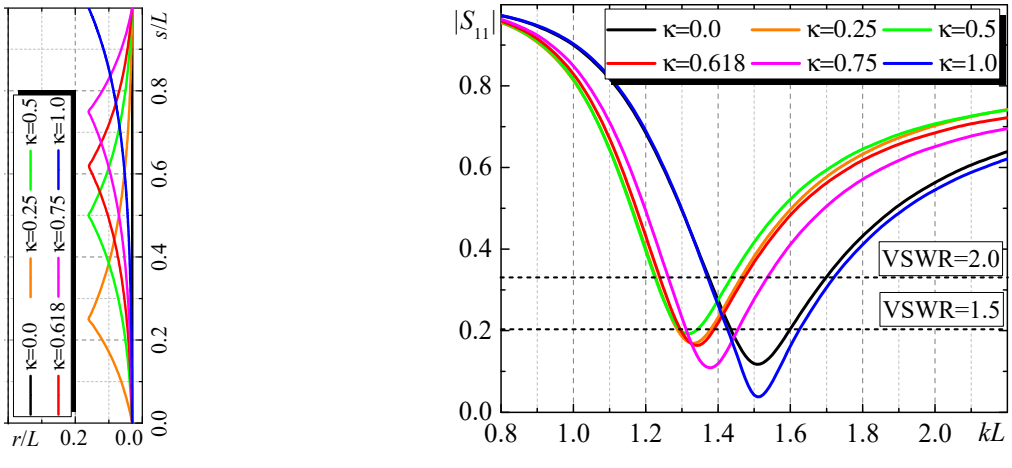

(a) (b)

Figure 6. The laws of change of radius along the monopole at $\psi=7.5^{\circ}$ and $\beta=\pi$ (a), the dependences of the reflection coefficient modulus $|S_{11}|$ in the feeder line from the electrical length of the monopole (b) for different κ

Fig. 6b shows the dependences of the reflection coefficient modulus $|S_{11}|$ in the feeder line corresponding to these laws. As can be seen, the best matching is observed at $\kappa = 1.0$ (conical monopole) with a practically unchanged resonant frequency compared to regular monopole ($\kappa = 0.0$, $r(s) = const$). In other cases, there is the decrease of the resonant frequency in comparison with a regular monopole. In Figs. 6 the red line indicates the value $\kappa = 0.618$. Fig. 7a shows the laws of change of radius along the monopole, determined by the formula (10) and $\kappa = 0.618$ for various β. Fig. 7b shows the dependences of the reflection coefficient modulus $|S_{11}|$ in the feeder line corresponding to these laws. As can be seen, the best matching is observed at $\beta = 4\pi$ and for all laws of change of radius the decrease is observed in the resonant frequency in comparison with a regular monopole.

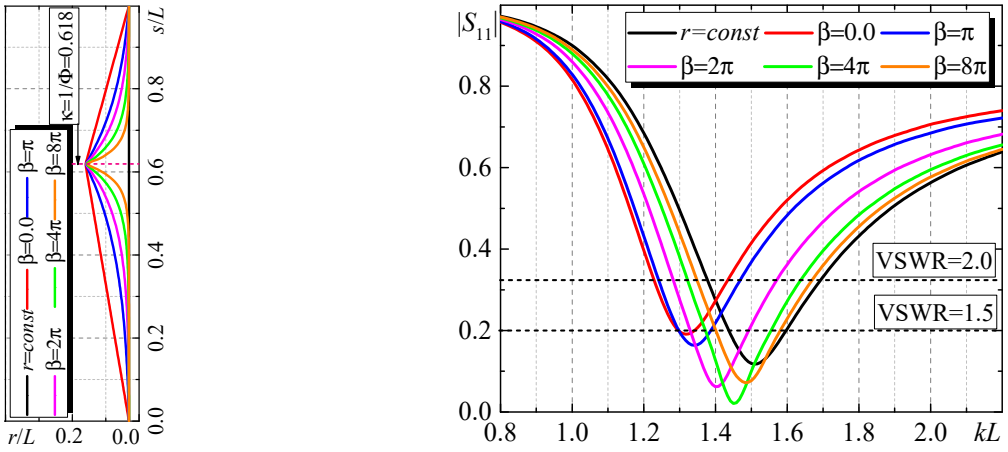

(a) (b)

Figure 7. The laws of change of radius along the monopole at $\psi = 7.5^{\circ}$ and $\kappa = 0.618$ (a), the dependences of the reflection coefficient modulus $|S_{11}|$ in the feeder line from the electrical length of the monopole (b) for different β

3. Numerical results for combined trigonometric law of $r(s)$

Let us further consider another law of change of radius along the monopole length, which is a combination of trigonometric functions [30] (Fig. 1d):

$$r(s) = r_0 + 4\kappa L \tan\psi \cos(\pi s / 2L)[1 - \cos(\pi s / 2L)]. \tag{11}$$

As can be seen, the best matching is observed at $\psi = 2.5^{\circ}$ (similar to Fig. 5b) and for all laws of change of radius a decrease is observed in the resonant frequency in comparison with a regular monopole.

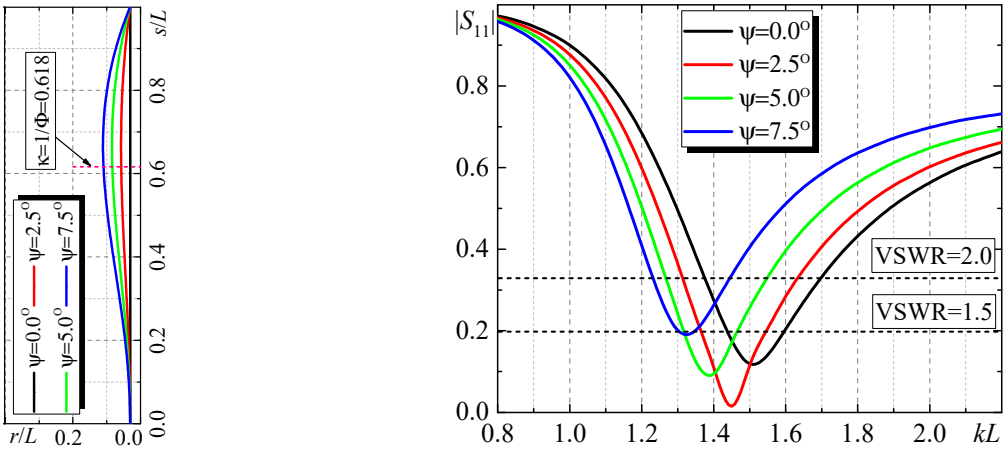

(a) (b)

Figure 8. The laws of change of radius along the monopole at $\kappa = 0.618$ (a), the dependences of the reflection coefficient modulus $|S_{11}|$ in the feeder line from the electrical length of the monopole (b) for different ψ

4. Numerical results for circle law of $r(s)$

Fig. 9a shows the laws of change of radius along the monopole, determined by the following formula (circle type, r_s is the radius of circle, see Fig. 1e)

$$r(s)=\begin{cases} r_0, \text{ at } s \le \kappa L - r_s \ \& \ s \ge \kappa L + r_s, \\ r_0 + [r_s^2 - (s-\kappa L)^2]/r_s, \text{at } s \ge \kappa L - r_s \ \& \ s \le \kappa L + r_s, \end{cases} \tag{12}$$

and Fig. 9b shows the dependences of the reflection coefficient modulus $|S_{11}|$ in the feeder line corresponding to these laws. As can be seen, the best matching is observed at $\kappa = 0.618$ and for the first time at $\kappa = 1.0$, an increase of the resonant frequency f_{res} is observed in comparison with a regular monopole ($\kappa = 0.0, r(s) = const$), in contrast to all previously considered laws of change in radius along the monopole.

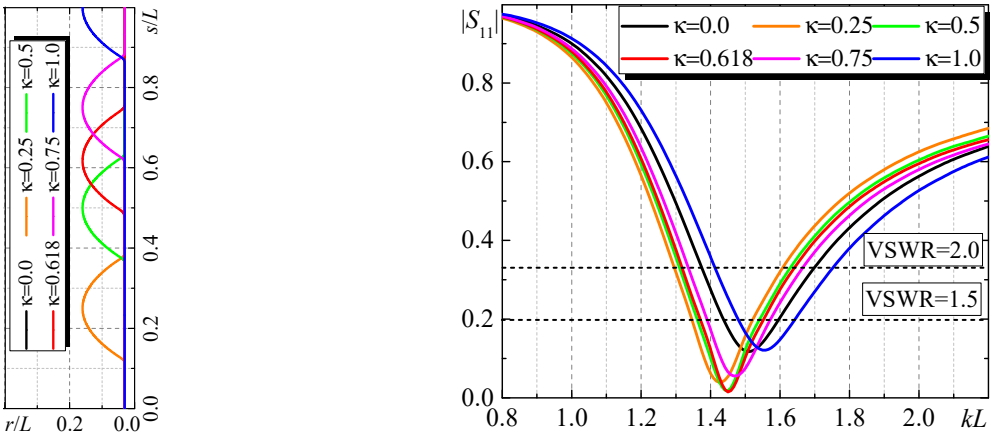

(a) (b)

Figure 9. The laws of change of radius along the monopole at $r_s = 6.516$ mm (a), the dependences of the reflection coefficient modulus $|S_{11}|$ in the feeder line from the electrical length of the monopole (b) for different κ

5. Numerical results for piecewise constant law of $r(s)$

Fig. 10a shows the laws of change of radius along the monopole, determined by the following formula (piecewise constant, $2h$ is the insert disc thickness, see Fig. 1f)

$$r(s)=\begin{cases} r_0, \text{ at } s \le \kappa L - h \ \& \ s \ge \kappa L + h, \\ r_m, \text{ at } s \in \kappa L \pm h, \end{cases} \tag{13}$$

and Fig. 10b shows the dependences of the reflection coefficient modulus $|S_{11}|$ in the feeder line corresponding to these laws. As can be seen, the best matching is observed at $\kappa = 0.75$ and at $\kappa = 1.0$ also increase in the resonant frequency f_{res} is observed in comparison with a regular monopole.

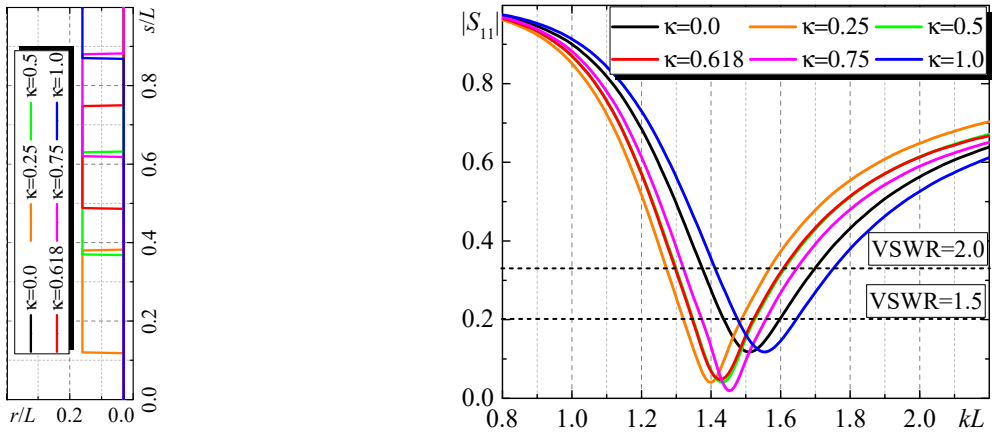

(a) (b)

Figure 10. The laws of change of radius along the monopole at $h = r_s = 6.516$ mm (a), the dependences of the reflection coefficient modulus $|S_{11}|$ in the feeder line from the electrical length of the monopole (b) for different κ

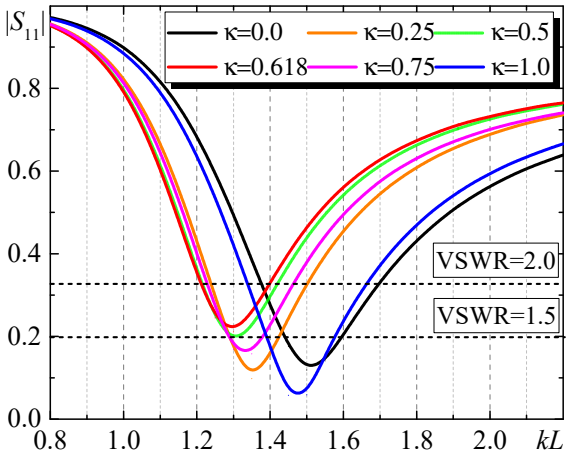

Figure 11. The dependences of the reflection coefficient modulus $|S_{11}|$ in the feeder line from the electrical length of the double-disk monopole structure for different κ at $h_n = 6.0$ mm ($n = 1 \div 6$)

If a second disk of the same or different thickness is added to one disk located at a certain distance along the length of the monopole, a double-disk structure is obtained. Obviously, instead of disks there can be any other structures (as well as their combinations) discussed above. Fig. 11 shows the dependences of the reflection coefficient modulus $|S_{11}|$ in the feeder line when the center of the first disk is located at point $\kappa_1 = s_m / L = 0.125$, and additional disks at $\kappa = 0.25; 0.5; 0.618; 0.75; 1.0$. The thicknesses of all disks are equal $2h$ =12.0 mm. As follows from the graphs, the best matching for this structure is observed (as before in Fig. 6) at $\kappa = 1.0$, and the greatest "shortening" of the monopole compared to that tuned monopole at $\kappa = 0.618$ (as before in Fig. 7).

TESTING OF THE ADEQUACY OF THE PROPOSED MATHEMATICAL MODEL TO A REAL PHYSICAL PROCESS

For testing of the adequacy of the proposed mathematical model to a real physical process, we briefly present numerical and experimental results for regular and conical dipoles located in a rectangular waveguide [24]. Let a dipole with a radius $r(s) = r_0 + |s| \tan\psi$ varying along the length (Fig. 12a) or a similar monopole (Fig.12b) be located in a rectangular waveguide with a cross-section $\{a \times b\}$.

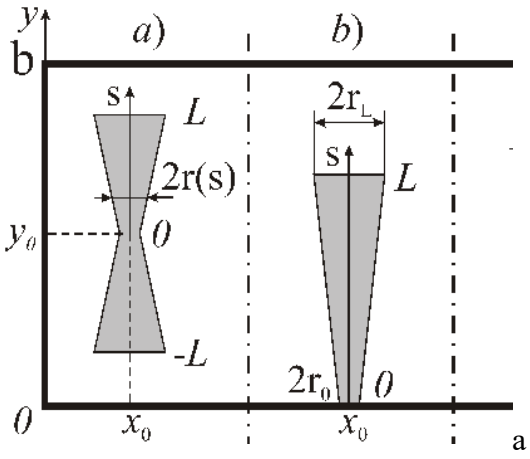

Figure 12. The geometries of the dipole (a) and monopole (b)

Then, when a fundamental type wave TE_{10} propagates in the waveguide, the reflection coefficient S_{11} from the monopole will be equal to

$$S_{11} = -\frac{4\pi i}{abk\gamma}\left(\frac{k}{\tilde{k}}\sin\frac{\pi x_0}{a}\right)^2 \frac{(\sin\tilde{k}L - \tilde{k}L\cos\tilde{k}L)^2}{Z_\psi^W(\tilde{k}L) + \mathrm{tg}\psi\tilde{Z}_\psi^W(\tilde{k}L) + \tilde{Z}_z(\tilde{k}L)}. \quad (14)$$

The solution is carried out by the generalized method of induced EMF with current approximation $J(s) = J_0(\cos\tilde{k}s - \cos\tilde{k}L)$). Expressions for the coefficients in formula (14) are presented in the Appendix I.

Fig. 13 shows the photographs of experimental samples of monopoles, which are located in the rectangular waveguide of size $\{a\times b\}$=58x25 mm^2. The axes of the monopoles are parallel to the narrow walls of the waveguide.

As can be seen, the value of the resonant wavelength λ_{res} for the conical dipole increases, correspondingly resonant frequency f_{res} is decreases, (curve 3) in comparison with the conductors of the constant radius (the curves 1, 2). Moreover, the radiuses of the latter equal to a smaller (curve 1) and a larger (curves 2) radiuses of the conical dipole, correspondingly. To our minds, this interesting fact is explained by the definite redistribution of energy of the near reactive fields between the E- and H-modes of the waveguide connected with the occurrence of some angle ψ between the axis $\{0y\}$ of the waveguide and $\{0s\}$ on the surface of the monopole. For the monopoles above the plane that we studied earlier, the same redistribution of reactive near fields obviously takes place.

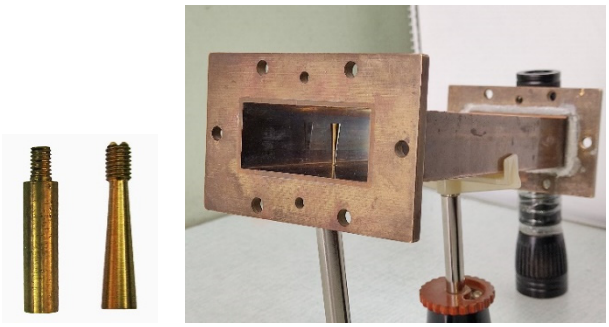

Figure 13. The experimental layouts of monopoles

Fig. 14 represents the dependences of the $|S_{11}|$ value on the wavelength for the cooper monopoles at L=15.0 mm, $x_0 = a/8$, $y_0 = 0$.

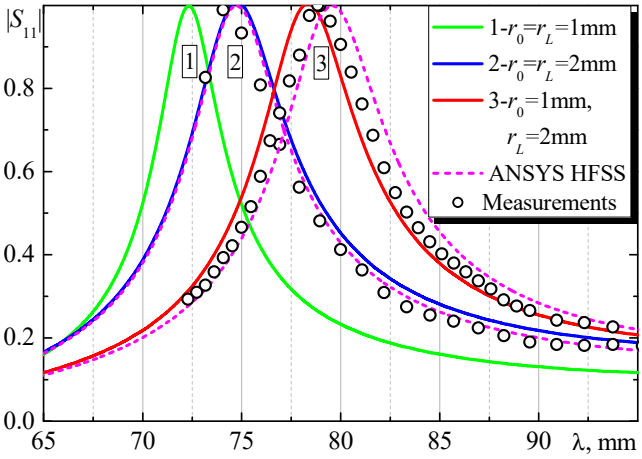

Figure 14. The dependences of the calculated and measured monopole reflection modulus $|S_{11}|$ in the waveguide at the constant and variable radiuses of their cross section: 1, 2, 3–calculation by the formula (12), 4–calculation by means of the package "ANSYS HFSS", 5–experimental data

CONCLUSION

Based on the obtained approximate analytical solution of the problem of current distribution along a radiating dipole with a variable cross-section radius, the input characteristics of a monopole over an infinite ideally conducting plane are investigated. It is shown that the use of different laws of radius variation along the monopole allows one to significantly improve the matching of the monopole with a feeder line with a standard characteristic impedance, and to change the resonant frequency of the monopole with its constant length. Thus, for successful matching of a monopole with a feeder line of a standard characteristic impedance, there is no need to change this impedance, but it is sufficient to change the antenna cross-section according to a certain law. This law can be chosen taking into account the requirements for changing or maintaining the resonant frequency of the radiator in comparison with the resonant frequency of a regular monopole.

It should be especially emphasized that, unlike the currently widely used commercial packages, in the presented solution it is sufficient to make the required changes to the analytical formulas, rather than drawing new structures each time. Moreover, the calculation time (using a computer based on Intel® Core™ i5-7200 processor) of input characteristics at one structure geometry using the proposed approach is about 0.5-1.0 seconds. The total time of calculation using a commercial ANSYS HFSS package, taking into account the finding of intermediate parameters, was approximately 2-3 minutes.

APPENDIX I

Coefficients in the formula (14):

$$Z_{\psi}^{W}(\tilde{k}L)=\frac{8\pi}{ab}\sum_{m=1}^{\infty}\sum_{n=0}^{\infty}\frac{\varepsilon_n(k^2-k_y^2)\tilde{k}}{kk_z(\tilde{k}^2-k_y^2)}e^{-k_z r_0}\sin^2 k_x x_0\cos^2 k_y y_0[\sin\tilde{k}L\cos k_y L-(\tilde{k}/k_y)\cos\tilde{k}L\sin k_y L]F_{\psi}(\tilde{k}L),$$

$$\tilde{Z}_{\psi}^{W}(\tilde{k}L)=\frac{4\pi}{ab}\sum_{m=1}^{\infty}\sum_{n=1}^{\infty}\frac{\tilde{k}^2}{k(\tilde{k}^2-k_y^2)}e^{-k_z r_0}\sin^2 k_x x_0[\cos\tilde{k}L(\cos k_y L-1)+(k_y/\tilde{k})\sin\tilde{k}L\sin k_y L+(k_y/\tilde{k})^2(\cos k_y L-1)]F_{\psi}(\tilde{k}L),$$

$$F_{\psi}(\tilde{k}L)=\frac{1/2}{(\tilde{k}+k_y)^2+(k_z\tan\psi)^2}\left\{e^{-k_z L\tan\psi}[(\tilde{k}+k_y)\sin(\tilde{k}+k_y)L-k_z\tan\psi\cos(\tilde{k}+k_y)L]+k_z\tan\psi\right\}$$

$$-\frac{\cos\tilde{k}L}{k_y^2+(k_z\tan\psi)^2}\left\{e^{-k_z L\tan\psi}[k_y\sin k_y L-k_z\tan\psi\cos k_y L]+k_z\tan\psi\right\}+\frac{1/2}{(\tilde{k}-k_y)^2+(k_z\tan\psi)^2}\left\{\begin{matrix}e^{-k_z L\tan\psi}[(\tilde{k}-k_y)\sin(\tilde{k}-k_y)L\\-k_z\tan\psi\cos(\tilde{k}-k_y)L]+k_z\tan\psi\end{matrix}\right\},$$

$\tilde{Z}_z(\tilde{k}L)=-\frac{i\omega z_l\sin 2\tilde{k}L}{2k\tilde{k}\cos\psi}$, $\varepsilon_n=\begin{cases}1, n=0\\2, n\neq 0\end{cases}$, $k_x=\frac{m\pi}{a}$, $k_y=\frac{n\pi}{b}$, $k_z=\sqrt{k_x^2+k_y^2-k^2}$, $\gamma=\sqrt{k^2-(\pi/a)^2}$, m and n are the integers.

ORCID

Mikhail V. Nesterenko, https://orcid.org/0000-0002-1297-9119; **Oleksandr M. Dumin,** https://orcid.org/0000-0001-5067-9689;
Yurii V. Arkusha, https://orcid.org/0000-0002-6483-4341

REFERENCES

[1] S. A. Schelkunoff, "Theory of antennas of arbitrary size and shape," Proc. IRE, **29**, 493-521 (1941). https://doi.org/10.1109/JRPROC.1941.231669
[2] C. T. Tai, "On the theory of biconical antennas," Journal Applied Phys., **19**, 1155-1160 (1948). https://doi.org/10.1063/1.1715036
[3] O. M. Woodward, and G. H. Brown, "Experimentally determined radiation characteristics of conical and triangular antenna," RCA (Radio Corp. Amer.) Rev., **13**, 425-453 (1952).
[4] R. M. Bevensee, *A Handbook of Conical Antennas and Scatterers*, (New York: Gordon and Breach, 1973).
[5] D. M. Bolle, and M. D. Morganstern, "Monopole and conic antennas on spherical vehicles," IEEE Trans. Antennas Propag., **17**, 477-484 (1969). https://doi.org/10.1109/TAP.1969.1139479
[6] T. T. Wu, and R. W. P. King, "The tapered antenna and its application to the junction problem for thin wires," IEEE Trans. Antennas Propag., **24**, 42-45 (1976). https://doi.org/10.1109/TAP.1976.1141274
[7] S. A. Saoudy, and M. Hamid, "Input admittance of a biconical antenna with wide feed gap," IEEE Trans. Antennas Propag., **38**, 1784-1790 (1990). https://doi.org/10.1109/8.102740
[8] S. S. Sandler, and R. W. P. King, "Compact conical antennas for wide-band coverage," IEEE Trans. Antennas Propag., **42**, 436-439 (1994). https://doi.org/10.1109/8.280735
[9] O. Givati, and A. P. C. Fourie, "Analysis of skeletal wire conical antennas" IEEE Trans. Antennas Propag., **44**, 844-858 (1996). https://doi.org/10.1109/8.509888
[10] F. E. S. Pereira, and M. H. C. Dias, "On the design of conical antennas for broadband impedance matching performance," Intern. J. Antennas Propag., 1-13 (2017).
[11] S. N. Samaddar, and E. L. Mokole, "Biconical antennas with unequal cone angles," IEEE Trans. Antennas Propag., **46**, 181-193 (1998). https://doi.org/10.1109/8.660962
[12] D. Ghosh, and T. K. Sarkar, "Design of a wide-angle biconical antenna for wideband communications," Prog. Electromagn. Res. B, **16**, 229-245 (2009). http://dx.doi.org/10.2528/PIERB09061508
[13] M. V. Nesterenko, V. A. Katrich, and S. V. Pshenichnaya, "Multiband asymmetric biconical dipole antenna with distributed surface impedance and arbitrary excitation," East European J. Physics, **2**, 450-455 (2024). https://doi.org/10.26565/2312-4334-2024-2-59
[14] M. V. Nesterenko, V. A. Katrich, Yu. V. Arkusha, and V. V. Katrich, "Radiation of electromagnetic waves by regular and biconical dipoles with variable distributed surface impedance and arbitrary excitation," East European J. Physics, **3**, 465-473 (2024). https://doi.org/10.26565/2312-4334-2024-3-56
[15] M. Nesterenko, V. Katrich, O. Dumin, and Yu. Arkusha, "Electrodynamic characteristics of biconical dipole with complex distributed surface impedance and asymmetric excitation," in Proc. XXIXth Int. Sem. Direct Inverse Problems of Electromagn. and Acoustic Wave Theory, 201-204 (2024). https://doi.org/10.1109/DIPED63529.2024.10706147
[16] M. V. Nesterenko, V. A. Katrich, S. V. Pshenichnaya, and S. A. Pogarsky, "Reducing influence of hardware of communication station on characteristics of asymmetric biconical dipole using magneto-dielectric substrate on finite-size metal screen," East European J. Physics, **2**, 424-430 (2025). https://doi.org/10.26565/2312-4334-2025-2-52
[17] K.-L. Wong, and S.-L. Chien, "Wide-band cylindrical monopole antenna for mobile phone," IEEE Trans. Antennas Propag., **53**, 2756-2758 (2005). https://doi.org/10.1109/TAP.2005.851784
[18] A. K. Amert, and K. W. Whites, "Miniaturization of the biconical antenna for ultrawideband applications," IEEE Trans. Antennas Propag., **57**, 3728-3735 (2009). https://doi.org/10.1109/TAP.2009.2026667
[19] C. S. Rao, and A. Sudhakar, "Analysis of edge terminated wide band biconical antenna," Access J., **30**, 804-809 (2015).
[20] F. F. Dubrovka, S. Piltyay, M. Movchan, and I. Zakharchuk, "Ultrawideband compact lightweight biconical antenna with capability of various polarizations reception for modern UAV applications," IEEE Trans. Antennas Propag., **71**, 2922-2929 (2023). https://doi.org/10.1109/TAP.2023.3247145
[21] D. B. Kuryliak, and O. M. Sharabura, "Diffraction of axially-symmetric TM-wave from bi-cone formed by finite and semi-infinite shoulders," Prog. Electromagn. Res. B, **68**, 73-88 (2016). http://dx.doi.org/10.2528/PIERB16041302
[22] O. Dumin, P. Fomin, V. Plakhtii, and M. Nesterenko, "Ultrawideband combined monopole-slot radiator of Clavin type," in Proc. XXVth Int. Sem. Direct Inverse Problems of Electromagn. and Acoustic Wave Theory, 32-36 (2020). https://doi.org/10.1109/DIPED49797.2020.9273399

[23] P. Fomin, O. Dumin, V. Plakhtii, and M. Nesterenko, "UWB antenna arrays with the monopole-slot radiator of Clavin type," in Proc. III-th Ukraine Conf. on Electrical and Computer Engineering, 258-261 (2021). https://doi.org/10.1109/UKRCON53503.2021.9575282
[24] M. V. Nesterenko, A. V. Gomozov, V. A. Katrich, S. L. Berdnik, and V. I. Kijko, "Scattering of electromagnetic waves by impedance biconical vibrators in a free space and in a rectangular waveguide," Prog. Electromagn. Res. C, **119**, 275-285 (2022). http://dx.doi.org/10.2528/PIERC22020304
[25] O. Dumin, V. Plakhtii, O. Skvortsova, and V. Katrich, "Tilted cone-enhanced ultrawideband monopole-slot radiators in antenna arrays," in Proc. XXIXth Int. Sem. Direct Inverse Problems of Electromagn. and Acoustic Wave Theory, 122-127 (2024). https://doi.org/10.1109/DIPED63529.2024.10706144
[26] M. V. Nesterenko, V. A. Katrich, Y. M. Penkin, V. M. Dakhov, and S. L. Berdnik, *Thin Impedance Vibrators. Theory and Applications*, (New York: Springer Science+Business Media, 2011). https://doi.org/10.1007/978-1-4419-7850-9
[27] T. W. Hertel, and G. Smith, "The insulated linear antenna-revisited," IEEE Trans. Antennas Propag., **48**, 914-920 (2000). https://doi.org/10.1109/8.865224
[28] S. A. Pogarsky, D. V. Mayboroda, and S. M. Mykhaliuk, "Influence of aperture of radiating strip structure on electrodynamic characteristics of patch antenna," East European J. Physics, 4, 274-280 (2023). https://doi.org/10.26565/2312-4334-2023-4-34
[29] M. Livio, *The Golden Ratio: The Story of PHI, the World's Most Astonishing Number*, (New York: Broadway Books, 2002).
[30] M. A. Barnes, "Ultra-wideband magnetic antenna," US patent 6,091,374, July 18, (2000).

ВХІДНІ ХАРАКТЕРИСТИКИ ЕЛЕКТРИЧНО ТОНКОГО ДИПОЛЯ ЗІ ЗМІННИМ РАДІУСОМ ВЗДОВЖ АНТЕНИ

М. В. Нестеренко, О. М. Думин, Ю. В. Аркуша
Харківський національний університет імені В.Н. Каразіна, майдан Свободи, 4, Харків, Україна, 61022

Представлено наближене аналітичне розв'язання задачі випромінювання (дифракції) електромагнітних хвиль диполем (монополем) зі змінним радіусом вздовж довжини антени. Розв'язання виконано з використанням узагальненого методу індукованих електрорушійних сил (ЕРС). Чисельно досліджено вплив зміни радіуса монополя на вхідні характеристики. Теоретичні результати порівнюються з експериментальними даними.

Ключові слова: *диполь; монополь; змінний радіус; вхідні характеристики; узагальнений метод наведених ЕРС*

East European Journal of Physics. 4. 601-606 (2025)
DOI:10.26565/2312-4334-2025-4-63 ISSN 2312-4334

EFFECT OF TiO_2 LAYER THICKNESS ON ELECTRODE DEGRADATION IN REDOX FLOW BATTERIES

Shukhrat Ch. Iskandarov*, Ilyos Kh. Khudaykulov, Temur K. Turdaliev, Usmonjon F. Berdiyev, Sardor A. Tulaganov, Boburjon R. Kakhramonov
Institute of Ion-Plasma and Laser Technologies named after U.A. Arifov, Academy of Sciences of the Republic of Uzbekistan, 100125, Durmon yuli st. 33, Tashkent, Uzbekistan
**Corresponding Author e-mail: iskandarov@iplt.uz*
Received August 21, revised October 7, 025; in final form October 14, 2025; accepted October 17, 2025

In this work, TiO_2 coatings of varying thicknesses were deposited on carbon felt fibers via ALD (Atomic Layer Deposition), and the mechanical and electrochemical properties of the electrodes were studied. The experimental results show that the TiO_2 coating effectively protects and enhances the stability of carbon wet electrodes. While a 4% mass loss was observed on the untreated cathode electrode, this decreased to 1.6-1.7% with a TiO_2 coating. When the coating thickness was increased from 50 nm to 300 nm, no significant change in mass loss was observed, which indicates that even thin coatings provide effective protection. The mass loss in the anode electrode was relatively small, ranging from 2% in the untreated state and 0.5-1.1% in the coated states. This is explained by the lower anode potential than the cathode and the low sensitivity of the V^{2+}/V^{3+} redox reaction at the anode. It was found that the titanium dioxide coating plays an important role in increasing the electrodes' electrochemical degradation and corrosion resistance, as well as extending battery life. It was also shown that a 50 nm thick TiO_2 coating can provide effective protection, whereas very thick coatings can limit electron mobility. These results confirm that TiO_2 coatings are one of the promising solutions for protecting electrode materials in vanadium flow batteries.
Keywords: *Electrodes; Electrocatalysts; Redox flow batteries; Energy storage systems; Metals; Metal oxides*
PACS: 82.45.Fk; 82.47.Rs; 81.15.Gh; 81.05.Je;

INTRODUCTION

Currently, the main advantage of RFB technology is that it allows the use of various redox couples (for example, vanadium, iron-chromium or zinc bromide ions). The most widely studied and effectively used in practice is the fully vanadium redox battery (VRFB). This technology allows for efficient energy storage by using vanadium ions from a homogeneous element as an electrolyte [1]. The main components required for the operation of RFB include electrolytes [2], electrodes [3] and membranes [4].

Numerous scientific studies by scientists around the world have identified carbon-based materials that not only exhibit superior electrical conductivity for vanadium redox battery electrolytes but are also the most cost-effective materials for use in both the negative and positive half-cells of vanadium redox batteries. Commonly used carbon-based materials for RFBs include graphite felt (GF), carbon paper (CP), carbon nanotubes (CNTs), graphene oxide (GO), graphite, and graphene.

Graphite felt (GF) has a three-dimensional (3D) porous structure with high specific surface area [5] and many outstanding properties, such as excellent electrical conductivity, flexibility, corrosion resistance, and electrochemical stability [6,7]. Therefore, it has been widely studied as an electrode for energy and environmental protection, including vanadium-reduction-flow batteries (VRFBs) [8,9].

To improve the electrochemical activity of GF, the hydrophobic surface of the original GF should be changed to a hydrophilic surface, and in addition, the GF should maintain its natural good electrical conductivity at the same time. Several methods have been successfully used to modify the surface of GF, including plasma treatment [10], chemical cleaning [11], thermal treatment [12,13], nitrogenization treatment [14], carbon nanomaterial-based modification [15, 16], nanostructured metals [17], and metal oxides [18], among others.

In addition, the modified GF should exhibit long-term hydrophilicity stability and excellent chemical stability to protect electrochemical devices such as vanadium redox flow batteries (VRFBs), aluminum-ion batteries [19], etc., from corrosive electrolytes.

TiO_2 is an n-type semiconductor with natural hydrophilicity and excellent chemical stability in acidic media, and is used in various applications such as solar cells, photocatalysts, and sensors [20]. In addition, TiO_2 has been reported to enhance the wettability of the catalyst layer and is also chemically stable [21].

The hydrophobic surface of GF can be changed to hydrophilic by coating with TiO_2 films. When TiO_2-modified GF is applied to electrochemical devices, the TiO_2 surface coating can withstand the corrosion of a strong acidic electrolyte.

ALD is an advanced technique for growing highly conformal thin films on the surfaces of three-dimensional complex structures and nanostructures with atomic-level thickness control and excellent coating uniformity. Therefore,

Cite as: Sh.Ch. Iskandarov, I.Kh. Khudaykulov, T.K. Turdaliev, U.F. Berdiyev, S.A. Tulaganov, B.R. Kakhramonov, East Eur. J. Phys. 4, 601 (2025), https://doi.org/10.26565/2312-4334-2025-4-63

TiO_2 films of different thicknesses can be uniformly coated on the surface of GF by ALD technology with precise control of the film thickness at the nanoscale.

In this work, we have grown a nano-coated TiO_2 film (with different thicknesses) on the surface of GF, an ultra-thin TiO_2 film with nanocrystalline structure through atomic layer deposition (ALD) to modify the surface of GF, which not only imparts hydrophilicity to GF, but also ensures sufficient conductivity of ALD-TiO_2 modified GF (ALD-TiO_2/GF)[22]. With its good electrochemical properties, the ALD-TiO_2/GF electrode is expected to have potential applications in vanadium redox flow batteries (VRFB), aluminum-ion batteries, and other electrochemical energy storage devices.

METHODS AND EQUIPMENT

Electrode modification: The sample was coated with titanium dioxide using thermal atomic layer deposition (ALD). The process was performed using a precursor pair of titanium tetraisopropoxide (TTIP) and deionized water. The deposition parameters were as follows: nitrogen flow rate 120 cm^3/min, reactor pressure approximately 60 Pa, substrate temperature approximately 250 ^{0}C, and cycle duration 8 s. Each ALD cycle consisted of the following five steps: initial purge; 0.5 s TTIP pulse; 3 s nitrogen purge; 1.5 s H_2O pulse; and a final 3 s nitrogen purge. Under these conditions, the growth per cycle (GPC) was determined to be 0.2 nm. A detailed description of the deposition process can be found in the literature below [23].

Electrolyte preparation: We used recycled V_2O_5 powder, sulfuric acid, and deionized water to prepare a 1.5 mol/l vanadium electrolyte. For this purpose, we ground the recycled V_2O_5 powder in a special mill and passed it through a 400 μm sieve to separate the V_2O_5 oxide powder of the same size for melting. In addition, a single-cell membrane electronic block (MEB) was assembled to test the electrode system.

Laboratory model of the membrane electronic block (MEB): We used a Nafion-117 membrane as a separator between the prepared graphite bipolar plate to assemble the MEB. We used a 2 mm thick silicone rubber gasket as the compression layer for the graphite bipolar plate, with a working area of 42 mm × 40 mm. Instead, two identical electrodes of the same dimensions and 3 mm thickness, made of carbon felt (Zibo Ouzheng Carbon Co., Ltd., China), were employed to assemble a single-cell MEB. To prevent the graphite bipolar plate from breaking and to compress it with uniform force, an external compression mold was made using HP panels. This HP panel not only protects the graphite plate from cracking but also uses a 0.5 mm thick copper sheet as a collector between the graphite plate and the HP panel to remove electrons generated by the oxidation-reduction reaction at the electrodes [24].

RESULTS AND DISCUSSIONS

Carbon felt was used as the electrode. Figure 1 below shows an image of carbon felt coated with titanium oxide using the ALD method. Figure 1 (left) shows a general image of carbon felt coated with titanium dioxide (TiO_2) using the ALD (Atomic Layer Deposition) method (200 μm). Figure 1 (right) shows an image of carbon fiber coated with titanium dioxide (TiO_2) using the ALD (Atomic Layer Deposition) method (10 μm). Here we can observe a change in the color of the fibers and an increase in their brightness. This optical effect is observed due to a change in the light scattering properties of the ray's incident on the surface of titanium dioxide.

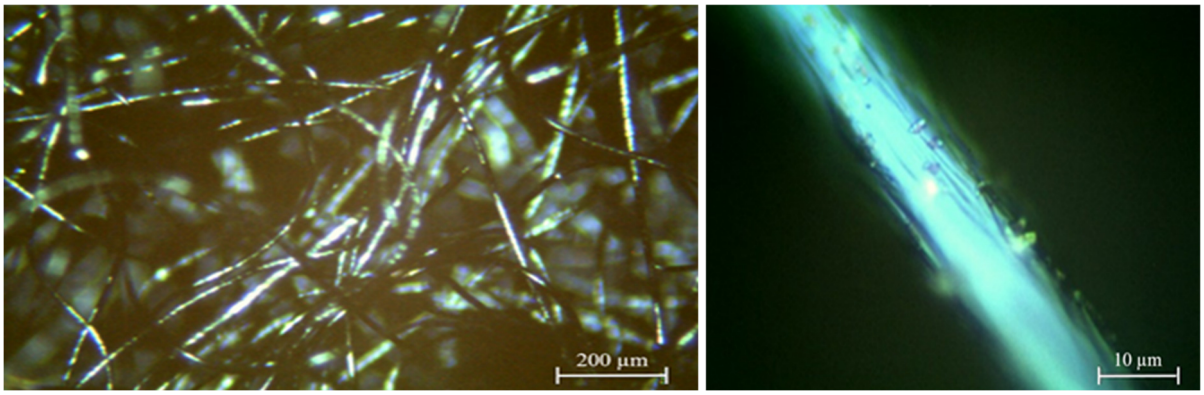

Figure 1. Optical microscope image of carbon felt. General view of the TiO_2 coated sample; (left), image of carbon fiber after TiO_2 coating; (right)

The images show that the fibers change color after being coated with titanium dioxide using ALD. This phenomenon is related to the interaction of light with the surface, the refractive index of titanium dioxide, and optical dispersion.

Since titanium dioxide has a high refractive index, the ability of the fibers to scatter light increases, making them appear brighter. As shown in the image above, the difference between the carbon felt coated with titanium oxide by ALD is visually apparent.

However, we conducted another method, Raman spectroscopy, to verify that the surface of the carbon felt was indeed coated with TiO_2 by ALD. The results of our analysis are presented in Figure 2. The red dashed line below shows

the Raman spectrum of the carbon felt without any treatment. The blue line shows the Raman spectrum of the carbon felt with a thin layer of TiO_2, that is, modified.

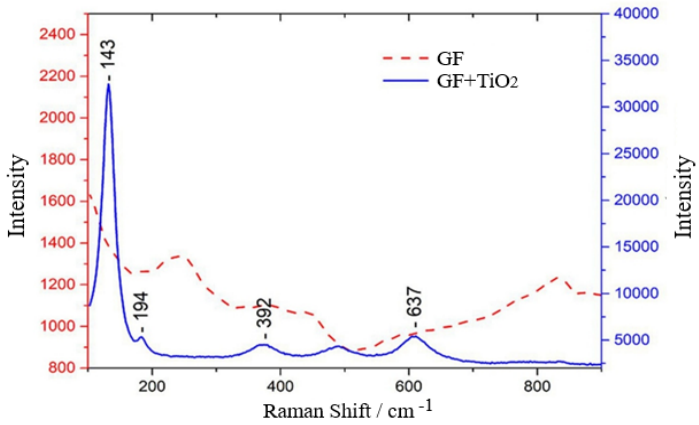

Figure 2. Raman spectra of carbon felt with and without TiO_2 nanocoating

In this graph, the peaks in the red dashed lines that characterize the sample without carbon felt treatment are not clearly distinguished by their intensity. However, we can observe characteristic Raman peaks in the blue line on the TiO_2-coated, i.e. modified electrode. Here, 143 cm^{-1} (main peak) is characteristic of the anatase phase of TiO_2, indicating the presence of nanostructured TiO_2 on the carbon felt surface [25]. The remaining peaks at 194 cm^{-1}, 392 cm^{-1}, 637 cm^{-1} are also associated with nanoscale structures of TiO_2, reflecting their phonon vibrational properties. From the above optical microscope image and Raman spectrum results, it is clear that a TiO_2 anatase phase coating was formed on the surface of the carbon felt. Thus, we assembled a laboratory model of a single-cell vanadium flow battery to test our modified electrode by coating the TiO_2 coating on the surface of the carbon felt. We conducted a series of test experiments to test the resistance of the TiO_2 coated electrode to the charging and discharging processes.

We conducted our experiments by testing modified electrode materials with different thicknesses. The mechanism of the change in the open-circuit voltage curve over time during the charging process of our modified electrode with different thicknesses is shown in Figure 3 below.

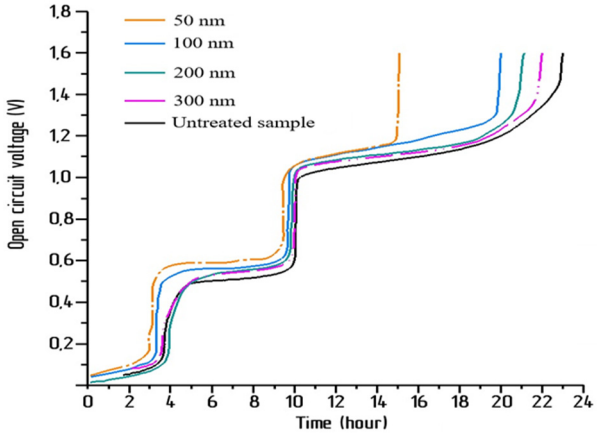

Figure 3. Graph of the open circuit voltage versus charging time of electrodes with TiO_2 coatings of different thicknesses during the first charge

Several studies have been conducted to prevent electrolysis corrosion of the carbon felt surface during the operation of a vanadium flow battery. Here, since the environment is acidic, a certain amount of corrosion is observed on the surface of the electrodes. For this reason, a material with good electrical conductivity and resistance to acidic environments is required as an electrode material. During charging and discharging (direct chemical oxidation), electrolysis can further accelerate the corrosion of the electrode surface. To avoid this problem, researchers are trying to modify the electrode surface with various metal oxides.

As mentioned above, a 50-300 nm thick TiO_2 coating was applied to the carbon felt surface using the ALD method, compared to an untreated sample. Figure 3 shows that the charging time for the untreated sample is 23 hours. For the modified electrode with a thickness of 50 nm, the charging time was reduced to 15.2 hours (1.5 times). At 100, 200 and 300 nm, the charging time is almost approaching the charging time of the untreated sample. This is because in the modified electrode with a thickness of 50 nm, TiO_2 fully demonstrates its catalytic and hydrophilic properties. At 100, 200 and 300 nm, the movement of electrons is hindered. This, in turn, causes the charging time to increase.

In addition, the studies were carried out several times, and after each study, the mass of the electrodes was measured. Initially, samples coated with TiO_2 coatings of 50 nm, 100 nm, 200 nm, and 300 nm thickness were selected and the mass loss (degradation) of each sample at the anode and cathode was measured over 300 cycles. Figure 4 presents the mass loss of the cathode and anode electrodes after modification with different thicknesses, compared to the initial sample.

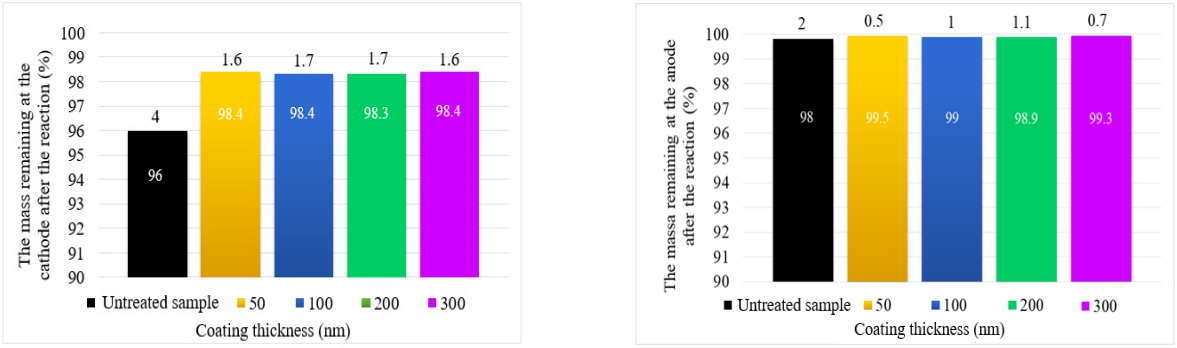

Figure 4 Histogram of electrode degradation (mass loss) during the first charging process. (a) Mass loss in untreated and modified cathodes; (b) Mass loss in untreated and modified anodes

In Figures 4a and 4b, the black columns represent the initial sample (without titanium oxide coating), where electrode degradation reaches up to 4%. In the samples with a TiO_2 coating, the mass loss decreased sharply, falling within the range of approximately 1.6–1.7%. Due to the chemical stability of the TiO_2 coating, it protects the electrode surface from corrosion. In samples with a coating, passivation is formed, which limits the reaction of soluble material with the electrolyte. There was no significant difference between the coating thicknesses of 50 nm and 300 nm, which indicates that the carbon felt was effectively protected with a thin layer of TiO_2.

Thus, cathode electrodes coated with titanium dioxide allowed to reduce mass loss by up to 2.3 times. Increasing the thickness can prevent the release of electrons from the electrode surface. This confirms the effectiveness of the 50 nm TiO_2 coating in protecting the electrode materials.

As can be seen from Figure 4-b), the mass loss in the anode system of vanadium flow batteries is very low - 2% for the untreated sample, and in the case of TiO_2 coating, we can observe a mass loss in the range of 0.5–1.1%. The anode process in vanadium flow batteries occurs through the V^{2+} - V^{3+} reaction. This process usually does not cause significant material loss, since the electron exchange does not significantly change the structure of the anode electrode.

CONCLUSIONS

The study's results confirmed that titanium dioxide (TiO2) coatings effectively enhance the mechanical and electrochemical stability of carbon felt electrodes. In the initial case, a 4% mass loss was observed in the cathode, but this decreased to 1.6–1.7% when the TiO_2 coating was applied. The fact that increasing the coating thickness from 50 nm to 300 nm did not result in a significant difference in mass loss indicates that even thin coatings can provide effective protection. The mass loss in the anode electrode was relatively small, initially at 2%, and in the range of 0.5–1.1% when the TiO_2 coating was applied. This is explained by the low sensitivity of the V^{2+}/V^{3+} reaction at the anode in vanadium flow batteries, and by the lower anode potential relative to the cathode. Titanium dioxide coating increases the resistance of electrodes to corrosion and electrochemical corrosion, extending their service life. In coated samples, mass loss in cathode electrodes was reduced by a factor of 2.3. Thin coatings (50 nm) can also provide effective protection, but very thick coatings are likely to restrict electron mobility.

TiO_2 coating plays an important role in protecting electrode materials in vanadium flow batteries. Coatings protect the anode and cathode electrodes from mechanical and electrochemical corrosion, ensuring long-term stability of batteries. Therefore, TiO_2 coating is a promising method for improving the efficiency of energy storage systems in the future.

Acknowledgments

This research was conducted with the support of budgetary and grant funding from the Academy of Sciences of the Republic of Uzbekistan.

ORCID

Shukhrat Ch. Iskandarov, https://orcid.org/0000-0002-3002-9141; **Ilyos Kh. Khudaykulov,** https://orcid.org/0000-0002-2335-4456
Temur K. Turdaliev, https://orcid.org/0000-0002-0732-9357; **Usmonjon F. Berdiyev,** https://orcid.org/0000-0003-2808-0105
Sardor A. Tulaganov, https://orcid.org/0000-0003-1881-2165;

REFERENCES

[1] Kh.B. Ashurov, B.M. Abdurakhmanov, Sh.CH. Iskandarov, and T.K. Turdaliev, “Solving the problem of energy storage for solar photovoltaic plants (review),” Applied Solar Energy, **55**(2), 119–125 (2019). https://doi.org/10.3103/S0003701X19020038
[2] M. Skyllas-Kazacos, L. Cao, M. Kazacos, N. Kausar, and A. Mousa, “Vanadium Electrolyte Studies for the Vanadium Redox Battery-A Review,” Chem. Sus. Chem. **9**(13), 1521–1543 (2016). https://doi.org/10.1002/cssc.201600102

[3] K.J. Kim, M.-S. Park, Y.-J. Kim, J.H. Kim, S.X. Dou, and M. Skyllas-Kazacos, "A technology review of electrodes and reaction mechanisms in vanadium redox flow batteries," Journal of Materials Chemistry A, **3**(33), 16913–16933 (2015). https://doi.org/10.1039/c5ta02613j
[4] U.F. Berdiev, I.K. Khudaykulov, S.C. Iskandarov, A.J. Amirova, and K.B. Ashurov, "Influence of SiO_2 Nanoparticles on the Characteristics of a Polyvinyl Alcohol-Based Proton Exchange Composite Membrane," East European Journal of Physics, (1), 265-271 (2025). https://doi.org/10.26565/2312-4334-2025-1-30
[5] Z. Zhang, J. Xi, H. Zhou, and X. Qiu, "KOH etched graphite felt with improved wettability and activity for vanadium flow batteries," Electrochim. Acta, **218**, 15–23 (2016). https://doi.org/10.1016/j.electacta.2016.09.099
[6] L. Wu, J. Wang, Y. Shen, L. Liu, and J. Xi, "Electrochemical evaluation methods of vanadium flow battery electrodes," Phys. Chem. Chem. Phys. **19**, 14708–14717 (2017). https://doi.org/10.1039/c7cp02581e
[7] L.F. Castañeda, F.C. Walsh, J.L. Nava, and C.P.D. León, "Graphite felt as a versatile electrode material: Properties, reaction environment, performance and applications," Electrochim. Acta, **258**, 1115–1139 (2017). https://doi.org/10.1016/j.electacta.2017.11.165
[8] D.M. Kabtamu, J.Y. Chen, Y.C. Chang, and C.H. Wang, "Water-activated graphite felt as a high-performance electrode for vanadium redox flow batteries," J. Power Sources, **341**, 270–279 (2017). https://doi.org/10.1016/j.jpowsour.2016.12.004
[9] F. Jianga, Z. Heb, D. Guoa, and X. Zhoua, "Carbon aerogel modified graphite felt as advanced electrodes for vanadium redox flow batteries," J. Power Sources, **440**, 227114 (2019). https://doi.org/10.1016/j.jpowsour.2019.227114
[10] D. Dixon, D.J. Babu, J. Langner, M. Bruns, L. Pfaffmann, and A. Bhaskar, "Effect of oxygen plasma treatment on the electrochemical performance of the rayon and polyacrylonitrile based carbon felt for the vanadium redox flow battery application," J. Power Sources, **332**, 240–248 (2016). https://doi.org/10.1016/j.jpowsour.2016.09.070
[11] D. Hidalgo, T. Tommasi, S. Bocchini, A. Chiolerio, A. Chiodoni, and I. Mazzarino, "Surface modification of commercial carbon felt used as anode for Microbial Fuel Cells," Energy, **99**, 193–201 (2016). https://doi.org/10.1016/j.energy.2016.01.039
[12] B. Sun, and M. Skyllas-Kazacos, "Modification of graphite electrode materials for vanadium redox flow battery application-I. Thermal treatment," Electrochim. Acta, **37**, 1253–1260 (1992). https://doi.org/10.1016/0013-4686(92)85064-r
[13] A.M. Pezeshki, J.T. Clement, G.M. Veith, T.A. Zawodzinski, and M.M. Mench, "High performance electrodes in vanadium redox flow batteries through oxygen-enriched thermal activation," J. Power Sources, **294**, 333–338 (2015). https://doi.org/10.1016/j.jpowsour.2015.05.118
[14] S. Chen, W. Hu, J. Hong, and S. Sandoe, "Electrochemical disinfection of simulated ballast water on PbO_2/graphite felt electrode," Mar. Pollut. Bull. **105**, 319–323 (2016). https://doi.org/10.1016/j.marpolbul.2016.02.003
[15] S. Wang, X. Zhao, T. Cochell, and A. Manthiram, "Nitrogen-doped carbon nanotube/graphite felts as advanced electrode materials for vanadium redox flow batteries," J. Phys. Chem. Lett. **3**, 2164–2167 (2012). https://doi.org/10.1021/jz3008744
[16] A.A. Rakhimov, *et al*. "Analysis of Temperature-Dependent Surface Properties in the Ni/SiO_2/Si System During Electron Beam Deposition," East European Journal of Physics, (3), 436-441 (2025). https://doi.org/10.26565/2312-4334-2025-3-47
[17] R. Solmaz, A. Gündoğdu, A. Döner, and G. Kardaş, "The Ni-deposited carbon felt as substrate for preparation of Pt-modified electrocatalysts: Application for alkaline water electrolysis," Int. J. Hydrogen Energy, **37**, 8917–8922 (2012). https://doi.org/10.1016/j.ijhydene.2012.03.008
[18] Y. Xiang, and W.A. Daoud, "Investigation of an advanced catalytic effect of cobalt oxide modification on graphite felt as the positive electrode of the vanadium redox flow battery," J. Power Sources, **415**, 175–183 (2019). https://doi.org/10.1016/j.jpowsour.2019.01.079
[19] I.K. Ashurov, M.M. Adilov, and K.B. Ashurov, "Understanding the Influence of Electrolyte Optimization and Graphene Paper Cathodes on the Electrochemical Performance of Aluminum Dual-Ion Batteries," Appl. Sol. Energy, **60**, 727–735 (2024). https://doi.org/10.3103/S0003701X24603405
[20] S. Bagheri, N.M. Julkapli, and S.B.A. Hamid, "Titanium Dioxide as a Catalyst Support in Heterogeneous Catalysis," The Scientific World Journal, **2014**, 1–21 (2014). https://doi.org/10.1155/2014/727496
[21] W.-K. Chao, R.-H. Huang, C.-J. Huang, K.-L. Hsueh, and F.-S. Shieu, "Effect of Hygroscopic Platinum/Titanium Dioxide Particles in the Anode Catalyst Layer on the PEMFC Performance," Journal of The Electrochemical Society, **157**(7), B1012 (2010). https://doi.org/10.1149/1.3428725
[22] G.B. De Souza, D. Hotza, R. Janßen, K.P. Furlan, and C.R. Rambo "Functionalization of Carbon Electrodes with Nanotitania by Atomic Layer Deposition," Advances in Materials Science and Engineering, **2022**, 9575845 (2022). https://doi.org/10.1155/2022/9575845
[23] T.K. Turdaliev, "Optical Performance and Crystal Structure of TiO_2 Thin Film on Glass Substrate Grown by Atomic Layer Deposition," East European Journal of Physics, (1), 250-255 (2025). https://doi.org/10.26565/2312-4334-2025-1-27
[24] Sh.Ch. Iskandarov, I.Kh. Ashurov, U.F. Berdiyev, U.B. Khursandov, and Kh.B. Ashurov, "Preparation of electrolyte from recycled V_2O_5 for vanadium redox flow batteries and evaluation of its application potential," Physics and Chemistry of Materials Treatment, **2**, 77-82 (2025). https://doi.org/10.30791/0015-3214-2025-2-77-82
[25] T.K Turdaliev, K.B. Ashurov, and R.K. Ashurov, "Morphology and Optical Characteristics of TiO_2 Nanofilms Grown by Atomic-Layer Deposition on a Macroporous Silicon Substrate," J. Appl. Spectrosc. **91**, 769–774 (2024). https://doi.org/10.1007/s10812-024-01783-z

ВПЛИВ ТОВЩИНИ ШАРУ TiO_2 НА ДЕГРАДАЦІЮ ЕЛЕКТРОДІВ В ОКИСНОВІДНОВНИХ ПРОТОЧНИХ АКУМУЛЯТОРАХ

Шухрат Ч. Іскандаров, Ільос Х. Худайкулов, Темур К. Турдалієв, Усмонджон Ф. Бердієв, Сардор А. Тулаганов, Бобурджон Р. Кахрамов

Інститут іонно-плазмових та лазерних технологій імені У.А. Аріфова, Академія наук Республіки Узбекистан, 100125, вул. Дурмон йулі, 33, Ташкент, Узбекистан

У цій роботі покриття TiO_2 різної товщини були нанесені на вуглецеві волокна фетру методом ALD (атомно-шарове осадження), а також досліджені механічні та електрохімічні властивості електродів. Експериментальні результати показують, що покриття TiO_2 ефективно захищає та підвищує стабільність вуглецевих мокрих електродів. Хоча втрата маси необробленого катодного електрода спостерігалася на рівні 4%, цей показник зменшився до 1,6-1,7% після нанесення покриття TiO_2. Коли товщина покриття збільшилася з 50 нм до 300 нм, суттєвої зміни втрати маси не спостерігалося, що свідчить про те, що навіть тонкі покриття забезпечують ефективний захист. Втрата маси анодного електрода була відносно невеликою, коливаючись від 2% у необробленому стані до 0,5-1,1% у покритому стані. Це пояснюється нижчим анодним потенціалом, ніж у катода, та низькою чутливістю окисно-відновної реакції V2+/V3+ на аноді. Було виявлено, що покриття з діоксиду титану відіграє важливу роль у підвищенні електрохімічної деградації та корозійної стійкості електродів, а також у подовженні терміну служби батареї. Також було показано, що покриття TiO2 товщиною 50 нм може забезпечити ефективний захист, тоді як дуже товсті покриття можуть обмежувати рухливість електронів. Ці результати підтверджують, що покриття TiO_2 є одним із перспективних рішень для захисту електродних матеріалів у ванадієвих проточних батареях.

Ключові слова: *електроди; електрокаталізатори; окисно-відновні проточні батареї; системи накопичення енергії; метали; оксиди металів*

East European Journal of Physics. 4. 607-619 (2025)
DOI:10.26565/2312-4334-2025-4-64 ISSN 2312-4334

SIMULATION OF FOCUSING A HOLLOW ELECTRON BEAM BY THE SYMMETRIC MAGNETIC LENS FOR INDUSTRIAL APPLICATION IN ADDITIVE TECHNOLOGIES

Igor V. Melnyk[1]*, Serhii B. Tuhai[1], Mykhailo Yu. Skrypka[1], Mykola S. Surzhikov[1], Oleksandr M. Kovalenko[1], Dmytro V. Kovalchuk[2]

[1]National Technical University of Ukraine "Igor Sikorsky Kyiv Polytechnical Institute", Kyiv, Ukraine
**Corresponding Author e-mail: imelnik@phbme.kpi.ua; Tel: 066-981-70-66*
[2]Joint Stock Company, Scientific and Industrial Association "Chervona Hvylia", Kyiv, Ukraine
Received July 22, 2025; revised November 11, 2025; in final form November 18, 2025; accepted November 20, 2025

The article studies the focusing features of a short-focus hollow electron beam formed from a wide surface of a cold cathode in high-voltage glow discharge electron guns using numerical simulation techniques. Such a type of electron beam is widely used today for producing new kinds of metals with unique properties by melting wire, which moves in a vertical direction through the ring-like beam focus. After that, the melted metal is crystallized on the horizontally moving substrate, which is located near the focus of the electron beam below. Such modern technology is considered three-dimensional printing of metal, or additive technologies. The original software created by the authors in the Python programming language has been used to obtain the corresponding simulation results. Analysis of the obtained numerical simulation results proved that with a small change in the beam trajectory divergence angle or the radius of the initial point on the cathode surface, the beam focus position, as a rule, does not change. Therefore, the annular focus of the beam is usually in a stable position on the longitudinal coordinate, and the thickness of the focal ring is always in the range of several millimeters. The corresponding theoretical results were compared with experimental data, and the difference between the theoretical and experimental results is in the range of 10-15% depending on the accelerating voltage and size of the cathode surface. High-voltage glow discharge electron guns with such parameters, by the thickness of the focal ring, can be successfully used in advanced industrial additive technologies for three-dimensional printing on metal surfaces by uniform heating along the perimeter of moving wires or rods with a variable diameter in the range of 0.5 – 10 mm.
Keywords: *Additive technologies; Electron beam technologies; Magnetic focusing; Hollow conical electron beam; Numerical simulation*
PACS: 29.25.Bx, 03.50.De

INTRODUCTION

Electron beam technologies are widely used in different branches of industry, especially in the technologies of additive production [1 – 16]. The special place in these technologies occupied the High-Voltage Glow Discharge Electron Guns (HVGDEG), which formed profile electron beams [15, 16]. It caused by such advanced particularities of HVGDEG, as relative simplicity of engineering construction, [17 – 29], operation with different active and noble technological gases [28, 29], as well as simplicity of control of Electron Beam (EB) current both aerodynamically by changing operation pressure in the gun chamber with controlled gas inlet and uninterrupted pumping [29] and electrically by changing the current of additional low-voltage gas discharge [30, 31]. Another advantage of HVGDEG is the possibility of forming EB with complex spatial geometry, including hollow conical EB with ring-like focus and ribbon electron EB with line focus. General approaches for estimating the geometry parameters of such types of HVGDEG are given in the papers [15, 16]. Generally, this possibility is explained by the relatively small current density from the cathode surface; therefore, enlarging the surface for forming a powerful EB is really necessary [28].

Today EB equipment is widely used in advanced technologies of additive production [1 – 16]. The main distinguishing features of additive technologies are significant savings in electricity and consumables, high equipment productivity, and, most importantly, the ability to obtain new ultra-high purity materials with unique properties. Therefore, the main areas of industry in which additive technologies are used today are the chemical industry, shipbuilding, aircraft manufacturing, and the space industry. Generally, lasers and EB as technological instruments, are used today in equipment for additive production. The process of laser heating can be realized in air; therefore, such equipment is usually cheaper [1 – 15]. But, on the contrary, the advantages of EB equipment are high productivity and high purity of production, as well as unique physical and chemical properties of obtained materials [15].

Expanded capabilities for designing electron-beam equipment in modern additive technologies, including the use of High-Voltage Glow Discharge Electron Guns (HVCDEG), which form a hollow conical EB [15, 16]. The main advantage of using this type of gun in the implementation of additive technologies with wire melting directly near the substrate is that the hollow conical electron beam uniformly heats the wire along its entire perimeter [15, 16].

It should be pointed out that there are two possible ways to form the hollow conical EB in HVGDEG, namely, using electrostatic focusing with cathode geometry as part of a sphere [15] and focusing in a short magnetic lens with the plane cathode geometry [16]. The basic structure scheme of HVGDEG construction with electrostatic focusing with cathode geometry as part of a sphere is presented in Fig. 1 [16]. The main advantage of this construction is the stable position of

Cite as: I.V. Melnyk, S.B. Tuhai, M.Yu. Skrypka, M.S. Surzhikov, O.M. Kovalenko, D.V. Kovalchuk, East Eur. J. Phys. 4, 607 (2025), https://doi.org/10.26565/2312-4334-2025-4-64

the electron beam focus, simplicity of the focusing systems, as well as the relatively stable focal current density throughout the whole time of providing the technological process. But, on the contrary, HVGDEG electrode systems with electrostatic focusing are difficult to exploit and assemble. Corresponding recommendations on parameters of HVGDEG from the point of view of the coaxial arrangement of gun parts have been considered in papers [15]. Changing the diameter of EB focal ring, as well as its thickness, for different wire diameters in such construction, is also impossible without changing the electrode system.

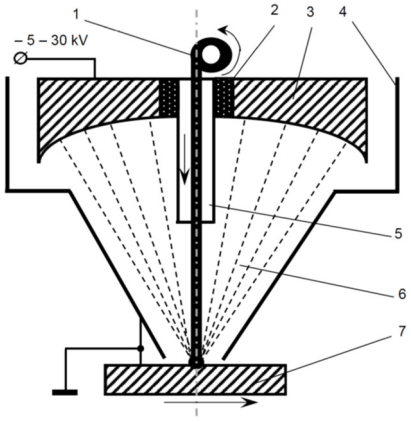

Figure 1. Generalized constructive scheme of HVGDEG with spherical cathode for three-dimensional printing by metal. 1 – moving ware, 2 – high-voltage insulator, 3 – cathode of HVGDEG, 4 – anode of HVGDEG, 5 – wire feed mechanism, 6 – hollow conical EB, 7 – moving substrate

Therefore, the aim of this paper is estimation of trajectories of hollow conical EB, which is formed from the cathode with plane geometry by focusing in a short magnetic lens [16]. It is clear that the main advances of this HVGDEG electrode system are the possibility of changing the diameter of the focal ring of the hollow EB and its thickness [16]. For providing these researches, the original computer software [32–34], created in the Python programming language [35-37], has been used.

STATEMENT OF SIMULATION PROBLEM AND MODEL PARAMETERS

The basic structure scheme of HVGDEG construction with plane cathode geometry and magnetic lens for focusing of hollow EB is presented in Fig. 2 [16].

From the point of view of the fundamental laws of electron optics [38–42], it is well known that only a diverging electron beam can be focused in the magnetic field of a short-focus lens. Since the cathode surface is flat, the divergence of electrons in the initial section of the trajectory near the cathode is caused by their dissipation on the atoms of the residual gas, in accordance with the Rutherford model [39, 41–45]. As for the defocusing of the beam by the intrinsic space charge of the electrons, under the physical conditions of a high-voltage glow discharge (HVGD), it is absent, since it is compensated for by the space charge of the positive ions of the residual gas [43–45].

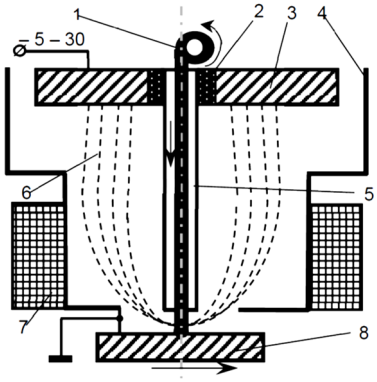

Figure 2. Generalized constructive scheme of HVGDEG with plane cathode and focusing magnetic lens for three-dimensional printing by metal. 1 – moving ware, 2 – high-voltage insulator, 3 – cathode of HVGDEG, 4 – anode of HVGDEG, 5 – wire feed mechanism, 6 – hollow EB, 7 – focusing magnetic lens, 8 – moving substrate

Another important property of HVGD electrode systems is the presence of anode plasma (AP) in the near-anode region. AP always has a clearly defined boundary. Therefore, in numerical modeling problems, it is usually considered as a source of ions' flow and as an electrode with a fixed potential transparent for the electron beam [28, 31]. The anode plasma (AP) region in HVGD photographs is always separated from the region of charged particle acceleration in the electric field, which is usually called the cathode fall region (CFR). Indeed, the AP is always the brighter part of the HVGD combustion region image [28, 31].

In general, from a physical point of view, in theoretical estimates, the AP boundary is usually defined as a fraction of the volume it occupies in the electrode system under consideration. Therefore, the position of the AP boundary always depends significantly on the accelerating voltage and the type and pressure of the residual gas, as well as on the geometry of the electrodes, including a spherical or flat cathode and a hollow anode of the HVGD. The geometry of the AP boundary always changes with a change in the discharge current in accordance with the geometry of the hollow anode surface. With an increase in the HVGD current and the pressure in the volume where the discharge is ignited, the AP boundary moves asymptotically toward the cathode surface and, at high discharge currents, becomes geometrically similar to it [21–25]. A correct estimate of the position of the AP boundary in an electrode system with a flat cathode surface and a cylindrical hollow anode is given in [16].

If the above-described physical conditions of the HVGD combustion in the electrode system presented in Fig. 2 are taken into account, the input parameters of the statement simulation task are as follows.

1. Acceleration voltage U_c.
2. Operation pressure p_g, and, correspondently, current of EB I_b, which is usually defined by the current-voltage characteristic of HVGD [28].
3. Angle of beam divergence α near the cathode surface.
4. Maximal and minimal value of EB radius $r_{b_{\max}}$ and $r_{b_{\min}}$ in the region of AP boundary, there zone of free moving of electrons is started.
5. Start point on transversal coordinate z_{start}, which correspond to position of AP boundary.
6. Parameters of magnetic lens, including its current I_l, number of coils N_l, as well as necessary geometry parameters, corresponding to considered model for defining magnetic inductivity, which will be described later.

Output parameters of considered simulation task are as follows.

1. Position of focal beam ring F_b.
2. Radius of focal beam ring R_b.
3. Thickness of focal beam ring T_b.

Corresponding input and output geometry parameters of the hollow conical EB are clearly explained in Fig. 3.

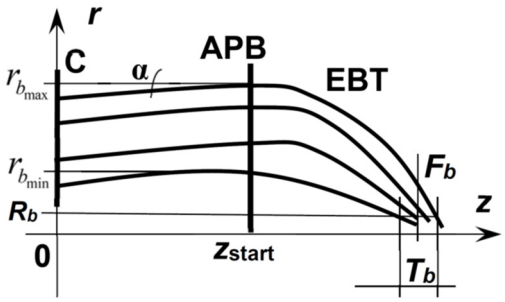

Figure 3. Input and output parameters of simulated hollow EB.
C – cathode surface, APB – anode plasma boundary, EBT – EB trajectories

The main problem in this research is the possibility of changing the radius of the focal beam ring R_b by changing the magnetic lens parameters, which has been described before. Dependencies of EB focus position on acceleration voltage U_{ac}, EB current I_b, and angle of beam divergence α are also necessary from the point of view of the practical application of HVGDEG.

Corresponding analytical relations for describing the approach of simulating the trajectories of the electron beam will be given in the next section of the article. It should be pointed out that the main aim of this research is to calculate the EB trajectories in the region of free movement in the AP in the magnetic field of a short-focusing lens, after acceleration of electrons in the electric field of the cathode fall region. The task of simulating electrode systems in the cathode fall region, including defining AP boundary position, is separate. This task, for the HVGD system with the plane cathode surface, like presented in Fig. 2, has been considered early in the paper [16].

BASIC MATHEMATICAL RELATIONS

It is well-known from the basic conceptions of electron optics that the inductivity of magnetic lenses in electrode systems, similar to those presented in Fig. 2, is interpolated with an accuracy range of 1,5 – 3 % by the Galejs model [39-42]. The corresponding analytical relation for axial magnetic induction B_{z0} is written via lens electrical and geometry parameters as follows [39–42]:

$$B_{z0} = \frac{1.257 \cdot 10^{-4} I_l N_l}{2 S_l} \left(\frac{z_l + \frac{S_l}{2}}{\sqrt{\left(\frac{D_l}{3}\right)^2 + \left(z_l + \frac{S_l}{2}\right)^2}} - \frac{z_l - \frac{S_l}{2}}{\sqrt{\left(\frac{D_l}{3}\right)^2 + \left(z_l - \frac{S_l}{2}\right)^2}} \right), \tag{1}$$

where I_l is the lens current, A, N_l is the number of lens coils, z_l is the width of lens, m, S_l is the width of nonmagnetic lens gap, m, and D_l is the thickness of the region, where winding wire, m. Precision construction of short magnetic lens with defining the geometry parameters z_l, S_l, and D_l is given in paper [16].

With known axial magnetic inductivity distribution $\mathbf{B}_{z0}(\mathbf{z})$, calculated using relation (1), its transversal distribution at every point on the longitudinal coordinate z in the simulated electrode system, corresponding to Galejs model, simply recalculated as expansion to Taylor series for B_r and B_z components as follows [39 – 42]:

$$B_r = -\frac{r}{2}B'_{z0} + \frac{r^3}{16}B'''_{z0} + \ldots; \quad B_z = B_{z0} - \frac{r^2}{4}B''_{z0} + \ldots . \tag{2}$$

For calculation the EB trajectories in the region of free movement in magnetic field of focusing lens, which induction is calculated by relations (1, 2), such important physical effects have been taking into account [39 – 45].

1. Owns space charge of beam electrons.
2. Space charge of ions of residual gas, which compensate the self space charge of beam electrons.
3 Magnetic focusing of an electron beam in an ionized gas, or pinch-effect, as relativistic effect in the condition of space charge of beam electrons compensation. Really, for considered acceleration voltage, smaller than 500 kV, this effect can be ignored [39 – 42]. Results of computer simulation, given in next part of the article, are confirm this presumption.
4. Influence of the magnetic field of focusing lens and twisting of the electrons' trajectories in it.
5. Dissipation of beam electrons on the atoms of residual gas corresponding to Rutherford model [44 – 46].

Therefore, corresponding set of algebraic-differential equation is written as follows [39 – 42]:

$$n_{i0} = \sqrt{\pi} r_b^2 B_i p n_e \sqrt{\frac{M\varepsilon_0 n_e}{m_e U_c}} \exp\left(-\frac{U_c}{\varepsilon_0 n_e r_b^2}\right), \quad f = \frac{n_e}{n_{i0} - n_e}; \quad C = \frac{I_b\left(1 - f - \beta^2\right)}{4\pi\varepsilon_0 \sqrt{\frac{2e}{m_e}} U_c^{3/2}};$$

$$\tan\left(\frac{\theta_{\min}}{2}\right) = \frac{10^{-4} Z_a^{4/3}}{2\gamma\beta^2}; \tan\left(\frac{\theta_{\max}}{2}\right) = \frac{Z_a^{3/2}}{2\gamma\beta^2}; \tag{3}$$

$$\bar{\theta}^2 = \frac{8\pi r_b^2 n Z_a^2 z}{\beta^4\gamma^2} \ln\left(\frac{\theta_{\max}}{\theta_{\min}}\right), \quad \theta = \frac{d^2 r_b}{dz^2} dz + \theta_s, \quad \frac{d^2 r_b}{dz^2} = \frac{C\left(R_{\max} - R_{\min}\right)}{l_{an}} - \frac{e\left(R_{\max} - R_{\min}\right) B_{z0}^2}{16 m_e U_c},$$

where U_c is acceleration voltage, I_b is beam current, p is residual gas pressure, $R_{\max}$ is maximal radius of EB, $R_{\min}$ is its minimal radius, l_{an} is length of anode aperture, B_i is the level of gas ionizing, n_e is concentration of electrons, m_e is mass of electron, ε_0 is dielectric constant, f is level of beam space charge compensation by ions of residual gas, $\theta_{\min}$ is minimal scattering angle, $\theta_{\max}$ is maximal scattering angle, Z_a – charge of nuclear for residual gas atoms, $\beta = v/c$ is relation of electrons velocity v to light velocity c, r_b is EB radius, n is concentration of gas atoms, $\bar{\theta}$ is average angle of electrons dissipation.

Generally, the set of equations (3) is only slightly different from well-known equations for EB with point focus by taking into account maximal and minimal radius of hollow cylindrical EB [48, 49].

Dependence of EB current on acceleration voltage and residual gas pressure $I_b(U_c, p)$ for HVGDEG is usually considered as a simple power function [28, 29]:

$$I_b\left(U_c, p\right) = C_I U_c^m p^k, \tag{4}$$

where C_I, m and k is semiempirical coefficients, which depended on the geometry of electrodes system, operation gas and cathode material [28, 29]. As it is proven in the theory of HVGD, the values of coefficients m and k are always lead in the range from 1 to 2.

In elaborated computer software the set of algebraic-differential equations (3), taking into account (1, 2, 4), has been solved using the fourth-order Runge – Kutta method [47 – 57].

Another approach to finding the trajectories of relativistic EB in the high-frequency electromagnetic fields has been proposed in papers [58 – 60]. This approach is generally based on statistical analysis of experimental results using microcomputers, connected with experimental equipment.

PARTICULARITIES OF SIMUALTION TECHNIQUE

For providing computer simulation of EB trajectories, the original computer software EBTIAE (Electorn Beam Trajectories Interpolation, Approximation and Extrapolation), created directly for analyzing parameters of short-focus

EB, propagated at low pressure in ionized gas, has been used [43]. This software has been developed using the advanced means of Python programing language, particularly, paradigms of functional and matrix programming [32 – 34].

It should be pointed out that the main particularity of elaborated computer software is its multifunctionality and orientation to solving different practical tasks connected with simulation of EB propagation in ionized gas [32 – 34]. Another distinguishing feature of elaborated software is the inclusion of advanced means of graphic user interface for each scientific and engineering task, which is solved. Therefore, for the convenience of users working with the developed software, all the various tasks, which can be solved, are located on separate tabs of the corresponding graphic window [32 – 34]. For example, one of these windows is a window in which an important engineering problem of simulating the guiding of short-focus EB in the equipotential channel in the field of short magnetic lenses is solved. The corresponding interface window of elaborated computer software is presented in Fig. 4.

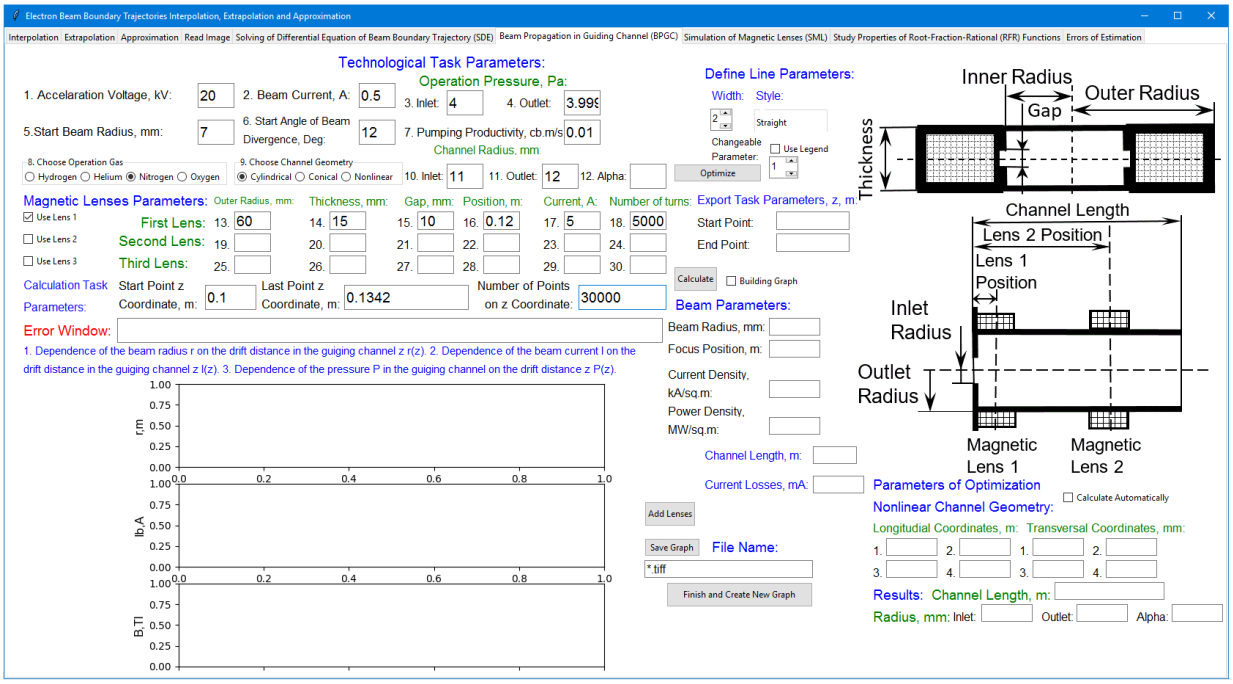

Figure 4. Interface window of the elaborated computer software EBTIAE, designed for solving the task of short-focus EB propagation in the equipotential channel in the field of magnetic lens. Screen copy

But it should be pointed out that solving the problem of finding the trajectories of hollow EB, propagated in an electrode system with a plane cathode, a cylindrical anode, and one focusing magnetic lens, is generally different and needs a specific approach for defining simulation parameters. Main presumptions in this aspect are connected with basic conceptions of vacuum science and technology [61, 62] and can be formulated as follows.

1. Inlet and outlet operation pressures are given as close values, which correspond to operation pressure in the electron gun, but outlet pressure has to be slightly smaller. For example: inlet pressure – 4 Pa, and outlet – 3.999 Pa.

2. Pumping productivity is taken as an extra small value, for example, 0.001 m³/s.

3. Inlet and outlet channel radii are given as close values, which correspond to the maximum value of the EB radius $r_{b_{\max}}$, but they are slightly greater. For example: if $r_{b_{\max}} = 10$ mm, the inlet channel radius can be taken as 11 mm, and the outlet, correspondingly, as 12 mm.

It is obvious that with such limitations and assumptions on the parameters of the computer model, the description of the propagation of a hollow EB in an electrode system with a plane cathode, a cylindrical anode, and a focusing magnetic lens is completely correct. For the real tasks, the parameters of the virtual channel for EB propagation are selected so that its length corresponds to the extent of the electrons' drift region along the longitudinal coordinate z, up to the ring focus of the EB. Thus, the set simulation problem is completely reduced to the previously solved problem of simulating the process of guiding an EB with a point focus in an equipotential channel. In general, such an approach simplifies the structure of the developed computer software and its operation. It is generally clear that the expansion of the range of engineering problems solved in one software complex always leads to significant complications in computer software.

OBTINED SIMULATION RESULTS

Let's considering now some simulation tasks, which given basic dependences of position F_b and radius R_b of focal beam ring on location of lens z_l, lens current I_l and number of coils N_l, as well as acceleration voltage U_c and EB current I_b.

Task 1. Calculate EB trajectories for parameters of the beam and electromagnetic lens, given in Table 1.

Obtained graphic dependences for different values of start EB radius r_{b0} are given in Fig. 5.

Table 1. Parameters of EB and electromagnetic lens for Task 1

Type of parameters	#	Parameter	Value
EB propagation parameters	1.	Acceleration voltage, kV	20
	2.	Beam current, A	0.5
	3.	Operation pressure, Pa	4
	4.	Type of gas	N_2
	5.	Pumping productivity, m^3/s	$1.7 \cdot 10^{-3}$
	6.	Start point on *z* coordinate, m	0.1
	7.	Maximal value of EB radius, mm	10
	8.	Minimal value of EB radius, mm	7
	9.	Angle of EB divergence, degree	12
Parameters of magnetic lens	1.	External radius, mm	60
	2.	Thickness, mm	15
	3.	Gap, mm	10
	4.	Position, m	0.12
	5.	Current, A	5
	6.	Number of turns	5000

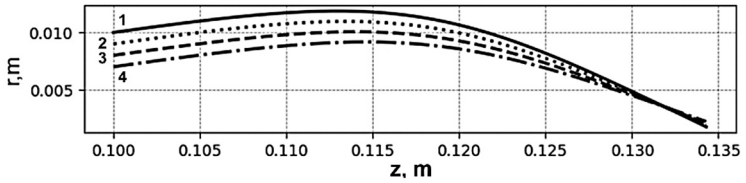

Figure 5. Simulation results, have been obtained for Task 1.
1 – r_{b0} = 10 mm; 2 – r_{b0} = 9 mm; 3 – r_{b0} = 8 mm; 4 – r_{b0} = 7 mm

As it is clear from the obtained simulation results, electron beam trajectories, started from different points by the transversal coordinate r, are focused by a short magnetic lens in one point with the position of the focal beam ring F_b = 0.1323 m and the radius of the focal ring R_b = 4.63 mm. The thickness of the focal ring for this task is T_b = 2.4 mm. Generally, simulation results, obtained by solving this task, confirm the basic statement of electron optics, that all electrons, which started from different points at the same angle, when they have the same velocity, are collected by the magnetic lens to the single-point region, located at the corresponding distance [38 – 42].

Task 2. Calculate EB trajectories for parameters, given in Table 1, but for angle of EB divergence $\alpha = 8^0$ and minimal value of EB radius $r_{b_{\min}} = 5$ mm. Compare obtained results with results, which have been obtained in the Task 1.

The graphic dependencies, have been obtained by solving this task for EB trajectories with different start radii r_{b0}, are given in Fig. 6.

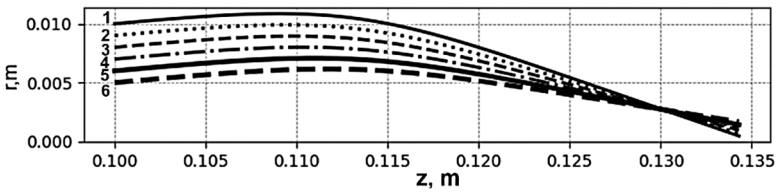

Figure 6. Simulation results, have been obtained for Task 2.
1 – r_{b0} = 10 mm; 2 – r_{b0} = 9 mm; 3 – r_{b0} = 8 mm; 4 – r_{b0} = 7 mm; 5 – r_{b0} = 6 mm; 6 – r_{b0} = 5 mm

It is obvious, that for this simulation task EB trajectories also converge at the region of one point with focal parameters F_b = 0.1295 and R_b = 2.61 mm. The thickness of the focal beam ring in this case is T_b = 1.8 mm. Generally, for a smaller value of EB divergence angle α, the position of focus approaches the cathode, and the radius of the focal ring and its thickness become smaller. These results are also in good agreement with the basic principles of electron optics [38 – 42].

Task 3. Calculate EB trajectories for parameters given in Table 1, but for different angles of EB divergence: $\alpha = 12^0$, $\alpha = 10^0$, $\alpha = 8^0$, and $\alpha = 6^0$. Compare the obtained results with the results, which just have been obtained in the Task 1 and Task 2.

The graphic dependencies, have been obtained by solving this task for different angles of EB divergence α and start radius r_{b0} are given in Fig. 7.

From the computer-solved of this simulation task, it is clear that with the dispersion of angles of EB divergence, the position of the focal ring is changed, and its thickness becomes generally greater. Position of focal ring without divergence of angles corresponds to Task 1, F_b = 0.1323 m, but since from the start point with radial coordinate r_{b0} = 10 mm inlet

few EB trajectories with different divergence angles, which are smaller, that the basic angle $\alpha = 12^0$, the focal beam ring approaches to the cathode slightly. For this task, the corresponding value is $F_b = 0.1284$ m. The thickness of the focal ring is also becoming significantly greater, $T_b = 4.4$ mm. Therefore, with the dissipation of divergence angles of electrons, the focal power density of EB is significantly smaller. Generally, this result also fully corresponded to basic principles of electron optics and had to be taken into account in the construction of electron guns for industrial applications [38, 42].

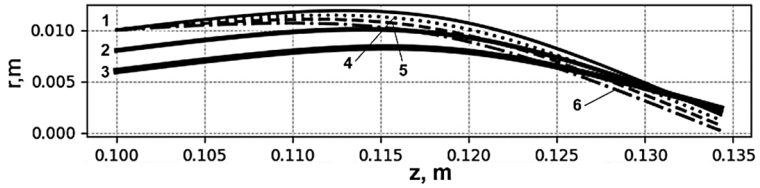

Figure 7. Simulation results, have been obtained for Task 3.
1 – $r_{b0} = 10$ mm, $\alpha = 12^0$; 2 – $r_{b0} = 8$ mm, $\alpha = 12^0$; 3 – $r_{b0} = 6$ mm, $\alpha = 12^0$; 4 – $r_{b0} = 10$ mm, $\alpha = 10^0$; 5 – $r_{b0} = 10$ mm, $\alpha = 8^0$; 6 – $r_{b0} = 5$ mm, $\alpha = 8^0$

Task 4. Calculate EB trajectories for parameters given in Table 1, but for the position of the magnetic lens, $z_l = 0.13$ mm and the minimal value of EB radius $r_{b_{\min}} = 5$ mm. Provide a simulation also for another gap of the magnetic lens, $G_l = 5$ mm. Compare the obtained results with the results, which have been obtained in Task 1.

The graphic dependences, have been obtained by solving this task are given in Fig. 8.

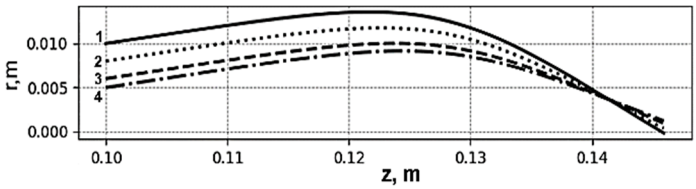

Figure 8. Simulation results, have been obtained for Task 4.
1 – $r_{b0} = 10$ mm; 2 – $r_{b0} = 8$ mm; 3 – $r_{b0} = 6$ mm; 4 – $r_{b0} = 5$ mm

As shown in Fig. 8, when the magnetic lens is moved further away from the cathode, the ring focus of the electron beam also shifts to a greater distance. In this case, $F_b = 0.1418$ m. On the contrary, the radius of the focal ring is generally similar: $R_b = 4.65$ mm and $T_b = 2.53$ mm. It is also interesting that for $G_l = 5$ mm the simulation results are similar, with no significant difference from those that are given in Fig. 8.

Task 5. Calculate EB trajectories for the same EB and lens parameters, as in Task 4, but for different currents of the magnetic lens: $I_l = 4$ A and $I_l = 6$ A.

The graphic dependencies, have been obtained by solving this task, are given in Fig. 9.

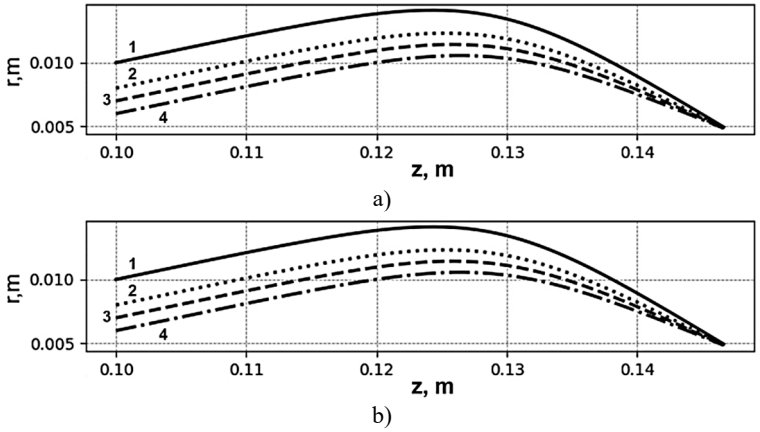

Figure 9. Simulation results, have been obtained for Task 5.
a – $I_l = 4$ A, b – $I_l = 6$ A. 1 – $r_{b0} = 10$ mm; 2 – $r_{b0} = 8$ mm; 3 – $r_{b0} = 6$ mm; 4 – $r_{b0} = 5$ mm

It is clear from the obtained dependencies that in the case of reducing the current of the magnetic lens, the ring focus of the hollow conical EB is located further from the cathode. If in Task 4, in the case of $I_l = 5$ A, the value of $F_b = 0.1418$ m, for $I_l = 4$ A, this value is greater, $F_b = 0.1482$ m. And in this case, the radius of the focal beam ring is also greater, the corresponding value is $R_b = 5.1$ mm. On the contrary, as it is clear from Fig. 9, b, in the case of increasing the current of the magnetic lens, the ring focus of EB approaches the cathode, and the radius of the focal ring becomes smaller. For example, in case $I_l = 4$ A corresponding EB parameters are $F_b = 0.138$ m and $R_b = 2.4$ mm. Therefore, changing of

magnetic lens current is a very suitable way to adjust the parameters of forming EB to the requirements of the technological process, for example, to the wire diameter in technologies of three-dimensional printing by metal [1 – 16].

Task 6. Calculate EB trajectories for the same EB and lens parameters, as in Task 1, but for different number of turns in magnetic lens: $N_l = 4000$ and $N_l = 6000$.

The graphic dependences, have been obtained by solving this task are given in Fig. 10.

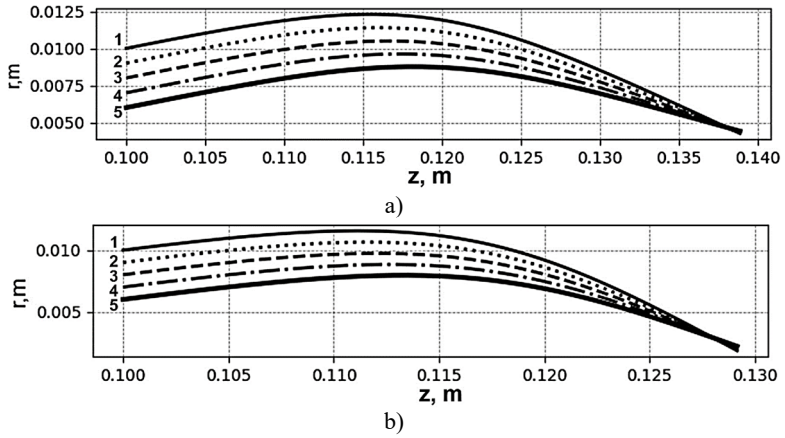

Figure 10. Simulation results, have been obtained for Task 6.
a – $N_l = 4000$, b – $N_l = 6000$. 1 – $r_{b0} = 10$ mm; 2 – $r_{b0} = 9$ mm; 3 – $r_{b0} = 8$ mm; 4 – $r_{b0} = 7$ mm; 5 – $r_{b0} = 7$ mm

It is clear from the obtained dependencies, presented in Fig. 5 and Fig. 10, that in the case of reducing the number of turns of the magnetic lens, the ring focus of the hollow conical EB is also located further from the cathode, and the radius of the focal beam ring becomes greater. On the contrary, in the case of increasing the number of turns, the ring focus was located nearer to the cathode, and the radius of the focal beam ring became smaller. But the thickness of the focal ring with changing the number of turns of the magnetic lens is generally similar. Corresponding values for this example have been obtained as results of a computer simulation, are presented in Table 2.

Table 2. Focal parameters of EB for simulation Task 6

N_l	F_b, m	R_b, mm	T_b, mm
4000	0.1375	5.0	2.44
5000	0.1323	4.63	2.4
6000	0.1283	2.5	2.42

It should also be pointed out that increasing the number of turns in the magnetic lens gives the same influence to the focus position and focal beam ring as increasing the lens current. This fact is simply explained by relation (1), because the product of the quantities $I_l N_l$ appears directly in the numerator of this formula. Really, this rule is very important from a practical point of view and will be considered carefully in the next section of the article.

Task 7. Calculate EB trajectories for the simulation task parameters, given in Table 1, but for different values of acceleration voltage: $U_c = 15$ kV and $U_c = 25$ kV.

The graphic dependencies, have been obtained by solving this task, are given in Fig. 11.

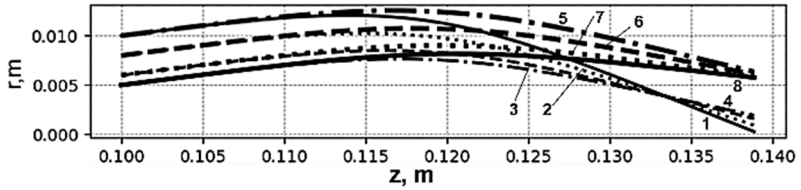

Figure 11. Simulation results, have been obtained for Task 7.
1 – $r_{b0} = 10$ mm, $U_c = 15$ kV; 2 – $r_{b0} = 8$ mm, $U_c = 15$ kV; 3 – $r_{b0} = 6$ mm, $U_c = 15$ kV; 4 – $r_{b0} = 5$ mm, $U_c = 15$ kV; 5 – $r_{b0} = 10$ mm, $U_c = 25$ kV; 6 – $r_{b0} = 8$ mm, $U_c = 25$ kV; 7 – $r_{b0} = 6$ mm, $U_c = 25$ kV; 8 – $r_{b0} = 5$ mm, $U_c = 25$ kV

It is clear from the obtained simulation results that with increasing acceleration voltage, the focal beam ring is located further from the cathode and its radius becomes greater. Values of these EB parameters, obtained as a result of solving this simulation task, are presented in Table 3.

Table 3. Focal parameters of EB for simulation Task 7

U_c, kV	F_b, m	R_b, mm	T_b, mm
15	0.1311	3.95	2.8
20	0.1323	4.63	2.4
25	0.1398	5.21	1.9

Task 8. Calculate EB trajectories for the simulation task parameters, given in Table 1, but for different values of EB current: I_b = 0.3 A and I_b = 0.7 A.

The graphic dependencies, have been obtained by solving this task are given in Fig. 12.

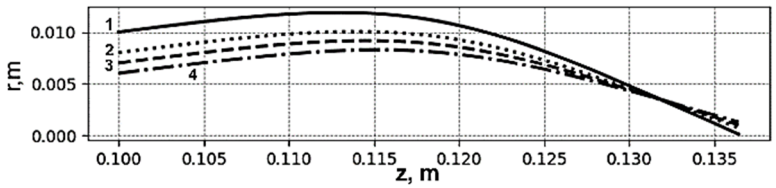

Figure 12. Simulation results, have been obtained for Task 8.
1 – r_{b0} = 10 mm; 2 – r_{b0} = 8 mm; 3 – r_{b0} = 7 mm; 4 – r_{b0} = 6 mm

It is generally clear that dependencies for EB trajectories, presented in Fig. 12 and obtained for the case I_b = 0.3 A, are in particularity the same as dependencies for the case I_b = 0.5 A, given in Fig. 5. Therefore, focal parameters of EB are also the same. For the value of EB current I_b = 0.7 A, the graphs of EB trajectories also do not practically differ from the graphs already presented in Fig. 5 and Fig. 12. Therefore, EB focal parameters generally don't depend on the current of EB. From the theoretical point of view, this fact can be simply explained by the compensation of the owner space charge of electrons by the positive ions of ionized gas [39 – 42].

The same simulation results have been obtained with changing operation pressure from 4 Pa to 7 Pa, generally, EB trajectories aren't deferred, and focal parameters were the same as in Task 1.

Experimental focal parameters of hollow EB, have been obtained with the values of its input parameters and parameters of magnetic lens, given in Table 1, but for different acceleration voltage and number of turns of magnetic lens, are presented in Table 4.

Table 4. Measurement focal parameters of hollow EB for different acceleration voltage

U_c, kV	N_l	F_b, m	R_b, mm	T_b, mm
15	5000	0.129	3.42	2.67
20	4000	0.1384	4.83	2.12
20	5000	0.1337	4.48	2.08
20	6000	0.1256	2.37	2.31
25	5000	0.1419	5.18	1.57

Overall, it is clear that the obtained simulation results presented in Tables 2 and 3 and the experimental data on the focal EP parameters presented in Table 4 are in excellent agreement. The difference between them does not exceed 15%. Therefore, the developed software can be effectively used by design engineers for preliminary evaluation of the focal parameters of a hollow EP focused by a magnetic lens. Corresponding practical recommendations will be given in the next subsection of the article.

ANALIZING OF OBATINED SIMULATION RESULTS AND PRACTICAL RECOMMENDATIONS

Generally, the provided scientific studies have shown that the developed computer software, based on the mathematical approach and physical assumptions described in the previous subsections, yields accurate calculations of the hollow EP focal parameters, which correlate well with the obtained experimental data. Therefore, it is strongly recommended to use this software in the simulation and computer-aided design of an improved HVGDEG for future industrial applications.

On the basis of the provided simulation and obtained theoretical results, some important practical recommendations in the aspect of designing novel HVGDEG constructions with the plane cathode and magnetic EB focusing have been formulated. Generally, the most significant physical effects that characterize dependencies between input and output EB parameters are as follows. Generally, the provided scientific studies have shown that the developed computer software, based on the mathematical approach and physical assumptions described in the previous subsections, yields accurate calculations of the hollow EP focal parameters, which correlate well with the obtained experimental data. Therefore, it is strongly recommended to use this software in the simulation and computer-aided design of an improved HVGDEG for future industrial applications.

1. In accordance with the law of electron optics, beam electrons that have the same speed and initial divergence angles, but start in the region of free motion with different transverse coordinates r_{b0}, are focused after passing through a short magnetic lens at one point.

2. As the divergence angle of the electron beam increases, its ring focus moves further from the cathode surface, and the radius of the focal ring in this case becomes greater.

3. With a large spread of the initial angles of entry of the beam electrons into the drift region in the magnetic lens, the thickness of the focal ring increases significantly, which leads to a significant decrease in the electron beam current density on the workpiece. In general, at small entry angles, the focus of the electron beam is located closer to the cathode surface, and at large entry angles, it is further away. On the one hand, a large spread of the entry angles of the beam

electrons at the entrance to the drift region in the AP, caused by their collisions with residual gas atoms, is a characteristic feature of the operation of HBGD electron sources. Therefore, electrons with different entry angles are scattered after passing through the magnetic lens. However, if the electron beam current density at the focus of the ring is sufficient to perform a specific technological operation, magnetic focusing offers significant advantages in terms of the ability to control the focal parameters of the beam, including the focus position, the radius of the focal ring, and its thickness. The corresponding theoretical foundations for estimating the thickness of the focal ring EB are considered in [16].

4. When the magnetic lens is moved to a greater distance from the cathode, the ring focus of the electron beam is also located further away. The thickness of the focal ring in this case is generally similar.

5. In the case of reducing the current of the magnetic lens, the ring focus of the hollow conical EB is located further from the cathode, and its radius becomes greater. On the contrary, in the case of increasing current of the magnetic lens ring, the focus of EB is approached to the cathode, and the radius of the focal ring becomes smaller. But the thickness of the focal ring in this case is also generally similar.

6. Generally, increasing the number of turns in the magnetic lens gives the same influence on the focus position and the radius of the focal beam ring as increasing the lens current.

7. In the case of reducing the number of turns of the magnetic lens, the ring focus of the hollow conical EB is located further from the cathode, and its radius becomes greater. On the contrary, in the case of an increasing number of turns of the magnetic lens, the ring focus of EB approaches the cathode, and the radius of the focal ring becomes smaller. The thickness of the focal ring in this case is generally similar.

8. In case of changing the magnetic lens gap, the focus position and focal ring radius are generally unchanged.

9. In the case of increasing acceleration voltage, the ring focus of the EB is located further away from the cathode, and the radius of the focal ring becomes larger. Among the dependencies that have been obtained and studied, this is the most clearly expressed. When the accelerating voltage changes by 5%, the position of the beam focus and its focal diameter always change within 15 - 20%. Therefore, the correct selection and stabilization of the accelerating voltage using the appropriate design tools for high-voltage technology is a primary necessary condition for the stable operation of electron-beam technological equipment with magnetic focusing of the EP [16]. In general, this fact is quite simply explained by the basic laws of electron optics, since, as is known, the focusing power of a magnetic lens is very strongly dependent on the velocity of electrons, which is directly related, namely, to the accelerating voltage [39 – 42].

10. When the EB current and the HVGD operating pressure change, the focal position and focal ring radius generally remain unchanged. This effect is explained primarily by the fact that the beam electrons move under conditions of space charge compensation by residual gas ions. Generally, the EB current and the operating pressure under VTR ignition conditions are related by relation (4).

Consequently, in accordance with the rules of physical laws, which are described above, general recommendations regarding the engineering development of the EB equipment with HVGDEG, which uses a short magnetic focusing lens for forming EB, have been formulated as follows.

1. The basic condition of updating HVGDEG with magnetic focusing to meet certain requirements of the technological process is defining the correct acceleration voltage. The values of beam current and operation pressure are defined after that by the necessary current density for melting the moving wire. Corresponding analytical relations are given in the paper [29].

2. Changing the position of the magnetic lens relative to the cathode allows, when designing electron-beam equipment, positioning the focus of the electron beam at a given distance in the chamber of the item treatment in accordance with the requirements of the technological process.

3. The correct choice of the EB focus position and the radius of its focal ring can be done in two ways: by changing the current of the focusing magnetic lens or by changing the number of its turns. When designing an electron beam installation, the best method is to increase the number of lens turns rather than to increase its current, since in this case the lens heats up less and its heating has less effect on the parameters of the technological process. On the other hand, the method of changing the lens current is easier to implement and can be implemented when reconfiguring technological equipment for another type of product, as well as directly during the realization of the technological process.

4. The installation can be easily reconfigured to heat a wire of a different diameter by changing the magnetic lens current, which allows the use of HVGDEG with magnetic focusing of the EB in small-scale production while maintaining the high quality of the products obtained. This technology is extremely cheap and very effective, since it does not require highly qualified service personnel to disassemble the electron gun to reconfigure the equipment for a new technological operation.

5. Automatic control of the focus position of the EB during the technological process can be easily accomplished by changing the current of the magnetic lens on the small values.

In general, the obtained simulation results showed that the flat-cathode HVGDEG with magnetic focusing of the EB, as a technological tool, has a number of advantages over guns with a spherical cathode and electrostatic focusing in the technologies of three-dimensional printing by metal. They, like guns with electrostatic focusing, form a hollow converging EB with a ring focus and provide uniform heating of the wire along the perimeter, but are much easier to operate. In addition, an important technological advantage of guns with magnetic focusing of the EB is the ability to adjust the radius of the focal ring by changing the current of the magnetic lens. In general, the theoretical studies have

shown that this type of HVGDEG can be successfully used for melting wires or rods with various diameters, from 0.5 to 10 mm. Further development and application of such advanced technologies is very promising for the development of the transport industry and mechanical engineering and the chemical, aviation, and space industries, in particular, for the production and reconstruction of blades of aircraft and marine engines.

CONCLUSIONS

Provided numerical computer experiments and scientific research directed to the study of focusing EB trajectories with different parameters in short magnetic lenses, showing that in the physical conditions of HVGD, it is possible to form a hollow EB with ring focus. Therefore, uniform heating of treated wire or rods is guaranteed. Since, in comparison with experimental results, the accuracy of the simulation is very high, in the range of 5 – 15%, the elaborated computer software with corresponding assumptions for creating the simulation tasks can be successfully used on the preliminary steps of HVGDEG engineering designing for certain industrial technologies' three-dimensional printing by metal.

Based on the obtained theoretical and experimental results, important physical laws and rules have also been formulated, which can be further effectively used for the design of electron-beam technological equipment using the developed software.

Generally, the provided research has shown that by using HVGDEG with a plane cathode and a short magnetic lens, the formation of hollow EB with a radius of the focal ring range of 1 – 5 mm. Using EB with such parameters for melting wire or rods with a diameter from 0.5 to 10 mm is really possible.

A significant technological advantage of using magnetic focusing for electronic lasers is the ability to easily change the focus position and focal ring radius by adjusting the magnetic lens current. This allows for easy reconfiguration of the process equipment for new product types, as well as automatic control of the focus position during the process. The developed software can also be effectively used to select the optimal magnetic lens current.

In general, the conducted studies have shown that the development and wide implementation in industry of the HVGDEG with a flat cathode and magnetic focusing of the electron beam will significantly contribute to the further development and improvement of modern electron-beam technologies of three-dimensional printing on metal. Today, the engineers and experts working in the fields of production of transport vehicles, mechanical engineering, chemical industry, shipbuilding, aircraft construction, and space industry are most interested in the use and further improvement and development of such advanced technologies.

Overall, the conducted research has shown that the development and widespread industrial adoption of a flat-cathode HTEG with magnetic focusing of the electron beam will significantly contribute to the further development and improvement of modern electron-beam 3D printing technologies on metal. Currently, engineers and specialists working in the vehicle manufacturing, mechanical engineering, chemical industry, shipbuilding, aircraft manufacturing, and space industries are showing the greatest interest in the use and further improvement of such promising technologies.

Acknowledgements

The work has been carried out at the Scientific and Educational Laboratory of Electron Beam Technological Devices of the National Technical University of Ukraine “Igor Sikorsky Kyiv Polytechnical Institute”. It has been financially supported by the Ministry of Education and Science of Ukraine. Priority area: new substances and materials; priority thematic area: ceramic and composite materials and coatings for extreme conditions of use; state registration number is 0124U001525. The experimental research, which has been provided, is supported by the Joint Stock Company, Scientific and Industrial Association “Chervona Hvylia”.

ORCID

Igor V. Melnyk, https://orcid.org/0000-0003-0220-0615; **Serhii B. Tuhai**, https://orcid.org/0000-0001-7646-1979
Mykhailo Yu. Skrypka, https://orcid.org/0009-0006-7142-5569; **Dmytro V. Kovalchuk,** https://orcid.org/0000-0001-9016-097X

REFERENCES

[1] Wohlers Report 2023. Analysis. Trends. Forecasts. 3D Printing and Additive Manufacturing State of the Industry. ASTM International. (2023). https://wohlersassociates.com/product/wr2023/
[2] An Additive Manufacturing Breakthrough: A How-to Guide for Scaling and Overcoming Key Challenges. White Paper. World Economic Forum, edited by F. Betti, C. Seidel, M. Meboldt, (2022). https://www3.weforum.org/docs/WEF_Additive_Manufacturing_Breakthrough_2022.pdf
[3] *A Guide to Additive Manufacturing*, edited by D. Godec, J. Gonzalez-Gutierrez, A. Nordin, E. Pei, and J.U. Alcazar, (Springer, 2022). https://doi.org/10.1007/978-3-031-05863-9
[4] M. Armstrong, H. Mehrabi, N. Naveed, Journal of Manufacturing Processes, **84**, 1001 (2022). https://doi.org/10.1016/j.jmapro.2022.10.060
[5] Identifying current and future application areas, existing industrial value chains and missing competences in the EU, in the area of additive manufacturing (3D-printing). European Commission. Final Report. Brussels, 15th of July, 2016. https://op.europa.eu/en/publication-detail/-/publication/b85f5e09-7e2b-11e6-b076-01aa75ed71a1/language-en
[6] W. Frazier, Journal of Materials Engineering and Performance, **23**(6), (2014). https://doi.org/10.1007/s11665-014-0958-z
[7] *Additive Manufacturing for the Aerospace Industry*, edited by: F. Froes, and R. Boyer, (Elsevier, 2019). https://doi.org/10.1016/C2017-0-00712-7
[8] R. Brooke, https://www.tctmagazine.com/additive-manufacturing-3d-printing-news/additive-manufacturing-can-lower-aircraft-building-and-oper/

[9] TCT Team, https://www.tctmagazine.com/additive-manufacturing-3d-printing-news/sciaky-metal-3d-printing-lockheed-martin-space/
[10] K. Taminger, and R. Hafley, "Electron beam freeform fabrication: A rapid metal deposition process," *Proceedings of the 3rd Annual Automotive Composites Conference*, (Troy, MI, USA, September, 9–10, 2003.
[11] S. Stecker, K.W. Lachenberg, H. Wang and R.C. Salo, in: *Proceedings of FABTECH and AWS Welding Show*, (Atlanta, GA, USA, 2006). pp. 35–46.
[12] Patent #8,344,281 B2, 2013. (USA).
[13] F. Pixner, F. Warchomicka, P. Patrick, A. Steuwer, H. Colliander, R. Pederson, and N. Enzinger, Materials, **13,** 3310 (2020). https://doi.org/10.3390/ma13153310
[14] W.J. Sames, F.A. List, S. Pannala, R.R. Dehoff, and S.S. Babu, International Materials Reviews. **61**, 5 (2016). https://doi.org/10.1080/09506608.2015.1116649
[15] I. Melnyk, S. Tuhai, O. Kovalenko, M. Skrypka, and D. Kovalchuk, in: *2024 IEEE 7th International Conference on Smart Technologies in Power Engineering and Electronics (STEE),* (Kyiv, Ukraine, 2024), pp. TT3.01.1-TT3.01.6. https://doi.org/10.1109/STEE63556.2024.10748050
[16] I.V. Melnyk, S.B. Tugay, V.O. Kyryk, and I.S. Shved, System Research and Information Technologies, **2021**(3), 17 (2021). https://doi.org/10.20535/SRIT.2308-8893.2021.3.02 (in Ukrainian)
[17] H. Xu, X. Sang, B. Yang, Y. Peng, and J. Fan, Chinese journal of vacuum science and technology, **41**(3), 284 (2021). http://cjvst.cvs.org.cn/en/article/doi/10.13922/j.cnki.cjvst.202005028?viewType=citedby-info
[18] Chang Jiawei, Li Shengbo, Lin Zhishu, Bai Fengmin, Li Guozheng, and Bai Zongzheng, Chinese journal of vacuum science and technology, **44**(5), (2024). http://cjvst.cvs.org.cn/en/article/doi/10.13922/j.cnki.cjvst.202401009
[19] Gu Liang, Yang Jie, Zhao Hua, Tan Wei, and Li Jinrong, Chinese journal of vacuum science and technology, **44**(2), 184 (2024). http://cjvst.cvs.org.cn/en/article/doi/10.13922/j.cnki.cjvst.202306003
[20] Qui Yufan, Li Shengbo, Zheng Xinjian, Fu Shengping, and Bai Fengmin, Chinese journal of vacuum science and technology, **41**(11), 1094 (2021). http://cjvst.cvs.org.cn/en/article/doi/10.13922/j.cnki.cjvst.202101027
[21] Deng Chenhui, Wang Yan, Liu Junbiao, and Han Li, Chinese journal of vacuum science and technology, **40**(9), 847 (2020). http://cjvst.cvs.org.cn/en/article/doi/10.13922/j.cnki.cjovst.2020.09.09
[22] Wang Jian, Chinese journal of vacuum science and technology, **40**(4), 381 (2020). http://cjvst.cvs.org.cn/en/article/doi/10.13922/j.cnki.cjovst.2020.04.17
[23] Xiang Yidong, Zhao Ding, Xue Qianzhong, and Li Xiaofei, Chinese journal of vacuum science and technology, **40**(3), 226 (2020). http://cjvst.cvs.org.cn/en/article/doi/10.13922/j.cnki.cjovst.2020.03.08
[24] Wang Yan, Zhao Weixia, Deng Chenhui, Liu Junbiao, and Han Li, Chinese journal of vacuum science and technology, **40**(1), 1 (2020). http://cjvst.cvs.org.cn/en/article/doi/10.13922/j.cnki.cjovst.2020.01.01
[25] Gu Yunting, Lin Yanjian, Yan Baojun, Liu Shulin, Yang Yuzhen, Yu Yang, Wen Kaile, and Wang Yuman, Chinese journal of vacuum science and technology, **39**(12), 1009 (2019). http://cjvst.cvs.org.cn/en/article/doi/10.13922/j.cnki.cjovst.2019.12.11
[26] Huo Weijie, Hu Jing, Cao Xiaotong, Fu Yulei, and Zhao Wansheng, Chinese Journal of Vacuum Science and Technology, **39**(8), 631 (2019). http://cjvst.cvs.org.cn/en/article/doi/10.13922/j.cnki.cjovst.2019.08.03
[27] Fu Xuecheng, Wang Ying, Quan Xueling, Ju Minni, and Wang Fengdan, Chinese journal of vacuum science and technology, **39**(5), 396 (2019). http://cjvst.cvs.org.cn/en/article/doi/10.13922/j.cnki.cjovst.2019.05.07
[28] S.V. Denbnovetsky, I.V. Melnyk, V.G. Melnyk, B.A. Tugai, and S.B. Tuhai, in: *2016 International Conference Radio Electronics & Info Communications UkrMiCo*, (Kyiv, Ukraine, 2016). pp. 1–4. https://ieeexplore.ieee.org/document/7739615
[29] S.V. Denbnovetsky, I.V. Melnyk, V.G. Melnyk, B.A. Tugai, and S.B. Tuhai, in: *2017 IEEE 37th International Conference on Electronics and Nanotechnology ELNANO*, (Kyiv, Ukraine, 2017). pp. 369-373. https://ieeexplore.ieee.org/document/7939781
[30] S.V. Denbnovetsky, V.I. Melnik, I.V. Melnik, and B.A. Tugay, in: *XVIII-th IEEE International Symposium on Discharges and Electrical Insulation in Vacuum*, (ISDEIV, 1998, Eindhoven, The Netherland), vol. 2. pp. 637–640. https://ieeexplore.ieee.org/stamp/stamp.jsp?tp=&arnumber=738530
[31] I.V. Melnik, and S.B. Tugay, Radioelectronics and Communications Systems, **55**(11), (2012). https://doi.org/10.3103/S0735272712110064
[32] I. Melnyk, S. Tuhai, M. Skrypka, T. Khyzhniak, and A. Pochynok, in: *Information and Communication Technologies and Sustainable Development. ICT&SD 2022. Lecture Notes in Networks and Systems*, edited by S. Dovgyi, O. Trofymchuk, V. Ustimenko, and L. Globa, vol. 809, (Springer, 2023). pp. 395–427. https://doi.org/10.1007/978-3-031-46880-3_24
[33] I. Melnyk, A. Pochynok, and M. Skrypka, System Research and Information Technologies, **2024, #4**. (2024). https://doi.org/10.20535/SRIT.2308-8893.2024.4.11 http://journal.iasa.kpi.ua/issue/view/18934/11880
[34] I. Melnyk, A. Pochynok, M. Skrypka, System Research and Information Technologies, **2024**(3), (2024). https://doi.org/10.20535/SRIT.2308-8893.2024.3.05
[35] W. McKinney, *Python for Data Analysis: Data Wrangling with Pandas, NumPy, and Jupyter*, 3rd Edition, (O'Reilly Media, 2023).
[36] F. Chollet, *Deep Learning with Python. Second Edition*. (Manning, 2022).
[37] M. Lutz, *Learning Python*, Fifth Edition. (O'Reilly, 2013).
[38] S. Schiller, U. Heisig, and S. Panzer, *Electron Beam Technology*, (New-York, John Wiley & Sons, 1995).
[39] M. Szilagyi, *Electron and Ion Optics*, (Springer Science & Business Media, 2012).
[40] E. Kasper, and P. Hawkes. *Principles of Electron Optics: Applied Geometrical Optics*. (Elsevier Science, 1989).
[41] P. Grivet, P.W. Hawkes, and A. Septie, *Electron Optics*, (Elsevier, 2013).
[42] *Electron Beams, Lenses, and Optics*, edited by A. B. El-Kareh, (Academic Press, 2012).
[43] B.M. Smirnov, *Theory of Gas Discharge Plasma*, (Springer, 2015).
[44] M.A. Lieberman, and A.J. Lichtenberg. *Principles of Plasma Discharges for Materials Processing*, (New York, Wiley Interscience, 1994).
[45] Yu.P. Raizer, *Gas Discharge Physics*, (New York: Springer, 1991).

[46] J.F. Epperson, *An Introduction to Numerical Methods and Analysis*, Revised Edition, (Wiley-Interscience, 2007).
[47] M.K. Jain, S.R.K. Iengar, and R.K. Jain, *Numerical Methods for Scientific & Engineering Computation*. (New Age International Pvt. Ltd., 2010).
[48] S.C. Chapra, and R.P. Canale, *Numerical Methods for Engineers*, 7th Edition, (McGraw Hill, 2014).
[49] R.L. Burden, J.D. Faires, and A.M. Burden, *Numerical Analysis*, **(**Cengage Learning, 2015).
[50] T. Sauer, *Numerical Analysis*, (Pearson, 2017).
[51] R.W. Hamming, *Numerical Methods for Scientists and Engineers*, **(**Dover Publications, 1987).
[52] E. Isaacson, and H.B. Keller, *Analysis of Numerical Methods*, **(**Dover Publications, 1994).
[53] F.B. Hildebrand, *Introduction to Numerical Analysis*, **(**Dover Publications, 1987).
[54] A. Greenbaum, and T.P. Chartier, *Numerical Methods: Design, Analysis, and Computer Implementation of Algorithms*. (Princeton University Press, 2012).
[55] A.J. Salgado, and S.M. Wise, *Classical Numerical Analysis: A Comprehensive Course.* **(**Cambridge University Press, 2023).
[56] D.E. Stewart, *Numerical Analysis: A Graduate Course*, (Springer; 2022).
[57] J.H. Mathews, and K.D. Fink, *Numerical Methods. Using Matlab*, third edition (Amazon, 1998).
[58] V.G. Rudychev, M.O. Azarenkov, I.O. Girka, V.T. Lazurik, and Y.V. Rudychev, Radiation Physics and Chemistry, **206**, 110815 (2023). https://doi.org/10.1016/j.radphyschem.2023.110815
[59] V.G. Rudychev, V.T. Lazurik, and Y.V. Rudychev, Radiation Physics and Chemistry, **186**, 109527 (2021). https://doi.org/10.1016/j.radphyschem.2021.109527
[60] V. Lazurik, S. Sawan, V. Lazurik, and O. Zolotukhin, in: *4th International Maghreb Meeting of the Conference on Sciences and Techniques of Automatic Control and Computer Engineering Proceedings*, (IEEE, Maghreb, 2024), pp. 649–653. https://doi.org/10.1109/MI-STA61267.2024.10599694
[61] G. Lewin, *Fundamentals of Vacuum Science and Technology*. (McGraw-Hill, 1965).
[62] J.M. Lafferty. *Foundations of Vacuum Science and Technology*. (John Wiley & Sons, 1998).

МОДЕЛЮВАННЯ ФОКУСУВАННЯ ПОРОЖНИСТОГО ЕЛЕКТРОННОГО ПУЧКА СИМЕТРИЧНОЮ МАГНІТНОЮ ЛІНЗОЮ ДЛЯ ПРОМИСЛОВОГО ЗАСТОСУВАННЯ В АДИТИВНИХ ТЕХНОЛОГІЯХ

Ігор В. Мельник[1], Сергій Б. Тугай[1], Михайло Ю. Скрипка[1], Микола С. Суржиков[1], Олександр М. Коваленко[1], Дмитро В. Ковальчук[2]

[1]Національний технічний університет України «Київський політехнічний інститут імені Ігоря Сікорського»
[2]Приватне акціонерне товариство «НВО «Червона Хвиля»

У статті, з використанням методів чисельного моделювання, досліджено особливості фокусування короткофокусного порожнистого пучка електронів, сформованого з широкої поверхні холодного катода в електронних гарматах високовольтного тліючого розряду. Для отримання відповідних результатів моделювання використано оригінальне програмне забезпечення, створене авторами на мові програмування Python. Аналіз отриманих результатів чисельного моделювання показав, що у разі невеликої зміни кута розбіжності траєкторії пучка або радіуса початкової точки на поверхні катода положення фокусу пучка, як правило, не змінюється. Тому кільцевий фокус пучка зазвичай займає стійке положення по поздовжній координаті, а товщина фокального кільця завжди знаходиться в межах кількох міліметрів. Відповідні теоретичні результати порівнювалися з експериментальними, та різниця між теоретичними та експериментальними результатами знаходиться в межах 10-15% залежно від прискорювальної напруги та розміру поверхні катода. Високовольтні електронні гармати тліючого розряду з такими параметрами за товщиною фокального кільця можуть бути успішно використані в прогресивних промислових адитивних технологіях тривимірного друку на металевих поверхнях шляхом рівномірного нагрівання за периметром рухомого дроту або стрижнів різного діаметра, в діапазон 0,5 – 10 мм.

Ключові слова: *Адитивні технології; Електронно-променеві технології, Магнітне фокусування, Порожнистий конусний електронний пучок, Числове моделювання*

East European Journal of Physics. 4. 620-626 (2025)
DOI:10.26565/2312-4334-2025-4-65 ISSN 2312-4334

THE IMPACT OF VARIOUS LIGHTING CONDITIONS ON THE PHOTOSENSITIVE PROPERTIES OF SI<B,S> AND SI<B,Rh> STRUCTURES

Akramjon Y. Boboev[1], Shakhriyor Kh. Yulchiev[2], Ziyodjon M. Ibrokhimov[3], Nuritdin Y. Yunusaliyev[1]
[1]Andijan State University, named after Z.M. Babur, Andijan, Uzbekistan
[2]Andijan State Pedagogical Institute, Andijan, Uzbekistan
[3]Andijan State Technical Institute, Uzbekistan
**Corresponding Author e-mail: aboboevscp@gmail.com*
Received July 25, 2025; revised November 4, 2025; in final form November 10, 2025; accepted November 13, 2025

The paper analyses the results of experimental studies investigating the photosensitive properties of Si<B,S> and Si<B,Rh> structures under the influence of various types of radiation. It was found that the sensitivity of photodiodes fabricated based on Si<B,S> and Si<B,Rh>, increases several times (from 0.35 to 2.6 $A \cdot W^{-1}$) at decreasing temperature (from 300 K to 77 K). The threshold sensitivity of Si<B,S> based photodetectors was found to be significantly higher compared to Si<B,Rh> based photodetectors ($\Phi \approx 1.2 \cdot 10^{-11}$ $lm \cdot Hz^{-1/2}$). Increasing the concentration of sulphur (S) or rhodium (Rh) in silicon increases photosensitivity, but sensitivity decreases by 3-4 times when the permissible concentration is exceeded ($N_{Rh} > 2.6 \cdot 10^{15}$ cm^{-3}). It was found that photodetectors based on Si<B,S> and Si<B,Rh> retain their sensitivity parameters at high levels of radiation exposure (from protons, neutrons, electrons, and γ-quanta). In diodes based on p^+-n-p-n^+, an S-shaped I-V characteristic is observed, as well as the disappearance of the gating voltage (U_{sp} = 0.5÷10 V) with increasing temperature. Relaxation of photoconductivity in diodes based on Si<B,S> and Si<B,Rh> is due to increased charge-carrier lifetimes.
Keywords: *Sulfur; Rhodium; Photoconductivity; Dopant concentration; Radiation; Monochromatic Sensitivity; Relaxation*
PACS: 85.60.Dw

INTRODUCTION

Improving the photoelectric properties of silicon through doping is crucial to the development of modern electronic devices such as photodetectors, photodiodes, and radiation sensors. Purposeful modification of the silicon structure, namely, doping it with various donor and acceptor elements, allows for control over its carrier concentration, permitted energy states, and optical sensitivity. This significantly enhances the sensitivity, reliability, and stability of devices produced on the base of silicon. In particular, doping with elements such as sulfur (S) or rhodium (Rh) leads to the formation of a p^+ layer on the surface of the silicon [1]. This particular layer serves as a reliable hole-type carrier source, enhancing efficient photoelectric control at the surface upon illumination [2]. The configuration enables the production of both p^+-i-p^+ and p^+-i-n^+ asymmetric and symmetric photodetector structures. These structures are widely used in conventional photodetectors, radiation-resistant sensors, infrared detectors, night-vision imaging systems, astronomical instruments, and high-precision devices [3]. The use of intrinsic (i-) material layers in this design shows that light doping together with quasi-intrinsic behavior enhances the well-defined, and highly efficient photoelectric effect [4].

Silicon obtains an n^+-layer through the encapsulation of phosphorus (P) as a donor material. The creation of p^+–i–n^+ structures become possible through this process because the built-in electric field enables quick and efficient photo generated carrier separation [5]. The sensitivity of the device along with its response speed improves through this fabrication. The devices designed through these processes and structures demonstrate operational stability regardless of temperature changes and radiation exposure levels [6]. These designs prove most appropriate for environments characterized by high levels of radiation found in nuclear power systems and within space exploration and defense industries.

MATERIALS AND METHODS

In this research, the response of Si<B,S> and Si<B,Rh>-based structures to different types of radiation was examined and analyzed from the perspective of their photosensitivity. Silicon (Si) was selected as the base material for forming p^+-i–n^+ semiconductor structures. Boron-doped p-type silicon wafers with a specific resistivity of approximately $\rho \approx 2 \cdot 10$ Ω·cm were used as the starting material in the experiments. During the experimental procedures, either S or Rh solution was applied to one surface of the silicon wafer. This would generate p^+-regions of the p-type semiconductor with high hole carrier concentrations. Then donor sites were formed using applying phosphorus (P) solution to the other surface of wafer, forming an n^+- type layer. In this way, a three-layer structure was developed, that are shown as a p^+- type layer to the top of the semiconductor layer, a i-layer in the middle, and n^+-type layer to the bottom. The silicon wafers were glued together with adequate pressure to provide good electrical and physical properties between the layers. This method ensured that the dopants could be uniformly distributed in the Si crystal lattice, and were well integrated.

Cite as: A.Y. Boboev, Sh.Kh. Yulchiev, Z.M. Ibrokhimov, N.Y. Yunusaliyev, East Eur. J. Phys. 4, 620 (2025), https://doi.org/10.26565/2312-4334-2025-4-65

After the fabrication of the structures, we thermally treated them at temperatures between 1250 to 1300 °C, in diffusion atmospheres of either air or inert gases (nitrogen or argon). Thus, using the oven method to fabricate structures, the p^+ and n^+ dopants would diffuse into the silicon crystal, allowing the material to develop suitable p^+–i–n^+ structures with respect to depth.

To investigate radiation-induced modifications, irradiation experiments were carried out at the Institute of Nuclear Physics of the Academy of Sciences of the Republic of Uzbekistan (INP AS RUz). Proton irradiation was performed using the U-150-II isochronous cyclotron, which accelerates protons up to 18 MeV. Neutron irradiation was conducted using the NG-150 neutron generator, producing a quasi-monochromatic neutron flux with an energy of about 14 MeV. Electron irradiation was performed using the LINAC-1000 linear accelerator, generating electron beams with energies up to 10 MeV. All irradiation parameters – including fluence, energy, and exposure time – were precisely controlled to ensure the stability and reproducibility of the experimental conditions.

The compensation ratio $K = \bar{P}/N_S$ was evaluated using the effective carrier concentration $\bar{P}$ and the concentration of sulfur impurity N_S. The value of $\bar{P}$ was determined from the measured electrical resistivity using the expression

$$P = \frac{1}{q \cdot \mu_p \cdot \rho} \cdot 100\%] \quad (1)$$

where q is the elementary charge and μ_p is the hole mobility at room temperature. The sulfur concentration N_S was estimated from the diffusion profile parameters and solubility data reported for compensated crystals based on Si<B,S> in the study [1]. The sulfur concentration N_S was estimated from the diffusion profile parameters and solubility data reported for Si<B,S>-based compensated crystals in study [1].

RESULTS AND DISCUSSION

Photovoltaic characteristics

In our experimental investigations, spectral characteristics of p^+–i–p^+ and p^+–i–n^+ devices were studied by their comparison with spectral characteristics of the reference industry photodiode – FD-28KP. Thanks to experiments, it was feasible to estimate with high precision the spectral sensitivity and operating parameters for the described structures. Figures 1a and 1b depict the measured spectral sensitivity curves of the devices, and Table 1 lists the corresponding device parameters. The photodetector sensitivity was dramatically enhanced, particularly when the operating temperature was lowered to 77 K. Cooling of the operating temperature from 300 K to 77 K enhanced the spectral sensitivity of the Si<B,S> structure from $S_\lambda \approx 0.35$ A·W^{-1} to about 2.6 A·W^{-1} at a wavelength $\lambda = 0.625$ μm. In the same temperature range, the sensitivity of the Si<B,Rh> structure grew from $S_\lambda \approx 0.28$ A·W^{-1} up to about 0.74 A·W^{-1}. These facts prove that the sensitivity of these structures is enhanced several times when operating at cold (cryogenic) temperatures and thus they can be used as low-light sensors in cryogenic detector systems [7].

The minimum light sensitivities (Φ) of the photodetectors were also measured in the experiments. When a load resistance of $R_H = 50$ kΩ was employed, the corresponding Φ values of the Si<B,S> and Si<B,Rh> structures were $\Phi \approx 1.2 \cdot 10^{-11}$ lm·Hz$^{-1/2}$ and $\Phi \approx 4.0 \cdot 10^{-10}$ lm·Hz$^{-1/2}$, respectively. These extremely low Φ values evidently confirm that structures enable the detection of extremely weak light signals with high precision.

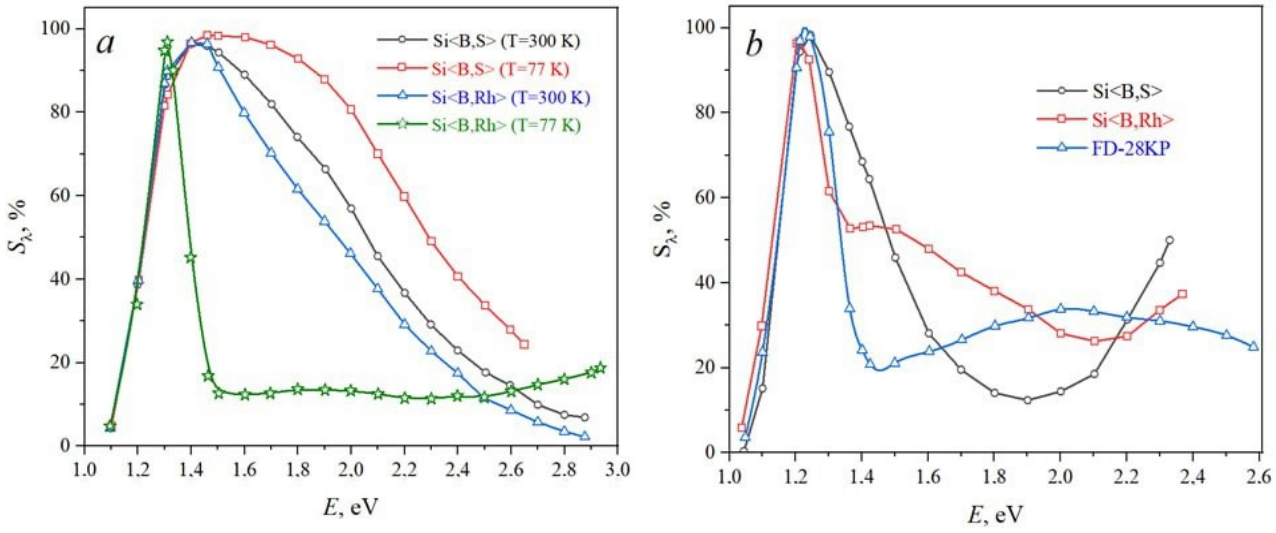

Figure 1. Spectral characteristics of photodetectors based on Si<B,S> and Si<B,Rh>: (a) p^+–i–p^+ structures; (b) p^+–i–n^+ structures, compared with the FD-28KP photodiode.

Furthermore, the Si<B,S> structures exhibit higher responsivity and lower threshold sensitivity compared to their Si<B,Rh> counterparts, confirming their effectiveness for use in high-precision photoelectric applications [8].

Table 1. Parameters of photosensitive structures based on Si<B,S> and Si<B,Rh>

no.	Parameter	Si<B,S>	Si<B,Rh>
1	Noise voltage (U_N), μV	2÷10	2÷10
2	Monochromatic sensitivity (S_λ) λ=0.85 μm, A/W	0.50÷0.75	0.50÷0.75
3	Integral current sensitivity (S_I), mA/lm	40÷50	40÷50
4	Photoresponse time constant (τ), s	(2÷50)·10⁻⁴	(2÷50)·10⁻⁴

Effect of Dopant Concentration

The conducted studies have shown that when p-type silicon is treated with sulfur (S) or rhodium (Rh), an increase in dopant concentration leads to a corresponding rise in photosensitivity. The silicon crystal lattice was able to effectively retain charge carriers under illumination, while the dopant elements helped reduce recombination effects [9]. However, when the dopant is added in excess beyond a certain threshold, an overcompensated state occurs, resulting in donor–acceptor compensation. This significantly reduces the number of free carriers [10]. Consequently, the sensitivity of the photodetectors typically drops by a factor of 3 to 4. Furthermore, this situation can lead to the formation of potential barriers within the structure, which are associated with structural defects and contribute to a reduction in photocurrent. For Si-based structures with varying Rh concentrations, the dark current (I_d)**,** measured in the absence of illumination, and the photocurrent (I_{ph})**,** measured under illumination, are presented in Table 2. This table also illustrates the influence of Rh concentration on the photoelectric response of the structures. The data in the table show that once the Rh concentration exceeds the optimal level, the steady-state photocurrent decreases, and the I_{ph}/I_d ratio changes. When the Rh concentration is approximately $N_{Rh} \approx 2.6 \cdot 10^{15}$ cm^{-3}, the I_{ph}/I_d ratio reaches a value of 10^7 at a temperature of 77 K, indicating very high sensitivity. However, when Rh concentration surpasses the threshold, no further improvement in sensitivity is observed, as excessive dopant levels ultimately lead to the degradation of the functional system [12].

Table 2. Photocurrents as a function of Rh concentration

N_{Rh}, cm^{-3}	300 K			77 K		
	I_d, A	I_{ph}, A	I_{ph}/I_d	I_d, A	I_{ph}, A	I_{ph}/I_d
$7 \cdot 10^{14}$	$1.1 \cdot 10^{-4}$	$1.0 \cdot 10^{-3}$	9.1	$2.3 \cdot 10^{-6}$	$8 \cdot 10^{-5}$	35
$1.5 \cdot 10^{15}$	$4 \cdot 10^{-6}$	$3.8 \cdot 10^{-5}$	9.5			$1.6 \cdot 10^{6}$
$2.6 \cdot 10^{15}$	$1.6 \cdot 10^{-6}$	$1.8 \cdot 10^{-5}$	11	$1 \cdot 10^{-10}$	$1.8 \cdot 10^{-3}$	$1.8 \cdot 10^{7}$

Effect of irradiation

The effect of radiation on the sensitivity parameters (S_λ and S_I) of structures formed on the basis of Si<B,Rh> and Si<B,S> is presented in Tables 3 and 4. These tables analyze the changes in current sensitivity of the structures under the influence of various types of radiation, such as protons, neutrons, electrons, and γ-quanta. According to the experimental results, in most cases, structures based on Si<B,Rh> demonstrated a greater increase in sensitivity compared to those based on Si<B,S>. Experimental results show that Si<B,Rh> and Si<B,S>-based photodetectors retain high levels of sensitivity under γ-irradiation fluences ranging from 10^{14} cm^{-2} to approximately 10^{18} cm^{-2} (Table 3). The retention of sensitivity at such high fluence levels indicates the robustness and stability of the defect-mixture complexes formed in the crystal lattice.

Table 3. Changes in current sensitivity under the influence of radiation type and currents

no.	Type of radiation	Integral flow (см$^{-2}$)	ΔS_I (%) Si<B,S>
1	Protons (E=18 MeV)	$5 \cdot 10^{12}/1 \cdot 10^{13}/5 \cdot 10^{13}$	20/50/92
2	Neutrons (E≥0.1 MeV)	$3 \cdot 10^{13}/5 \cdot 10^{13}/8 \cdot 10^{13}$	12/42/55
3	Electrons (E=6 MeV)	$10^{14}/10^{15}/10^{16}$	7/44/87
4	γ-quanta (^{60}Co)	$1.1 \cdot 10^{18}/2.5 \cdot 10^{18}/3.5 \cdot 10^{18}$	7/38/70

Table 4 presents how the key parameters — S_λ, S_I, and τ — of components based on Si<B,S> and Si<B,Rh> change before and after irradiation. Although the sensitivity of both structures decreased slightly after radiation exposure, their values remained above the industry-accepted thresholds.

Table 4. Parameters of Si<B,S> and Si<B,Rh> based structures before and after irradiation with fast neutrons

Parameter	Si<B,S> before	Si<B,S> after a fast neutron fluence of ~10^{14} cm^{-2}	Si<B,Rh> before	Si<B,Rh> after a fast neutron fluence of ~10^{14} cm^{-2}
Monochromatic sensitivity (S_λ), A/W	0.70	0.40	0.78	0.26
Integral current sensitivity (S_I), mA/lm	49.4	21	55	13.29
Photoresponse time constant (τ), s	$1 \cdot 10^{-4}$	$8 \cdot 10^{-5}$	$1 \cdot 10^{-4}$	$6 \cdot 10^{-5}$

Sensors based on Si<B,S> and Si<B,Rh> continued to operate reliably and stably even after being subjected to irradiation. These structures demonstrate notable utility for long-term wireless applications in high-radiation environments, providing a solid scientific basis for their future implementation [13].

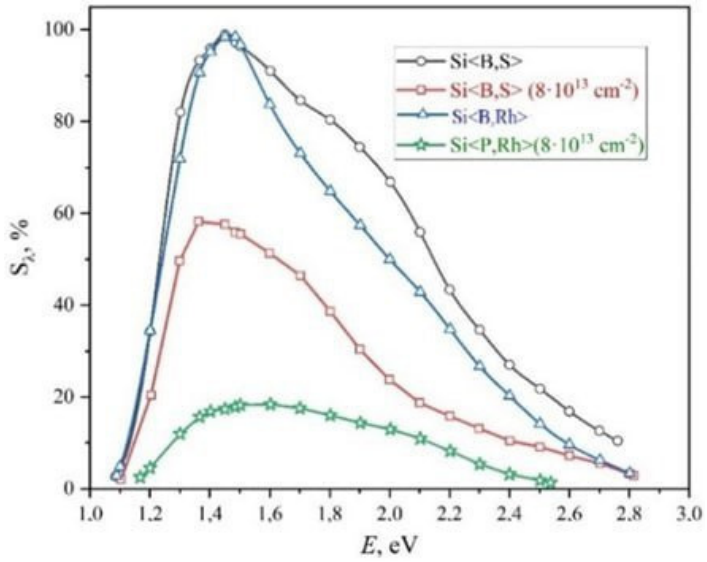

Figure 2. Spectral characteristics of Si<B,S> and Si<B,Rh> structures without irradiation and after irradiation with fast neutrons with a fluence of $8 \cdot 10^{13}$ cm^{-2}

The spectral characteristics shown in Figure 2 present an analysis of the photodetectors both before and after neutron irradiation. It was observed that silicon-based photodetectors containing boron and sulfur (n-Si<B,S>) demonstrated greater resistance to radiation-induced changes in spectral responsivity compared to conventional silicon counterparts. Silicon photodiodes fabricated from specially modified materials showed a neutron radiation resistance that is three to four times higher than that of standard industrial-grade photodiodes. This conclusion is further supported by the data in Table 5, which illustrates how exposure to fast neutrons ($E \geq 0.1$ MeV) affects the integral current responsivity of different photodetector types. The table provides a comparative analysis of the relative change in integral responsivity - expressed as $[S_I = \frac{S_I^0 - S_I^{rad}}{S_I^0} \cdot 100\%]$ - for photodetectors based on n-Si<B,S> and the industrial reference model FD-10K. According to the results, photodetectors built on n–Si<B,S> substrates maintained stable integral responsivity over the entire irradiation range, with relative variations within 10–31%. In contrast, the FD-10K industrial photodiode exhibited a significantly larger decrease in responsivity (80–88%), indicating that its performance degrades much more strongly under neutron irradiation.Thus, the results showed that the n–Si<B,S>-based photodetectors maintain their functional stability significantly better under neutron irradiation than the FD-10K device, which indicates that they are suitable for long-term operation in environments with high radiation levels [14].

Table 5. Relative change in integral susceptibility under the influence of fast neutrons

Fluence (cm^{-2})	Si<B,S> (%)	FD-10K (%)
$2 \cdot 10^{13}$	10	80
$4 \cdot 10^{13}$	17	83
$6 \cdot 10^{13}$	26	86
10^{14}	31	88

A specific group of diodes fabricated using p^+–n–p–n^+ type semiconductor structures was observed to exhibit an S-shaped current - voltage (I-V) characteristic. During the experiments, it was found that these diodes undergo a sudden switching behavior, resulting in what is known as a snapback voltage (U_{sp}). When the applied voltage approached a certain critical threshold, the diode's operating state changed abruptly. It was also noted that as the temperature increased, the S-shaped portion of the I–V curve gradually disappeared, making the curve smoother overall. This behavior makes such diodes particularly well-suited for temperature-sensitive devices like photorelays and thermal sensors. The measurements showed that snapback typically occurs within a voltage range of approximately $U_{sp} \approx 0.5$ to 10 V, with the corresponding current values ranging between $I_{sp} \approx 0.2$ and 1 mA [15]. At elevated temperatures, the snapback region faded, confirming the diode's suitability for thermal-responsive switching applications [16,17]. Further investigation revealed that the magnitude of the snapback voltage is directly influenced by two internal parameters of the diode: the base resistivity (ρ) and the level of compensation (K) [18]. This relationship was explored by analyzing the $U_{sp}^{max}/U_{sp}^{min}$ ratios presented in Table 6, which reflect how changes in compensation and base resistivity affect snapback behavior. The experimental results clearly demonstrated that increasing the compensation level leads to a wider snapback voltage range. This opens up the possibility of fine-tuning diode parameters and gaining precise control over the device's switching domain. By selecting an optimal compensation level in p^+–n–p–n^+ structures, it is possible to adjust the snapback voltage to meet specific technological requirements, enabling flexible and efficient use across a wide range of real-world electronic applications [19].

Table 6. Ratio $U_{sp}^{max}/U_{sp}^{min}$ depending on ρ and compensation level

ρ, Ω·cm	$U_{sp}^{max}/U_{sp}^{min}$	$K = \bar{P}/N_S$
1	-	0.51
3	1.5	0.78
10	3.5	0.91
20	5	0.95

γ-irradiation effect and relaxation

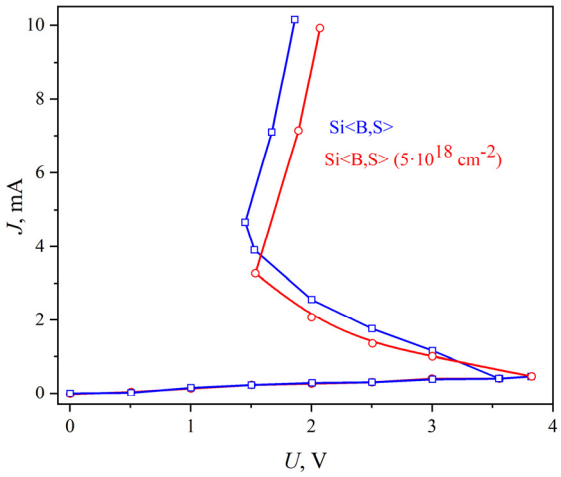

Figure 3. Current-voltage characteristics of S-diodes prepared based on Si<B,S> before and after irradiation (***γ*-**irradiation)

Silicon-based S-diodes show excellent radiation resistance due to their stable performance. The (U_{sp}) and (I_{sp}) measurements of the diodes remained stable when γ-radiation from ^{60}Co had been applied according to experimental findings (Figure 3). Data findings about the material's excellent resistance to radiation confirms the evidence strongly. The research investigated photoconductivity relaxation mechanisms in either Si<B,S> or Si<B,Rh> based diodes separately. The experimental results matched previously recorded data, which indicated that the relaxation of photoconductivity depends directly on increased carrier lifetime [20].

It is known that the relaxation of photoconductivity in silicon-based materials is directly related to the lifetime of unbalanced charge carriers. After illumination is removed, the excess carriers recombine through defect trap centers located within the forbidden band gap. The recombination-generation dynamics in such systems is described by Shockley-Read-Hall (SRH) statistics, where the presence of deep-level traps, shifting the Fermi level to a position away from the recombination centers, can significantly extend the carrier lifetime by reducing the effective recombination rate. The introduction of sulfur or rhodium into the compensated Si<B,S> and Si<B,Rh> structures created local deep energy states that stabilized the unbalanced carriers, thereby increasing the relaxation time of photoconductivity and the photosensitivity. Thus, the observed long-term relaxation behavior was consistent with the SRH model and confirmed that the increase in photoconductivity is directly related to the increase in the carrier lifetime. An extended carrier lifetime improves photo detector stability through photosensitive materials when operated over extended time span [21].

The research findings demonstrate that S-diodes containing Si<B,S> and Si<B,Rh> show promising performance in high-dose radiation environments due to their reliable operation and stable photosensitivity characteristics [22].

CONCLUSIONS

Based on the analysis of experimental investigations into the effects of various types of radiation on the photosensitivity properties of Si<B,S> and Si<B,Rh> structures, the following conclusions can be drawn:

Photodiodes using Si<B,S> and Si<B,Rh> become much more sensitive – increasing several times (from 0.35 to 2.6 A·W^{-1}) – when cooled down (from 300 K to 77 K). This makes them usable as very cold sensors and detectors for recording dim radiation.

The threshold sensitivity for Si<B,S> photodetectors is much better ($\Phi \approx 1.2\cdot10^{-11}$ lm·Hz$^{-1/2}$) than Si<B,Rh> ones. This means they can spot really weak light signals with great precision.

More sulfur (S) or rhodium (Rh) in the silicon boosts photoelectric sensitivity. But, if you add too much ($N_{Rh} > 2.6\cdot10^{15}$ cm^{-3}), the sensitivity drops by 3–4 times.

Si<B,S> and Si<B,Rh> photodetectors retain their sensitivity even under high-radiation environments (protons, neutrons, electrons, and γ-rays).

In p^+–n–p–n^+ diodes, we saw an S-shaped I-V behavior and the breakdown voltage (U_{sp} = 0.5÷10 V) disappeared as the temperature went up. Because of this, these diodes can be used as very sensitive photorelays and temperature sensors.

The photoconductivity relaxation in Si<B,S> and Si<B,Rh> diodes is due to the charge-carrier lifetime increasing. This helps photodetectors remain stable for a long time, enabling reliable, effective use in environments with high radiation levels.

Conflict of Interests

The authors declare that they have no conflicts of interest.

Funding

The present research was funded by the FZ-292154210 project, granted by the Ministry of Innovative Development of the Republic of Uzbekistan.

ORCID

A.Y. Boboev, https://orcid.org/0000-0002-3963-708X; **Sh.Kh. Yulchiev,** https://orcid.org/0009-0007-2576-4276
N.Y. Yunusaliyev, https://orcid.org/0000-0003-3766-5420; **Z.M. Ibrokhimov**, https://orcid.org/0009-0003-6931-661X

REFERENCES

[1] A.Y. Boboev, Kh.A. Makhmudov, Z.M. Ibrokhimov, A.K. Rafikov, N.Y. Yunusaliyev, and S.Kh. Ibrokhimov, "Long-term relaxation processes of electrical conductivity in compensated Si<B,S> and Si<B,Rh> monocrystals," East European Journal of Physics, (2), 436–440 (2025). https://doi.org/10.26565/2312-4334-2025-2-54
[2] H. Zhang, and N.-G. Park, "Progress and issues in p-i-n type perovskite solar cells," DeCarbon, **3**, 100025 (2024). https://doi.org/10.1016/j.decarb.2023.100025
[3] K.S. Daliev, Sh.B. Utamuradova, J.J. Khamdamov, M.B. Bekmuratov, O.N. Yusupov, Sh.B. Norkulov, and Kh.J. Matchonov, "Defect Formation in MIS Structures Based on Silicon with an Impurity of Ytterbium," East Eur. J. Phys. (4), 301-304 (2024). https://doi.org/10.26565/2312-4334-2024-4-33
[4] T. Taima, M. Chikamatsu, Y. Yoshida, K. Saito, and K. Yase, "Effects of intrinsic layer thickness on solar cell parameters of organic p-i-n heterojunction photovoltaic cells," Appl. Phys. Lett., **85**(26), 6412–6414 (2004). https://doi.org/10.1063/1.1841479
[5] F.P. Ziemba, G. Pelt, G. Ryan, L. Wang, and R. Alexander, "Properties of an n+ i p+ Semiconductor Detector," IRE Trans. Nucl. Sci., 9(3), 155–159 (1962). https://doi.org/10.1109/tns2.1962.4315987
[6] S.Z. Zainabidinov, A.Y. Boboev, N.Y. Yunusaliyev, and J.N. Usmonov, "An optimized ultrasonic spray pyrolysis device for the production of metal oxide films and their morphology," East Eur. J. Phys. (3), 293 (2024). https://doi.org/10.26565/2312-4334-2024-3-30
[7] M.S. Kukurudziak, "Analysis of the Spectral Characteristics of the Responsivity of Diffusion p-i-n; Photodiode Based on High Resistivity p-Si," Microsystems, Electronics and Acoustics, **28**(1), 47-51 (2023). https://doi.org/10.20535/2523-4455.mea.275010
[8] A.S. Saidov, Sh.N. Usmonov, M.U. Kalanov, and Kh.M. Madaminov, "Effect of gamma irradiation on photoconductivity and photosensitivity of $Si_{1-x}Sn_x$ solid solutions," Heliotechnical Mater. Sci. **47**, 48–51 (2011). https://doi.org/10.3103/S0003701X11010142
[9] M. Karimov, and A. K. Karakhodzhaev, "Investigation of Si<B,S> and Si<B,Rh> compensated photoresistors," Russ. Phys. J. **43**(6), 509–511 (2000). https://doi.org/10.1007/bf02508633
[10] M. Koopmans, M.A.T. Leiviskä, J. Liu, J. Dong, L. Qiu, J. C. Hummelen, G. Portale, *et al*., "Electrical Conductivity of Doped Organic Semiconductors Limited by Carrier–Carrier Interactions," ACS Appl. Mater. Interfaces, **12**(50), 56222–56230 (2020). https://doi.org/10.1021/acsami.0c15490
[11] H.A. Hadi, R.A. Ismail, and A.R. Abdulwahhab, "Effect of Gamma Irradiation on the Optoelectronics Properties of Porous Si/c-Si Heterojunction photodetector," Silicon, **16**(3), 1097–1106 (2023). https://doi.org/10.1007/s12633-023-02731-w
[12] A.Y. Boboev, B.M. Ergashev, N.Y. Yunusaliyev, J.S. Madaminjonov, "Electrophysical nature of defects in silicon caused by implanted platinum atoms," East Eur. J. Phys. (2), 431 (2025), https://doi.org/10.26565/2312-4334-2025-2-53
[13] Y. Wei, Ch. Lan, et al., "Recent Advances in Photodetectors Based on Two-Dimensional Material/Si Heterojunctions," Appl. Sci. **13**, 11037 (2023). https://doi.org/10.3390/app131911037V.
[14] N.K. Tailor, C.A. Aranda, *et al*., "Negative Photoconductivity: Bizarre Physics in Semiconductors," ACS Mater. Lett. **4**(11), 2298–2320 (2022). https://doi.org/10.1021/acsmaterialslett.2c00675
[15] A.O. Goushcha, B. Tabber, *et al*., "Silicon photoresistive sensors with improved performance," J. Appl. Phys. **123**, 044505 (2018). https://doi.org/10.1063/1.5006819
[16] G.-F. Dalla and J. Ye, "Silicon Radiation Detector Technologies: From Planar to 3D," Chips, **2**, 83–101 (2023). https://doi.org/10.3390/chips2020006
[17] W. Jiang, T. Li, L. Yin, J. Chen, D. Niu, G. Li, Y. Shi, *et al*., "Thermal switch with tunable thermal conductivity via external stimuli and thermal diodes," Appl. Therm. Eng. **275**, 126848 (2025). https://doi.org/10.1016/j.applthermaleng.2025.126848
[18] V. Terracciano, A. Borghese, M. Boccarossa, V. d'Alessandro, and A. Irace, "A Geometry-Scalable Physically-Based SPICE Compact Model for SiC MPS Diodes Including the Snapback Mechanism," Solid State Phenom. **360**, 67–74 (2024). https://doi.org/10.4028/p-b9imzl
[19] F. Chen, D.S. Chao, M.-J. Chen, P. Yen, J.-T. Yeh, C.-M. Lee, W.-H. Wang, *et al*., "S-shaped negative differential resistance modeling in electro-thermal simulation of phase-change memory programming," in: *Proceedings of the 2007 Non-Volatile Memory Technology Symposium (NVMT)*, 2007, pp. 67–70. https://doi.org/10.1109/NVMT.2007.4389949
[20] T. Asada, Y. Ichikawa, and M. Kato, "Carrier lifetime measurements in semiconductors through the microwave photoconductivity decay method," Journal of Visualized Experiments (JoVE), **146**, 31058909 (2019). https://doi.org/10.3791/59007
[21] C.R. Doerr, "Silicon photonic integration in telecommunications," Front. Phys. **3**(37), (2015). https://doi.org/10.3389/fphy.2015.00037
[22] M.S. Yunusov, M. Karimov, and B.L. Oksengendler, "On the mechanisms of long-term relaxation of the conductivity in compensated Si<B,S> and Si<B,Rh> as a result of irradiation," Semiconductors, **32**(3), 238–240 (1998). https://doi.org/10.1134/1.1187387

ВПЛИВ РІЗНИХ УМОВ ОСВІТЛЕННЯ НА ФОТОЧУТЛИВІ ВЛАСТИВОСТІ СТРУКТУР Si<B,S> ТА Si<B,Rh>

Акрамджон Й. Бобоєв[1], Шахріор Х. Юльчієв[2], Зіоджон М. Іброхімов[3], Нурітдін Й. Юнусалієв[1]

[1]Андижанський державний університет імені З.М. Бабура, Андижан, Узбекистан

[2]Андижанський державний педагогічний інститут, Андижан, Узбекистан

[3]Андижанський державний технічний інститут, Узбекистан

У статті проаналізовано результати експериментальних досліджень фоточутливих властивостей структур Si<B,S> та Si<B,Rh> під впливом різних видів випромінювання. Було виявлено, що чутливість фотодіодів, виготовлених на основі Si<B,S> та Si<B,Rh>, зростає в кілька разів (від 0,35 до 2,6 $А \cdot Вт^{-1}$) при зниженні температури (від 300 К до 77 К). Порогова чутливість фотодетекторів на основі Si<B,S> виявилася значно вищою порівняно з фотодетекторами на основі Si<B,Rh> ($Ф \approx 1{,}2 \cdot 10^{11}$ $лм \cdot Гц^{-1/2}$). Збільшення концентрації сірки (S) або родію (Rh) у кремнії підвищує фоточутливість, але чутливість зменшується в 3-4 рази при перевищенні допустимої концентрації ($NRh > 2{,}6 \cdot 10^{15}$ $см^{-3}$). Було виявлено, що фотодетектори на основі Si<B,S> та Si<B,Rh> зберігають свої параметри чутливості при високих рівнях радіаційного опромінення (від протонів, нейтронів, електронів та γ-квантів). У діодах на основі p^+-n-p-n^+ спостерігається S-подібна вольт-амперна характеристика, а також зникнення напруги затвора (Usp = 0,5÷10 В) зі збільшенням температури. Релаксація фотопровідності в діодах на основі Si<B,S> та Si<B,Rh> зумовлена збільшенням часу життя носіїв заряду.

Ключові слова: *сірка; родій; фотопровідність; концентрація легуючої домішки; випромінювання; монохроматична чутливість; релаксація*

EAST EUROPEAN JOURNAL OF PHYSICS. 4. 627-634 (2025)
DOI:10.26565/2312-4334-2025-4-66 ISSN 2312-4334

IMPACT OF DONOR-ACCEPTOR POSITIONS TO TUNE EFFICIENT DYE-SENSITIZED SOLAR CELLS: DFT/TD-DFT STUDY

F. Bahrani*, S. Resan, R. Hameed, M. Al-Anber
Molecular Engineering and Computational Modeling Lab, Department of Physics, College of Science, University of Basrah, Basrah, Iraq
**Corresponding Author email: fatimah.bahrani@uobasrah.edu.iq,*
Received August 2, 2025; revised November 10, 2025; accepted November 19, 2025

The anthracene molecule was adopted as a π-conjugation bridge for the D–π–A system with a methyl group CH_3 and a nitro group NO_2 acting as donor and acceptor groups. The influence of the anthracene nature junction with the donor and acceptor sides was evaluated on the performance of a dye-sensitized solar cell (DSSC). The donor and acceptor positions in this study changed around the anthracene. Density functional theory (DFT) has been utilized at the B3LYP theory level. The donor group could bind to anthracene at two specific sites, while the acceptor group could bind to the remaining anthracene sites, excluding the donor group site. The photovoltaic and electronic properties have been investigated. The results showed that the best-performing molecular dyes, $D_{10}A_7$, $D_{10}A_8$, and D_1A_6, are suitable for use as sensitizers due to their energetically favorable photovoltaic parameters, which are attributed to the potential for electron injection and regeneration.
Keywords: *D–π–A; TD-DFT; DSSC; Photovoltaic properties; Anthracene*
PACS: 88.40.hj, 31.15.es**,** 82.47.Jk

INTRODUCTION

Following Grätzel's initial publication, DSSC research garnered significant interest in renewable energy studies because of its affordability, straightforward manufacturing process, and eco-friendly characteristics [1]. Like inorganic dyes, Ruthenium complex-based dyes have good chemical and thermal stability, but are expensive and unavailable [2]**.** Metal complex dye molecules, such as Zn-porphyrin, based on DSSCs have high light-harvesting ability [3]. Metal-free organic dyes have low cost and high absorption coefficients [4]. Although Zn-porphyrin metal complexes based on DSSCs have achieved higher conversion efficiency than metal-free organic dyes, they are costly, highly toxic, and of limited resource [5]. The donor-π-acceptor (D–π–A) moieties are the most prevalent structure in DSSCs due to their light harvesting nature and appropriate modification of the nature of the intramolecular charge transfer [1, 6]. The dye sensitizer absorbs the incident light; therefore, the electron is excited by photoexcitation and moves from the highest occupied molecular orbital (HOMO) to the lowest unoccupied molecular orbital (LUMO) of the dye, as shown in Figure 1 which explain the working principle of DSSCs. The electron is injected into the titanium dioxide (TiO_2) conduction band; therefore, the charge separation occurs at the dye and semiconductor interface through the photo-induced electron injection process. Then, the electron transfers from the TiO_2 to the transparent conducting oxides (TCO) [7]. Thus, the electron reaches from the anode to the cathode and diffuses from the cathode to the electrolyte, so the regeneration of the dye occurs. Based on that, the dye is oxidized to make the DSSC stable and long-lasting [2].

Additionally, the energy level of the redox couple (iodide I^-/triiodide I_3^-) should be higher than the HOMO level of the dye for successful regeneration to occur. The conduction band of the semiconductor metal oxide photo-anode should be below the LUMO level of the dye. The conduction band of TiO_2 should be lower than the LUMO energy level of the dye to allow the electron to be transported to the anode [8]. For potential electron injection and dye regeneration, the HOMO and LUMO levels of the dye should lie with the redox electrolyte (I^-/I_3^-) and the conduction band of TiO_2, respectively [9]. In a molecule, the location of the most energetic electrons is typically considered the HOMO, and it is the most likely location to react with an electrophile. According to a study conducted by Bulat et al. on the HOMO in a molecule, it confidently points to the site of the most energetic electron. It is noted that the HOMO does not consider that the lower energy orbitals in different parts of the molecule may still be occupied by electrons. The lowest values of the average local ionization energy have a considerable influence on the magnitudes and locations of electron density. The HOMO is delocalized and does not point to the lower-lying orbital contributions. Consequently, it is essential to be caution when considering the HOMO as the best energetic electron in a molecule and the most reactive site for the electrophile [10].

Recently, anthracene has been used in DSSCs due to its unique photophysical properties, such as bright blue electroluminescence [11]. When investigating DSSCs, the electron diffusion properties matter, not the luminescent or fluorescent properties. Rapid intramolecular charge transport is crucial in successful electron injection from the anchoring groups of the dye into the conduction band of the semiconductor and successful regeneration back into the dye via the electrolyte. Recombination is crucial in electroluminescence but is a drawback in DSSCs. Anthracene compound is reported in various applications such as light-emitting diodes, thin film transistors, and bulk heterojunction solar cells due to its outstanding optical properties, excellent stability, easy tunability, low cost, and high carrier mobility [12].

Cite as: F. Bahrani, S. Resan, R. Hameed, M. Al-Anber, East Eur. J. Phys. 4, 627 (2025), https://doi.org/10.26565/2312-4334-2025-4-66

The π-conjugated bridge groups help in the electronic transition charge transfer from the ground state to the excited state to enhance the light absorption of DSSCs at a longer wavelength [5, 14, 15], and specify how the π-spacer can facilitate charge transport between different dye fragments. The charge recombination and dye aggregation reduce the efficiency of the metal-free organic dyes [16]. In organic solar cells, fullerenes [15, 17-18] facilitate electron transport, although they have not been studied extensively.

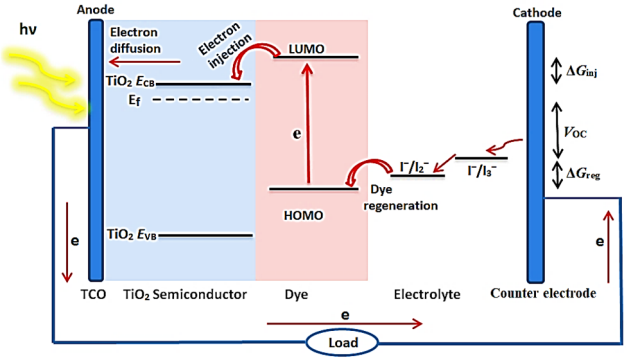

Figure 1. Schematic diagram of the dye-sensitised solar cell (DSSCs) working principle. hν is incident light (photon), e is electron, TCO stands for transparent conducting oxide, TiO_2 is titanium dioxide, E_{CB} is the conduction band edge energy level, E_{VB} is the valence band edge energy level, E_f is the Fermi level, I^-/I_3^- is the iodide/triiodide redox couple, I^-/I_2^- is the iodide/diiodide radical redox pair, HOMO is the highest occupied molecular orbital, LUMO is the lowest unoccupied molecular orbital, ΔG_{inj} is the injection driving force, ΔG_{reg} is the regeneration driving force, and V_{OC} is the open circuit voltage.

Additionally, nanotubes [19, 20] have recently been used in organic solar cells. Nitro group (NO_2) has been employed as a strong electron acceptor group because of its remarkable electron-withdrawing ability and a strong anchoring ability to bond through chemisorption with the semiconductor [21, 22]. In a previous study on benzene and triphenylamine as donors, dimethylanisole as π-conjugated and CN, COOH, and NO_2 as acceptors, Mathiyalagan et al. concluded that triphenylamine and NO_2 have the most potent effect as electron donors and acceptors, respectively, and have perfect optoelectronic properties for use in DSSCs [22]. Methyl group (CH_3) is a substantial electron donor due to its strong electron-donating nature [23]. In a recent work by Bora and Kalita on tetrathiafulvalene as a donor and both cyanoacrylic and carboxylic as acceptors with thiophene as π-conjugation, the dye electron density increased when the CH_3 group and the NO_2 were attached in the donor and acceptor parts, respectively, which maximized the redshift by reducing the energy bandgap [23]. The previous literature generally searched for affective LUMO or HOMO groups to use in D–π–A to get better DSSC efficiency. These studies did not modify the binding sites of these groups; therefore, they did not examine the effect of the choice of binding site to know how the changing sites affected the working cells. In the current research, this has been addressed by studying the D–π–A structure by adding LUMO and HOMO groups and changing their binding sites to find out what effect this change had on the photovoltaic parameters.

This paper used anthracene as a π-spacer between the CH_3 donor and NO_2 acceptor. The position of the donor and acceptor groups around the anthracene was investigated. To evaluate the impact of changing the position of donor and acceptor groups around the π-conjugation on photovoltaic (PV) performance, a molecular orbital with the highest occupied energy E_{HOMO} and a molecular orbital with the lowest unoccupied energy E_{LUMO}, optical bandgap energy (E_g), the maximum absorption wavelengths, oscillator strength (f), light harvesting efficiency (LHE), excited state lifetime (τ), injection driving force (ΔG_{inj}), regeneration driving force (ΔG_{reg}), open circuit voltage (V_{OC}) and fill factor (FF) were illustrated.

COMPUTATIONAL AND THEORETICAL METHODOLOGY

In the D–π–A design, the CH_3, and NO_2 were selected as the donor and acceptor groups, respectively, and they are linked by the anthracene, which acts as a π-conjugation fragment (see Figure 2).

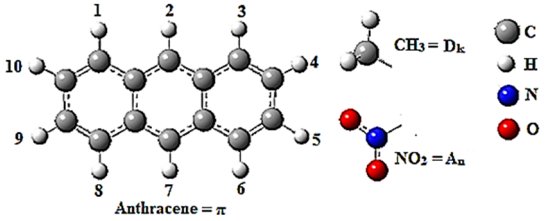

Figure 2. The numbering scheme is used for the variation in functional group positions: D-donor (D_k = CH_3 methyl group) and A-acceptor (A_n = NO_2 nitro group) around the anthracene molecule (π = anthracene); (D_k–π–A_n), where k = 1 or 10, and n = 1, 2,…,10, with k≠n. C, H, N, and O represent carbon, hydrogen, nitrogen, and oxygen, respectively.

According to the numbering D_kA_n = (D_k–π–A_n) in Figure 2, the donor group (D_k) is fixed on anthracene and limited to only two positions, either k = 1 or k = 10, while the acceptor group (A_n) is fixed around the other anthracene positions so that n = 1, 2…10 and k≠n. In this case, when the donor group is fixed on k = 1, the acceptor group will vary on positions

of anthracene (n = 2–10), and when the CH_3 groups are fixed on k = 10, the acceptor groups will vary on positions of anthracene (n = 1–9); therefore, 18 isomers of D_k–π–A_n were obtained. The molecular dye has been studied to explore the influence of changing the position of donor and acceptor groups around the π-conjugated system on the geometries, electronic, and PV properties of the DSSCs.

Complete optimization of these 18 cases was carried out with TD-DFT approaches [24] at B3LYP/6-311G(d,p), where 6-311G(d,p) basis sets for C, H, O, and N, usually approved as a beneficial plan to speculate the molecular structures, based on optimized ground state geometry, were used to evaluate the oscillator strengths and excited state energy calculations. The ground state geometry optimizations for the D_k–π–A_n structure were performed with the Gaussian 09 program package using DFT [25, 26] at the hybrid functional of exchange-correlation B3LYP (Becke three-parameter Lee-Yang-Parr) theory level [26]. Furthermore, all calculations were performed in the gas phase. DSSCs calculations in the real case are more complex than those of the gas phase, where in real DSSCs, dye molecules stick to the TiO_2 surface and are surrounded by a liquid electrolyte. Therefore; the values of ΔG_{inj}, ΔG_{reg}, V_{OC}, and *FF* should be interpreted as qualitative trends. The gas phase does not take these factors into account, and this can affect the dye performance in addition to the overall cell efficiency [27]. However, gas phase calculations are still extremely valuable since they provide initial insights about the electrical and optical properties of the dye [28].

For practical applications, simple chemical methods can be used to bind the methyl ($-CH_3$) donor group and nitro ($-NO_2$) acceptor group to the anthracene π -bridge. These groups are added to the anthracene part of the dye to improve DSSCs performance. Common methods such as Friedel-Crafts alkylation or Suzuki coupling can be used to attach the $-CH_3$ group, whilst the $-NO_2$ group can be bound through aromatic nitration [28]. Furthermore, a carboxylic acid group is added in the dye to make it stick strongly to the TiO_2 surface [29]. These methods are well established and have been successfully utilized in photovoltaic research [27, 29, 31], our D- π -A dyes are actual and can be surely employed in DSSCs devices.

For PV characterisation, the substantial factor in DSSC is V_{OC} and can be estimated using the commonly used approximately [13]:

$$V_{OC} = E_{\mathrm{LUMO}} - E_{\mathrm{CB}}\,(\mathrm{TiO_2}) \tag{1}$$

where E_{LUMO} is the LUMO energy level of the dye, E_{CB} is the reduction potential of TiO_2 conduction band edge of the semiconductor, with the widely used experimental value of TiO_2 E_{CB} ($E_{\mathrm{CB}} = -4.0$ eV) [33]. All energy values are presented in volts (V), and this expression is intended as a preliminary theoretical estimate. The *FF* have a crucial role in the device efficiency and can be determined as [34]:

$$FF = V_{\mathrm{OC}} - \ln\,(V_{\mathrm{OC}} + 0.72)/(V_{\mathrm{OC}} + 1) \tag{2}$$

LHE, one of the key factors that affects the J_{SC}, is expressed as [35]:

$$LHE = 1 - 10^{-f} \tag{3}$$

where *f* is the oscillator strength of the adsorbed dye molecule related to λ_{max}. The Lambert-Beer law proposes that the *LHE* of a cell relies on the coefficient of dye extinction, the concentration of dye, and the optical path length within the semiconductor film [36]. The lifetime (τ) of the molecular dye can be determined as follows [35]:

$$\tau = 1.499/fE^2 \tag{4}$$

where *E* is the different electron states' excitation energy (cm^{-1}) of the different electronic states. In addition, photovoltaic performance depends on the electron injection rate (ΔG_{inj}) from the dye to the TiO_2 (E_{CB}). Therefore, ΔG_{inj} is beneficial for examining the injection driving force of electrons injected from the dye-excited state E_{LUMO} level to the conduction band of the semiconductor oxide [25]. A negative sign suggests the process of spontaneity [13]. ΔG_{inj} can be determined according to Preat's method [37] as follows [38]:

$$\Delta G_{inj} = E_{\mathrm{dye}*} - E_{CB}(\mathrm{TiO_2}) \tag{5}$$

$E_{\mathrm{dye}*}$ is the oxidation potential energy of the dye molecule in the excited state and can be estimated by:

$$E_{\mathrm{dye}*} = E_{\mathrm{dye}} - E_{0-0} \tag{6}$$

E_{dye} is the oxidation potential of the dye molecule in the ground state (donate $-E_{\mathrm{HOMO}}$), and E_{0-0} is an electronic vertical transition energy corresponding to λ_{max}. ΔG_{reg} is another critical factor that affects the J_{SC} [39]. The significant driving forces of dye regeneration, promote the regeneration efficiency resulting in high J_{SC} [40]. ΔG_{reg} can be calculated as follows [41]:

$$\Delta G_{\mathrm{reg}} = E_{\mathrm{redox}} - E_{\mathrm{dye}} \tag{7}$$

where E_{redox} is the redox potential of the applied electrolyte. Iodide/triiodide (I^-/I_3^-) is typically used as an electrolyte, and the level of couple redox electrolyte (I^-/I_3^-) is about −4.80 eV [25]. Both ΔG_{inj} and ΔG_{reg} represent the change in the free energy in eV for the injection and rejection electrons [13].

RESULTS AND DISCUSSION

Ground state geometry

Knowing the most stable structure for 18 isomers of the D_k–π–A_n is essential to examine the relative energy (ΔE_t). The ground state geometry of D_k–π–A_n was determined using the B3LYP/6-311G(d,p) levels. The differences in ground state energy of the D_k–π–A_n due to the position of donor and acceptor groups around the anthracene are listed in Table 1. The five most stable structures of the anthracene derivatives, with the minimum relative energy (ΔE_t) of 18 isomers, are $D_{10}A_5$, $D_{10}A_4$, D_1A_9, D_1A_4, and D_1A_5, respectively. This indicates that the lowest ground state energy is for $D_{10}A_5$. Generally, a comparison with the previous studies' significant differences [14,18]. Furthermore, no available experimental data are available for comparison.

Frontier molecular orbitals and energy levels

The electronic distribution of frontier orbitals is vital in transferring the effective charge from the donor to the acceptor [5]. The effective charge transfers between the E_{HOMO} and E_{LUMO} levels are substantial for studying the molecular structure of organic PV. The E_{HOMO} levels should be located below the electrolyte I^-/I_3^- (−4.80 eV) [33] to get an efficient dye in DSSCs, and the E_{LUMO} levels should be located above the TiO_2 E_{CB} (−4.0 eV) [33]. Therefore, the electronic and transition properties of the molecule dyes were investigated employing the B3LYP/6-311G(d,p) levels. In our results, all the values of the HOMO level are located below the value of the TiO_2 E_{CB}; therefore, the electron can inject efficiently from the dye to the TiO_2 E_{CB} and the electron can then transfer from the TiO_2 E_{CB} to the TCO and diffuse to the electrolyte. In addition, all the values of the LUMO level are located above the value of the TiO_2 E_{CB}; therefore, the dye can be successfully regenerated back into the dye through electron acceptance from the electrolyte I^-/I_3^-.

The DFT calculated results of E_{HOMO}, E_{LUMO}, and E_g for various positions of the acceptor and donor for D_1A_n and $D_{10}A_n$ are listed in Figure 3. The E_{HOMO} level values of D_k–π–A_n, located below the electrolyte, are in the order D_1A_2, $D_{10}A_1$, $D_{10}A_8$, D_1A_3 and $D_{10}A_3$, respectively. Thus, D_1A_2, $D_{10}A_1$, $D_{10}A_8$, D_1A_3 and $D_{10}A_3$ may enhance the efficient regeneration of electrons back into the dye in DSSCs. In addition, they have the highest ground state energy due to the electrolyte I^-/I_3^-; therefore, they can occur easily and enhance the ΔG_{reg}. E_{HOMO} is often related to the ability [42,43] to donate electrons. Thus, D_1A_2 and $D_{10}A_1$ have the highest electron-donating ability. However, for the E_{LUMO} levels that should be located above the TiO_2 E_{CB}, the highest maximum value in the order of D_k–π–A_n is D_1A_2, $D_{10}A_1$, $D_{10}A_2$, $D_{10}A_7$ and D_1A_7, respectively. The highest value of the E_{LUMO} levels is D_1A_2 despite its high relative stability. Therefore, the effective values of the E_{LUMO} levels that improve the V_{OC} and ΔG_{inj} are for D_1A_2 and D_1A_{10}, respectively, and show the highest electron-accepting ability. Figure 3 illustrates that the energy gap values of D_1A_3, D_1A_6, $D_{10}A_7$, $D_{10}A_6$, and $D_{10}A_3$ are smaller than those of the other dyes (isomers). From previous studies, we expect that the sensitisers with smaller gaps of E_{LUMO}−E_{HOMO} energy show favourable characteristics beneficial to higher *LHE* in the DSSC and facilitate the injection of electrons and the regeneration of dye, which enhances efficiency. Therefore, our designed dyes D_1A_3, D_1A_6, $D_{10}A_7$, $D_{10}A_6$, and $D_{10}A_3$ may have better light harvesting ability than the others [5, 44-46]. Interestingly, we noticed that the decrease in energy gap values is mainly due to decreased LUMO energy levels. This result confirms that the energy levels of the dye sensitisers can be tuned through the donating group's position around the π-conjugated bridge.

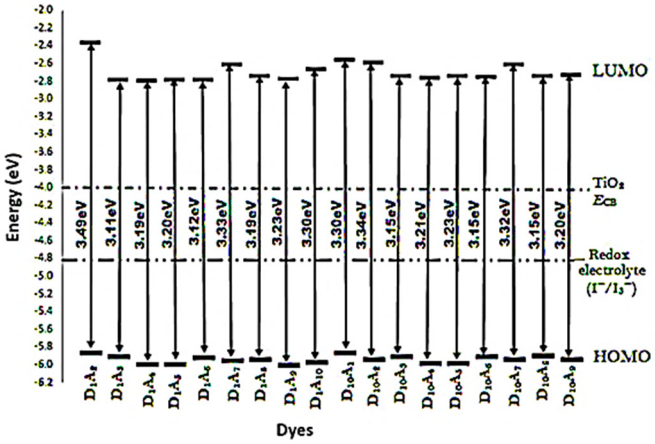

Figure 3. Calculated HOMO- LUMO electronic structures of all studied dyes. TiO_2 E_{CB} represents the conduction band edge of the titanium dioxide (TiO_2); I^-/I_3^- is the redox couple (iodide I^-/triiodide I_3^-), HOMO is the highest occupied molecular orbital, LUMO is the lowest unoccupied molecular orbital

The absorption ability of dye sensitizers plays an essential role in promoting J_{SC}. The solar radiation, including the visible and near-IR range, should be absorbed by a suitable sensitizer in DSSCs [47] as much as possible. Position modifications in the donor-acceptor groups would tune the photo absorption spectra of 18 dye isomers. As Figure 4 shows, the designed dyes D_1A_{10} and $D_{10}A_1$ have the broadest absorption spectra, except for blue shifts. The maximum absorption coefficients of dyes are D_1A_8, D_1A_6, $D_{10}A_5$, D_1A_4, D_1A_9 and $D_{10}A_3$, respectively. The origins of these absorptions are detailed by calculating the singlet electronic transition in the Gaussian 09W program. The maximum absorption peaks of

isomer dyes D_1A_6, $D_{10}A_3$ and D_1A_3 have more redshifts than others. Therefore, we selected D_1A_6, $D_{10}A_3$ and D_1A_3 to design novel dyes further.

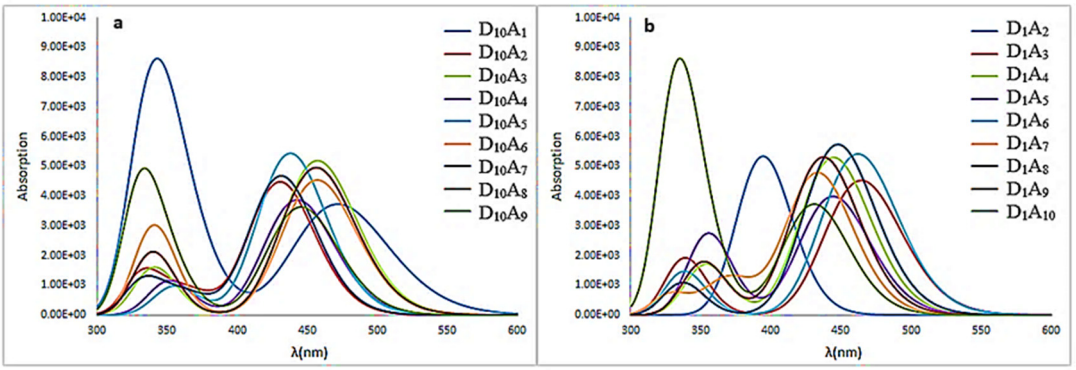

Figure 4. Absorption spectra of 18 dye isomers as a function of wavelength (λ). (a) isomers where the donor group is fixed on the anthracene at site D10, and the acceptor group is bound to the remaining sites. (b) isomers where the donor group is fixed on the anthracene at site D1, and the acceptor group is bound to the remaining sites

Photovoltaic properties

The fundamental factors for characterising an efficient photovoltaic device are V_{OC}, *FF*, *LHE*, τ, ΔG_{inj}, and ΔG_{reg} and are listed in Table 1. These parameters were investigated using TD-DFT theory levels. The impact of the positions of the donor-acceptor groups on the device performance was illustrated.

For increased light-capturing, the *LHE* should be as high as possible to promote the photocurrent and enhance the photovoltaic efficiency. The *LHE* and *f* are directly proportional to each other [13]. The higher *LHE* values in the order are $D_{10}A_7$, D_1A_6, $D_{10}A_5$, $D_{10}A_3$ and $D_{10}A_8$, respectively. Here, $D_{10}A_7$ has the highest *LHE* and can therefore encourage the absorption of the photons and maximise the photocurrent [48]. *LHE* is considered one of the most critical parameters for determining dye efficiency.

Table 1. Calculated relative energy (ΔE_t), oscillator strength (*f*), light harvesting efficiency (*LHE)*, excited state lifetime (τ), injection driving force (ΔG_{inj}), regeneration driving force (ΔG_{reg}), open circuit voltage (V_{OC}), fill factor (*FF*) of dye isomers (D_k–π–A_n)

Position	ΔE_t(eV)	*F*	*LHE*	τ (ns)	ΔG_{inj} (eV)	ΔG_{reg} (eV)	V_{OC} (V)	*FF*
D_1A_2	0.556	0.047	0.103	4.021	−0.955	1.065	1.631	0.890
D_1A_3	0.223	0.062	0.133	2.920	−0.985	1.107	1.212	0.862
D_1A_4	0.047	0.072	0.152	2.838	−0.732	1.192	1.203	0.861
D_1A_5	0.047	0.054	0.116	3.567	−0.821	1.192	1.214	0.862
D_1A_6	**0.228**	**0.075**	**0.159**	**2.485**	**−0.928**	**1.116**	**1.211**	**0.861**
D_1A_7	0.384	0.063	0.134	3.242	−0.774	1.152	1.380	0.875
D_1A_8	0.217	0.065	0.138	2.803	−0.947	1.140	1.255	0.865
D_1A_9	0.037	0.069	0.146	2.959	−0.722	1.207	1.225	0.863
D_1A_{10}	0.240	0.050	0.109	3.848	−0.821	1.175	1.326	0.871
$D_{10}A_1$	0.289	0.052	0.112	4.022	−0.831	1.069	1.436	0.878
$D_{10}A_2$	0.326	0.063	0.134	3.359	−0.739	1.143	1.405	0.876
$D_{10}A_3$	0.183	0.073	0.155	2.628	−0.895	1.107	1.251	0.865
$D_{10}A_4$	0.005	0.055	0.119	3.486	−0.823	1.181	1.237	0.864
$D_{10}A_5$	0.000	0.075	0.158	2.777	−0.711	1.186	1.251	0.865
$D_{10}A_6$	0.184	0.066	0.141	2.770	−0.964	1.109	1.248	0.865
$D_{10}A_7$	**0.329**	**0.079**	**0.167**	**2.463**	**−0.840**	**1.142**	**1.386**	**0.875**
$D_{10}A_8$	**0.185**	**0.073**	**0.155**	**2.540**	**−0.947**	**1.101**	**1.256**	**0.865**
$D_{10}A_9$	0.150	0.052	0.112	3.507	−0.947	1.144	1.263	0.866

A fundamental parameter for DSSC performance is *τ,* which represents the number of diffusing electrons from the excited dye into the TiO_2 E_{CB} semiconductor [39]. In the long lifetime, the charge transfer is facilitated, leading to a potential J_{SC} [49], in contrast, in the short lifetime, the transfer of the charge becomes faster because of electron recombination [39]. *τ* is inversely proportional to *f*. The longer *τ* values for dye isomers order are for $D_{10}A_1$, D_1A_2, D_1A_{10}, D_1A_5, and $D_{10}A_9$, respectively. D_1A_5, $D_{10}A_1$, and D_1A_2 have approximately the most extended value of *τ*; therefore, they can promote the J_{SC} since they have higher generated charge transfer efficiency.

ΔG_{inj} affects the electron injection [39]. The higher absolute value (more negative values) of ΔG_{inj} makes the electron injection more efficient and improves the J_{SC} [39]. E_{dye^*} (E_{LUMO}), which, must be 0.5 eV above TiO_2 E_{CB} to have adequate solar energy converted to current while E_{dye} (E_{HOMO}), which must be 0.2 eV below the redox electrolyte [50-51]. Generally, all the calculated values of ΔG_{inj} have negative sign values; therefore, the electronic injection from the excited state of the dye to the TiO_2 E_{CB} is spontaneous [13]. All values of ΔG_{inj} have less negative potential than the TiO_2 E_{CB} (−4.0eV), which enhances the electron injection from the excited dyes to the TiO_2 E_{CB}. D_1A_3, $D_{10}A_6$, D_1A_2, D_1A_8, $D_{10}A_8$,

and $D_{10}A_9$ exhibit noticeably more negative values and a more stable structure; therefore, they have more efficient electron injection and a higher J_{SC}. J_{SC} is also influenced by the regeneration efficiency of dye (η_{reg}), which is determined by the driving force of regeneration ΔG_{reg}. The regeneration process of dye can significantly influence the efficiency of DSSC. However, higher ΔG_{reg} leads to lower recombination efficiency and represents the increased proportion of absorbed light converted into electrical power [13]. The calculated results of ΔG_{reg} for the dye molecules show that all D_1A_n and $D_{10}A_n$ values have E_{HOMO} levels lower than the electrolyte (−4.80eV), as listed in Table 1 and plotted in Figure 4. The larger ΔG_{reg} values are for D_1A_9, D_1A_4, D_1A_5, $D_{10}A_4$, and $D_{10}A_5$ respectively. D_1A_9 has the greatest ΔG_{reg} values, which enhances the V_{OC} due to the reduction of the recombination reaction, leading to higher photocurrent generation.

In DSSC, the difference in energy between the E_{LUMO} of dye and TiO_2 E_{CB} and the loss in energy via the photo charge generation represents the V_{OC} [52]. The higher E_{LUMO} will produce a higher V_{OC}. The highest V_{OC} values of dyes in the order are for D_1A_2, $D_{10}A_1$, $D_{10}A_2$, $D_{10}A_7$, and D_1A_7, respectively. The highest V_{OC} value for D_1A_2 is equal to 1.631eV. However, *FF* values depend on the V_{OC} [34]. For D_k–π–A_n, the *FF* values are in the order D_1A_2, $D_{10}A_1$, $D_{10}A_2$, $D_{10}A_7$, and D_1A_7, respectively. The range of the *FF* values is between (0.890 to 0.875). The calculated results suggest that D_1A_2, $D_{10}A_1$, $D_{10}A_2$, $D_{10}A_7$, and D_1A_7 have excellent values for V_{OC} and *FF*. Generally, based on our findings, including *LHE*, V_{OC}, *FF*, and ΔG_{in}, we can roughly extrapolate the theoretical current density value and deduce the efficiency's speculative value. Furthermore, according to these results, $D_{10}A_7$, $D_{10}A_8$, and D_1A_6 as molecular dyes could be used as sensitisers since the electron injection process from the excited molecule to TiO_2 E_{CB} is possible.

We evaluate our results by comparing the V_{OC} and *LHE* calculations of our 18 dyes with the theoretical and experimental research. The V_{OC} values of our 18 dyes range from 1.203 to 1.631 V, and *LHE* values range from 0.103 to 0.167, which are consistent with theoretical studies based on DFT [5, 22]. However, for the experimental studies, results of our 18 dyes were compared with those of well-known commercial dyes such as N719 and D149. The V_{OC} values of N719 and D149 [53] range approximately from 0.70 to 0.80 V, and the *LHE* values are about 0.79, as calculated from the absorption spectra of N719 in the 200–500 nm range [54]. Although the calculated *LHE* values for the studied dyes are lower than experimental values for commercial dyes such as N719 and D149, the V_{OC} values are notably higher (1.203-1.631 V) compared to these dyes (0.70–0.80 V), highlighting the potential of our dyes for improved photovoltaic performance. The discrepancy in values is due to difference between theoretical modelling and practical measurement conditions. Overall, the calculated results demonstrate the promising potential of our dyes for improved photovoltaic performance.

CONCLUSIONS

CH_3 and NO_2 were adopted as donor and acceptor groups, respectively, and attached as moieties to the anthracene. Structural, electronic, and photovoltaic parameters affected by the position changing of the donor and acceptor groups around the anthracene were examined theoretically at the B3LYP/6-311G(d,p) level. E_{HOMO}, E_{LUMO}, V_{OC}, *FF*, *LHE*, τ, ΔG_{inj}, and ΔG_{reg} were illustrated to determine their influence on the photovoltaic properties based on the donor and acceptor position around the anthracene. Our results show that all dye molecules in excited states are effective at injecting electrons into the TiO_2 ECB, and that oxidized dyes that lose electrons in the ground state can be restored by accepting electrons from the redox potential. Therefore, the injection and regeneration process is energetically permitted. Notably, the D10A7, D10A8, and D1A6 dyes can be essential for PV parameters, including *LHE*, ΔG_{reg}, V_{OC}, ΔG_{inj}, and *FF*, suggesting that the PV device concept can employ these dye molecules, D10A7, D10A8, and D1A6, as sensitizers.

ORCID

M. Al-Anber, https://orcid.org/0000-0001-9093-6811; **F. Bahrani,** https://orcid.org/0009-0005-4785-0701
S. Resan, https://orcid.org/0000-0003-4214-1314; **R. Hameed,** https://orcid.org/0000-0002-4844-2313

REFERENCES

[1] S. ElKhattabi, A. Fitri, A.T. Benjelloun, *et al*. "Theoretical investigation of electronic, optical and photovoltaic properties of alkylamine-based organic dyes as sensitizers for application in DSSCs," J. Mater. Environ. Sci., **9**(3), 93 (2018). https://doi.org/10.26872/JMES.2018.9.3.93

[2] S.A. Mahadik, H. M. Pathan, and S. Salunke-Gawali, "An Overview of Metal Complexes, Metal-Free and Natural Photosensitizers in Dye-Sensitized Solar Cells,", **24**(0), 1078 (2024) https://doi.org/10.30919/ESEE1078

[3] S.H. Kang, S.Y. Jung, Y.W. Kim, Y.K. Eom, and H.K. Kim, "Exploratory synthesis and photovoltaic performance comparison of D–π–A structured Zn-porphyrins for dye-sensitized solar cells," Dye. Pigment, **149**, 341–347 (2018). https://doi.org/10.1016/J.DYEPIG.2017.10.011

[4] L.C.C. Coetzee, A.S. Adeyinka, and N. Magwa, "A theoretical investigation of decorated novel triazoles as DSSCs in PV devices," J. Mol. Model. **27**(12), 1–16 (2021). https://doi.org/10.1007/S00894-021-04975-Y

[5] A. Slimi, A. Fitri, A.T. Benjelloun, *et al*. "Molecular Design of D-π-A-A Organic Dyes Based on Triphenylamine Derivatives with Various Auxiliary Acceptors for High Performance DSSCs," J. Electron. Mater. **48**(7), 4452–4462 (2019). https://doi.org/10.1007/S11664-019-07228-0

[6] F. Bahrani, R. Hameed, S. Resan, *et al*. "Impact of Torsion Angles to Tune Efficient Dye-Sensitized Solar Cell/Donor-π-Acceptor Model Containing Triphenylamine: DFT/TD-DFT Study," AcPPA, **141**(6), 561–568 (2022). https://doi.org/10.12693/APHYSPOLA.141.561

[7] F.M. Mustafa, A.A.A. Khalek, A.A. Mahboob, and M.K. Abdel-Latif, "Designing Efficient Metal-Free Dye-Sensitized Solar Cells: A Detailed Computational Study," Molecules, **28**(17), 6177 (2023). https://doi.org/10.3390/MOLECULES28176177

[8] A. Azaid, M. Raftani, M. Alaqarbeh, *et al*. "New organic dye-sensitized solar cells based on the D–A–π–A structure for efficient DSSCs: DFT/TD-DFT investigations," RSC Adv. **12**(47), 30626 (2022). https://doi.org/10.1039/D2RA05297K
[9] S. Rahman, A. Haleem, M. Siddiq, *et al*. "Research on dye sensitized solar cells: recent advancement toward the various constituents of dye sensitized solar cells for efficiency enhancement and future prospects," RSC Adv. **13**(28), 19508 (2023). https://doi.org/10.1039/D3RA00903C
[10] F.A. Bulat, J.S. Murray, and P. Politzer, "Identifying the most energetic electrons in a molecule: The highest occupied molecular orbital and the average local ionization energy," Comput. Theor. Chem. **1199**, 113192 (2021). https://doi.org/10.1016/J.COMPTC.2021.113192
[11] B. Li, B. Hou, and G.A.J. Amaratunga, "Indoor photovoltaics, The Next Big Trend in solution-processed solar cells," InfoMat. **3**(5), 445–459 (2021). https://doi.org/10.1002/INF2.12180
[12] M. Harikrishnan, S. Murugesan, and A. Siva, "Novel star-shaped D–π–D–π–D and (D–π)2–D–(π–D)2 anthracene-based hole transporting materials for perovskite solar cells," Nanoscale Adv. **2**(8), 3514–3524 (2020). https://doi.org/10.1039/D0NA00299B
[13] A. Saha, and B. Ganguly, "A DFT study to probe homo-conjugated norbornylogous bridged spacers in dye-sensitized solar cells: An approach to suppressing agglomeration of dye molecules," RSC Adv. **10**(26), 15307–15319 (2020). https://doi.org/10.1039/c9ra10898j
[14] S. Resan, R. Hameed, A. Al-Hilo, and M. Al-Anber, "The Impact of Torsional Angles to Tune the Nonlinear Optical Response of Chalcone Molecule: Quantum Computational Study," Revista Cubana De FiSica, **37**(2), 95–100 (2020).
[15] M. Al-Anber, and S. Resan, "Opto-electronics and nonlinear optical properties of isoindoline-1,3-dione-fullerene20-isoindoline-1,3-dione using density functional theory," Rev. la Fac. Ciencias, **12**(2), 42–63 (2023). https://doi.org/10.15446/REV.FAC.CIENC.V12N2.107224
[16] J. Luo, Z. Wan, C. Jia, Y. Wang, and X. Wu, "A co-sensitized approach to efficiently fill the absorption valley, avoid dye aggregation and reduce the charge recombination," Electrochim. Acta, **215**, 506–514 (2016). https://doi.org/10.1016/J.ELECTACTA.2016.08.072
[17] M. Al-Anber, "Theoretical Semi-empirical Study of the Glycine Molecule Interaction with Fullerene C60," Orbital Electron. J. Chem. **6**(3), 491 (2014). https://doi.org/10.17807/ORBITAL.V6I3.491
[18] M.J. Al-Anber, A.H. Al-Mowali, and A.M. Ali, "Theoretical Semiempirical Study of the Nitrone (Anticancer Drug) Interaction with Fullerene C60 (as Delivery)," Acta Phys. Pol. A, **126**(3), 845–848 (2014). https://doi.org/10.12693/APHYSPOLA.126.845
[19] E. Muchuweni, E.T. Mombeshora, B.S. Martincigh, and V.O. Nyamori, "Recent Applications of Carbon Nanotubes in Organic Solar Cells," Front. Chem. **9**, 733552 (2022). https://doi.org/10.3389/FCHEM.2021.733552
[20] M.J. Al-Anber, "Butyric Acid Interaction with Carbon Nanotubes: Modeling by a Semi-Empirical Approach," Rev. Cuba. Física, **30**(2), 72–76 (2013).
[21] F. Tessore, G. Di Carlo, A. Forni, S. Righetto, F. Limosani, and A.O. Biroli, "Second Order Nonlinear Optical Properties of 4-Styrylpyridines Axially Coordinated to A4 ZnII Porphyrins: A Comparative Experimental and Theoretical Investigation," Inorganics, **8**(8), 45 (2020). https://doi.org/10.3390/INORGANICS8080045
[22] A. Mathiyalagan, K. Manimaran, K. Muthu, and M. Rajakantham, "Density functional theory study on the electronic structures and spectral properties of 3,5-Dimethylanisole dye sensitizer for solar cell applications." Results Chem. **3**, 100164 (2021). https://doi.org/10.1016/J.RECHEM.2021.100164
[23] S.R. Bora, and D.J. Kalita, "Tuning the charge transfer and optoelectronic properties of tetrathiafulvalene based organic dye-sensitized solar cells: a theoretical approach," RSC Adv. **11**(62), 39246–39261 (2021). https://doi.org/10.1039/D1RA05887H
[24] M.E. Casida, C. Jamorski, K.C. Casida, and D.R. Salahub, "Molecular excitation energies to high-lying bound states from time-dependent density-functional response theory: Characterization and correction of the time-dependent local density approximation ionization threshold," J. Chem. Phys. **108**(11), 4439–4449 (1998). https://doi.org/10.1063/1.475855
[25] P.N. Samanta, D. Majumdar, S. Roszak, and J. Leszczynski, "First-Principles Approach for Assessing Cold Electron Injection Efficiency of Dye-Sensitized Solar Cell: Elucidation of Mechanism of Charge Injection and Recombination," J. Phys. Chem. C, **124**(5), 2817–2836 (2020). https://doi.org/10.1021/acs.jpcc.9b10616
[26] B. Miehlich, A. Savin, H. Stoll, and H. Preuss, "Results obtained with the correlation energy density functionals of becke and Lee, Yang and Parr," Chem. Phys. Lett. **157**(3), 200–206 (1989). https://doi.org/10.1016/0009-2614(89)87234-3
[27] E. Mosconi, A. Selloni, and F. De Angelis, "Solvent effects on the adsorption geometry and electronic structure of dye-sensitized TiO_2: A first-principles investigation," J. Phys. Chem. C, **116** (9), 5932–5940 (2012). https://doi.org/10.1021/jp209420h
[28] M.S. Ebied, M. Dongol, M. Ibrahim, M. Nassary, S. Elnobi, and A.A. Abuelwafa, "Effect of carboxylic acid and cyanoacrylic acid as anchoring groups on Coumarin 6 dye for dye-sensitized solar cells: DFT and TD-DFT study," Struct. Chem. **33**(6), 1921-1933 (2022). https://doi.org/10.1007/s11224-022-01957-5
[29] M. Xu, X. Li, Z. Sun, and T. Tu, "Suzuki–Miyaura cross-coupling of bulky anthracenyl carboxylates by using pincer nickel N-heterocyclic carbene complexes: An efficient protocol to access fluorescent anthracene derivatives," Chem. Commun. **49**(98), 11539–11541 (2013). https://doi.org/10.1039/c3cc46663a
[30] G.E. Zervaki, P.A. Angaridis, E.N. Koukaras, G.D. Sharma, and A.G. Coutsolelos, "Dye-sensitized solar cells based on triazine-linked porphyrin dyads containing one or two carboxylic acid anchoring groups," Inorg. Chem. Front. **1**(3), 256–270 (2014). https://doi.org/10.1039/c3qi00095h
[31] A. Siddiqui, N. Islavath, T. Swetha, and S.P. Singh, "D–π–A organic dyes derived from the indacenodithiophene core moiety for efficient dye-sensitized solar cells,"Energy Adv. **2**(7), 1045–1050 (2023). https://doi.org/10.1039/d3ya00060e
[32] B. O'Regan, and M. Grätzel, "A low-cost, high-efficiency solar cell based on dye-sensitized colloidal TiO_2 films," Nature, **353**(6346), 737–740 (1991). https://doi.org/10.1038/353737a0
[33] A.K. Biswas, S. Barik, A. Sen, A. Das, and B. Ganguly, "Design of efficient metal-free organic dyes having an azacyclazine scaffold as the donor fragment for dye-sensitized solar cells," J. Phys. Chem. C, **118**(36), 20763–20771 (2014). https://doi.org/10.1021/jp5049953
[34] B. Kippelen, and J.L. Brédas, "Organic photovoltaics," Energy and Environmental Science, **2**(3), 251–261 (2009). https://doi.org/10.1039/b812502n

[35] A.K. Biswas, A. Das, and B. Ganguly, "Can fused-pyrrole rings act as better π-spacer units than fused-thiophene in dye-sensitized solar cells? A computational study," New J. Chem. **40**(11), 9304–9312 (2016). https://doi.org/10.1039/c6nj02040b
[36] R. Hoffmann, "Interaction of Orbitals through Space and through Bonds," Acc. Chem. Res. **4**(1), 1–9 (1971). https://doi.org/10.1021/ar50037a001
[37] R. Nithya, and K. Senthilkumar, "Theoretical studies on the quinoidal thiophene based dyes for dye sensitized solar cell and NLO applications," Phys. Chem. Chem. Phys. **16**(39), 21496–21505 (2014). https://doi.org/10.1039/c4cp02694b
[38] A. Mahmood, S.U.D. Khan, and U.A. Rana, "Theoretical designing of novel heterocyclic azo dyes for dye sensitized solar cells," J. Comput. Electron. **13**(4), 1033–1041 (2014). https://doi.org/10.1007/s10825-014-0628-2
[39] M.A.M. Rashid, D. Hayati, K. Kwak, and J. Hong, "Theoretical investigation of azobenzene-based photochromic dyes for dye-sensitized solar cells," Nanomaterials, **10**(5), 914 (2020). https://doi.org/10.3390/nano10050914
[40] Z. Yang, C. Liu, C. Shao, C. Lin, and Y. Liu, "First-Principles Screening and Design of Novel Triphenylamine-Based D-A Organic Dyes for Highly Efficient Dye-Sensitized Solar Cells," J. Phys. Chem. C, **119**(38), 21852–21859 (2015). https://doi.org/10.1021/acs.jpcc.5b05745
[41] M. Karuppusamy, V. Surya, K. Choutipalli, D. Vijay, and V. Subramanian, "Rational design of novel N-doped polyaromatic hydrocarbons as donors for the perylene based dye-sensitized solar cells," J. Chem. Sci. (2019), https://doi.org/10.1007/s12039-019-1723-5
[42] H. Assad, R. Ganjoo, and S. Sharma, "A theoretical insight to understand the structures and dynamics of thiazole derivatives," J. Phys. Conf. Ser. **2267**(1), 012063 (2022). https://doi.org/10.1088/1742-6596/2267/1/012063
[43] W. Wang, J. Zhu, Q. Huang, *et al*. "DFT Exploration of Metal Ion-Ligand Binding: Toward Rational Design of Chelating Agent in Semiconductor Manufacturing," Molecules, **29**(2), 203 (2024). https://doi.org/10.3390/MOLECULES29020308
[44] S. El Mzioui, S.M. Bouzzine, I. Sidir, *et al*. "Theoretical investigation on π-spacer effect of the D–π–A organic dyes for dye-sensitized solar cell applications: a DFT and TD-BHandH study," J. Mol. Model. **25**(4), 1–12 (2019). https://doi.org/10.1007/s00894-019-3963-1
[45] A.K. Biswas, A. Das, and B. Ganguly, "The influence of noncovalent interactions in metal-free organic dye molecules to augment the efficiency of dye sensitized solar cells: A computational study," Int. J. Quantum Chem. **117**(18), e25415 (2017). https://doi.org/10.1002/qua.25415
[46] M.I. Abdullah, M.R.S.A. Janjua, A. Mahmood, S. Ali, and M. Ali, "Quantum chemical designing of efficient sensitizers for dye sensitized solar cells," Bull. Korean Chem. Soc. **34**(7), 2093–2098 (2013) https://doi.org/10.5012/BKCS.2013.34.7.2093
[47] M. Prakasam, R. Baskar, K. Gnanamoorthi, and K. Annapoorani, "Triphenylamine Based Organic Dyes with Different Spacers for Dye-Sensitized Solar Cells: A First Principle Study," Int. J. Adv. Sci. Eng. **5**(4), 1118–1124 (2019). https://doi.org/10.29294/IJASE.5.4.2019.1118-1124
[48] Y. Li, Y. Li, P. Song, F. Ma, J. Liang, and M. Sun, "Screening and design of high-performance indoline-based dyes for DSSCs," RSC Adv. **7**(33), 20520–20536 (2017). https://doi.org/10.1039/c6ra28396a
[49] C. Sun, Y. Li, P. Song, and F. Ma, "An experimental and theoretical investigation of the electronic structures and photoelectrical properties of ethyl red and carminic acid for DSSC application," Materials (Basel), **9**(10), 813 (2016). https://doi.org/10.3390/ma9100813
[50] M. Xie, F.-Q. Bai, H.-X. Zhang, and Y.-Q. Zheng, "The influence of inner electric field on the performance of three types of Zn-porphyrin sensitizers in dye sensitized solar cells: A theoretical study," J. Mater. Chem. C, **4**, 10130-10145 (2016). https://doi.org/10.1039/C6TC02457B
[51] M. Xie, L. Hao, R. Jia, J. Wang, and F. Q. Bai, "Theoretical study on the influence of electric field direction on the photovoltaic performance of aryl amine organic dyes for dye-sensitized solar cells," New J. Chem. **43**(2), 651–661 (2019)m https://doi.org/10.1039/C8NJ04360D
[52] M. Hachi, S. El Khattabi, A. Fitri, *et al*. "DFT and TD-DFT studies of the π-bridge influence on the photovoltaic properties of dyes based on thieno[2,3-bindole," J. Mater. Environ. Sci. **9**(4), 1200–1211 (2018).
[53] P.J. Holliman, K.J. Al-Salihi, A. Connell, M.L. Davies, E.W. Jones, and D.A. Worsley, "Development of selective, ultra-fast multiple co-sensitizations to control dye loading in dye-sensitized solar cells," RSC Adv. **4**(5), 2515–2522 (2013). https://doi.org/10.1039/C3RA42131G
[54] E.C. Prima, H.S. Nugroho, Nugraha, G. Refantero, C. Panatarani, and B. Yuliarto, "Performance of the dye-sensitized quasi-solid state solar cell with combined anthocyanin-ruthenium photosensitizer," RSC Adv. **10**(60), 36873–36886 (2020). https://doi.org/10.1039/D0RA06550A

ВПЛИВ ПОЗИЦІЙ ДОНОР-АКЦЕПТОР НА НАЛАШТУВАННЯ ЕФЕКТИВНИХ СОНЯЧНИХ ЕЛЕМЕНТІВ, СЕНСИБІЛІЗОВАНИХ БАРВНИКОМ: DFT/TD-DFT ДОСЛІДЖЕННЯ

Ф. Бахрані, С. Ресан, Р. Хамід, М. Аль-Анбер
Лабораторія молекулярної інженерії та обчислювального моделювання, кафедра фізики, Коледж природничих наук, Університет Басри, Басра, Ірак

Молекулу антрацену було прийнято як π-сполучений місток для системи D–π–A з нітрогрупою CH_3 та нітрогрупою NO2, що діють як донорна та акцепторна групи. Вплив антраценового з'єднання з донорною та акцепторною сторонами було оцінено на продуктивність сонячного елемента, сенсибілізованого барвником (DSSC). Положення донора та акцептора в цьому дослідженні змінювалися навколо антрацену. Теорія функціоналу густини (DFT) була використана на рівні теорії B3LYP. Донорна група могла зв'язуватися з антраценом у двох певних місцях, тоді як акцепторна група могла зв'язуватися з рештою антраценових місць, за винятком донорного місця. Були досліджені фотоелектричні та електронні властивості. Результати показали, що молекулярні барвники з найвищими показниками, $D_{10}A_7$, $D_{10}A_8$ та D_1A_6, придатні для використання як сенсибілізатори завдяки своїм енергетично вигідним фотоелектричним параметрам, які пояснюються потенціалом для інжекції та регенерації електронів.
Ключові слова: *D–π–A; TD-DFT; DSSC; фотоелектричні властивості; антрацен*

East European Journal of Physics. 4. 635-639 (2025)
DOI:10.26565/2312-4334-2025-4-67 ISSN 2312-4334

CALCULATED FORBIDDEN BANDGAP OF Si_3MnS PHASE IN SUPERCELL (1X1X3) AND EXPERIMENTALLY DETERMINED FORBIDDEN BANDGAP OF Si<MnS>

Sh.B. Utamuradova, Sh.Kh. Daliev, A.Sh. Mavlyanov*, F. Yuldashev
Institute of Semiconductor Physics and Microelectronics at the National University of Uzbekistan, 20 Yangi Almazar st., Tashkent
**Corresponding Author e-mail: aziz.mavlon73@gmail.com*
Received July 2, 2025; revised November 11, 2025; in final form November 13, 2025; Accepted November 20, 2025

The paper presents the results of a quantum chemical calculation of a hypothetical *Si_3MnS* structure representing a "hybrid" of the cubic lattice of silicon *Si* and sphalerite *ZnS*. The *Si* lattice with a diamond structure, scaled up to a supercell (1X1X3), has been chosen for further study and calculation. Several assumptions have been made regarding the most likely substitutional sites for S and Mn impurity atoms in the Si crystal lattice. The corresponding *Si_3MnS* phase is expected to form in the first coordination shell. For quantum chemical calculations, the *Quantum ESPRESSO* suite for first-principles electronic-structure calculations and materials modeling has been adopted. The calculated forbidden bandgap of *Si_3MnS* phase in a (1X1X3) supercell turns out to be *1.14 eV*. Also, the current-voltage characteristics of *Si<Mn,S>* samples with *p-n* junction have been measured by applying the technique of temperature scanning at two comparatively low and nearly adjacent temperatures with the aim to determine the experimental forbidden bandgap energy value. The original *n*-type single-crystal silicon (phosphor-doped, specific resistance 100 Ω·cm) and p-type single-crystal silicon (boron-doped, specific resistance 1 Ω·cm) were used as initial materials for the experiments. An attempt has been made to perform a comparative analysis of forbidden bandgap values determined both during quantum-chemical calculations of the density of electronic states of the Si3MnS phase and during experimental measurements. Thorough quantum chemical calculations of IV/III-V and IV/II-VI-type "hybrid" structures in the cubic lattice of silicon and experimental measurements could incidentally shed light onto the possibility of engineering high-performance structures for future solar cells based on single crystal silicon.
Keywords: *Silicon; Hybrid Structure; Semiconductor; Current-voltage characteristics; Forbidden bandgap; Cubic Lattice*
PACS: 61.82.Fk, 61.72.Vv, 61.72.Tt, 71.20.Nr, 31.15.Ct, 31.15.−p, 31.15.Ne

INTRODUCTION

Targeted engineering of chemical molecules from a small number of defects with an ordered arrangement of impurity atoms and the atoms of the basic material in the lattice, with a partially ionic and partially covalent nature of bonds between them, could help to extend functional properties of semiconductor structures and thus vary their properties [1].

In particular, one of the promising areas is harnessing the functional properties of single crystalline silicon with non-isovalent compounds in the crystal lattice (*$Si_2A_{II}B_{VI}$* -type), representing a "hybrid" of the cubic lattice of silicon *Si* and sphalerite *ZnS* (cubic modification).

Theoretical studies, quantum chemical calculations, and experiments focused on engineering a novel class of hybrid chemical complexes with a cubic diamond-structured lattice that consists of elements of groups *IV/III-V* and *IV/II-VI*, are conducted at leading universities and research centers around the world. In particular, in [1, 2], the possibilities of nonequilibrium growth of complexes of *Si-IV/III-V* and *Si-IV/II-VI* -type compounds to obtain optically sensitive materials based on *Si* have been described. In [2,3] the authors suggest that the "hybrid" phases of *Si_2AlP* (or *Si_2ZnS*) with lattice constants close to the lattice constant of the base matrix might be ideal materials with controlled local chemical order around *Si* atoms. In all the above-mentioned studies using first-principles calculation methods, the authors discuss how chemical order impacts the electronic and optical properties of non-isovalent solid solutions. The authors in the above-mentioned papers further demonstrated, that the decomposition of the *Al-P-Si3* units leads to the formation of *Si_3AlP* containing *Al-P* "chains" as a new structural motif, as well as the *Al-P* pairs. The synthesized *Si_3AlP* shows higher absorption than bulk material of *Si* in the visible range, however the intensity of absorption is substantially lower than the theoretical result for the models based on the *Al-P* pairs.

In this regard, this paper deals with modelling and quantum-mechanical calculation of a hypothetical *Si_3MnS*-structure which is similar to the cubic structure *F43m-β-MnS* (zinc blende). The reason behind choosing for quantum-chemical calculations *Si_3MnS* was that, rich polymorphism and interesting physical properties have prompted many laboratories to study *MnS* nanocrystals in view of their possible application as photoluminescent components, catalysts, as anode material for lithium-ion batteries, and also as supercapacitors [4]. Also, in *β-MnS*, ions of S^{2-} form an *FCC* lattice, while Mn^{2+} ions occupy half of the tetrahedral voids. The ionicity of constituents in *β-MnS* phase was documented in the Materials Project international database. Thus, for further theoretical studies and calculations, a hypothetical cubic *Si_2MnS* structure of *F43m - β -MnS* space group has been chosen. For natural experiments *Si<MnS>* samples were studied. However, no ultimate objective was set to perform a comparative analysis between the results of quantum chemical calculations and the experimental results, besides some careful attempts to compare the calculated and experimentally measured forbidden bandgaps.

Cite as: Sh.B. Utamuradova, Sh.Kh. Daliev, A.Sh. Mavlyanov, F. Yuldashev, East Eur. J. Phys. 4, 635 (2025), https://doi.org/10.26565/2312-4334-2025-4-67

MATERIALS AND METHODS

All calculations were performed using the *Quantum ESPRESSO* suit for first-principles electronic-structure modelling and calculations. Using the available quantum-chemical and molecular-dynamic methods, the *Si* lattice scaled up to a supercell *(1X1X3)* with a diamond structure with location of impurity atoms S and Mn in substitutional positions in the first coordination shell in the lattice a hypothetical diamond structure was built.

The corresponding lattice parameters $a = 5.43095$ Å, b *(A-B)* $= 2.35167$ Å, and *d(A-A)* $= 33.84026$ Å were initially set for *Si* and Mn and S atoms were positioned in lattice sites in substitutional positions so to form a cubic Si_2MnS structure of $F43m$ - β -*MnS* space group (Fig. 1)

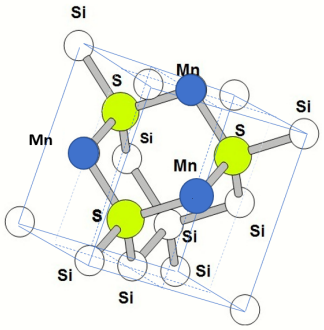

Figure 1. Cubic Si_2MnS structure of $F43m$ - β -*MnS* space group

Before the calculation, the parameters for the Si_3MnS phase in a scaled-up (1X1X3) supercell were entered (Table 1), after which the Quantum ESPRESSO software package built a phase model, representing a scalable cubic *Si* structure scaled up to (1X1X3) supercell with a single atoms of *Mn* and *S* in substitutional positions in the first upper coordination shell (Fig.2).

Table 1. Parameters of Si_3MnS-phase in the scaled-up (1X1X3)-supercell

Parameters	Phase
	Si_3MnS
a	5.46873e+00
b	2.18749e+01
c	5.46873e+00
degauss	1.00000e-02
ecutrho	4.55000e+02
ecutwfc	4.50000e+01
ibrav	8
nat	33
nbnd	141
nspin	1
ntyp	3
occupations	"smearing"
smearing	"gaussian"

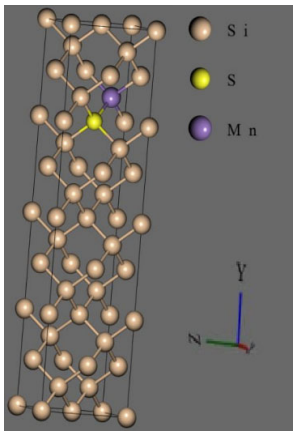

Figure 2. Si_3MnS phase in *(1X1X3)* supercell group *Fd 3m*

Of all the above parameters of ultimate interest was the parameter *"smearing"*. The point is: in case if the calculated silicon structure with impurities would have been regarded as non-metal, the option *"fixed"* should have been used instead of *"smearing"*. Incidentally, the authors of the present investigations have opted for *"smearing"*. Both options belong to Self-Consistent-Field (SCF) theory for convergence that solves the Schrodinger equation with either conventional Hartree–Fock (HF) molecular orbital theory or generalized Kohn–Sham Density Functional Theory methods. ibrav stands for Bravais lattice type.

In order to optimize the time and computational resources required for calculations, a semi-empirical method might be desirable due to less time and computational resources required for executing the method comparing to density functional theory (DFT). However, it worth noting that the accuracy of DFT is traditionally higher.

DFT offers much more accurate solutions of the Schrödinger equation compared to the classical Hartree-Fock method. The computational complexity of DFT is $O(N^3)$ [5-8]. For modeling and calculation of the density of electron states (DOS) and the band diagram of the *Si_3MnS* phase in the supercell (1X1X3), the capacity of the server station installed in the Uzbek-Japanese Innovation Center of Youth (*UJICY*) was used. To calculate the density of electronic states (DOS) for phase *Si_3MnS* in the supercell (1X1X3), the density functional theory (DFT) method was used in the *Quantum ESPRESSO* software package with Hubbard U correction (DFT+U). For calculations, no spin polarization of Mn^{2+} was taken into account.

Preliminarily, it was necessary to figure out whether the structure was geometrically correct. Thereafter, a relaxation calculation was performed, yielding the ionic positions in the relaxed structure. In the next step, instead of a relaxation calculation, we have chosen to perform a fixed-point self-consistent field (*SCF*) calculation for various ionic positions.

In *Quantum ESPRESSO*, a calculation='SCF' could be performed to find out the key state energy for a fixed ion position. For information, the SCF (self-consistent field) method is an iterative approach to solving the Schrödinger equation for a multiparticle system, on the basis of which many quantum chemical methods are built, the most famous of which is the Hartree-Fock method.

In the present work, the quantum chemical calculation considers the doped silicon model as a metal (i.e., the *occupations='smearing'* option is used) to achieve convergence more quickly, whereas in reality, the doped silicon is a semiconductor with certain value of the bandgap. In this case, by checking the output DOS file (the graph is shown in Fig. 2), we could extract the values needed to calculate the band gap value.

Regarding the experimental part, the initial *n*-type (silicon doped by phosphor with specific resistance 100 Ω·cm) and *p*-type (silicon doped with boron with specific resistance 1 Ω·cm) were used for the experiments. Doping with sulfur and manganese was performed by applying diffusion doping technique in vacuumed (10^{-4} bar) and sealed quartz ampoules at temperature of 1260^0C and 1200^0C, respectively, for a duration sufficient to ensure uniform doping. After doping with Mn and S, the initial silicon remained of *p*-type, but the resistivity increased to $\rho = 2.4 \cdot 10^4$ Ω·cm.

The forbidden band gap of the *p-n* junction formed on the basis of an *n*-type conductivity phosphor-doped silicon samples with initial resistivity of ρ=100 Ω·cm was measured (Fig.3).

At various temperatures, the current-voltage characteristics (CVC) of the *p-n* junction samples were measured. Their spectral sensitivity was also measured at room temperature by using an IKS-12 spectrophotometer in the visible light range. The current-voltage characteristics of the samples were measured using a DC source with a voltage of U=5V and U=12V, a multi-stage potentiometer with a resistance of 10 kΩ, while current measurements were carried out using a Rigol DM3068-type device, voltage measurements were carried out with a Mastech MS8040 device, a thermostat connected to a constant voltage source, digital temperature meter type Espada TPM10 with scale division of $\Delta t = 0.1^0$C. To prevent significant overheating of *p-n* structures, measurements were performed using short-term impulse voltages. The results of the current-voltage characteristics of samples with a *p-n* junction are shown in Fig. 3.

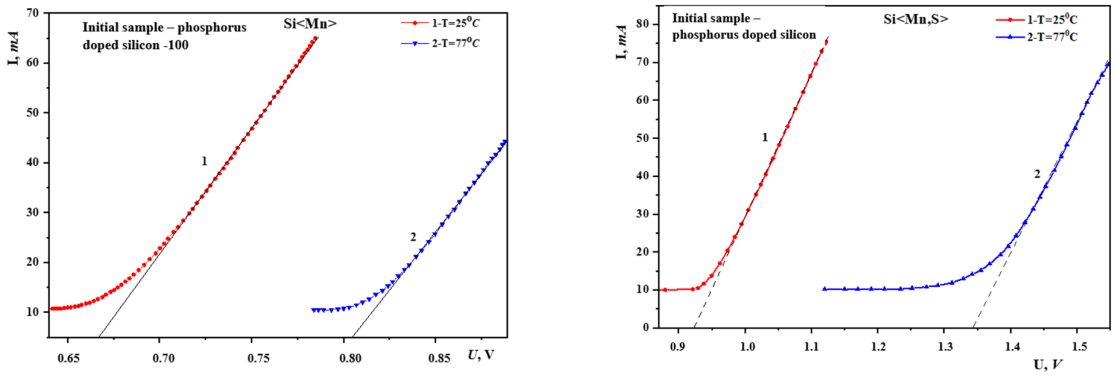

a) b)

Figure 3. Current-voltage characteristics (CVC) of silicon samples containing impurity atoms of manganese and sulfur, measured at temperatures: T= 25^0C and 2- T= 77^0C: a) Si<Mn> b) Si<Mn,S>

RESULTS AND DISCUSSION

For quantum chemical calculation of the bandgap, the *occupations='smearing'* option instead of the *occupations='fixed'* option was applied only for the reason to achieve convergence more quickly. When it comes to determining the forbidden bandgap, both options give comparatively accurate results, except for the technique of finding the forbidden bandgap from a pile of calculated databases. As the result of quantum chemical calculations by implementing the density functional theory (DFT) method, the *Quantum ESPRESSO* software suite has built the density of electronic states diagram which is illustrated on Fig.4. Based on this diagram and by checking the DOS (density of states) output file, we were able to extract the values needed to calculate the forbidden band gap.

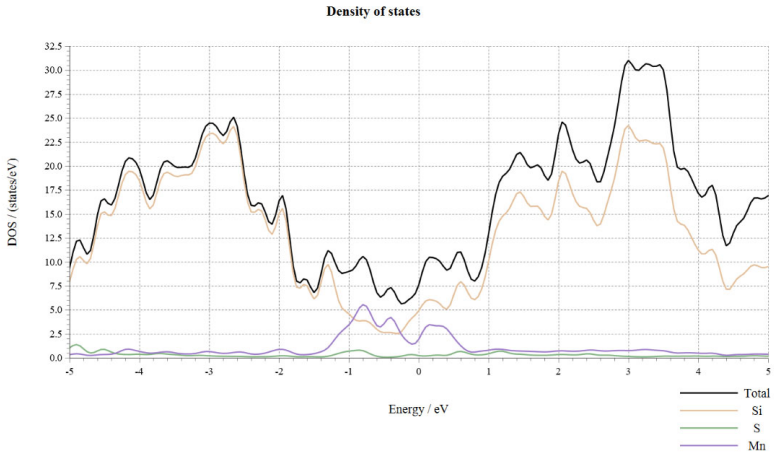

Figure 4. Density of electron states (DOS) of the Si_3MnS phase in a supercell (1X1X3) space group Fd 3m

The first line in *espresso.dos* file looks like this:

 # E (eV) dos(E) Int dos(E) EFermi = 7.049 eV

Near the Fermi level of 7.049 eV, all subsequent DOS values equal to zero were tracked. Afterwards, energy values where the first zero DOS value occurs were scanned. The first zero value appears to be 6.140 eV. Then we have scrolled up and looked for where the first non-zero DOS value appears. It appears at 7.280 eV. Incidentally the difference between these two energy values gives us the band gap value. Thus, at:

 # E (eV) dos(E) Int dos(E) EFermi = 7.049 eV

So, the bandgap of Si_3MnS phase is *(7.280 −6.140) eV=1.14 eV.*

We have also been able to determine the band gap energy of *Si<Mn>* and *Si<Mn,S>* samples, based on building temperature curve of the reverse current of the diffusive *p-n* junction. The measurements were carried out at temperatures $T = 25^0C$ and $T = 77^0C$. As a result of the measurements, the band gap value of the *Si<Mn>* sample was calculated to be 1.14 eV and that of *Si<Mn,S>* was 1.42 eV.

Tentative investigations of the short-circuit current and open-circuit voltage of *p-n*-structures, as well as the phase transitions in such structures, together with the analysis of their lux-ampere characteristic previously showed that these structures could in principle be seen as potential photodiodes and/or solar cells. Further calculations of the fill factor and efficiency ratio of these structures would pave the way for prospective application of these structures as solar cells that would allegedly extend the absorption wavelengths range. Also, as the band gap (E_g) is a core parameter of a semiconductor material, so, the authors think that an exact knowledge of the band gap in such materials makes it possible to manipulate key performance characteristics of semiconductor devices developed on the basis of such materials.

A model and results of quantum-chemical calculation of a hypothetical phase of Si_3MnS, similar to the cubic structure of *F43m-β-MnS* were proposed. The results of a comparative analysis of the bandgap value E_g of the Si_3MnS phase obtained in the process of quantum-chemical numerical calculation and the bandgap value determined during the measurement of current-voltage characteristics at two temperature points, have been compared. Preliminary geometry optimization has preceded quantum-chemical calculation of the Si_3MnS phase in supercell (1X1X3) even though as a matter of fact, frequent optimization and subsequent calculation by the density functional theory (DFT) results in the overlap of valence and conduction bands (VBM and CBM).

CONCLUSIONS

Quantum chemical calculation of the bandgap of a hypothetical Si_3MnS structure that represents a “hybrid” of the cubic lattice of silicon, Si, and sphalerite ZnS, and experimental measurements of the bandgap of *Si* samples doped with *Mn* and *S* impurity atoms have been performed. The quantum-chemical calculation yields a 1.14 eV bandgap, whereas the results of natural experiments were *1.42 eV*. The authors assume that the discrepancy between these two values may

be because, for the quantum chemical calculation, a "pristine" Si3MnS phase in a supercell (1×1×3) was used, with only *Si, Mn,* and *S* atoms in substitutional positions. In natural samples, there is a certain concentration (~10^{15}cm^{-3}) of boron atoms and oxygen atoms (~10^{17}cm^{-3}) mostly in interstitial positions. Also, larger concentrations of boron and other impurities, the absence of ideal *Si_3MnS* phases in real samples, and a variety of local irregularities in the composition and concentrations of impurity atoms in real samples, allegedly led to discrepancies in the values of the forbidden bandgaps obtained quantum chemically and experimentally.

For calculations, no spin polarization of Mn^{2+} has been anticipated, and the value of the Hubbard U parameter has not been indicated. To conduct further quantum-chemical calculations of the new "hypothetical" phases in silicon, we plan to use these parameters to improve calculation accuracy.

We assume that further in-depth theoretical studies, the detailed quantum-chemical calculations, and more thoroughly performed experiments in the field of engineering a novel class of hybrid compounds with a cubic lattice of the diamond type, where the elements of groups IV/III-V and IV/II-VI are embedded in a Si matrix, could help to forecast novel crystal structures in the future.

Meanwhile, an experimental study of the structural and electrical properties of such materials on single-crystal silicon doped with impurity atoms that theoretically form Si-IV/III-V and Si-IV/II-VI-type compounds would expand the parameter space of single-crystal silicon. It could also shed light on the potential to engineer silicon materials with closely spaced absolute minima in momentum space. In this case, it is necessary to take into account the fact that the electronic properties of such structures will differ depending on the ordered and random arrangement of impurity atoms in the silicon lattice.

ORCID

Sharifa B. Utamuradova, https://orcid.org/0000-0002-1718-1122; **Abdulaziz Sh. Mavlyanov**, https://orcid.org/0000-0003-3895-1664

REFERENCES

[1] M.K. Khakkulov, A.Sh. Mavlyanov, O.E. Sattarov, N.A. Akbarova, and Kh.K. Kamalova, "Formation of Binary Compounds of Impurity Atoms of Sulfur and Zinc in Silicon," Surface Engineering and Applied Electrochemistry, **60**(6), 826–830 (2024). https://doi.org/10.3103/S106837552470042X

[2] L. Jiang, T. Aoki, D.J. Smith, A.V.G. Chizmeshya, J. Menendez, and J. Kouvetakis, "Nanostructure-Property Control in $AlPSi_3$/Si(100) Semiconductors Using Direct Molecular Assembly. Theory Meets Experiment at the Atomic Level," Chem. Mater 26, 4092-4101 (2014). https://doi.org/10.1021/CM500926Q

[3] J. Kang, J.-S. Park, P. Stradins, and S.-H. Wei, "Nonisovalent Si-III-V and Si-II-VI alloys: Covalent, ionic, and mixed phases," Physical Review B **96**, 045203-1-045203-5 (2017). https://doi.org/10.1103/PhysRevB.96.045203

[4] Y. Tang, T. Chen, and S. Yu, Chem. Commun. **51**, 9018–9021 (2015). https://doi.org/10.1039/c5cc01700a

[5] J.A. Pople, "Quantum-Chemical Models," Advances in Physical Sciences, **132**(3), 349-356 (2002). https://doi.org/10.3367/UFNr.0172.200203f.0349

[6] B.B. Gaibnazarov, G. Imanova, Sh.T. Khozhiev, I.O. Kosimov, I.Kh. Khudaikulov, Sh.K. Kuchkanov, F.K. Khallokov and I.R. Bekpulatov, "Changes in the Structure and Properties of Silicon Carbide under Gamma Irradiation," Integrated Ferroelectrics, **237**(1), 208-215, (2023). https://doi.org/10.1080/10584587.2023.2239097

[7] K.S. Daliev, Sh.B. Utamuradova, J.J. Khamdamov, M.B. Bekmuratov, O.N. Yusupov, Sh.B. Norkulov, and Kh.J. Matchonov, "Defect Formation in MIS Structures Based on Silicon with an Impurity of Ytterbium," East Eur. J. Phys. (4), 301-304 (2024). https://doi.org/10.26565/2312-4334-2024-4-33

[8] Sh. B. Utamuradova, A. Sh. Mavlyanov, Sh. A. Sobirova, and O. E. Sattarov, "Hybrid Secondary Structure of Manganese and Sulfur in Silicon," Surface Engineering and Applied Electrochemistry, **61**(5), 633–636 (2025). https://doi.org/10.3103/s1068375525700681

РОЗРАХУНОК ЗАБОРОНЕНОЇ ЗОНА ФАЗИ Si_3MnS У СУПЕРКОМІРЦІ (1X1X3) ТА ЕКСПЕРИМЕНТАЛЬНЕ ВИЗНАЧЕННЯ ЗАБОРОНЕНОЇ ЗОНИ Si<MnS>

Ш.Б. Утамурадова, Ш.Х. Далієв, А.Ш. Мавлянов, Ф. Юлдашев

Інститут фізики напівпровідників та мікроелектроніки Національного університету Узбекистану, Ташкент

У статті представлені результати квантово-хімічного розрахунку гіпотетичної структури Si3MnS, що являє собою «гібрид» кубічної решітки кремнію Si та сфалериту ZnS. Для подальшого дослідження та розрахунку обрана решітка Si з алмазною структурою, масштабована до надкомірки (1X1X3). Було зроблено кілька припущень щодо найбільш ймовірних місць заміщення домішкових атомів S та Mn у кристалічній решітці Si. Очікується, що відповідна фаза Si3MnS утворюється в першій координаційній оболонці. Для квантово-хімічних розрахунків було використано пакет програм Quantum ESPRESSO для розрахунків електронної структури з перших принципів та моделювання матеріалів. Розрахована заборонена ширина забороненої зони фази Si_3MnS у надкомірці (1X1X3) виявилася 1,14 еВ. Також було виміряно вольт-амперні характеристики зразків Si<Mn,S> з p-n переходом, застосовуючи метод температурного сканування при двох порівняно низьких і майже суміжних температурах з метою визначення експериментального значення енергії забороненої забороненої зони. Як вихідні матеріали для експериментів використовувалися оригінальний монокристалічний кремній n-типу (легований фосфором, питомий опір 100 Ом·см) та монокристалічний кремній p-типу (легований бором, питомий опір 1 Ом·см). Була зроблена спроба провести порівняльний аналіз значень забороненої ширини забороненої зони, визначених як під час квантово-хімічних розрахунків густини електронних станів фази Si_3MnS, так і під час експериментальних вимірювань. Ретельні квантово-хімічні розрахунки «гібридних» структур типу IV/III-V та IV/II-VI у кубічній решітці кремнію та експериментальні вимірювання можуть пролити світло на можливість розробки високопродуктивних структур для майбутніх сонячних елементів на основі монокристалічного кремнію.

Ключові слова: *кремній; гібридна структура; напівпровідник; вольт-амперна характеристика; заборонена зона; кубічна решітка*

East European Journal of Physics. 4. 640-645 (2025)
DOI:10.26565/2312-4334-2025-4-68 ISSN 2312-4334

EFFECT OF STOICHIOMETRIC DISTORTIONS ON ELECTRICAL AND PHOTOELECTRIC PROPERTIES OF LAYERED GeS CRYSTAL

R.S. Madatov[1], A.S. Alekperov[2,3], V.A. Abdurahmanova[2], R.K. Huseynov[4], R.J. Bashirov[5], Y.I. Aliyev[2,6]*

[1]*Institute of Radiation Problems, Ministry of Science and Education Republic of Azerbaijan, Baku, AZ-1143, Azerbaijan*
[2]*Azerbaijan State Pedagogical University, Baku, AZ-1000, Azerbaijan*
[3]*Baku Engineering University, Khirdalan, AZ-0101, Azerbaijan*
[4]*Ganja State University, Ganja, AZ-2000, Azerbaijan*
[5]*Azerbaijan Technical University, Baku, AZ-1073, Azerbaijan*
[6]*Western Caspian University, Baku, AZ-1001, Azerbaijan*
**Corresponding Author email: yusifafshar@gmail.com*
Received July 22, 2025; revised October 31, 2025; accepted November 10, 2025

The current-voltage characteristic, electrical conductivity, thermally stimulated current, and photoelectric properties of a layered GeS crystal with excess sulfur were investigated under an external electric field of 10-104 V/cm and at temperatures of 100-300 K. It was found that donor-type defects formed as a result of stoichiometric distortion due to excess sulfur in a GeS crystal obtained by the Bridgman method, leading to impurity conductivity. Charge transport occurs by a monopolar injection current limited by the volume of the charge region. It was found that thermal activation of photocurrent and thermal quenching of photocurrent in doped GeS crystals are associated with electron exchange between capture traps and recombination centers.
Keywords: *Layered crystal; Electrical conductivity; Monopolar injection; Thermally stimulated current; Photoconductivity*
PACS: 72.15.Eb, 73.50.Pz

1. INTRODUCTION

In low-dimensional layered crystals (GeS, GeSe, SnS, GaS, GaSe, InSe), the quantum effects observed during structure formation depend on the nature of the chemical bonds of the components and the shape of the crystal lattice. In such systems, the relationship between physical properties and structure was studied in binary systems $A^{III}B^{VI}$ and $A^{IV}B^{VI}$ [1-4]. It was found that the electrical, photoelectric, and radiation-resistance properties of layered crystals depend on the nature of the interactions between layers and within layers. Within the layer, this interaction is powerful and ionic-covalent in nature [5-7]. The formation of weak van der Waals bonds between layers leads to the emergence of anisotropic properties characteristic of layered crystals. The effects observed in low-dimensional structures form new areas of research in layered crystals and expand the possibilities of their practical application. Therefore, by selecting different components, it is possible to control the type of chemical bond intentionally.

A comparative analysis of the results obtained in the study of binary systems $A^{III}B^{VI}$ and $A^{IV}B^{VI}$ shows that the electrical, especially photoelectric properties of layered crystals depend on the electron configuration of the components and the nature and properties of the electron transitions of cation vacancies, which occur depending on external influences (temperature, illumination, radiation rays, etc.). On the other hand, elements with a large ionic radius and chemical activity, electrons in the p-layer of cations during the formation of chemical bonds have a strong effect on the electrical, photoelectric, and optical properties of the crystal [8]. In the GeS crystal, which is one of the binary compounds $A^{IV}B^{VI}$ with the above properties, information on the formation of chemical bonds, the structure of the crystal lattice and the influence of impurity atoms on the physical properties has been studied [9]. The studies show that the GeS crystal is a semiconductor with a complex band structure. The elementary lattice consists of two layers, each layer of two molecules. Since the atoms of adjacent layers are linked to each other by weak van der Waals bonds, many of the physical properties of the crystal are two-dimensional [10].

Since layered semiconductors crystallize in defect structures, the study of the electronic structure of localized defects is particularly important. Dopant atoms are distributed non-periodically in different spaces (inside a layer or in the interlayer region). Although the above facts were investigated in a doped GeS crystal, the results obtained do not support the development of a universal model explaining the mechanism of dopant-atom distribution. One of the important properties of a GeS crystal is that it has high concentrations (10^{17}-10^{18} cm^{-3}) of specific defects (cation and anion vacancies, Frenkel defects), especially cation vacancies. This property causes low mobility of charge carriers in the direction of the c axis of the crystal and a short diffusion path. A high concentration of specific defects, coupled with their compensation by dopant atoms, enables targeted control of properties. The above is also supported by the results of the study of the electrical and photoelectric properties of the GeS crystal [11].

Despite the existence of a number of research works on the study of electrical, photoelectric and optical properties of semiconductor compounds of the $A^{IV}B^{VI}$ type, including the GeS crystal, there is no information on the mechanism of

Cite as: R.S. Madatov, A.S. Alekperov, V.A. Abdurahmanova, R.K. Huseynov, R.J. Bashirov, Y.I. Aliyev, East Eur. J. Phys. 4, 640 (2025), https://doi.org/10.26565/2312-4334-2025-4-68

the effect of defects on the current [12-14]. The obtained results do not allow us to study the mechanism of the effect of specific defects in the GeS crystal, including uncontrolled impurity atoms, on conductivity. The study of defects present in semiconductor crystals provides extensive information on the formation of their structural features and physical properties. Therefore, research has been carried out in this direction recently [15,16]. Therefore, in order to obtain additional information on the distribution, concentration and energy states of defects in layered crystals, it is planned to study the volt-ampere characteristics, electrical conductivity and photoconductivity of the GaS crystal with excess sulfur at temperatures of 100-300 K and external electric field values of 10-10^4 V/cm.

2. EXPERIMENTS

The GeS single crystal was grown by the Bridgman method, a standard method for chalcogenide semiconductors. High purity Ge and S (99.999%) were used in the synthesis process. Ge with a specific resistance of 50 Ohm·cm and B5 grade sulfur were used in the synthesis. To maintain the stoichiometric ratio and minimize sulfur vacancies, the quartz ampoule filled with components taken with excess sulfur was welded after reducing the pressure to 1.33×10^{-2} Pa. During synthesis, the ampoule heating rate at the first stage was set to 1.5 degrees/minute, and after melting the germanium, the heating rate was set to 2.5 degrees/minute. To ensure the safety of the synthesis process, the germanium crystal was ground into powder, and the evaporation and condensation zone temperatures were 1173 K and 1073 K, respectively. The homogeneity of the grown crystals and their single-phase nature were tested using differential thermal analysis (DTA), X-ray diffraction (XRD) and electron microscopy (SEM). The obtained crystals had *p*-type conductivity and a specific resistance of 10^5-10^6 Ohm·cm. The sample size during measurements was $2.0\times5.0\times0.2$ mm^3. The conductive contacts were applied to a natural flat surface using aquadag and had an ohmic character. The study of electrical and photoelectric properties was carried out at 100-300 K and in an electric field of 10^4 V/cm.

RESULTS AND DISCUSSIONS

During the research, the structure of the GeS crystal obtained with excess sulfur was studied by X-ray diffraction. The X-ray diffraction spectrum obtained at room temperature is shown in Figure 1. The spectrum shows six main maxima over the diffraction angle range 2θ = 20-70°. It was determined that these maxima correspond to the atomic planes (111), (020), (022), (131), (222) and (040). The obtained single crystal is single-phase and orthorhombic. The lattice parameters correspond to the values: a = 4.291 Å, b = 3.641 Å and c = 10.471 Å.

The volt-ampere characteristics of a GeS single crystal with excess sulfur at different temperatures were studied. The obtained dependences are shown in Fig. 2. From the nature of curves 1-3 it is evident that the $I \sim U^n$ dependences consist of ohmic, quadratic and sharply increasing regions. From the dependences it is evident that the GeS crystal has a semiconductor property, i.e. with decreasing temperature the resistance of the sample increases, due to which the ohmic region observed at room temperature shifts towards the region of high voltages.

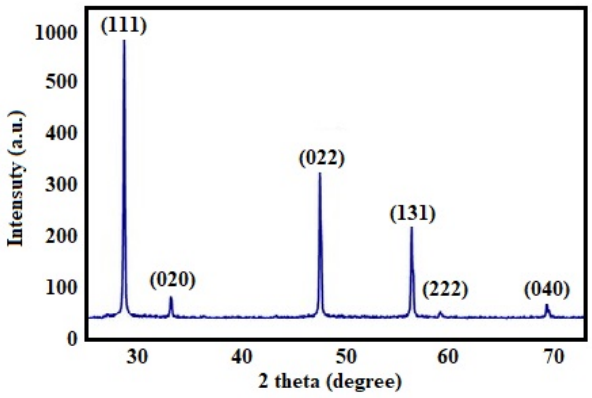

Figure 1. X-ray diffraction spectrum of a GeS crystal

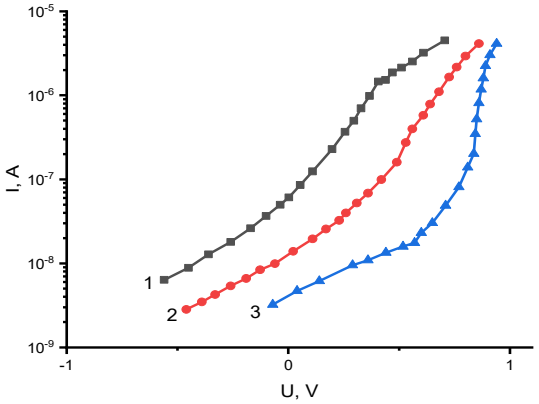

Figure 2. Current-voltage characteristics of a GeS crystal at different temperatures: 1) T = 100 K, 2) T = 160 K, 3) T = 300 K

According to Lambert's theory, the charge carriers injected from the electrode cannot completely fill the traps, and conductivity occurs due to thermal ionization of shallow levels. With a further increase in the voltage applied to the sample, the concentration of injected charge carriers increases and the traps are partially filled. After the traps are completely filled, with increasing voltage, the current increases sharply to the quadratic region without jumps (curves 1-3). Based on the value of the transition voltage from the ohmic part to the quadratic part for the crystals from Figure 2, the concentration and mobility of charge carriers in the equilibrium state in GeS crystals were calculated according to Lampert's theory ($n_0 \sim 4\cdot10^{13}$ cm^{-3}, μ = 20-30 cm^2/V·s) [12].

Based on the measured value of the electrical capacitance of the GeS sample at the input voltage U = 0 and the transition of the traps to a completely filled state ($C = 5\cdot10^{-10}$ F, E7-20 is an impedance meter), the trap concentration was calculated to be $Nt = CUttd/q\cdot V = 5\cdot10^{14}$ cm^{-3} (where V is the sample volume). The shift of the Fermi level from the equilibrium state and $\Delta E_t \approx 0.02$ eV was. This indicates that at low voltages (in the ohmic region) and low temperatures,

the charge carriers injected from the electrode cannot completely fill the traps and conductivity occurs due to the thermal ionization of shallow levels.

To study the electrical properties of semiconductor materials, it is necessary to analyze the temperature dependences of electrical conductivity. Previous studies have shown that a number of electronic processes occurring in these materials can be explained based on the temperature dependence of electrical conductivity [17-22]. Therefore, for the GeS crystal, a mechanism for changing electrical conductivity depending on temperature was determined. Figure 3 shows the temperature dependence of the electrical conductivity of the GeS crystal at different electric field strengths.

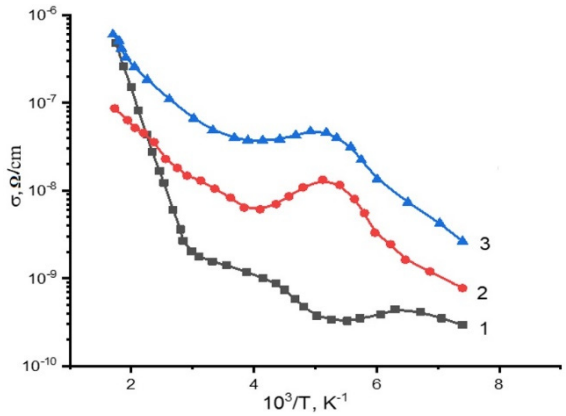

Figure 3. Electrical conductivity of doped GeS crystal at different field strengths: 1) 10^2 V/cm, 2) 10^3 V/cm, 3) 10^4 V/cm

The dependences show that in an undoped GeS crystal, a specific and additive region is observed, and with increasing temperature, the dark conductivity increases, passes through a minimum and increases again (curve 1). At high electric fields, an increase in temperature leads to the dark conductivity passing through a maximum and increasing again (curves 2 and 3). From a comparison of the experimental curves, it is clear that at low and high field strengths, the dark conductivity is explained by two opposing processes: thermal ionization and electroionization. Thus, in the GeS crystal, the dark conductivity in the layer direction obeys the law $\sigma_0 = A \cdot \exp(-\Delta E_0/2kT)$, and in strong fields – the law $\sigma_0 = A \cdot \exp(-\Delta E_r - 2e(eE/\varepsilon)^{1/2}/2\varepsilon kT)$. The calculated values of the activation energy of the energy levels from the slope of the curve from the dependence $\ln\sigma 0 \sim f(1/T)$ were 0.22 eV and 0.45 eV. From a comparison of curves 1 and 3 in Figure 3, it is evident that the slope of the curve increases with increasing field strength in the range of 120-250 K. At low field strengths ($E < 10^2$ V/cm), the conductivity occurs due to thermal ionization of the defect level, and in strong fields it increases exponentially as a result of field ionization.

To determine the energy depth, concentration and cross-section of filling centers located in the forbidden zone in the GeS crystal, the thermally stimulated current was studied, the results are presented in Figure 4.

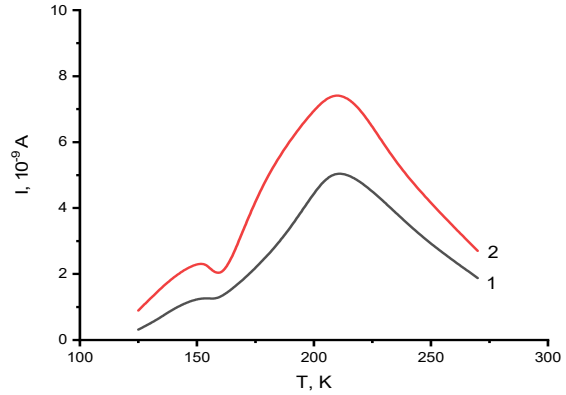

Figure 4. Thermally stimulating current in a doped GeS crystal at different field strengths: 1) 10^2 V/cm, 2) 10^4 V/cm

According to the research methodology, the GeS sample was cooled to a temperature of 100 K in vacuum, then illuminated with natural light for 5 minutes and heated at a rate of 0.40 degrees/second at different field strengths (10^2 V/cm, 10^4 V/cm), the resulting signal was recorded on a special recorder. From Figure 4 it is evident that the thermal signal increases with increasing temperature, and the maxima of low and high intensity are observed at temperatures of 150 K and 210 K, respectively. Based on the conditions given in the research [12], according to the values of T_{max} and $T_{1/2}$ from Figure 4, the activation energy of the filling center ΔE_t was $\Delta E_1 \approx 0.19$ eV and $\Delta E_2 \approx 0.27$ eV, the concentration $Nt_1 \approx 2 \cdot 10^{13}$ cm^{-3} and $N_{t2} \approx 1 \cdot 10^{17}$ cm^{-3}, and the filling cross-section $S_{t1} \approx 10^{-20}$ cm^{-3} and $S_{t2} \approx 10^{-19}$ cm^{-3}.

Figure 5 shows the spectral characteristics of photoconductivity in the layer direction in a GeS crystal at temperatures of 300 K and 100 K. It is evident from the dependences that two maxima ($\lambda = 0.75$ μm and $\lambda = 0.90$ μm) are observed on

the curve of the spectral distribution of photoconductivity in an undoped GeS crystal. The first maximum falls on the region of specific absorption, and the second on the doped region; therefore, it corresponds to the defect-zone transition. The observation of a doped absorption region in an undoped GeS crystal can be explained by the formation of partially irregular regions (low-resistance regions) in layered compounds.

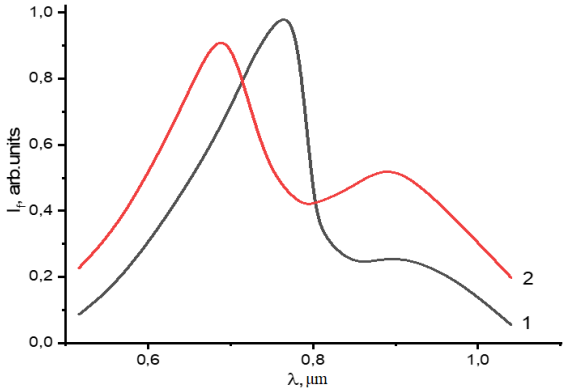

Figure 5. Spectral distribution of photoconductivity in undoped GeS crystal. 1) $T = 300$ K, 2) $T = 100$ K

During the synthesis of the GeS crystal, the excess of sulfur causes a violation of stoichiometry, which leads to the formation of a local impurity band in the crystal [23]. Figure 6 shows that at a temperature of $T \sim 100$ K (curve 2), both maxima shift to the short-wave region. This proves that the absorption outside the fundamental absorption band in the long-wavelength region is due to impurities. The temperature dependence of the photoconductivity in the GeS crystal upon excitation by natural light of varying intensity in the direction perpendicular to the layer surface and at an electric field strength of 10^4 V/cm is shown in Figure 6.

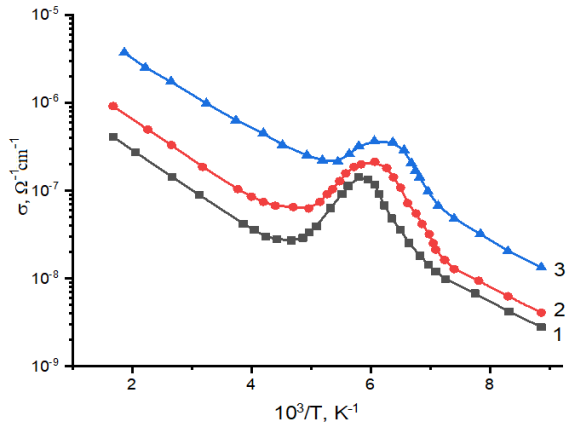

Figure 6. Temperature dependence of photocurrent in undoped GeS crystal. 1) 10 lx, 2) 10^2 lx, 3) 10^4 lx

It is evident from the figure that in the range of 100-160 K, as a result of thermal activation, the photocurrent increases (thermal activation), and in the region of 160-200 K, thermal quenching of photoconductivity is observed. With a further increase in temperature, the photocurrent increases again. It should be noted that with an increase in the illumination intensity the depth of the maximum decreases. It is evident from the experimental results that the dependence $\sigma_f \sim f(1/T)$ obeys the law $\sigma_f = \sigma_0 exp(\Delta Ef/kT)$ and two processes are observed - thermal activation and thermal quenching of photoconductivity. The activation energy determined from the slope of the curve was ~0.27 eV. It should be noted that there is no information on thermal quenching of photoconductivity in the doped GeS crystallite, but it is noted that there is specific conductivity. The activation of the photocurrent observed by us in the GeS crystal with excess sulfur occurs as a result of the nonequilibrium exchange of the majority charge carriers between the photoactivation trap and the recombination center, as shown in [24].

The results of the study of electrical conductivity and photoelectric properties of alloyed GeS crystals (with an excess of sulfur), obtained by the Bridgman method at different temperatures and external electric fields, show that the capture and recombination processes in alloyed GeS crystals largely depend on the chemical nature of the components, including alloying atoms, and less on the degree of disorder in the crystal. In contrast to previous studies, we found that complex defects (complexes, dislocations, point defects) formed in alloyed GeS crystals with an excess of sulfur, as well as in alloyed GeS, have a strong influence on the electronic processes occurring in the crystal under external excitation (light, temperature, radiation). Therefore, as a result of exposure to an electric field and illumination in the alloyed region of conductivity of the GeS crystal, thermal quenching is observed (Fig. 3, curve 1). The reason for this is that excess sulfur causes the formation of defect regions with activation energies of 0.17 eV and 0.27 eV. This fact is confirmed by the

dependence presented in Figure 4. As you can see, excess sulfur causes partial disorder of the crystal, both due to stoichiometric distortion and due to the formation of new structural defects.

At the same time, the temperature dependence of the charge-carrier mobility partially confirms the correctness of the observed effect (Fig. 7).

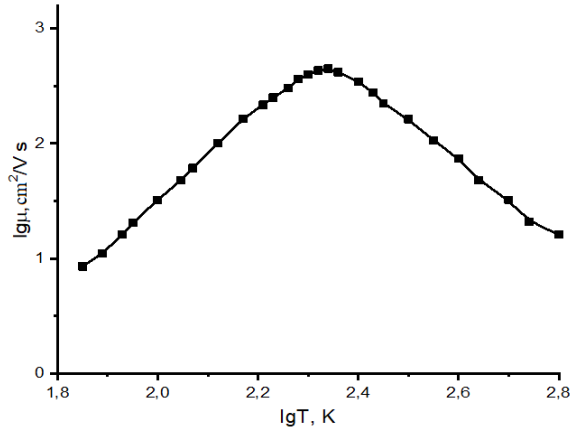

Figure 7. Temperature dependence of charge-carrier mobility in an undoped GeS crystal

According to the theory, the centers formed as a result of the introduction of an impurity atom into a crystal, especially a layered crystal, can cause thermal quenching of photoconductivity, thermal activation and quenching of the photoluminescence process. As shown in Fig. 6, the effects of thermal activation and thermal quenching of photoconductivity were observed in the dependence $\sigma_f \sim f(1/T)$.

CONCLUSIONS

The obtained results show that the activation energy resulting from the stoichiometric disorder in layered crystals, depending on the ratio of components, plays the role of the center of generation and recombination of the majority charge carriers, the defect level of which is 0.27 eV in the low-temperature region and 0.41 eV in the high-temperature region, depending on the ratio of components. The concentration of these centers varies with temperature and illumination intensity in undoped GeS crystals. The results obtained in a comprehensive study of the electric, photoelectric, and thermally stimulating current in an undoped layered GeS crystal show that the defects resulting from the stoichiometric disorder caused by excess sulfur in the crystal lattice of the orthorhombic GeS structure create the possibility of targeted control of electronic processes, i.e. electrical and photoelectric properties. This, as shown in the scientific literature, enables the practical application of the layered GeS crystal, particularly for the creation of highly efficient photo- and thermal converters.

ORCID

Y.I. Aliyev, https://orcid.org/0000-0001-8896-2180

REFERENCES

[1] A.S. Alekperov, A.O. Dashdemirov, T.G. Naghiyev, and S.H. Jabarov, "Effect of gamma irradiation on the thermal switching of a GeS:Nd single crystal," Semiconductors, **55**(6), 574-577 (2021). https://doi.org/10.1134/S1063782621070034

[2] R.S. Madatov, A.S. Alekperov, F.N. Nurmammadova, N.A. Ismayilova, and S.H. Jabarov, Preparation of n-Si-p-GaSe heterojunctions based on an amorphous GaSe layer without impurities and study of their electrical properties, East European Journal of Physics, (1), 322-326 (2024). https://doi.org/10.26565/2312-4334-2024-1-29

[3] Y.I. Aliyev, N.A. Ismayilova, R.F. Novruzov, A.O. Dashdamirov, H.J. Huseynov, S.H. Jabarov, and A.A. Ayubov, "Electron structure and density of states' calculations of Ag_2S and Ag_2Se crystals from first-principle," Modern Physics Letters B, **33**(21), 1950242 (2019). https://doi.org/10.1142/S0217984919502427

[4] S.R. Azimova, N.M. Abdullayev, Y.I. Aliyev, M.N. Mirzayev, V.A. Skuratov, A.K. Mutali, and S.H. Jabarov, "Study on the thermodynamic behavior of Sb-Te binary systems with swift heavy-ions irradiation at the high temperatures," Journal of the Korean Physical Society, **77**, 240-246 (2020). https://doi.org/10.3938/jkps.77.240

[5] S.H. Jabarov, T.G. Mammadov, A.I. Mammadov, S.E. Kichanov, V.B. Aliyeva, and E.V. Lukin, "Structural phase transition in $TlGaSe_2$ under high pressure," Journal of Surface Investigation. X-ray, Synchrotron and Neutron Techniques, **9**, 35-40 (2015). https://doi.org/10.1134/S102745101501005X

[6] Y.I. Aliyev, Y.G. Asadov, A.O. Dashdemirov, R.D. Aliyeva, T.G. Naghiyev, and S.H. Jabarov, "Polymorphic transformations and thermal expansion of some modifications in $Ag_{1.5}Cu_{0.5}Se$ and $Ag_{0.4}Cu_{1.6}Se$," International Journal of Modern Physics B, **33**(23), 1950271 (2019(. https://doi.org/10.1142/S0217979219502710

[7] Z. Chen, W. Hwang, M. Cho, A.T. Hoang, M. Kim, D. Kim, D.H. Kim, *et al.*, "In-plane optical and electrical anisotropy in low-symmetry layered GeS microribbons," NPG Asia Materials, **14**, 41 (2022). https://doi.org/10.1038/s41427-022-00390-8

[8] R.S. Madatov, A.S. Alekperov, and Dzh.A. Magerramova, "Influence of rare earth elements (Nd, Sm, Gd) on the physicochemical properties of GeS crystal," Crystallography Reports, **60**, 921-923 (2015). https://doi.org/10.1134/S1063774515060188

[9] G.B. Jensen, "Physics and chemistry of materials with layered structures," Vol. 4. Optical and electrical properties edited by P.A. Lee, Acta Crystallographica Section A, **35**(2), 347-348 (1979). https://doi.org/10.1107/S0567739479000863
[10] D.I. Bletskan, I.F. Kopinets, P.P. Pohoretsky, E.N. Salkova, and D.V. Chepur, "Production of GeS single crystals, investigation of their morphology and of latter influence on the hologram recording," Kristallografiya, **20**, 1008-1012 (1975).
[11] J.D. Wiley, S. Pennington, and E. Schönherr, "Electrical conductivity of GeS," Physica Status Solidi B, **96**(1), K37-K42 (1979). https://doi.org/10.1002/pssb.2220960162
[12] R.S. Madatov, A.S. Alekperov, and O.M. Hasanov, "Effect of Nd impurity on photoconductivity and optical absorption spectra of GeS single crystal," Journal of Applied Spectroscopy, **84**, 136-139 (2017). https://doi.org/10.1007/s10812-017-0440-4
[13] A.S. Alakbarov, A.O. Dashdemirov, R.B. Bayramli, and K.S. Imanova, "Effect of the gamma irradiation on the structure and exciton photoconductivity of layered GeS: Sm single crystal," Advanced Physical Research, **3**, 39-45 (2021).
[14] R.Z. Ibaeva, G.B. Ibragimov, A.S. Alekperov, and R.E. Huseynov, "Obtained and studied structural aspects of the $Ge_{0.9}Er_{0.1}S$ compound with Ge → Er substitutions," East European Journal of Physics, (4), 360-363 (2024). https://doi.org/10.26565/2312-4334-2024-4-41
[15] E. Demir, M.N. Mirzayev, B.A. Abdurakhimov, B. Mauyey, and S.H. Jabarov, "Characterization of lattice parameter variations, defect dynamics, and surface morphology in Al_2O_3-B_4C coatings on 321 stainless steel under swift heavy ion irradiation," Physica E: Low-dimensional Systems and Nanostructures, **165**, 116103 (2025). https://doi.org/10.1016/j.physe.2024.116103
[16] S.H. Jabarov, A.Kh. Nabiyeva, S.F. Samadov, A.S. Abiyev, A.A. Sidorin, N.V.M. Trung, O.S. Orlov, *et al*., "Study defects formation mechanism in $La_{1-x}Ba_xMnO_3$ perovskite manganite by positron annihilation lifetime and Doppler broadening spectroscopy," Solid State Ionics, **414**, 116640 (2024). https://doi.org/10.1016/j.ssi.2024.116640
[17] S.H. Jabarov, S.I. Ibrahimova, F.V. Hajiyeva, E.M. Huseynov, and Y.I. Aliyev, "Structural, vibrational, and dielectric properties of $CuInZnSe_3$ chalcogenide compound," Arabian Journal for Science and Engineering, **47**(6), 7817-7823 (2022). https://doi.org/10.1007/s13369-022-06745-1
[18] M.A. Mehrabova, N.I. Huseynov, S.G. Asadullayeva, A.M. Nazarov, V.N. Poladova, and S.P. Suleymanli, "Photoelectrical properties of CdMnSe thin films," Advanced Physical Research, **6**, 203-210 (2024). https://doi.org/10.62476/apr63203
[19] S.H. Jabarov, A.Kh. Nabiyeva, A.V. Trukhanov, S.V. Trukhanov, H.J. Huseynov, and Y.I. Aliyev, "Dielectric and electrical properties of the $La_{0.73}Ba_{0.27}MnO_3$ compound at hıgh temperatures," SOCAR Proceedings, **4**, 171-175 (2023). http://dx.doi.org/10.5510/OGP20230400931
[20] G. Jaffé, "Theory of conductivity of semiconductors," Physical Review, **85**, 354 (1952). https://doi.org/10.1103/PhysRev.85.354
[21] A.Kh. Nabiyeva, S.H. Jabarov, N.A. Ismayilova, and H.J. Huseynov, "First principles study of electron structure of $La_xBa_{1-x}MnO_3$ crystals," Ferroelectrics Letters Section, **51**, 9-13 (2024). https://doi.org/10.1080/07315171.2023.2300594
[22] R.Z. Mehdiyeva, A.I. Mammadov, S.H. Jabarov, N. Demirci, T. Coşkun, and M.Yu. Seyidov, "Dielectric and ferroelectric properties of $K_2Pb_4Nb_{10}O_{30}$–$Na_2Pb_4Nb_{10}O_{30}$–$K_6W_4Nb_6O_{30}$ across morphotropic phase region," Journal of Alloys and Compounds, **645**, 496-503 (2015). https://doi.org/10.1016/j.jallcom.2015.05.109
[23] S. Ishida, T. Fukunaga, T. Kinosada, and K. Murase, "Carrier localization and impurity band conduction in GeSe," Physica B+C, **105**, 70-73 (1981(. https://doi.org/10.1016/0378-4363(81)90217-5
[24] Y. Ishihara, and I. Nakada, "Electrical conduction of GeSe at low temperatures," Physica Status Solidi B, **105**, 285-290 (1981). https://doi.org/10.1002/pssb.2221050131

ВПЛИВ СТЕХІОМЕТРИЧНИХ СПОТВОРЕНЬ НА ЕЛЕКТРИЧНІ ТА ФОТОЕЛЕКТРИЧНІ ВЛАСТИВОСТІ ШАРУВАТИХ КРИСТАЛІВ GeS

Р.С. Мадатов[1], А.С. Алекперов[2,3], В.А. Абдурахманова[2], Р.К. Гусейнов[4], Р.Дж. Баширов[5], Ю.І. Алієв[2,6]*

[1]Інститут радіаційних проблем, Міністерство науки та освіти Азербайджанської Республіки, Баку, AZ-1143, Азербайджан
[2]Азербайджанський державний педагогічний університет, Баку, AZ-1000, Азербайджан
[3]Бакинський інженерний університет, Хирдалан, AZ-0101, Азербайджан
[4]Гянджінський державний університет, Гянджа, AZ-2000, Азербайджан
[5]Азербайджанський технічний університет, Баку, AZ-1073, Азербайджан
[6]Західно-Каспійський університет, Баку, AZ-1001, Азербайджан

Вальт-амперна характеристика, електропровідність, термостимульований струм та фотоелектричні властивості шаруватого кристала GeS з надлишком сірки досліджувалися в умовах зовнішнього електричного поля 10-104 В/см та при температурах 100-300 К. Було виявлено, що дефекти донорного типу утворюються в результаті стехіометричного спотворення через надлишок сірки в кристалі GeS, отриманому методом Бріджмена, що призводить до домішкової провідності. Перенесення заряду відбувається за допомогою монополярного струму інжекції, обмеженого об'ємом області заряду. Було виявлено, що термічна активація фотоструму та термічне гасіння фотоструму в легованих кристалах GeS пов'язані з електронним обміном між пастками захоплення та центрами рекомбінації.

Ключові слова: *шаруватий кристал; електропровідність; монополярна інжекція; термостимульований струм; фотопровідність*

EAST EUROPEAN JOURNAL OF PHYSICS. 4. 646-650 (2025)
DOI:10.26565/2312-4334-2025-4-69 ISSN 2312-4334

PRODUCTION OF MAGNETIC NANOPARTICLE-BASED FERRITES AND COMPREHENSIVE CHARACTERIZATION OF THEIR ELECTRICAL AND MAGNETIC PROPERTIES IN COLLOIDAL SYSTEMS

O.K. Kuvandikov, U.E. Nurimov*
Samarkand State University, named after Sharof Rashidov, 140001, Samarkand, Uzbekistan
**Corresponding Author email: nurimovumid1@gmail.com*
Received August 31, 2025; revised November 11, 2025; accepted November 18, 2025

This study investigates the synthesis, structural characterization, and physicochemical properties of magnetic nanoparticles derived from iron group metals (Fe, Co, Ni) and their corresponding ferrite dispersions. Magnetic nanoparticles were synthesized via chemical condensation, and their morphology and structure were analyzed using transmission electron microscopy (TEM) and X-ray diffraction (XRD). The synthesized magnetic nanoparticles, comprising Fe_3O_4, $CoFe_2O_4$, and $NiFe_2O_4$ ferrites, exhibited nano-scale dimensions ranging from 10 to 50 nm. The precise correlation between TEM and XRD measurements validated the structural and dimensional characteristics of the synthesized nanoparticles. Aqueous-based magnetic liquids with varying nanoparticle concentrations were prepared, enabling systematic investigation of their electrical conductivity and magnetic susceptibility at ambient temperature. The experimental findings provide critical insights into the fundamental properties of magnetic nanoparticle-based colloidal systems, potentially facilitating advanced applications in materials science, magnetic device engineering, and emerging technological domains. The methodological approach and results presented herein contribute to the expanding understanding of magnetic fluid behavior and performance.
Keywords: *Magnetic nanoparticles; Ferrite dispersions; Colloidal systems; Magnetic fluid; Nanostructured materials; Electrical conductivity; Magnetic susceptibility*
PACS: 75.50.Tt; 75.75.-c; 75.50.Gg; 81.20.-n; 81.07.Bc.

INTRODUCTION

Magnetic fluids, a class of smart materials, have attracted significant attention in modern materials science and technology due to their ability to alter their physical properties under an external magnetic field [1,2]. These fluids primarily consist of magnetic nanoparticles dispersed in a liquid medium, forming a stable colloidal suspension. The unique responsiveness of magnetic fluids to external magnetic fields enables dynamic changes in their viscosity, electrical conductivity, magnetic susceptibility, and other key physical properties, thereby expanding their applicability across various scientific and industrial domains [3]. Typically, the magnetic nanoparticles in these fluids range in size from 10 to 50 nm, and their ability to undergo controlled modifications under an external magnetic field distinguishes them from conventional industrial fluids [4]. The exceptional tunability of their electrical and rheological properties makes magnetic fluids highly valuable for applications in automotive engineering, aerospace technology, biomedicine, sensors, and advanced cooling systems. The ability to manipulate their viscosity and conductivity through external magnetic stimuli is particularly advantageous in the design of next-generation functional materials [5]. The synthesis and characterization of magnetic fluids are crucial to advancing nanotechnology and materials science. Their adaptability to external stimuli and their integration into novel smart material systems pave the way for groundbreaking technological innovations. The physicochemical properties of magnetic fluids, including nanoparticle size, shape, dispersion, and interactions within the fluid medium, fundamentally influence their performance [6]. Therefore, comprehensive studies focusing on the electrical conductivity and magnetic behavior of these materials are essential for both scientific exploration and practical applications.

This study investigates the synthesis of magnetic fluids with varying nanoparticle concentrations and systematically analyzes their electrical and magnetic properties. Key factors such as nanoparticle classification, dispersion stability, and carrier fluid viscosity are considered, as each plays a significant role in determining the overall behavior of magnetic fluids. The interaction between magnetic fluid components and the correlation between their electronic and magnetic characteristics remains of substantial scientific interest, with implications for both fundamental research and technological innovation [7]. Despite extensive research in this field, a unified theoretical framework for understanding the structural, electrical, and magnetic properties of magnetic fluids, particularly those based on spinel ferrite nanoparticles such as Fe_3O_4, $CoFe_2O_4$, and $NiFe_2O_4$, has yet to be established [8]. Furthermore, the variations in their magneto-electronic properties remain insufficiently explored. In this study, we synthesized magnetic nanoparticles based on 3d transition metals (Fe, Co, Ni) and investigated their size, chemical composition, crystal structure, and the electrical conductivity and magnetic susceptibility of their corresponding magnetic fluids at room temperature. By systematically analyzing these properties, we aim to contribute to the understanding of their fundamental behavior and potential technological applications.

Cite as: O.K. Kuvandikov, U.E. Nurimov, East Eur. J. Phys. 4, 646 (2025), https://doi.org/10.26565/2312-4334-2025-4-69

METHODOLOGY

The preparation of magnetic fluids involved a two-step process: (I) the synthesis of colloidal magnetic nanoparticles and (II) their stabilization with a surfactant layer, followed by dispersion in water to obtain a homogeneous magnetic fluid. A low-concentration magnetic fluid containing magnetic nanoparticles was synthesized to ensure colloidal stability and optimal dispersion [9]. The chemical co-precipitation method was employed, as it is one of the most widely used and straightforward techniques for the synthesis of magnetic materials [10]. This method allows simultaneous precipitation of multiple metal ions, resulting in magnetic nanoparticles with uniform chemical composition.

Synthesis of Fe_3O_4, $CoFe_2O_4$, and $NiFe_2O_4$ Magnetic Nanoparticles

For the synthesis of Fe_3O_4, ferric chloride hexahydrate ($FeCl_3 \cdot 6H_2O$), ferrous sulfate heptahydrate ($FeSO_4 \cdot 7H_2O$), and sodium hydroxide (NaOH) were used, and the procedure was carried out as follows:

1. Preparation of precursor solution: A 1 M solution of the$FeSO_4 \bullet 7H_2O$ and a 2 M solution of the$FeCl_3 \bullet 6H_2O$ were prepared separately and dissolved in 200 mL of distilled water.
2. Heating and mixing: The solution was heated to 90°C and stirred vigorously to ensure uniform distribution.
3. Precipitation reaction: A 100 mL solution of 1 M NaOH was added dropwise to the mixture while stirring continuously using a magnetic stirrer. The pH of the solution was maintained at 9–10 to facilitate controlled precipitation.
4. Ageing process: The reaction mixture was further heated at 80 °C for 2 hours to enhance nanoparticle crystallization.
5. Magnetic separation: A small portion of the reaction mixture was extracted, diluted to twice its volume, and placed in a 0.2 T permanent magnetic field to separate the precipitated magnetic nanoparticles.
6. Drying process: The obtained precipitate was washed thoroughly, dried at room temperature for 48 hours, and collected for further characterization.

The synthesis of $NiFe_2O_4$ (Nickel ferrite) and $CoFe_2O_4$ (Cobalt ferrite) followed the same procedure, using appropriate metal salts as precursors. The chemical reaction equations for the synthesis are presented below:

a) $3\,Fe\underline{X}^{2+} + 6\,Fe\underline{X}^{3+} + 24\,OH\underline{X}^{-} \rightarrow 3\,Fe(OH)\underline{X}_2 + 6\,Fe(OH)\underline{X}_3 \overset{80\underline{X}^{\circ}C}{\rightarrow} 4\,Fe\underline{X}_3O\underline{X}_4 + 12\,H\underline{X}_2O$

b) $Co\underline{X}^{2+} + 2\,Fe\underline{X}^{3+} + 8\,OH\underline{X}^{-} \rightarrow Co(OH)\underline{X}_2 + 2\,Fe(OH)\underline{X}_3 \overset{80\underline{X}^{\circ}C}{\rightarrow} CoFe\underline{X}_2O\underline{X}_4 + 4\,H\underline{X}_2O$

c) $Ni\underline{X}^{2+} + 2\,Fe\underline{X}^{3+} + 8\,OH\underline{X}^{-} \rightarrow Ni(OH)\underline{X}_2 + 2\,Fe(OH)\underline{X}_3 \overset{80\underline{X}^{\circ}C}{\rightarrow} NiFe\underline{X}_2O\underline{X}_4 + 4\,H\underline{X}_2O$

The synthesized magnetic nanoparticles were mixed with oleic acid ($C_{18}H_{34}O_2$) as a surfactant and distilled water as the liquid medium, followed by heating at 90°C for 1 hour to ensure uniform dispersion. Magnetic fluids with varying volumetric concentrations were prepared using Fe_3O_4, $CoFe_2O_4$, and $NiFe_2O_4$ magnetic nanoparticles. The volumetric concentrations of the samples were determined using the following formula:

$$\varphi = \frac{m_1/\rho_1}{(m_1/\rho_1) + (m_2/\rho_2) + (m_3/\rho_3)} \cdot 100\%$$

RESULTS AND DISCUSSION

We investigated the crystal structure of Fe_3O_4, $CoFe_2O_4$, and $NiFe_2O_4$ magnetic nanoparticles using X-ray diffraction (XRD) analysis. The synthesized nanoparticles were dried, finely powdered, and placed in a special sample holder. Monochromatic Cu Kα X-rays (λ = 1.5406 Å) were directed onto the sample surface at incident angles ranging from 10° to 80°.The diffracted rays were analyzed at angles satisfying the Wulf-Bragg condition, allowing us to determine the crystallographic structure of the nanoparticles. The relationship between the intensity of the diffracted X-rays and the angle of incidence on the nanoparticle surface is presented in Figure 1.

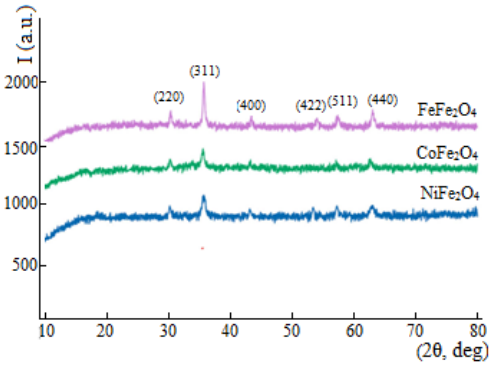

Figure 1. X-ray spectrum of magnetic nanoparticles MFe_2O_4 (M=Fe,Co, Ni)

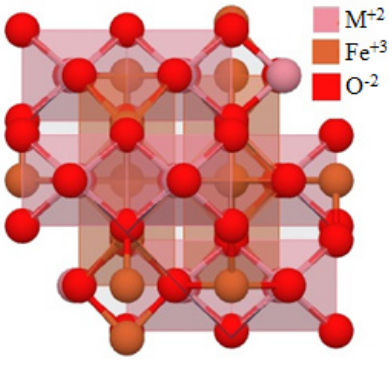

Figure 2. Crystal structure of (M=Fe,Co, Ni) MFe_2O_4 magnetic nanoparticles

The crystal structure of the synthesised magnetic nanoparticles was analysed based on the relationship between the X-ray diffraction (XRD) intensity and the angle of incidence. As shown in Figure 1, the intensity peaks in the XRD spectrum of the obtained Fe_3O_4, $CoFe_2O_4$, and $NiFe_2O_4$ nanoparticles correspond to the (220), (311), (400), (422), (511), and (400) planes. The diffracted X-ray spectrum confirms that all observed diffraction peaks are characteristic of a single-phase inverted cubic spinel structure, which [11]. Spinel ferrites follow the general chemical formula M Fe_2O_4, where M = Fe, Co, or Ni represents the divalent metal ion, while Fe^{3+} exists in the trivalent state. These materials exhibit remarkable physicochemical properties, making them highly relevant for various applications. As illustrated in Figure 2, MFe_2O_4 spinel ferrites comprise 64 tetrahedral and 32 octahedral crystal lattice sites within a single magnetic nanoparticle. The Fe^{3+} ions predominantly occupy octahedral sites, while the M^{2+} (Fe^{2+}, Co^{2+}, or Ni^{2+}) ions are positioned within tetrahedral sites. In these spinel structures (Figure 2), half of the Fe^{3+} ions are also located in tetrahedral sites, whereas the remaining half ones occupy octahedral sites [12]. The magnetic properties of these nanoparticles are primarily governed by the M^{2+} (Fe^{2+}, Co^{2+}, Ni^{2+}) ions. The average crystallite size of Fe_3O_4, $CoFe_2O_4$, and $NiFe_2O_4$ nanoparticles was estimated using the Debye-Scherrer equation $D = \frac{K\lambda}{\beta \cos(\theta)}$, based on the most intense (311) diffraction peak. The results of transmission electron microscopy (TEM)are presented in Figure 3.

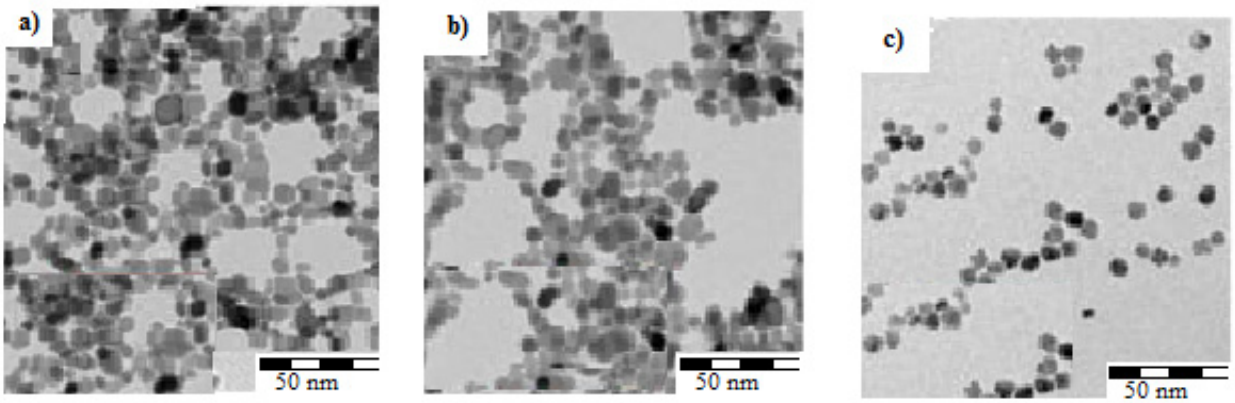

Figure 3. TEM images of magnetic nanoparticles a) Fe_3O_4,b) $CoFe_2O_4$ and c) $NiFe_2O_4$

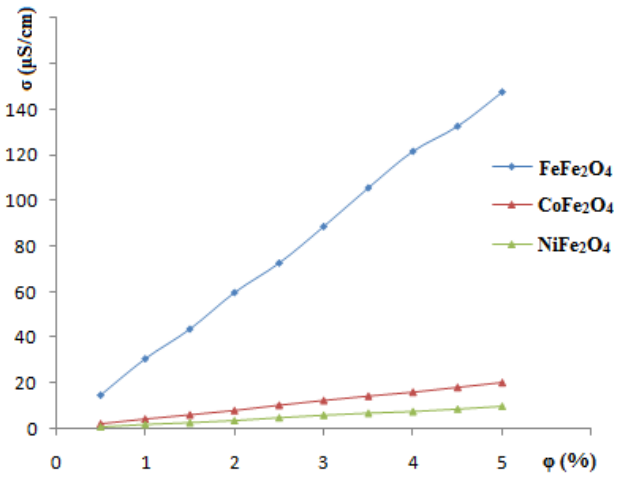

Figure 4. Concentration dependence of the electrical conductivity of magnetic fluids at room temperature

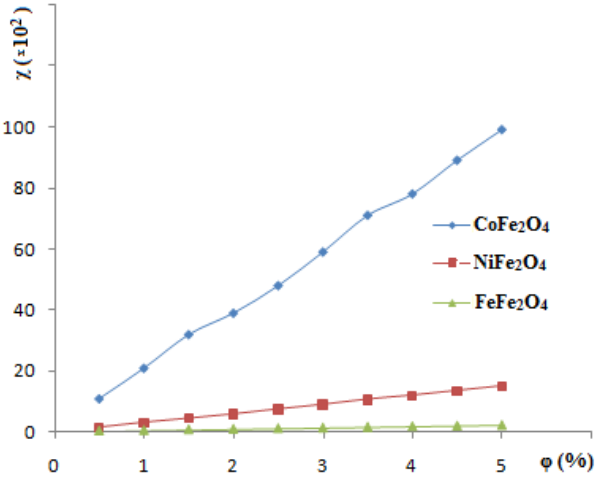

Figure 5. Concentration dependence of the magnetic susceptibility of magnetic liquids at room temperature

The electrical conductivity and magnetic susceptibility of magnetic fluids based on Fe_3O_4, $CoFe_2O_4$, and $NiFe_2O_4$ nanoparticles were measured at room temperature (t = 25 °C) across various concentrations. The results are presented in Figures 4 and 5. The electrical conductivity of magnetic fluids is highly complex and depends on several factors, including their internal structure, the properties of the surfactant, the liquid base (distilled water), and the concentration of magnetic nanoparticles within the fluid.

Ferrites such as $CoFe_2O_4$, $NiFe_2O_4$, and Fe_3O_4 (Magnetite) exhibit intrinsically low electrical conductivity, as they are primarily dielectric materials. However, as the concentration of magnetic nanoparticles in these magnetic fluids increases, their electrical conductivity rises significantly. As shown in Figure 4, the electrical conductivity of the synthesized magnetic fluids at room temperature was as follows:

- For the Fe_3O_4-based magnetic fluid, the electrical conductivity increased linearly from 15.6 μS/cm to 147.8 μS/cm as the magnetic nanoparticle concentration increased from 0.5 % to 5 %.
- For the Co Fe_2O_4-based magnetic fluid, the electrical conductivity increased linearly from 2.1 μS/cm to 20.2 μS/cm within the same concentration range (0.5 % to 5 %).
- For the $NiFe_2O_4$-based magnetic fluid, the electrical conductivity increased linearly from 0.23 μS/cm to 10.4 μS/cm, also within the same concentration range (0.5 % to 5 %).

Ferrites such as $CoFe_2O_4$, $NiFe_2O_4$ and Fe_3O_4 are mainly ferrimagnetic materials in their properties. However, magnetic fluids based on magnetic nanoparticles are mainly paramagnetic. As the concentration of magnetic nanoparticles in these magnetic fluids increases, their magnetic susceptibility increases significantly. As can be seen from Figure 5, the magnetic susceptibility of the magnetic fluids at room temperature was as follows: for the $FeFe_2O_4$-based magnetic fluid, the magnetic susceptibility increased linearly from $0.2 \cdot 10^2$ to $1.9 \cdot 10^2$ with a magnetic nanoparticle concentration of 0.5 % to 5 %; For the $CoFe_2O_4$-based magnetic fluid, the magnetic susceptibility increased linearly from $11.1 \cdot 10^2$ to $98.7 \cdot 10^2$ with a magnetic nanoparticle concentration ranging from 0.5 % to 5 %; for the $NiFe_2O_4$-based magnetic fluid, the magnetic susceptibility increased linearly from $1.5 \cdot 10^2$ to $14.9 \cdot 10^2$ with a magnetic nanoparticle concentration ranging from 0.5 % to 5 %.

Table 1. General parameters of synthesized magnetic fluids

Magnetic fluid nanoparticle	Temperature (°C)	Concentration (%)	Density (g/cm^3)	Electrical conductivity (μS/cm)	Magnetic susceptibility ($\chi\ 10^2$)
Fe_3O_4	25	0.5	1.09	15.6	0.2
		5	1.24	147.8	1.9
$CoFe_2O_4$	25	0.5	1.11	2.1	11.1
		5	1.27	20.2	98.7
$NiFe_2O_4$	25	0.5	1.15	0.23	1.5
		5	1.32	10.4	14.9

CONCLUSIONS

Magnetic nanoparticles with the general formula (M = Fe, Co, Ni) M Fe_2O_4 were successfully synthesized using the chemical precipitation method. X-ray diffraction (XRD) analysis showed that the dominant diffraction peak appeared at the (311) plane, confirming the formation of single-phase cubic spinel structures in all (M = Fe, Co, Ni) M Fe_2O_4 samples. These results agree well with previously reported findings in the literature. The particle sizes of the (M = Fe, Co, Ni) M Fe_2O_4 nanoparticles were determined using transmission electron microscopy (TEM) and calculated using the Debye–Scherrer equation $D = \frac{K\lambda}{\beta \cos(\theta)}$. The estimated diameters ranged from approximately 20-40 nm for Fe_3O_4, 12–27 nm for $CoFe_2O_4$, and 8–20 nm for $NiFe_2O_4$.The lowest electrical conductivity measured at room temperature was 0.23 μS/cm at a concentration of 0.5 % for the $NiFe_2O_4$-based magnetic fluid, whereas the highest value, 147.8 μS/cm, was recorded at a concentration of 5 % for the Fe_3O_4-based magnetic fluid. Likewise, the lowest magnetic susceptibility was 0.2 × 10² at 0.5 % concentration for the Fe_3O_4-based fluid, while the highest value, 98.7×10², was obtained at 5 % concentration for the $CoFe_2O_4$-based fluid. These results demonstrate that both electrical conductivity and magnetic susceptibility vary significantly with increasing concentration, which is an important observation for the design of smart materials and highlights their potential use in advanced manufacturing technologies.

ORCID

O.K. Kuvandikov, https://orcid.org/0000-0001-8750-038X; **U.E. Nurimov,** https://orcid.org/0009-0006-2774-9558

REFERENCES

[1] A.-H. Lu, E.L. Salabas, and F. Schüth, "Magnetic Nanoparticles: Synthesis, Protection, Functionalization, and Application," Angew. Chem. Int. Ed. **46**, 1222–1244 (2007). https://doi.org/10.1002/anie.200602866

[2] S. Laurent, D. Forge, M. Port, A. Roch, C. Robic, L. Vander Elst, and R.N. Muller, "Magnetic Iron Oxide Nanoparticles: Synthesis, Stabilization, Vectorization, Physicochemical Characterizations, and Biological Applications," Chem. Rev. **108**, 2064–2110 (2008). https://doi.org/10.1021/cr068445e

[3] N. Ashrafi, A.H.M. Ariff, M. Sarraf, S. Sulaiman, and T. Hong, "Microstructural, thermal, electrical, and magnetic properties ofoptimized Fe_3O_4–SiC hybrid nano filler reinforced aluminium matrix composite," Mater. Chem. Phys. **258**, 123895 (2021). https://doi.org/10.1016/j.matchemphys.2020.123895

[4] S. Mokhosi, W. Mdlalose, S. Mngadi, M. Singh, and T. Moyo, "Assessing the structural, morphological and magnetic properties of polymer-coated magnesium-doped cobalt ferrite ($CoFe_2O_4$) nanoparticles for biomedical application," Journal of Physics: Conference Series, **1310**, 012014 (2019). https://doi.org/10.1088/1742-6596/1310/1/012014

[5] K.K. Kefeni, and B.B. Mamba, "Photocatalytic application of spinel ferrite nanoparticles and nanocomposites in wastewater treatment," Sustainable materials and technologies, **23**, e00140 (2020). https://doi.org/10.1016/j.susmat.2019.e00140

[6] D.H.K. Reddy, and Y.-S. Yun, "Spinel ferrite magnetic adsorbents: alternative future materials for water purification?" Coord. Chem. Rev. **315**, 90–111 (2016). https://doi.org/10.1016/j.ccr.2016.01.012

[7] P.N. Reddy, B.V. Kavyateja, and B.B. Jindal, "Structural health monitoring methods, dispersion of fibers, micro and macro structural properties, sensing, and mechanical properties of self-sensing concrete – A review," Struct. Concr. **22**, 793–805 (2021). https://doi.org/10.1002/suco.202000337

[8] H. Moradmard, S.F. Shayesteh, P. Tohidi, Z. Abbas, and M. Khaleghi, "Structural, magnetic and dielectric properties of magnesium doped nickel ferrite nanoparticles," J. Alloys Compd. **650**, 116–122 (2015). https://doi.org/10.1016/j.jallcom.2015.07.269
[9] J. Xu, H. Yang, W. Fu, K. Du, Y. Sui, J. Chen, Y. Zeng, *et al*., "Preparation and magnetic properties of magnetite nanoparticles by sol–gel method," J. Magn. Magn. Mater. **309**(2), 307–311 (2007). https://doi.org/10.1016/j.jmmm.2006.07.037
[10] M.D. Hossain, M.A. Hossain, M.S. Hossain, M.N.I. Khan, and S.S. Sikder, "Sintering temperature dependent characterization of Ni nano ferrite with the optimization of frequency dependent properties," Surf. Interfaces, **52**, 104952 (2024). https://doi.org/10.1016/j.surfin.2024.104952
[11] E. Fitriyanti, and B. Purnama, "Comparison XRD pattern of $CoFe_2O_4$ thin films and nanoparticles," J. Phys. Conf. Ser. **909**(1), 012010 (2017). https://doi.org/10.1088/1742-6596/909/1/012010
[12] D. Jiao, K. Lesage, M.Y. Yardimci, K. El Cheikh, C. Shi, and G. De Schutter, "Rheological behavior of cement paste with nano-Fe_3O_4 under magnetic field: Magneto-rheological responses and conceptual calculations," Cem. Concr. Compos. **120**, 104035 (2021). https://doi.org/10.1016/j.cemconcomp.2021.104035

ВИРОБНИЦТВО ФЕРИТІВ НА ОСНОВІ МАГНІТНИХ НАНОЧАСТИНОК ТА КОМПЛЕКСНА ХАРАКТЕРИЗАЦІЯ ЇХ ЕЛЕКТРИЧНИХ ТА МАГНІТНИХ ВЛАСТИВОСТЕЙ У КОЛОЇДНИХ СИСТЕМАХ

О.К. Кувандіков, У.Е. Нурімов
Самаркандський державний університет імені Шарофа Рашидова, 140001, Самарканд, Узбекистан

У цьому дослідженні досліджується синтез, структурна характеристика та фізико-хімічні властивості магнітних наночастинок, отриманих з металів групи заліза (Fe, Co, Ni) та їхніх відповідних феритових дисперсій. Магнітні наночастинки були синтезовані методом хімічної конденсації, а їх морфологія та структура були проаналізовані за допомогою просвічувальної електронної мікроскопії (TEM) та рентгенівської дифракції (XRD). Синтезовані магнітні наночастинки, що містять ферити Fe_3O_4, $CoFe_2O_4$ та $NiFe_2O_4$, демонстрували нанорозміри в діапазоні від 10 до 50 нм. Точна кореляція між вимірюваннями TEM та XRD підтвердила структурні та розмірні характеристики синтезованих наночастинок. Були підготовлені магнітні рідини на водній основі з різною концентрацією наночастинок, що дозволило систематично досліджувати їхню електропровідність та магнітну сприйнятливість за кімнатної температури. Експериментальні результати дають критичне розуміння фундаментальних властивостей колоїдних систем на основі магнітних наночастинок, що потенційно сприяє передовим застосуванням у матеріалознавстві, магнітній приладобудуванні та нових технологічних галузях. Методологічний підхід та результати, представлені тут, сприяють розширенню розуміння поведінки та характеристик магнітної рідини.

Ключові слова: *магнітні наночастинки; феритові дисперсії; колоїдні системи; магнітна рідина; наноструктуровані матеріали; електропровідність; магнітна сприйнятливість*

EAST EUROPEAN JOURNAL OF PHYSICS. **4.** 651-660 (2025)
DOI:10.26565/2312-4334-2025-4-70 ISSN 2312-4334

ASSESSMENT OF THE OPERATING TEMPERATURE OF ABSORBER ASSEMBLY STRUCTURAL COMPONENTS AND CONFIRMATION OF THEIR COOLING RELIABILITY IN VVER-440 REACTOR CORE

Zuyok Valeriy[1]*, Mazurok Oleksandr[2], Zigunov Volodymyr[1], Lankov Bohdan[2], Dzhamirzoiev Albert[1], Makarenko Anton[3], Tretyakov Mykhaylo[1], Godun Oleg[4]
[1]National Science Center "Kharkiv Institute of Physics and Technology", Kharkiv, Ukraine
[2]ES Group LLC, Kyiv, Ukraine
[3]Scientific and Technical Complex "E.O. Paton Electric Welding Institute", Kyiv, Ukraine
[4]Scientific and Technical Centre, JSC "NNEGC "Energoatom", Ukraine, Kyiv
**Corresponding Author e-mail: valeriyz@kipt.kharkov.ua*
Received July 13, 2025; revised September 20, 2025; accepted November 11, 2025

The specific energy release in the structural materials of the absorber assembly (control part of the accident control assembly – ACA, also known as the shim assembly) has been calculated. It depends on the power of the fixed fuel assemblies (FAs) in adjacent cells. The value of the energy release is 17.5 W/cm^3 on the most loaded section of the boron absorber insert for an average Kq=1.28 over sectors. The total energy release in the structural materials of the absorber assembly, in the coolant, and in the connecting bar material is 229 kW for fully inserted controls and 64 kW for controls lifted up by 154.8 cm from the core bottom. The surface temperature distribution in the absorber insert along the absorber assembly height is conservatively calculated based on the total energy release in the absorber insert material and the amount and rate of coolant flow through it. At a coolant temperature around the absorber insert corresponding to the maximum coolant heating in adjacent fixed FAs (46.6 °C), and in the absence of axial heat exchange, the maximum surface temperature of the absorber insert for fully inserted controls will be 312.7 °C (outer surface), and for controls lifted from the core bottom to 154.8 cm – 317.1 °C (inner surface), giving a margin to saturation of 14.3 °C and 9.9 °C, respectively, at a coolant saturation temperature of 327 °C. In the most conservative case considered in this paper, the maximum surface temperature of the absorber insert is lower than the coolant's saturation temperature. This indicates the absence of bulk and surface boiling of the coolant under operation of the most energy-loaded component, i.e., the absorber insert of the absorber assembly, meaning that the structural components of the absorber assembly will be reliably cooled in the VVER-440 reactor core.
Keywords: *VVER-440; Accident control assembly; Absorber assembly; Absorber insert; Energy release; Cooling*
PACS: 28.41.Bm, 28.41.Qb, 28.41.Vx

INTRODUCTION

The structural materials of the reactor core operate for long periods under severe mechanical loads, neutron irradiation, high coolant parameters, and significant thermal loads. The absorber assembly of the follower fuel assembly is an integral part of the VVER-440 nuclear fuel cycle and is operated in Units 1 and 2 of the Rivne NPP.

Reactor irradiation results in a series of phenomena that cause energy release not only in the core's structural materials but also in the coolant. In this regard, each structural component must be reliably cooled by the coolant flow, and there must be sufficient coolant volume to prevent boiling on its surface. The design of a core component must be sufficient to prevent any of its parts from melting, even under conservative operating conditions.

At present, the issue of justifying the implementation of nationally produced absorber assemblies is relevant for Ukrainian NPPs with VVER-440 reactors. This requires work to be done to justify their corrosion and radiation resistance, the compatibility of materials at contact temperatures, and specify the adequacy of mechanical characteristics to maintain the structural integrity of the absorber assembly components under all static and dynamic loads. Most of the listed phenomena and mechanisms depend on the temperature of the material, and corrosion resistance also depends on the state of the coolant (i.e. water, steam). The work to justify safe operation requires specifying the temperatures of the absorber assembly structural materials in a mixed core (fuel produced by JSC TVEL and Westinghouse). This will enable further materials research at temperatures close to real ones and justify its reliable cooling.

1. GENERAL DESCRIPTION OF THE VVER-440 ABSORBER ASSEMBLY DESIGN

The accident control assembly (ACA) is the actuating component of the VVER-440 control and protection system. The ACA consists of a follower fuel assembly (the fuel part) and an absorber assembly (the control part). ACAs are the reactivity control components (controls) of the reactor control and protection system and 37 of them are the part of the VVER-440 reactor core [1].

Cite as: V. Zuyok, O. Mazurok, V. Zigunov, B. Lankov, A. Dzhamirzoiev, A. Makarenko, M. Tretyakov, O. Godun, East Eur. J. Phys. 4, 651 (2025), https://doi.org/10.26565/2312-4334-2025-4-70

The follower FA and the absorber assembly of the ACA are connected by a connecting bar. The absorber assembly (Fig. 1) has a welded structure with a total mass of 110 kg. It is made of stainless steel and contains a boron steel hexagonal insert. The components of the absorber assembly are made of the following materials [2]:

- shroud – steel X6CrNiTi18-10 (1.4541);
- absorber insert – boron stainless steel (1.6…2.0% of boron);
- central tube and flow limiter – steel X6CrNiTi18-10 (1.4541);
- top nozzle – steel X6CrNiTi18-10 (1.4541);
- bottom nozzle – steel X6CrNiTi18-10 (1.4541).

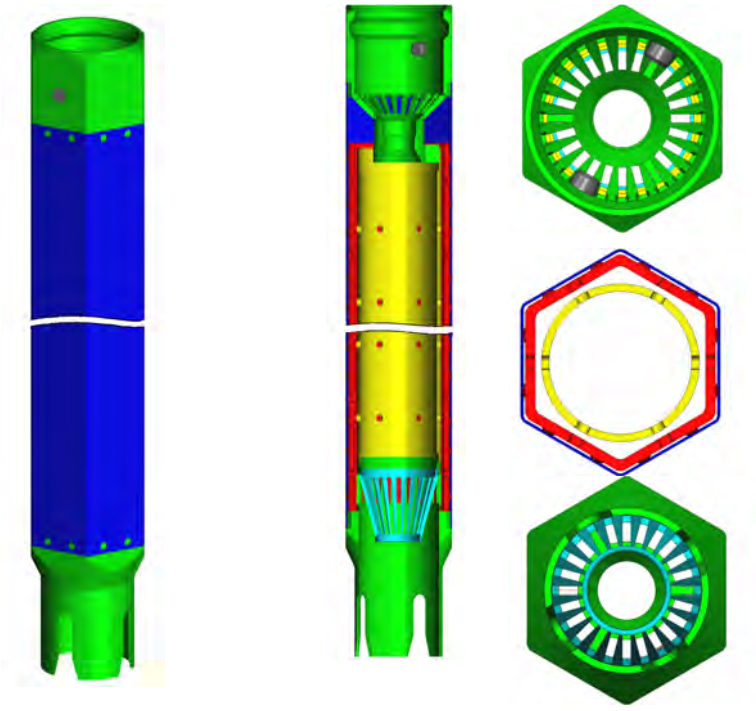

a b c

Figure 1. Schematic view of the absorber assembly: a – general view; b – vertical section; c – top view, cross-section, bottom view

The connecting bar linking the follower FA to the absorber assembly is made of 08Cr18Ni10T steel. As shown below, it is the chemical composition of the material and the position of the absorber assembly components in the reactor core that account for the energy release in it.

ACAs can move in a vertical channel formed by six adjacent fixed FAs, a hexagonal slot in the bottom plate of the core basket, and the bottom tubes of the core barrel (Fig. 2). When the ACA is in the lower position, the fuel part is located in the core barrel bottom tubes and the absorber assembly is in the core. In this position of the ACA, energy release in the absorber assembly materials will be maximal and the coolant temperature at the inlet will be minimal. The main positions of the ACA, namely full and partial insertion, are shown schematically in Fig. 2. Above the core, there is a protective tube unit that separates the fixed FAs and has protective tubes in which the ACAs can move vertically.

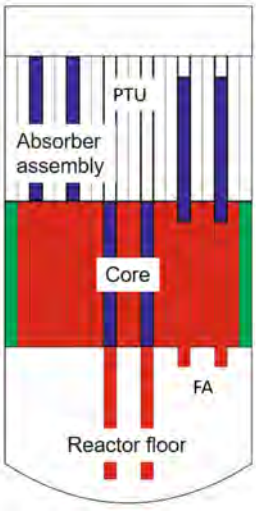

Figure 2. Schematic view of the lower part of the reactor pressure vessel and various positions of the ACAs

The design features of the VVER 440 reactor core affect the energy released in the absorber assembly materials and the coolant temperature at the inlet. Therefore, they are important for determining the operating temperature and ensuring cooling reliability.

2. ENERGY RELEASE IN THE ABSORBER ASSEMBLY MATERIALS

Reactor irradiation results in a series of phenomena that cause the release of energy in the core materials. For structural materials, this interaction involves γ-quanta and electrons; for neutron-absorbing materials, it also involves neutrons. In an operating reactor, γ-quanta and electrons are generated by the nuclear interaction of neutrons with fissile isotopes and are also emitted by radioactive decay products. During power operation, the fraction of fissionable sources is much larger than that of decay sources; therefore, the latter can be disregarded. The power of fission sources is proportional to the neutron flux density, which in turn is proportional to the energy release power of the nuclear fuel in the axial zone (according to the energy release profile at different heights (Kz)) in which the irradiated material is located.

The energy release profile for each stage of reactor core operation is characterized by a curve fitting the maximum energy release values along the height of the fuel assemblies from the same year of operation. These profiles were calculated for the beginning (BOC), middle (MOC), and the end (EOC) of the fuel cycle for assemblies in the first to fifth/sixth years of operation [3]. The BOC is characterized by a single-maximum profile with a maximum Kz close to

1.2, and the EOC – 1.1, which is less conservative for further calculations. Considering this, to calculate the energy release in the absorber assembly components, the profile with the maximum Kz (1.1985), which is typical of a "fresh" assembly at the BOC, was used (Fig. 3).

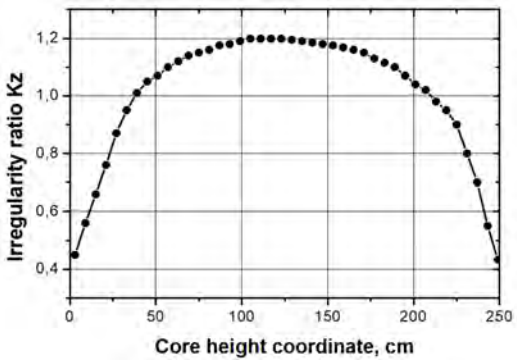

Figure 3. Distribution of relative energy release by height of the core at the BOC [3]

Reactor irradiation results in a series of phenomena that cause the release of energy in the core materials. For structural materials, this interaction involves γ-quanta and electrons; for neutron-absorbing materials, it also involves neutrons.

The absorber assembly materials do not contain fissile materials. The total energy release in the absorber assembly materials, which can result in heating of the coolant passing through it, depends on the energy release power of the fixed FAs located in adjacent cells. The Kq of the six assemblies in adjacent cells varies significantly, ranging from 1.4 to 1.1. It is assumed that the average Kq over sectors is 1.28.

For the absorber insert material, which is made of stainless steel containing 1.6-2.0% boron, energy release will also be due to neutron absorption and interaction with γ-quanta and electrons. For boron (B), the main energy release reaction is the interaction of a neutron with the ^{10}B isotope: $n + {}^{10}B \Rightarrow {}^{7}Li + {}^{4}He + 2.78$ MeV.

Using the calculation model developed in the HELIOS software (Fig. 4), the energy release in the absorber material containing 1.8% natural boron, with a ^{10}B isotope content of 19.8%, was calculated (Table 1).

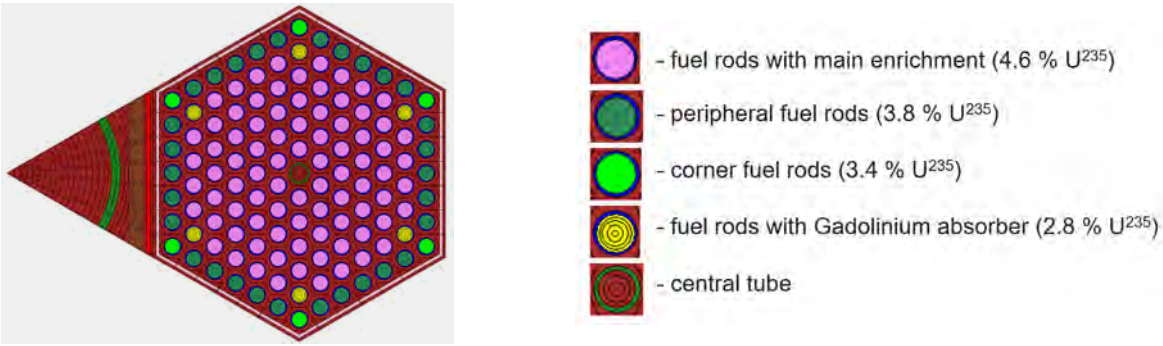

Figure 4. Calculation model of the absorber assembly segment at the level of the absorber inserts next to the fixed FA 427WN, implemented in the HELIOS software

The calculations reveal that, for the case considered in this paper, the maximum averaged over sectors specific energy release power in the most loaded part of the boron absorber insert is 17.5 W/cm^3. The energy release is almost the same across different sectors of the radial and azimuthal cross-sections of the absorber insert. Considering that the absorber insert material is mainly stainless steel, which has a high thermal conductivity, the average energy release across the cross-section of the absorber insert was used for further calculations.

Table 1. Energy release in the absorber inserts material of the absorber assembly

Energy release, W/cm^3							
	Cell number in the radial direction						
Cell number in the azimuthal direction		6	5	4	3	2	1
	1	**17.03**	**16.69**	**16.73**	**16.96**	**17.45**	**18.28**
	2	**17.05**	**16.79**	**16.86**	**17.15**	**17.73**	**18.72**
	3	**16.98**	**16.79**	**16.91**	**17.26**	**17.90**	**18.94**
	4	**17.00**	**16.82**	**16.95**	**17.31**	**17.96**	**19.01**
	5	**16.98**	**16.79**	**16.91**	**17.26**	**17.90**	**18.94**
	6	**17.05**	**16.79**	**16.86**	**17.15**	**17.73**	**18.72**
	7	**17.03**	**16.69**	**16.73**	**16.96**	**17.45**	**18.28**

When calculating energy release in the materials of the absorber assembly structural components, two positions of the controls in the VVER-440 reactor core during operation at the corresponding power level were considered:

- full insertion. The absorber insert of the absorber assembly is located in the middle of the core (in the area of maximum energy release);
- partial insertion (operating condition). The controls are partially inserted in the core to a lower position of 154.8 cm (from the core bottom).

In addition to the structural materials of the absorber assembly main components (Section 1), the coolant flowing through the absorber assembly will also be heated by the connecting bar and the energy release in the water (coolant) itself. The distribution of specific energy release power by height of the absorber assembly structural components for the fully inserted and lifted to 154.8 cm controls is shown in Fig. 5. Accordingly, with a change in the height of energy release in adjacent assemblies in the core (Fig. 3), the energy release in the materials of the absorber assembly structural components also changes (Fig. 5).

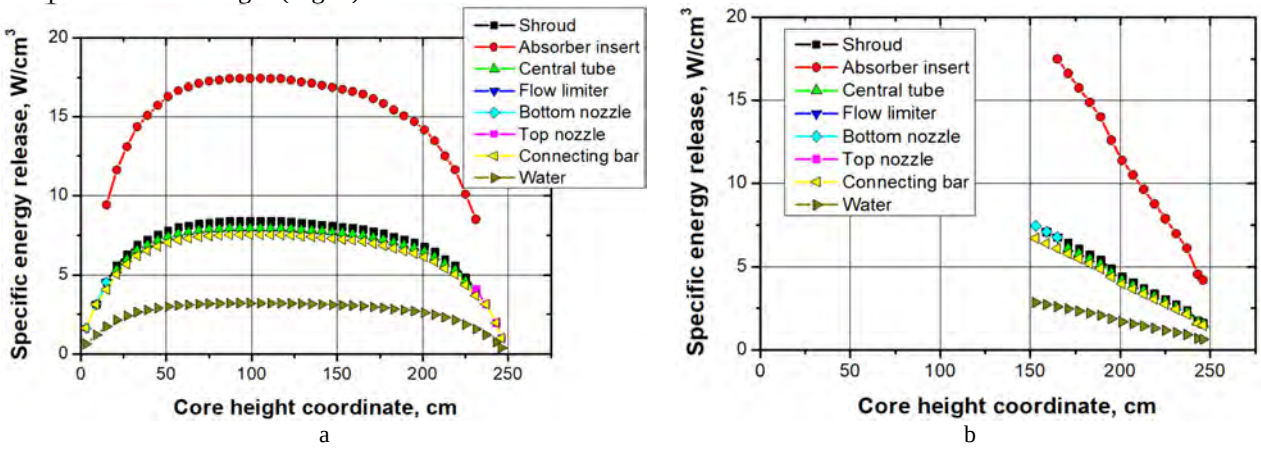

Figure 5. Distribution of specific energy release power by height of the absorber assembly structural components for the controls fully inserted (a) and lifted to 154.8 cm from the core bottom (b)

A comparison of the specific energy release in materials of the VVER-440 absorber assembly structural components and materials of the VVER-1000 rod cluster control assembly (RCCA), presented in the paper [4] shows that for fully inserted controls, the specific energy release in the structural materials (except for the absorber material) and water is comparable to the data given in the above-mentioned paper. This comparability may be due to the comparable neutron flux density in the mentioned reactors. However, the specific energy release in the VVER-1000 RCCA absorber (B_4C) is significantly higher than for the absorber material of the VVER-440 absorber assembly, which is due to the higher boron content per unit volume of the absorber.

The total energy release power in the absorber assembly materials at full insertion of the controls is 229 kW, and the maximum energy release is in the absorber insert material (95 kW) (Fig 6a, Table 2).

Table 2. Energy release in the absorber assembly structural materials for fully inserted controls

Structural component	Volume, cm^3	Total energy release, W
Shroud	2291	16388
Absorber insert	6265	95220
Central tube	3974	28116
Flow limiter	55	233
Bottom nozzle	447	1518
Top nozzle	899	2436
Connecting bar	1537	9452
Coolant	28845	75986
Total		**229 349**

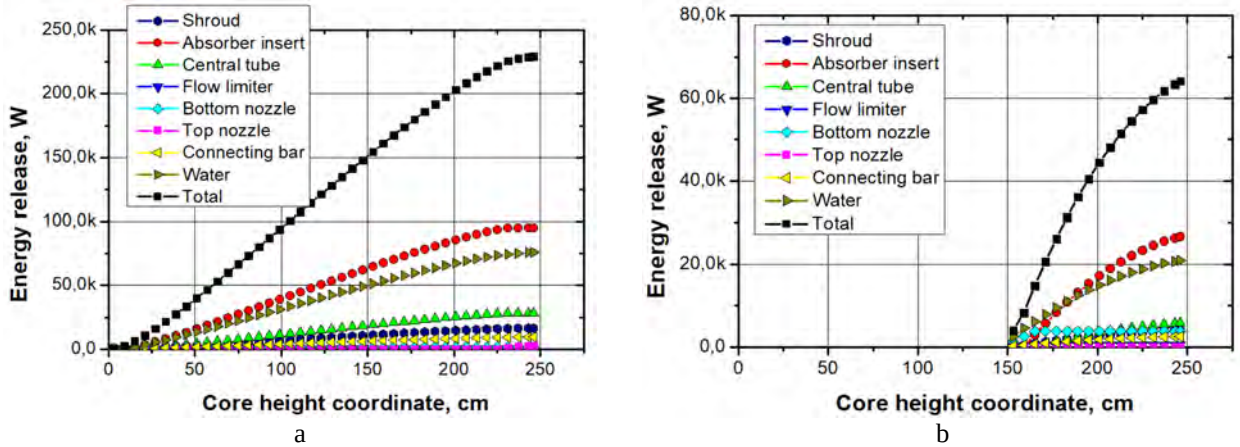

Figure 6. Distribution of total energy release power by height of the absorber assembly for the controls fully inserted (a) and lifted to 154.8 cm from the core bottom (b)

The total energy release in the absorber assembly materials of the lifted to 154.8 cm controls is 64 kW, while the maximum energy release in the absorber insert material is 26 kW (Fig. 6b, Table 3).

Table 3. Energy release power in the absorber assembly structural materials for the controls lifted to 154.8 cm

Structural component	Volume, cm^3	Total energy release, W
Shroud	907	4025
Absorber insert	2429	26680
Central tube	1484	5732
Flow limiter	55	422
Bottom nozzle	536	3816
Top nozzle	0	0
Connecting bar	609	2534
Coolant	11754	20911
Total		**64 120**

In both cases, the highest energy release occurs in the absorber insert material. It is reasonable to calculate the margin to the saturation temperature for the most heat-loaded component of the absorber assembly, i.e., the absorber insert.

3. COOLANT HEATING IN THE ABSORBER ASSEMBLY

Based on the data on the total volume of coolant flowing through the absorber assembly and the distribution of the total energy release power in the absorber assembly, the distribution of the coolant heating temperature along the height of the absorber assembly and the maximum coolant heating temperature in it are calculated.

The calculation assumes that all the heat from the absorber assembly structural components is spent on heating water in the absorber assembly channel. There is no heat exchange through the shroud. In accordance with [1], the coolant flow rate through the fixed FA and follower FA is not less than 100 m^3/hour. All coolant flowing through the follower FA also flows through the absorber assembly. According to Tables 3.3–3.8 of [5], the average coolant temperature at the reactor inlet is 266 °C, and the average coolant temperature at the outlet of the follower FA fuel rod bundle of the most heat-loaded second-generation ACA, manufactured in the russian federation and the NOVCC manufactured by Westinghouse, does not exceed 310 °C in all cases.

According to the basic thermal-hydraulic characteristics of the Rivne NPP Unit 1 reactor [6], the coolant flow rate through the follower FA is not less than 120 m^3/hour, and for the Rivne NPP Unit 2 [5] is 123 m^3/hour. In accordance with the operating conditions of the absorber assembly specified in the technical specifications [2], the minimum coolant flow rate through the follower FA and the absorber assembly is 100 m^3/hour, which at a coolant density of 0.777 g/cm^3 is 21.6 kg/s.

The water heat capacity (C_P) is 4936 J/(kg·°C) at temperatures above 266 °C and 6199 J/(kg·°C) at the maximum coolant temperature at the assembly outlet (310 °C). Coolant heating is described by the following expression:

$$\Delta T = \frac{Q}{(C_P \cdot m)}, \tag{3.1}$$

where:

ΔT – coolant heating, °C;
Q – total heat release capacity, W;
C_P – water heat capacity, J/(kg·°C);
m – coolant flow rate through the absorber assembly, kg/s.

The calculation results demonstrated that, in the absence of heat exchange through the absorber assembly shroud, the maximum coolant heating would be 1.9 °C for the fully inserted controls and 0.53 °C for the controls lifted to 154.8 cm (Fig.7, Table 4).

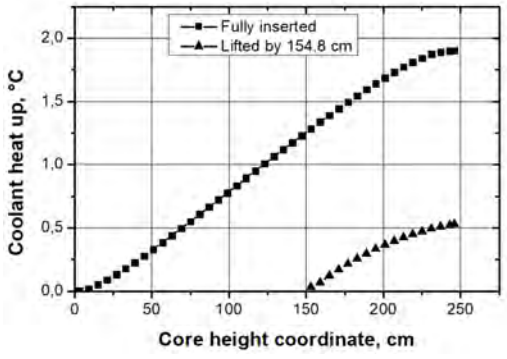

Figure 7. Coolant heating in the absence of heat exchange through the absorber assembly shroud

An increase in energy release in six fixed FAs located in adjacent cells, with the averaged for these FAs Kq = 1.28, to a value corresponding to Kq = 1.47 will result in increased energy release in structural materials. In the absence of heat exchange, this will cause the coolant to heat up to 2.4 °C in the case of a full insertion of the controls.

In the absence of heat exchange through the shroud, the coolant heating is insignificant, and the temperature at the outlet of the absorber assembly will be controlled by the temperature at the outlet of the follower FA. For the case of fully inserted controls, with a residual energy release in the follower FA of 250-300 kW, the coolant temperature at the inlet to the absorber assembly will be approximately ~2 °C higher than the coolant temperature at the inlet to the adjacent fixed FAs.

Table 4. Parameters for calculating coolant heating

Parameter	Fully inserted controls	Controls lifted to 154.8 cm
Coolant temperature at the inlet of the absorber assembly, °C	268	266
Coolant flow rate through the absorber assembly, kg/s	21.6	21.6
Total heat release in the absorber assembly, W	229349	64120
Coolant heating in the absorber assembly, °C	1.90	0.53

When the absorber assembly is partially inserted, due to significant energy release in the follower FA, the heating of the coolant flowing through the follower FA will be significant. The maximum heating of the coolant in the most thermally loaded follower FA is in the range of 40-41 °C (depending on the FA type, their number and positions in the mixed core). For the most conservative calculation (minimum coolant flow, etc.), the maximum heating reaches 44.4°C [5].

For further calculations of the cooling reliability of the absorber insert, which is the most energy-loaded structural component, it can be conservatively assumed that the coolant temperature at the inlet of the absorber assembly will correspond to the temperature at the outlet of the follower FA with heating in it, which is characteristic of this axial area and has a maximum of 44.4 °C at full withdrawal of the absorber assembly.

4. MAXIMUM TEMPERATURE OF THE ABSORBER INSERT AND MARGIN TO THE SATURATION TEMPERATURE

To increase the calculations' conservatism, it was assumed that the temperature of the shroud and coolant near the absorber insert corresponds to the coolant temperature of the adjacent fixed FAs, taking into account the corresponding axial position. According to Report [5], the maximum heating temperature of the Rivne NPP Unit 2 reactor core is 46.6 °C. In further calculations, it is assumed that the coolant heating temperature in all adjacent fixed FAs is 46.6 °C.

The surface temperature of the absorber insert was assessed for each segment with a characteristic specific energy release. As the absorber insert is a semi-hexagonal prism, temperature calculations were performed for a flat wall with two-sided cooling by solving conventional one-dimensional inhomogeneous differential equations for a steady-state case (axial heat flow was conservatively not taken into account).

The absorber inserts were conventionally divided into 5-6 cm segments by height, which conventionally have similar specific energy release power (Fig. 5) and heat transfer coefficient (coolant parameters) by height.

Taking into account that the heat fluxes from the considered wall on the outer surface (in the gap between the absorber insert and the shroud) and the inner surface (the gap between the central tube and the absorber insert) are different, the maximum temperature across the radial cross-section of the absorber insert (due to internal sources of energy release, the dependence is parabolic) is not located in the middle, but is offset from the center. In this regard, the wall thickness (δ) was conventionally divided into two zones by a floating point (with coordinate r). For the inner zone ($x \in 0 \ldots r$) of the absorber insert, the temperature distribution across the cross-section was obtained by solving the equation:

$$\frac{d^2T(x)}{dx^2} + f = 0, \tag{4.1}$$

boundary conditions:

$$\left(\frac{dT(x)}{dx}\right)_{x=r} = 0, \tag{4.2}$$

$$\lambda\left(\frac{dT(x)}{dx}\right)_{x=0} = \alpha_1(T_{IS} - T_C), \tag{4.3}$$

where:

f – specific energy release power;

T_{IS} – inner surface temperature of the absorber insert;

T_C – coolant temperature;

λ – thermal conductivity factor of the absorber insert material;

r – coordinate of the maximum temperature in the cross section of the absorber insert along its thickness;

α_1 – heat transfer factor from the inner wall to the coolant.

For the outer zone ($x \in r \ldots \delta$) of the absorber insert, the temperature distribution across the cross-section was obtained by solving equation (4.1) for $x \in r \ldots \delta$ with the following boundary conditions:

$$\left(\frac{dT(x)}{dx}\right)_{x=r} = 0 \tag{4.4}$$

$$-\lambda\left(\frac{dT(x)}{dx}\right)_{x=\delta} = \alpha_2(T_{OS} - T_C) \tag{4.5}$$

where:

δ – absorber insert wall thickness;

T_{OS} – outer surface temperature of the absorber insert;

α_2 – heat transfer factor from the outer wall to the coolant.

The coordinate of the maximum temperature "*r*" for each segment by height was obtained from the condition of temperature equality at point "*r*", obtained from two expressions, which are the solutions of equation (4.1) with boundary conditions (4.2, 4.3) and (4.4, 4.5):

$$r = \frac{\frac{\delta}{\alpha_2}+\frac{\delta^2}{2\lambda}}{\frac{1}{\alpha_1}+\frac{1}{\alpha_2}+\frac{\delta}{\lambda}} \tag{4.6}$$

In further calculations, it was assumed that the thermal conductivity of the absorber insert material is 20 W/(m·°C).

The heat transfer factors for each of the absorber insert surfaces were obtained from the following expression:

$$\alpha_i = \frac{l_i}{d_e} \cdot Nu_i, \text{ [W/(m}^2\text{·°C)]} \tag{4.7}$$

where:

i – absorber insert segment number by height,

l_i – coolant heat transfer factor on the segment *i*;

Nu_i – Nusselt number on the segment *i*;

d_e – equivalent (hydraulic) diameter.

The Nusselt number was calculated by the formula for ring-type cross-section channels (tube-in-tube [7]):

$$Nu_i = 0.017 \times Re_i^{0.8} \times Pr_i^{0.4} \times \left(\frac{d_{ida}}{d_{odt}}\right)^{0,18} \tag{4.8}$$

where:

Re – Reynolds number;

Pr – Prandtl number;

$\frac{d_{ida}}{d_{odt}}$ – the ratio of the absorber insert inner diameter to the tube outer diameter was calculated as the ratio of the wetted perimeters of the absorber insert inner surface to the outer perimeter of the central tube.

The Reynolds number depends on the coolant flow rate and parameters:

$$Re_i = \frac{\rho_i v_i d_{ei}}{\eta_i} \tag{4.9}$$

where:

ρ – coolant density;

v – coolant flow rate;

η – coolant dynamic viscosity.

Using the ANSYS software package [8] by the finite element method, a detailed calculation of the coolant flow rate throughout the entire volume of the absorber assembly was performed at a coolant flow rate through the ACA (follower FA + absorber assembly) of 100 m^3/hour. The coolant flow rate distribution at the most interesting segments of the absorber assembly (i.e. the coolant inlet (bottom nozzle) and outlet (top nozzle)) is shown in Fig. 8 and Tables 5 and 6.

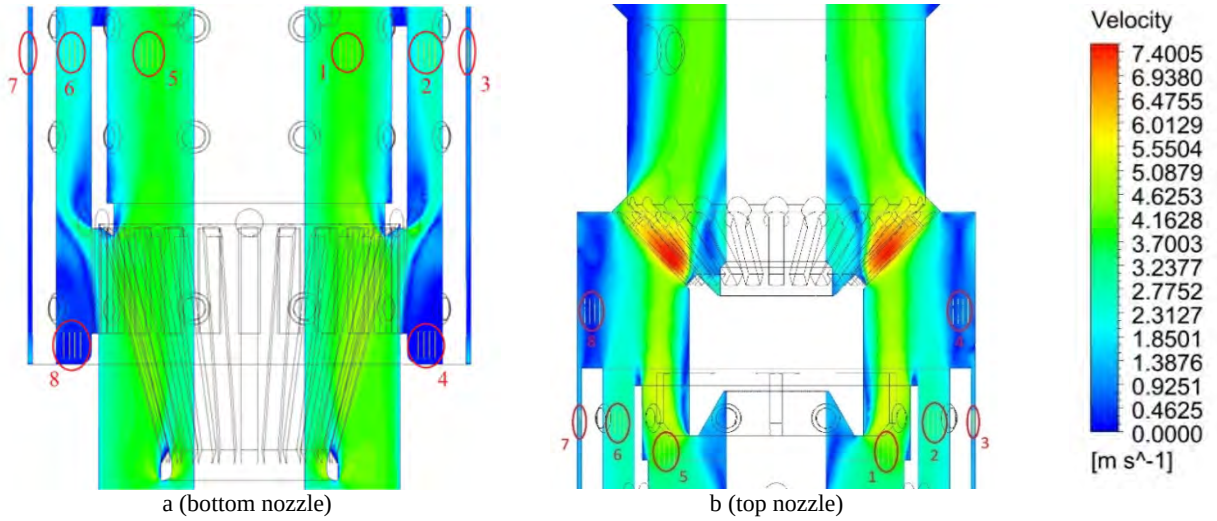

a (bottom nozzle) b (top nozzle)

Figure 8. Distribution of the coolant flow rate at the inlet (a) and outlet (b) of the absorber assembly was obtained using ANSYS CFD

Table 5. Coolant flow rate in the bottom nozzle area

Gap	Average rate, m/s
Connecting bar – central tube (1 and 5 positions)	3.77
Central tube – absorber insert (2 and 6 positions)	2.30
Absorber insert – shroud (3 and 7 positions)	0.95
Stagnant area (4 and 8 positions)	0.14

Table 6. Coolant flow rate in the top nozzle area

Gap	Average rate, m/s
Connecting bar – central tube (1 and 5 positions)	3.90
Central tube – absorber insert (2 and 6 positions)	2.71
Absorber insert – shroud (3 and 7 positions)	1.36
Stagnant area (4 and 8 positions)	0.57

Based on the data obtained (Tables 5, 6), it can be assumed that the most heat-loaded area of the absorber assembly will be near the bottom nozzle, since it is characterized by the highest energy release when the controls insertion is different from zero, and the lowest coolant flow rate is in the area of the absorber insert, as well as the presence of an area with a low coolant flow rate in contact with the absorber insert (stagnant area (positions 4 and 8) Table 5). The stagnant area in the upper part of the absorber assembly (top nozzle) will not affect the cooling of the absorber insert (Fig. 8.b). The top nozzle of the absorber assembly is located outside the fuel-containing core area when the controls insertion is different from zero. Therefore, in further calculations of the temperature on the surface of the absorber insert, the coolant flow rate values obtained for the lower part of the absorber assembly are used.

The calculations demonstrate (Fig. 9) that the lower part of the absorber insert (0 cm), in the stagnant area (positions 4 and 8), which is characterized by a low coolant flow rate in the inner part (0.14 m/s), the temperature of the inner surface of the absorber insert is higher than the temperature of the outer surface, and their difference for fully inserted controls (100%) will be ~5 °C, and ~10 °C for controls lifted to 154.8 cm from the core bottom. The difference is due to the different specific energy release values (Fig. 5) for fully and partially inserted controls.

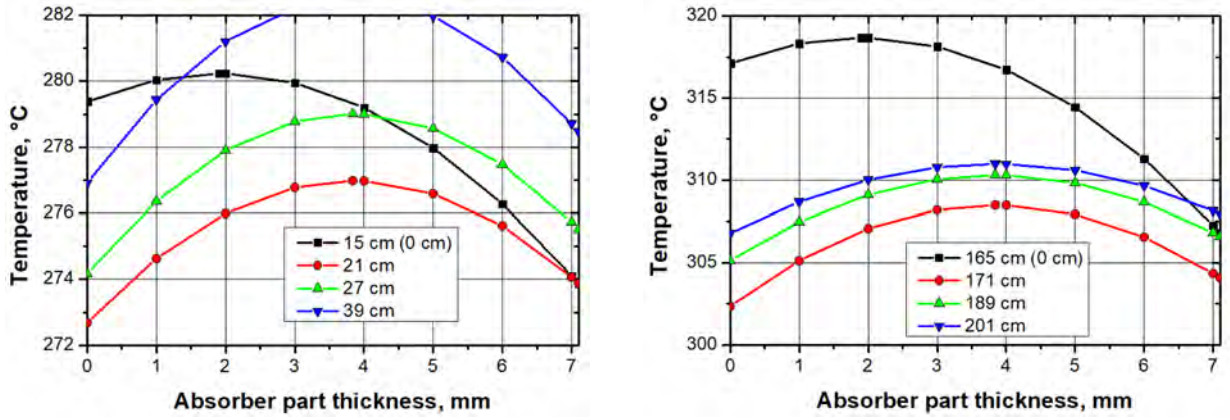

a (100%) b (154 cm)

Figure 9. Temperature distribution across the absorber insert wall cross-section at different axial positions of the absorber assembly in the reactor core for controls fully inserted (a) and lifted to 154.8 cm from the core bottom (b)

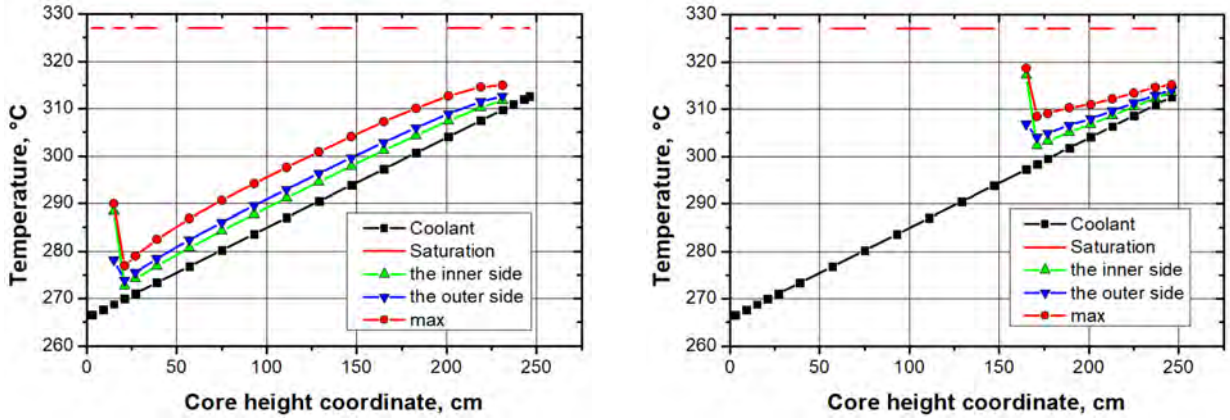

a (100%) b (154 cm)

Figure 10. Distribution of the coolant temperature on the absorber insert surface along the core height for fully inserted (a) and lifted to 154.8 cm (b) controls

With an increase in the axial position along the height of the core, the temperature of the inner surface of the absorber inserts decreases due to the increased coolant flow rate in the gap between the central tube and the absorber insert (positions 2, 6) (Fig. 9). The distribution of coolant temperature on the surface of the absorber insert along the height of the core for fully inserted and lifted to 154.8 cm controls is shown in Fig. 10.

The calculation results indicated that, at the coolant temperature around the absorber insert corresponding to the maximum coolant heating in adjacent fixed FAs (46.6 °C), the maximum surface temperature of the absorber insert will be 312.7 °C for fully inserted controls, and 317.1 °C for controls lifted to 154.8 cm from the core bottom, which at a coolant saturation temperature of 327 °C gives a margin to saturation of 14.3 °C and 9.9 °C, respectively.

Table 6. Results of calculating the cooling of the absorber insert

Parameter	Fully inserted	Lifted to 154.8 cm
Coolant temperature at the absorber assembly inlet, °C	268	295
Coolant flow rate through the absorber assembly, kg/s	21.66	21.66
Coolant temperature at the outlet from adjacent fixed FAs, °C	312.6	312.6
Max. surface temperature of the absorber insert, °C	312.7	317.1
Axial position of max. temperature, cm	~231	~165
Coolant saturation temperature, °C	327	327
Margin by saturation temperature, °C	14.3	9.9

According to the calculations, the maximum surface temperature of the absorber insert does not exceed 317.1 °C at a coolant saturation temperature of 327 °C for different controls' positions. This indicates the absence of bulk and surface boiling of the coolant during operation. Therefore, the absorber insert is reliably cooled in the VVER-440 reactor core. Increasing the energy release in six fixed FAs located in adjacent cells, with an average value of Kq=1.28 for these fixed FAs, to a value that corresponds to Kq=1.47, will cause an increase in energy release in the absorber insert material and an increase in its temperature from 317.1 °C to 320.1 °C, which is also below the saturation temperature (327 °C).

CONCLUSIONS

1. The specific energy release power in the structural materials of the absorber assembly depends on the power of the fixed FAs located in the adjacent cells. For the most loaded part of the boron absorber insert, with average Kq = 1.28 across sectors, the energy release is 17.5 W/cm^3. The total energy release power in the structural materials of the absorber assembly, coolant, and connecting bar material is 229 kW for fully inserted controls and 64 kW for lifted by 154.8 cm from the core bottom.

2. If no heat exchange occurs through the absorber assembly shroud, the maximum heating of the coolant due to energy release in the structural materials, at a conservative coolant consumption rate of 100 m^3/hour, will be 1.9 °C for fully inserted controls and 0.53 °C for controls lifted to 154.8 cm from the core bottom. In the most conservative case involving an increase in energy release in the adjacent fixed FAs to a value corresponding to Kq=1.47, the coolant heating does not exceed 2.4 °C. Due to the large area and the coolant's parameters, heat transfer through the shroud will cause the coolant in the gap between the shroud and the absorber insert to heat. To increase the conservatism of subsequent calculations, it was assumed that the shroud and surrounding coolant temperatures would correspond to the coolant temperature in the adjacent fixed FAs, for which the maximum allowed heating temperature is 46.6°C.

3. At a coolant temperature around the absorber insert that corresponds to the maximum coolant heating in adjacent fixed FAs (46.6 °C), and with no axial heat exchange, the maximum surface temperature of the absorber insert for fully inserted controls will be 312.7 °C (outer side), and 317.1 °C (inner side) for controls lifted to 154.8 cm, which at a coolant saturation temperature of 327 °C gives a margin to saturation of 14.3 °C and 9.9 °C, respectively. An increase in energy release in six fixed FAs located in adjacent cells with average Kq=1.28 to a value corresponding to Kq=1.47 will cause an increase in energy release in the absorber insert material and an increase in its temperature from 317.1 °C to 320.1 °C, which is also below the saturation temperature (327 °C).

4. The calculations and analysis performed reveal that the absorber insert, specifically its lower part when controls are partially inserted, is the most heat-loaded component of the absorber assembly structure. This position is characterized by high energy release and high coolant temperature at the inlet to the absorber assembly. For the most conservative case considered in this paper, the maximum surface temperature of the absorber insert remains below the coolant saturation temperature. This indicates an absence of both bulk and surface boiling of the coolant when the most energy-loaded component (i.e., the absorber insert) is in operation, confirming that the absorber assembly components will be reliably cooled in the VVER-440 reactor core.

ORCID

Zuyok Valeriy, https://orcid.org/0000-0003-4256-1714; **Mazurok Oleksandr,** https://orcid.org/0000-0002-0517-0493
Zigunov Volodymyr, https://orcid.org/0000-0002-2663-1033; **Lankov Bohdan,** https://orcid.org/0009-0005-1406-4034
Dzhamirzoiev Albert, https://orcid.org/0009-0001-1102-8012; **Makarenko Anton,** https://orcid.org/0000-0002-4713-9726
Tretyakov Mykhaylo, https://orcid.org/0000-0003-0062-8984; **Godun Oleg,** https://orcid.org/0000-0001-9447-7560

REFERENCES

[1] VVER-440 Assemblies. Catalog Description. U 0440.00.00.000 DKO.
[2] TU U 25.3-26444970-022:2022 Absorber assembly. Technical specifications.
[3] ZV-T.41.23.014-23. The Preliminary Report on the safety justification of the implementation of Westinghouse-manufactured VVER-440 fuel assemblies at the RNPP Unit 1. Book 1
[4] V. Zuyok, V. Gann, V. Zigunov, A. Dzhamirzoiev, O. Mazurok, O. Godun, and A. Makarenko, "Cooling of control rods and specification of critical temperatures to justify safe operation," Problems of Atomic Science and Technology, 4(152), 40-48 (2024). https://doi.org/10.46813/2024-152-040
[5] ZV-T.41.23.018-22 The Preliminary Report on the safety justification for the implementation of the Westinghouse-manufactured VVER-440 fuel assemblies at the RNPP Unit 2.
[6] ZV-T.41.23.014-23. Report. The Preliminary Report on the safety justification for the implementation of Westinghouse-manufactured VVER-440 fuel assemblies at the RNPP Unit 1. Book 2. Thermal-hydraulic analysis of mixed cores in stationary modes of normal operation. 2024.
[7] A.G. Korotkikh, and I.V. Shamanin, *Thermal-hydraulic processes in a nuclear reactor and calculation of their main parameters*, (Tomsk Polytechnic University Press, 2008).
[8] Ansys Fluent User's Guide. ANSYS, Inc. Southpointe 2600, Ansys Drive Canonsburg, PA 15317. July 2024 - https://ansyshelp.ansys.com/public/account/secured?returnurl=/Views/Secured/corp/v242/en/flu_ug/flu_ug.html

ВИЗНАЧЕННЯ ТЕМПЕРАТУРИ ЕКСПЛУАТАЦІЇ ЕЛЕМЕНТІВ КОНСТРУКЦІЇ НАДСТАВКИ, ПІДТВЕРДЖЕННЯ НАДІЙНОСТІ ЇХ ОХОЛОДЖЕННЯ В АКТИВНІЙ ЗОНІ ВВЕР-440

Зуйок Валерій[1], Мазурок Олександр[2], Зігунов Володимир[1], Ланьков Богдан[2], Джамірзоєв Альберт[1], Макаренко Антон[3], Трет'яков Михайло[1], Годун Олег[4]

[1]Національний науковий центр «Харківський фізико-технічний інститут», Харків, Україна
[2]ТОВ «ES Group», Київ, Україна
[3]Науково-технічний комплекс «Інститут електрозварювання імені Є.О. Патона», Київ, Україна
[4]Науково-технічний центр, АТ «НАЕК «Енергоатом», Україна, Київ

Розрахунковим шляхом визначено питому потужність енерговиділення в конструкційних матеріалах надставки АРК, яка залежить від потужності робочих касет, що знаходяться у сусідніх комірках. Для найбільш навантаженої частини борного вкладиша, для усередненого по секторам Kq=1,28, енерговиділення становить 17,5 Вт/см^3. Загальна потужність енерговиділення в конструкційних матеріалах надставки, теплоносії та матеріалі штанги проміжної становить 229 кВт для повністю зануреного та 64 кВт для піднятого на 154,8 см ОР СУЗ. Спираючись на загальне енерговиділення в матеріалі вкладишу надставки АРК, кількість та швидкість теплоносія, що його омиває, консервативно визначено розподіл температури поверхні вкладишу по висоті надставки АРК. За температури теплоносія навколо вкладиша, що відповідає максимальному підігріву теплоносія в сусідніх РК (46,6 °С), та відсутності аксіального теплообміну, максимальна температура поверхні вкладиша для повністю зануреного ОР СУЗ становитиме 312,7 °С (зовнішня сторона), а для піднятого на 154,8 см – 317,1 °С (внутрішня сторона), що за температури насичення теплоносія 327 °С дає запас до насичення 14,3 °С та 9,9 °С відповідно. Для найбільш консервативного випадку, розглянутого в даній роботі, максимальна температура поверхні вкладишу нижча, ніж температура насичення теплоносія. Це свідчить про відсутність об'ємного та поверхневого кипіння теплоносія під час експлуатації найбільш енергонавантаженого елемента – вкладиша надставки. Тобто елементи конструкції надставки будуть надійно охолоджуватися в активній зоні ВВЕР-440.

Ключові слова: *ВВЕР-440; касета АРК; надставка; вкладиш; енерговиділення; охолодження*

East European Journal of Physics. 4. 661–666 (2025)
DOI: 10.26565/2312-4334-2025-4-71 ISSN 2312-4334

EXPERIMENT DETAILS IN TIME RESOLUTION MEASUREMENTS OF LYSO SCINTILLATOR

I. Yakymenko[4*], **T. Szczesniak**[3], **O. Sidletskiy**[1,4], **P. Kuznietsov**[1], **A. Syntfeld-Każuch**[3], **M. Grodzicka-Kobylka**[3], **V. Trusova**[2], **V. Rudchyk**[1]

[1]*O.I. Akhiezer Department for Nuclear Physics and High Energy Physics, V.N. Karazin Kharkiv National University, Kharkiv, 61022, Ukraine*

[2]*Department of Medical Physics and Biomedical Nanotechnologies, V.N. Karazin Kharkiv National University, Kharkiv, 61022, Ukraine*

[3]*National Centre for Nuclear Research, A. Soltana 7, Otwock, PL 05-400, Poland*

[4]*Centre of Excellence ENSEMBLE3 Sp. z o.o, Warsaw, 01-919, Poland*

[*]*Corresponding Author e-mail: ivan.yakymenko@ensemble3.eu*

Received August 25, 2025; revised October 15, 2025; accepted November 10, 2025

In this research, we have performed experimental measurements of coincidence time resolution with a custom-built test-bench. In the scope of this work, we discussed technical issues and data validation in the CTR experiment on an example of Saint-Gobain 2 x 2 x 3 mm lutetium-yttrium oxyorthosilicate ($Lu_{1.8}Y_{.2}SiO_5 : Ce$) crystals. The primary objective of the presented experimental works is to develop instruments for the experimental validation of newly created scintillation materials, as a step toward way the 10-ps time-of-flight PET challenge.

Keywords: *coincidence time resolution (CTR); heterostructured scintillating matherials; 511 keV gamma detector; LYSO; PET; fast timing; constant fraction discriminator (CFD); annihilation events*

PACS: 29; 29.40.Mc; 29.40.-n

1. INTRODUCTION

The technical level of the modern, practically implemented PET (positron emission tomography scanners) with assistive CT (X-rays computed tomography) is declared in a range around 180-300 ps, coincidence resolution time (CTR). Reviewing the open data form industry leaders: Siemens Biograph Vision with time of flight performance 214 ps [1], Discovery MI with LightBurst Digital 4-Ring Detector with Timing Resolution 385 ps [2], Philips Vereos with PET timing resolution 310 ps FWHM (full width at the half maximum) [3], NeuEra Series PET/CT from Neusoft Medical with 180 ps grade fully digitzed based on third generation ASIC digital chip [4], Canon PET/CT scanner Cartesion Prime with SURECount digital PET detector 263 ps ToF (time-of-flight) resolution [5], MiFound ScintCare PET/CT 730T with 380 ps resolution, Mediso AnyScan TRIO-TheraMAX SPECT/CT with resolution of 3.3 mm (FWHM) maintained by high-density sensor arrangement (123 PMTs per detector head) [7], United Imaging uMI Panorama GS declared system with 189 ps temporal resolution first full-body PET/CT scanner with time-of-flight (TOF) resolution better than 200 ps [8].

In principle, the shown evolution of the technical design in the PET scanning industry affects to reducing the radiation dose (currently 5–25 mSv, whole body) and a shortening of the procedure time (currently around 15 min), with a patient's mental comfort [9]. To achieve this ambitious goal, it is essential to develop a PET experiment test-benches for the characterization of a new scintillation material [10]. Since the acquisition boards and data processing capabilities are far in the sub-picosecond range, the new scintillation materials should be significantly improved in light yield and decay time.

It might be some boost from speeding up the photo-sensors, self single-photon time resolution (SPTR) and photon detection efficiency [12, 11], improving the photon detection efficiency (PDE, currently 50-63%), and lower operation voltage V_{br} (breakdown voltage). In this direction, the main focus in the PET industry on developing and characterizing new scintillation materials is crucial.

2. MATERIALS AND METHODS

It was prepared two identical scintillators LYSO [14], cut and polished (all sides) in a size of 2 x 2 x 3 mm. Prepared crystals were installed on multi pixel photon counters (MPPC) Broadcom AFBR-S4N44P014M [11] with an Cargille Meltmount media [13]. Additional wrapping with PTFE tape (300 um) used to improve the entire light collection. A simplified experimental diagram is presented on Fig.1

Cite as: I. Yakymenko, T. Szczesniak, O. Sidletskiy, P. Kuznietsov, A. Syntfeld-Każuch, M. Grodzicka-Kobylka, V. Trusova, V. Rudchyk, East Eur. J. Phys. 4, 661 (2025), https://doi.org/10.26565/2312-4334-2025-4-71

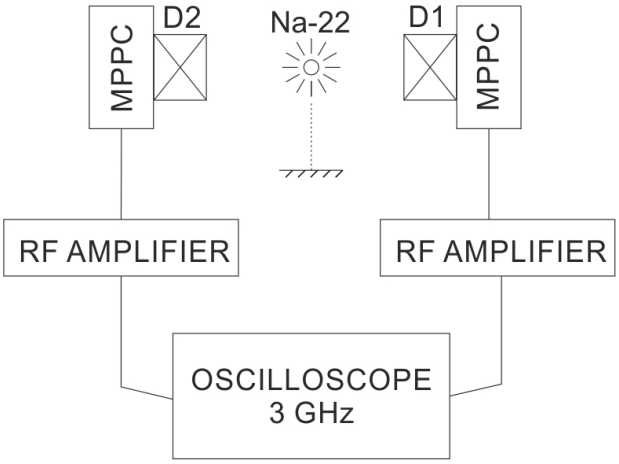

Figure 1. Experimental setup. D1, D2 - LYSO crystals. Readout outputs are connected directly to oscilloscope.

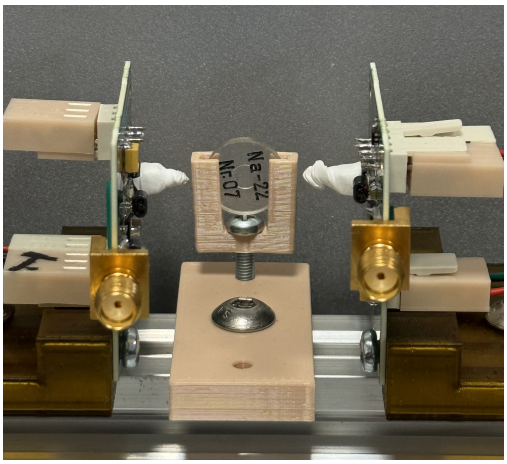

Figure 2. Dark box for CTR measurements with installed PCBs and mounted scintillators LYSO.

All the prepared acquisition parts were placed inside a dark box with external BNC connectors and power outputs. On the Fig.2 presented an experiment geometry, two acquisition boards (left and right channel) installed on the V-rail, Na-22 source mounted on beige holder in the geometrical center. It was used two custom HV boards (C11204-01 with the temperature feedback loop). MPPC boards with the installed crystals were connected directly to the oscilloscope Lecroy WP7300A (3GHz, 20GS/s in 2ch mode). High voltage was 39V for both channels. Typical signals of coincidence events are shown on Fig.3 Custom designed amplifier used for the MPPC readout, Fig.4 presents the schematic diagram of the

Figure 3. Pulses from coincident events from Na-22 isotope. Corresponding left and right channels, 20GS/s, full bandwidth 3GHz. Baseline noise 2mV avg.

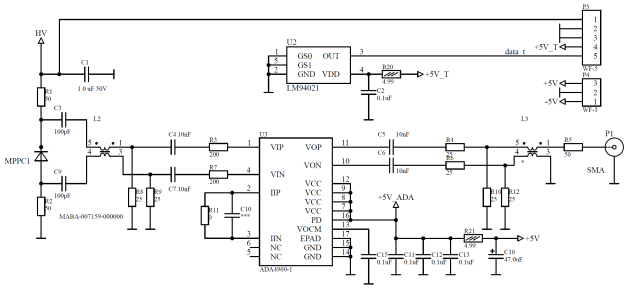

Figure 4. Schematic of the one channel, differential amplifier used with maximum gain 18dB

implemented topology: differential input to single output with balun decoupling. The ADA4960-1 is a high performance, differential amplifier (U3) optimized for RF and IF applications. Temperature feedback loop (U2) LM94021 is a linear, precision analog output temperature sensor.

3. DATA ANALYSIS

To verify the limits of time measurement capabilities the test run was processed. Test signal from LBE-1322 Fast Rise time Variable Frequency Pulser was split and applied to LeCroy Ch2 and Ch3 with coaxial cables (external cable delay added). Specified rise and fall time for used pulse generator was 30 ps Fig.5. Using the LeCroy builtin math functions it was measured CTR value for the test signals: FWHM = 9.5ps for 3870 ”coincidence” events, repeatable signal Fig.7.

In parallel, the raw test pulses were recorded to the host PC for further analysis with our custom code. In the Fig.12 presented results of signal processing with our code it is almost identical to the built-in LeCroy math results and correspond to the generator specification (oscilloscope bandwidth limitation of 3GHz).

4. EXPERIMENTAL RESULTS AND DISCUSSION

LYSO scintillator is a well-known material suitable for equipment verification. CTR results for LYSO but with different experimental equipment were examined by many researcher groups [15, 16, 17]. The measured value is in a

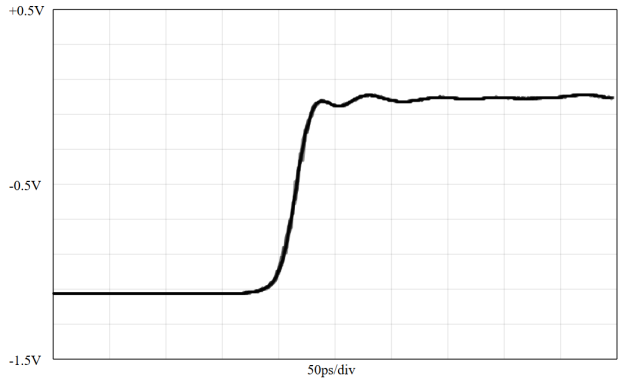

Figure 5. Typical test signal, rise time 30 ps.

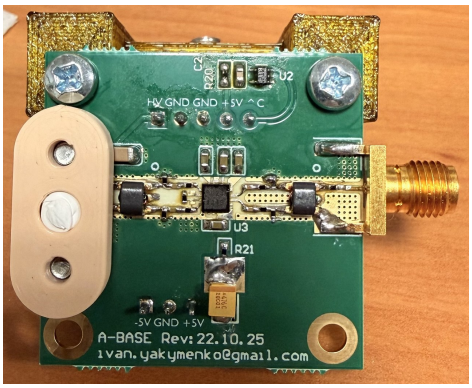

Figure 6. Designed PCB, one channel, MPPC covered with crystal holed (beige plastic), SMA output, U2 temperature sensor, U3 amplifier

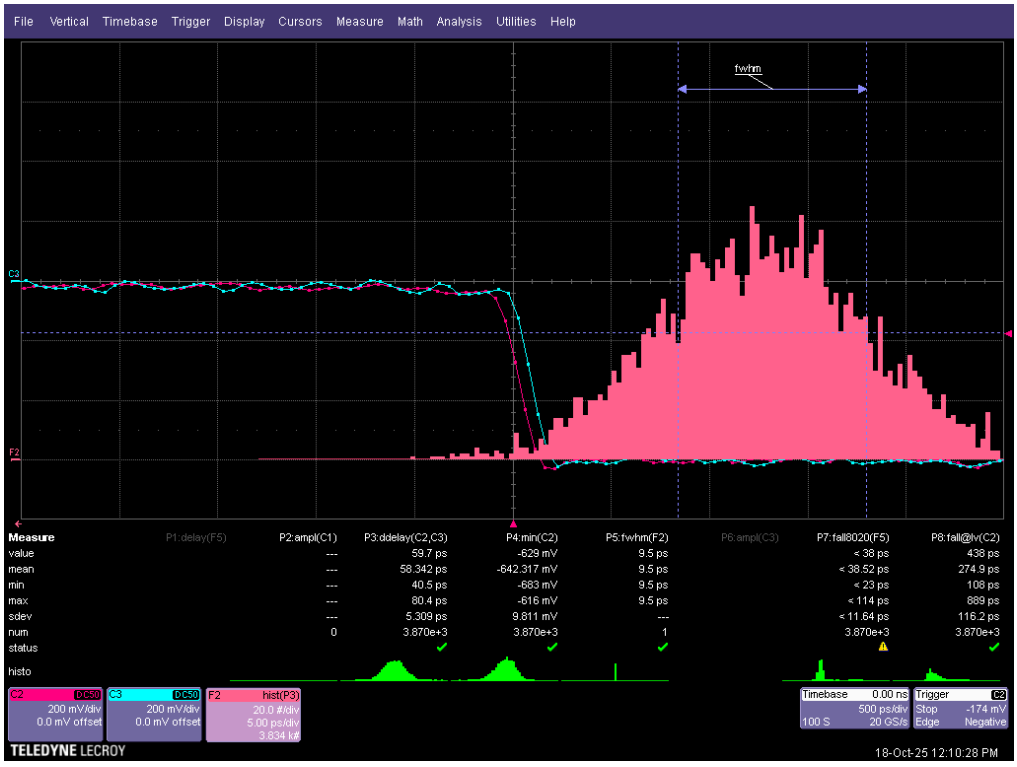

Figure 7. Experiment simulation using the external pico-second generator. Results: mean 58.342ps, sdev 5.309ps. DUT: LeCroy WP7300 3GHz 10-20GSa/s

range from 100 ps to 600 ps and depends on the used acquisition path, crystal quality, etc. On the first stage, we performed an energy cut to limit the ROI to 511 keV. Fig.9 represents the spectrum from both channels and Fig.10 demonstrates the selected photopeak. The prepared dataset was processed with the CFD function to correct the rise time walk, Fig.11, and achieve a zero crossing point. The final distribution Fig.8 represents the experimental CTR of 226 ps. Analyzing the presented result, we should consider several possible factors that may contribute to the resulting CTR: defects in LYSO crystals, possibly non-identical acquisition channels, and errors in the CTR calculation algorithm (such as the baseline calculation for zero-crossing detection). 226 ps result is in line with a lot of reported results. A pair of 511 keV γ-quanta could be recoiled in the surrounding material, entering the scintillator with lower energy. Different input energies may affect the resulting signal deviation. New scintillation material with a "stable" light production mechanism in a specified energy bandwidth may reduce the signal deviation in a coincidence registration experiment. This work aims to gain a deeper understanding of CTR measurement details and address the identified problems in future test-bench modifications.

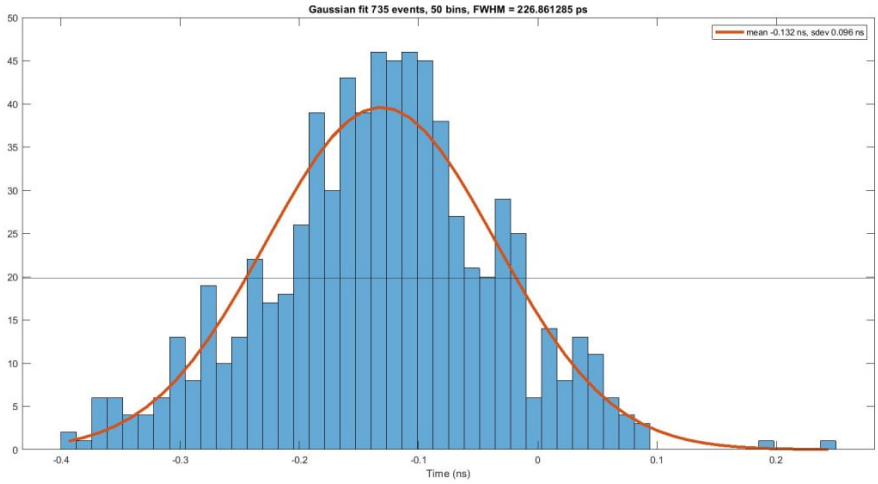

Figure 8. Experimental results for CTR measurements of LYSO scintillators.

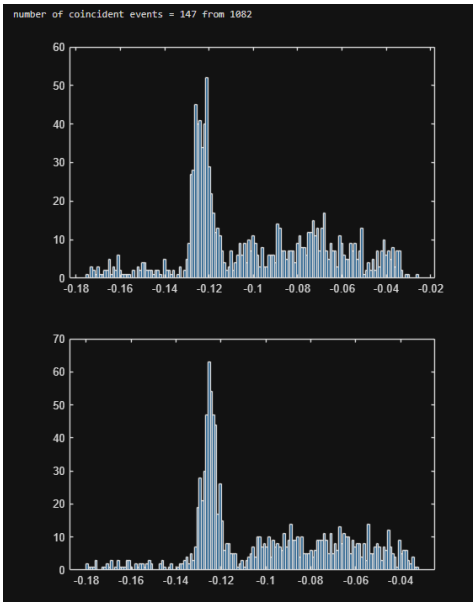

Figure 9. Spectra for LYSO scintillator, two channels, Na-22, input signal polarity negative

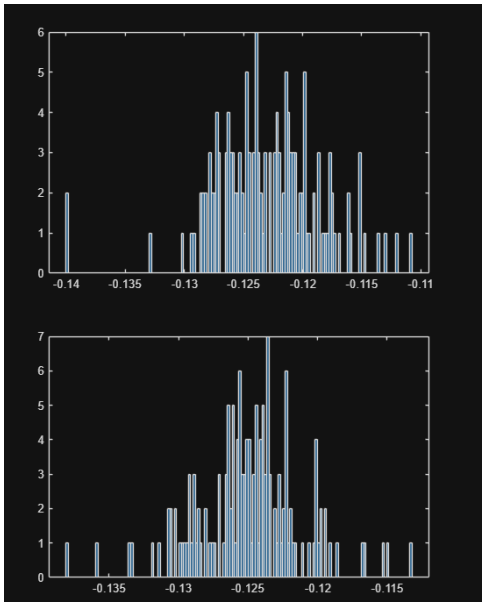

Figure 10. Energy cut applied for LYSO scintillator spectra

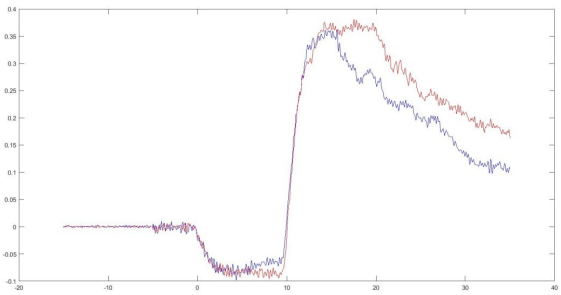

Figure 11. Pulses with applied CFD, zero crossing point

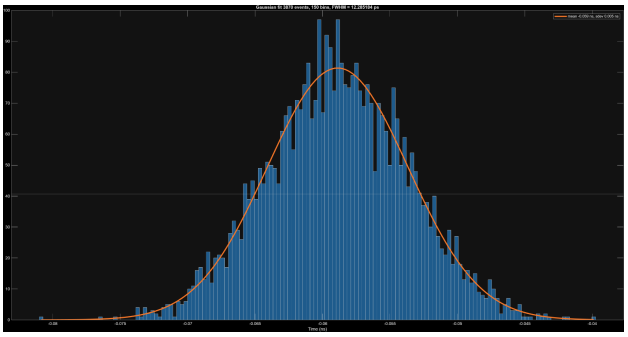

Figure 12. Raw pulses from generator processed with custom code: FWHM = 12.28ps 3870 events, mean 59ps, sdev 5ps.

Declaration of competing interest

The authors declare that they have no known competing financial interests or personal relationships that could have appeared to influence the work reported in this paper.

Acknowledgments

I.Y. and O.S. are grateful for the "ENSEMBLE3-Center of Excellence for nanophononics, advanced materials and novel crystal growth-based technologies" project (GA No. MAB/2020/14) carried out under the International Research Agenda programs of the Foundation for Polish Science that are co-financed by the European Union under the European Regional Development Fund and the European Union Horizon 2020 research and innovation program Teaming for Excellence (GA. No. 857543) and the project of the Minister of Science and Higher Education "Support for the activities of Centers of Excellence established in Poland under the Horizon 2020 program" under contract No. MEiN/2023/DIR/3797for supporting this work. This research was funded by OPUS project "Heterostructures for ultrafast scintillation detectors" under grant DEC-2022/47/B/ST5/02288 from the National Science Centre (NCN) of Poland. This work was supported by the Ministry of Education and Science of Ukraine (№ Д3/174-2025 and 0125U001050). Partly supported by the U.S. National Academy of Sciences (NAS) and the Office of Naval Research (ONRG) through the Science and Technology Center in Ukraine (STCU) under STCU contract number [7120] in the framework of the International Multilateral Partnerships for Resilient Education and Science System in Ukraine (IMPRESS-U). Supported in part by the European Union (ChETEC-INFRA, project no. 101008324). The project has received funding from the European Union's Horizon 2020 research and innovation programme under grant agreement No. 101008324 (ChETEC-INFRA).

ORCID

I. Yakymenko, https://orcid.org/0000-0002-0194-8376; **T. Szczesniak**, https://orcid.org/0000-0002-5301-7071; **O. Sidletskiy**, https://orcid.org/0000-0003-0865-6517; **P. Kuznietsov**, https://orcid.org/0000-0001-8477-1395; **A. Syntfeld-Każuch**, https://orcid.org/0000-0002-8071-7380; **M. Grodzicka-Kobylka**, https://orcid.org/0000-0001-6700-4821; **V. Trusova**, https://orcid.org/0000-0002-7087-071X; **V. Rudchyk**, https://orcid.org/0009-0005-1057-6243

REFERENCES

[1] https://www.siemens-healthineers.com/molecular-imaging/pet-ct/biograph-vision

[2] https://www.gehealthcare.com/products/molecular-imaging/pet-ct/discovery-iq-gen-2

[3] https://www.philips.co.uk/c-dam/b2bhc/gb/resource-catalog/landing/brightontender/vereos-petct-product-specification-lr.pdf

[4] https://www.neusoftmedical.com/en/products-solutions/petct/NeuEra%20Series-PETCT

[5] https://global.medical.canon/products/molecular-imaging/chart_the_right_clinical_course

[6] https://www.minfoundmedical.com/productsshow-34-32-ScintCare-PET-CT-730T.html

[7] https://mediso.com/global/en/product/general-purpose-dual-head-systems/anyscan-duo-spectct

[8] https://eu.united-imaging.com/pl-pl/product-service/products/mi/umi-panorama-gs

[9] P. Lecoq, "On the way to the 10 ps time-of-flight PET challenge. The European Physical Journal Plus," **137**(8), 964 (2022). https://doi.org/10.1140/epjp/s13360-022-03159-8

[10] N.Babayevska, M. Jancelewicz, I. Iatsunskyi, M. Jarek, I. Yakymenko, A. Padmanaban, O.Viahin, *et al.*, "BGO@ZNO heterostructures for ultrafast scintillation detectors," Crystals, **15**(9), 820 (2025). https://doi.org/10.3390/cryst15090820

[11] https://www.broadcom.com/products/optical-sensors/silicon-photomultiplier-sipm/afbr-s4n22p014m

[12] https://www.hamamatsu.com/eu/en/product/optical-sensors/mppc/mppc_mppc-array/S14160-3050HS.html

[13] https://www.cargille.com/about-cargille-mounting-media/

[14] https://luxiumsolutions.com/sites/default/files/2021-08/LYSO-Material-Data-Sheet.pdf

[15] S. Gundacker, G. Borghi, S.R. Cherry, A. Gola, D. Lee, S. Merzi, M. Penna, *et al.*, "On timing-optimized SiPMs for Cherenkov detection to boost low cost time-of-flight PET," Physics in Medicine and Biology, **68**(16), 165016 (2023). https://doi.org/10.1088/1361-6560/ace8ee

[16] K. Doroud, A. Rodriguez, M. C. S. Williams, A. Zichichi and R. Zuyeuski, "Comparative timing measurements of LYSO and LFS to achieve the best time resolution for TOF-PET," 2014 IEEE Nuclear Science Symposium and Medical Imaging Conference (NSS/MIC), Seattle, WA, USA, 2014, pp. 1-4, https://doi.org/10.1109/NSSMIC.2014.7430853

[17] N. Cucarella, J. Barrio, E. Lamprou, C. Valladares, J.M. Benlloch, and A.J. Gonzalez, "Timing evaluation of a PET detector block based on semi-monolithic LYSO crystals," Medical Physics, **48**(12), 8010–8023 (2021b). https://doi.org/10.1002/mp.15318

ОСОБЛИВОСТІ ЕКСПЕРИМЕНТУ З ВИЗНАЧЕННЯ ЧАСОВОГО РОЗДІЛЕННЯ СЦИНТИЛЯТОРА LYSO

І. Якименко[4], **Т. Шезняк**[3], **О. Сідлецький**[1,4], **П. Кузнєцов**[1], **А. Синфілд-Кажух**[3], **М. Гроджицька-Кобилка**[3], **В. Трусова**[2], **В. Рудчик**[1]

[1]*Кафедра фізики ядра та високих енергій імені О.І. Ахієзера,*
Харківський національний університет імені В.Н. Каразіна, Харків, Україна
[2]*Кафедра медичної фізики та біомедичних нанотехнологій,*
Харківський національний університет імені В.Н. Каразіна, Харків, Україна
[3]*Національний Центр Ядерних Досліджень, А. Солтана 7, Отвоцк, ПЛ, 05-400, Республіка Польща*
[4]*Центр Досконалості ENSEMBLE3 Sp. z o.o, Варшава, 01-919, Республіка Польща*

У цьому дослідженні ми провели експериментальні вимірювання роздільної здатності за часом збігу за допомогою спеціально розробленого випробувального стенду. В рамках цієї роботи ми обговорили технічні питання та валідацію даних в експерименті CTR на прикладі кристалів ортосилікату лютецію-ітрію ($LYSO:Ce$) Saint-Gobain розміром 2 x 2 x 3 мм. Основною метою представлених експериментальних робіт є розробка інструментів для експериментальної валідації новостворених сцинтиляційних матеріалів, на шляху до детекторів ПЕТ з часовим 10-пс.

Ключові слова: *роздільна здатность за часом збігу(РЗЧЗ); гетероструктуровані сцинтиляційні матеріали; 511 КеВ детектор гамма випромінювання; LYSO; ПЕТ; швидка обробка сигналів; дискримінатор постійної фракції (ДПФ); анігіляційні події*

East European Journal of Physics. 4. 667-674 (2025)
DOI:10.26565/2312-4334-2025-4-72 ISSN 2312-4334

POLARIZATION EFFECTS IN Si-n-p RADIATION RECEIVERS

Abdumalik G. Gaibov*, Kudbiddin I. Vakhabov, Marguba S. Mirkomilova, Utkir E. Djuraev
Tashkent State Technical University, Uzbekistan
**Corresponding Author email: gaibovabdumalik@gmail.com*
Received July 11, 2025; revised November 20, 2025; accepted November 23, 2025

This paper presents a comprehensive analysis of n-p junction currents and polarization effects in diffusion Si detectors (receivers) for radiation. The mechanisms of polarization induced by charge-carrier capture at localized centers and the formation of space charge in the detector's sensitive region are investigated. The relationship between the presence of "large-scale" traps, which are local clusters of impurity atoms, and the appearance of anomalous spectral characteristics in the form of doublets has been established. It has been experimentally shown that ultrasonic treatment of Si-n-p detectors leads to a significant reduction in polarization effects due to the redistribution of impurity atoms and smoothing of the potential relief in the semiconductor structure. A physical model is proposed to explain the mechanism by which ultrasonic influence affects the electrophysical and spectrometric characteristics of silicon detectors. The results obtained have practical significance for optimizing production technology and improving the operational parameters of Si-n-p radiation detectors.
Keywords: *Silicon detectors; n-p junctions; Polarization effects; Capture centers; Ultrasonic treatment; Spectrometric characteristics; Space charge; Potential relief; Diffusion detectors; Local impurity clusters*
PACS: 29.40.Wk

INTRODUCTION

The study of polarization effects in silicon n-p radiation detectors is one of the key areas of modern semiconductor electronics and detector technology. This issue is particularly relevant in the context of the ever-increasing demands on the accuracy, stability, and reliability of semiconductor detectors used in various fields of science and technology - from fundamental research in nuclear physics to applied problems in medical diagnostics, space technology, and radiation monitoring systems. Polarization effects that occur during the operation of Si-n-p detectors significantly limit their functionality, reduce temporal stability, and distort spectrometric characteristics, which makes the study of the nature of these phenomena and the development of methods for their minimization a critically important task [1].

The physical nature of polarization effects in silicon detectors is complex and is associated with charge-carrier capture and accumulation at localized centers within the semiconductor volume. The formation of a volume charge in the sensitive region of the receiver distorts the internal electric field, which in turn causes a change in the efficiency of collecting charge carriers generated by radiation and, as a consequence, degradation of the spectrometric characteristics of the detector [2]. The so-called "large-scale" traps play a special role in these processes: local clusters of impurity atoms that form inhomogeneities, the potential relief in the semiconductor structure, and contribute to the appearance of anomalous spectral characteristics, in particular, doublet peaks [3,4].

Traditional approaches to solving the polarization problem, based on increasing the purity of the source material and improving detector manufacturing technology, demonstrate some efficiency but do not fully eliminate undesirable effects. In recent years, alternative methods for modifying the properties of semiconductor structures, in particular, ultrasonic treatment, have attracted considerable interest from researchers. Experimental data indicate that the effect of ultrasound on Si-n-p-receivers can lead to a significant reduction in polarization effects due to the redistribution of impurity atoms and smoothing of the potential relief in the semiconductor structure [5,6].

In this paper, we present the results of a comprehensive study of n-p junction currents and polarization effects in diffuse Si radiation detectors. Particular attention is paid to the analysis of the mechanisms of polarization occurrence caused by the processes of charge carrier capture at localized centers and to the study of the effect of ultrasonic treatment on the electrophysical and spectrometric characteristics of silicon detectors. A physical model is proposed that explains the mechanism of ultrasound action on the semiconductor structure and allows one to predict changes in the parameters of Si-n-p detectors resulting from such treatment.

MATERIALS AND METHODS

For the fabrication of Si-SDD (semiconductor diffusion detectors) detectors, we used p-type monocrystalline silicon ingots with a resistivity of $\rho = (10 \div 14) \cdot 10^3 \Omega \cdot$cm and a minority carrier lifetime of $\tau = 450 \div 650$μs, as well as lower-resistance p-Si ingots with $\rho \leq (2 \div 5) \cdot 10^3 \Omega \cdot$cm and $\tau = 800 \div 1000$μs. The oxygen concentration No_2 was no more than 10^{16}cm^{-3} and the dislocation density $N_D \sim 10^4$cm^{-2}. The cylindrical ingots were cut into plates up to 0.5 mm thick. The plates had an area S from 0.25 cm^2 to 2.0 cm^2. The Si plates were ground on both sides with M15 abrasive powder. After appropriate chemical treatment, aluminum (Al) with a thickness of l≈0,45μm ÷ 0,5μm was sprayed onto one side of the

Cite as: A.G. Gaibov, K.I. Vakhabov, M.S. Mirkomilova, U.E. Djuraev, East Eur. J. Phys. 4, 667 (2025), https://doi.org/10.26565/2312-4334-2025-4-72

Si plates; during this technological procedure, the edges of the Si plates were protected with a mask. After that, a solution of phosphorus pentoxide P_2O_5 was applied to the other side of the Si plate, and this coating was dried. The next technological step was the phosphorus diffusion into the Si plates. The samples, located in quartz cassettes, were placed in a diffusion furnace. Phosphorus diffusion was carried out at a temperature of T = 1073K in a stream of inert gas for a time of t = 60 minutes. Then the temperature was slowly lowered to room temperature. Aluminum deposited on the Si wafer is alloyed with it at T≈820K and then, diffusing from the melt into the Si wafer, forms a heavily doped p^+-layer of silicon. After cooling, the Si wafer undergoes a series of chemical-technological operations to clean and remove the phosphosilicate glass on the n^+-layer obtained by phosphorus diffusion. Gold with a density of about 30÷50 μg/cm^2 was sputtered onto the input window of the Si-n-p structure. Electrical contacts to the n- and p-layers were made in the form of pressure or by attaching thin metal wires using conductive silver pastes. The structure was then mounted in a case. Large-area Si-n-p structures can be cut into smaller plates and also used to make SDD detectors for specific purposes. It is also envisaged to protect and seal the semiconductor detector edges with specialized protective coatings [7,8].

The theoretical analysis and experimental studies presented in this work aim to deepen the understanding of the physical processes underlying polarization effects in silicon detectors and to develop effective methods to minimize them. The results obtained are not only fundamentally important for semiconductor physics but also practically valuable for optimizing production processes and enhancing the operational performance of Si-n-p radiation detectors, opening new opportunities for their use in various scientific and technological fields.

It was found that local clusters of impurity atoms with an effective size l>6μm÷30μm are present in Si-n-p radiation detectors, determining the behavior of the signal amplitude in different intervals of electric and temperature fields. It was found that at E>1500 V/cm and T>168 K, the efficiency of collecting nonequilibrium charge carriers increases significantly and the doublets of spectral α-lines and "humps" in the temperature dependences of the signal amplitude disappear. The main physical processes and mechanisms determining the occurrence of the phenomenon of "polarization" of Si-n-p detectors were investigated. This phenomenon is due to the existence of local gold atoms that arise during the technology of manufacturing Si-n-p detectors and act as effective capture centers.

Previously, similar studies were carried out in detail for Si(Li)-p-i-n-detectors [9], where it was shown that the energy resolution is significantly affected by the inhomogeneities of the specific resistance of silicon. Since the process of compensation of inhomogeneity in the manufacture of SDD (semiconductor diffusion detector) - Si-n-p-detectors does not exist, then the effect of self-regulation of the system (sensitive region) does not occur here, as in the case of lithium-ion drift. Therefore, the potential relief of the concentration of the main dopant is preserved. This leads to fluctuations in the carrier lifetime and, in the case of the formation of local clusters of impurity atoms, leads to a strong inhomogeneity of the electric field in a given microvolume of the sensitive region of the radiation receiver [10].

The experiments conducted allowed us to establish critical parameters at which the influence of these inhomogeneities is significantly reduced: at an electric field strength exceeding 1500 V/cm and a temperature above 168 K, a significant increase in the efficiency of collecting nonequilibrium charge carriers is observed. Under these conditions, the characteristic anomalies in the spectral characteristics of the detectors, such as the doublet peaks of gamma lines and specific "humps" in the temperature dependence of the signal amplitude, practically disappear.

The physical interpretation of this effect is that the increased field strength provides sufficient energy for charge carriers to overcome potential barriers created by impurity clusters, while the increased temperature promotes thermal activation of carriers captured at localized centers. In the course of the study, the main physical processes and mechanisms underlying the well-known but poorly understood phenomenon of "polarization" of Si-n-p detectors were thoroughly studied. Our experiments convincingly showed that this phenomenon is directly related to the presence of local clusters of gold atoms in the semiconductor structure, which form during the manufacturing process of Si-n-p detectors.

Gold atoms, when they penetrate the silicon crystal lattice, form deep energy levels in the semiconductor's forbidden zone and act as effective centers for capturing charge carriers. The process of carrier capture and subsequent release at these centers has characteristic time constants that determine the dynamics of polarization effects. Charge accumulation at localized centers distorts the detector's internal electric field, which in turn alters the efficiency of charge collection and, consequently, degrades the spectrometric characteristics of the receiver. These effects are especially pronounced at low temperatures and low field strengths, when the probability of thermal release of captured carriers is minimal, and the drift velocity is insufficient to overcome potential barriers effectively.

For a more detailed study of the causes of polarization effects and low values of the functional characteristics of the radiation receivers, Si- SDD were selected. Then, Si- SDD were divided, in accordance with the selection, into 3 groups (recall that the polarization effect consists in the fact that, being in the operating mode, the radiation receiver gradually worsens its functional characteristics due to the strong capture of charge carriers by traps [6]. After heating to room temperatures, the radiation receiver restores its characteristics).

a) Group 1. In this group, Si- SDD had high functional characteristics and insignificant capture effects were observed in them, the linearity of the λ(1/E) dependence was preserved in a wide range of electric field strengths E;

b) Group 2. Capture effects were observed in the Si- SDD of this group (the field dependences λ(1/E) had a nonlinear form in the region of low values E≤1000 V/cm), which is associated with shallow capture centers. The detectors of this group had average spectrometric characteristics. In this case, the spectral lines had a long decline on the low-energy side, which is due to the presence of a certain number of local clusters of impurity atoms in the sensitive layer.

c) Group 3. The polarization effects of Si- SDD of this group manifested themselves most clearly and quickly for radiation registration times t_p<2 hours. The spectral lines of this Si-SDD group showed doublets (Fig. 1, spectra 1 and 2). As shown above, these Si- SDD have significant sizes of local clusters of impurity atoms, determined by us using the phase-frequency method [7].

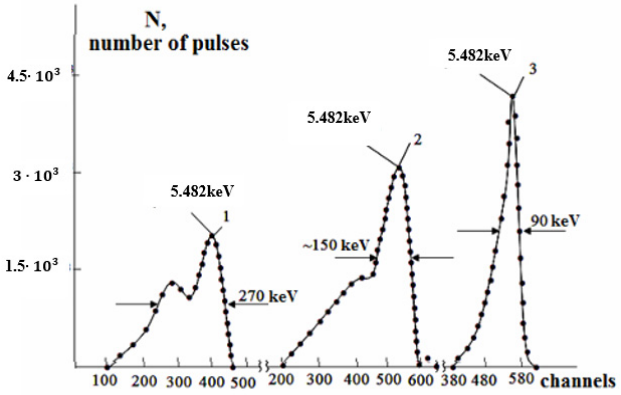

Figure 1. Spectral α-lines of the isotope ^{241}Am from Si-n-p-detector No. 12 d=130 μm, T=300 K. a) spectra 1 and 2 were obtained at E=400 V/cm and E=550 V/cm before irradiating the detector with ultrasound. b) spectra 3 were obtained at E=550 V/cm and T=300 K after irradiating the detector with ultrasound with I*=0.4 W/cm^2, f=15 MHz for 43 min.

It seems interesting to us to analyze the observed phenomena for Si- SDD of the second and third groups, using for this purpose not only the study of the shapes of the spectral lines, the dependences λ(1/E), λ(T), but also using such an important tool as the analysis of the electrophysical characteristics of these groups of radiation receivers.

RESULTS AND DISCUSSION

We conducted an independent study of the causes of the observed phenomena by analyzing the additional behavior of the dependence of the current density on the reverse bias voltage at temperatures T = 300 K based on the Fowler-Nordheim field emission model [11].

This model describes the behavior of this dependence quite well in the presence of inhomogeneities in the region of p-n-junctions [12,13].

The studies were carried out for 15 most prominent representatives of each group. Typical results for two of them are given below. For simplicity and convenience, we introduce the following designations: Si-receivers with a strong capture effect Si- SDD -R and with a weak one - Si- SDD -W, respectively. Figure 2 shows the measured dependences of the current on the reverse bias voltage V_b at a temperature of T = 300 K for two Si-n-p radiation detectors Si- SDD -R and Si- SDD -W, containing, respectively, large-scale and small-scale local accumulations of impurity atoms. It is evident from the graph that a sharp increase in the current (deterioration of the characteristics) of Si- SDD-R and Si- SDD -W begins at a voltage of V_b ≈ 1,5 V (curve 4 in Fig. 2) and V_b ≈ 3.0 V, (curve 1 in Fig. 2), respectively. In addition, it was found that the reverse current of Si- SDD -R is almost independent of temperature in the temperature range T = 77 ÷ 300 K, but at the same time a noticeable temperature dependence of the reverse current was observed in Si- SDD -W.

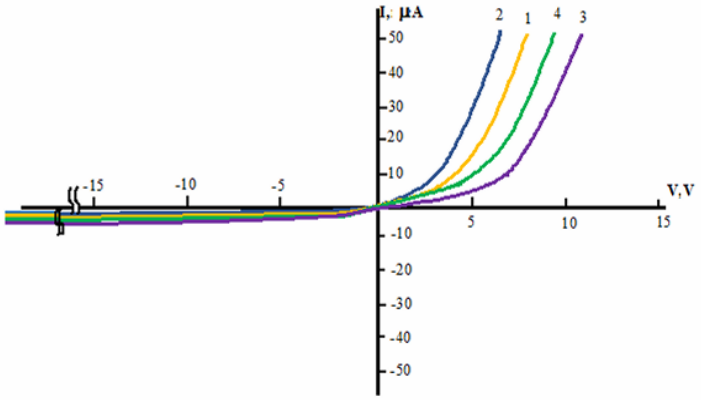

Figure 2. Current dependences on reverse voltage for Si- SDD -W and Si- SDD -R radiation receivers, T=300K
a) Si-PI-W-curve 1 before ultrasound irradiation, curve 2- after irradiation; b) Si- SDD -R-curve 3 before ultrasound irradiation, curve 4- after irradiation. Parameters of ultrasound I*=0.4 W/cm^2, f=15 MHz, t=45 min, T=300K.

The use of the Fowler-Nordheim model allows one to calculate the dependence of the reverse current density on the reverse bias voltage I(V_b) based on an equation of the following form [11]:

$$I(T,E) = \int_{-\infty}^{-\infty} A(T,E^1)D(E,E^1)dE^1 \quad (1)$$

where $A(T,E^1)$ is a function describing the process of charge carrier transfer to the barrier surrounding the local cluster of impurity atoms, $D(E,E^1)$ is the transmission coefficient describing the probability of charge carrier tunneling through the barrier. This is true, since the barrier becomes repulsive after the carriers are captured by the local cluster of impurity atoms, or the barrier is initially repulsive due to the nature of the atoms forming the cluster. Then, as calculations and computations show [11], the functions $A(T,E^1)$ and $D(E,E^1)$ can be written as follows:

$$A(T,E^1) = (4\pi m^* \cdot kT/h^3)\ln[1+\exp(-E^1/kT) \quad (2)$$

$$D(E,E^1) = \exp(-4(2m^*)^{1/2}(q\Phi_B - E^1)^{3/2} \cdot V(y))/2h^* qE, \quad (3)$$

$$\text{where } y = (q^3 \cdot E)^{1/3}/q\Phi_B \quad (4)$$

The following notations are used in the equations: m* - is the effective mass of charge carriers; k is the Boltzmann constant; T is the absolute temperature; h* - is the Planck constant; q is the electron charge; $\Phi_в$- is the barrier height; E - is the electric field strength; E^1 -is the carrier energy (electrons or holes); V(y) -is the Fowler-Nordheim function. In the calculations, it is assumed that V(y) = 1. For $T \rightarrow 0$, equation (1) will have the following form:

$$I(0,E) = q^3E^2\exp(-4(2m^*)^{1/2}(q\Phi_B)^{3/2}/3h^*qE)/16\pi^2h^{*2}q\Phi_B \quad (5)$$

It is natural to assume that near a local cluster of impurity atoms, the electric field is amplified by β times, since the presence of the cluster causes the emergence of a local p-n junction, the electric field of which determines the processes of carrier drift in a given place of the active element (sensitive region) of the radiation receiver [12]. That is, the expression for the electric field in this case will have the following form:

$$E = \beta(2qN_D/\varepsilon_s)^{1/2}(V_i+V_b)^{1/2}. \quad (6)$$

Where N_D is the donor concentration, ε_s - is the semiconductor permittivity, V_i - is the built-in voltage, and V_b - is the reverse bias voltage. The calculation is based on a model of an abrupt p-n junction, assuming that local clusters of impurity atoms are located near the region of the maximum field of the p-n junction of the Si radiation receiver. Given the above, the electric field gain can be calculated as follows.

First, by numerical integration of equation (1), the dependences $I(V_b)$ are calculated for different values of the effective barrier height $\Phi=(m^*/m_0)^{1/3}\Phi_B$ at temperatures T = 77 K and T = 300 K. These dependences for the values $q\Phi$ = 0,31; 0,52 and 0.72 eV at $N_D=1{,}2\cdot10^{15}cm^{-3}$ and $V_i=0$ were calculated, measured and presented as an example for the value $q\Phi$ = 0.31 eV in Figure 3. Then, a comparison of the experimental dependences $I(V_b)$ with the calculated dependences $I(V_b)$ was carried out until they completely coincided and the coefficient β was determined from a simple relationship (7):

$$\beta = [\ V_b \text{ (theoretical value)}/\ V_b \text{ (experimental value)}\ ]^{1/2} \quad (7)$$

It is easy to see that the values of the coefficients β for the Si- SDD -R and Si- SDD -W radiation receivers are $\beta_1 \approx 128$ and $\beta_2 \approx 13$, respectively. The effective barrier height Φ is also determined using the matching procedure described in [11]. It was found that the value of Φ for Si- SDD -R and Si- SDD -W is $\Phi_R \approx 0{,}62$ V and $\Phi w \approx 0.67$ V, respectively.

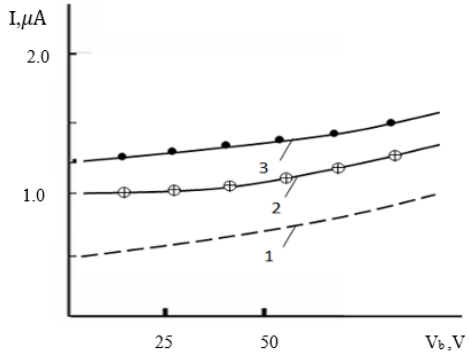

Figure 3. Volt-ampere characteristic of Si-n-p-detector no. 8 before (curve 1 - theory; curve 2 - experiment) and after (curve 3 - experiment) ultrasonic treatment at I* = 0.4 W/cm^2, f = 15 MHz, t = 125 min at T = 300 K.

The peculiarity of the presented model of the current transfer mechanism is that the temperature dependences of the reverse currents of the Si radiation receivers are calculated without introducing any special approximations. For this, as noted earlier, numerical integration of equation (1) is carried out for different values of β, Φ_B and reverse bias voltage V_b.

It was noted above that for Si- SDD -R the reverse current density depends weakly on temperature. This is explained by the fact that the temperature-independent coefficient D in equation (1) significantly exceeds the temperature-dependent function $A(T,E^1)$ due to the very small barrier width. The decrease in the barrier width is caused by a significant increase in the local field near the local cluster of impurity atoms. In the Si- SDD -W radiation receiver, the reverse current density strongly depends on temperature due to the low value of the parameter $\beta_2 \approx 13$, which is associated with smaller values of local clusters of impurity atoms in this type of Si- SDD -W compared to the values of the local cluster of impurity atoms existing in Si- SDD -R radiation receivers. From the analysis of the obtained data, it is possible to determine the values of the intensity of localized (internal) electric fields near local clusters of impurity atoms, the values of which are $E \approx 10^6$-10^7 V/cm, which is approximately two orders of magnitude greater than the maximum electric field in the p-n junction of Si radiation receivers. For example, if we take Si- SDD -R with a p-n junction width of W = 20 μm, at a voltage of V_b = 10 V, the value of $E^{max}_{p\text{-}n}$ = 5000 V/cm, and for a receiver of the Si- SDD -W type, the value of $E^{max}_{p\text{-}n} = 2{,}5 \cdot 10^4$ V/cm.

The figures (2, 3) show changes in the current characteristics after ultrasonic waves with a frequency f = 15 MHz and an intensity I* = 0.4 W/cm^2 pass through Si receivers.

It is clearly seen that the curves of the dependence of the reverse current on the bias voltage V_b shift toward lower current values (Fig. 2, curves 2 and 4; Fig. 3, curve 3). We believe that after the ultrasonic treatment of Si-receivers, a decrease in the value of $q\Phi$ occurred, that is, a decrease in the height of the potential barrier of the p-n-junctions formed by the presence of local clusters of impurity atoms occurred, which is reflected in Table 1.

Table 1. The effect of ultrasonic treatment on the value of $q\Phi$

$q\Phi$, eV, before ultrasonic treatment	$q\Phi$, eV, after ultrasonic treatment
0.31	0.25
0.52	0.45
0.72	0.66

Thus, the decrease in the reverse currents of Si-n-p-receivers after the passage of ultrasonic waves through them is most likely associated with the decay of local clusters in ultrasonic fields.

The spectral lines of Si-receivers measured after ultrasonic processing also underwent significant changes, namely:

a) the energy resolution and shape of the spectral lines improved (the low-energy "tail" decreased, the "humps" smoothed out (Fig. 1, spectrum 3);

b) the amplitude of the signal "A" increased, which is determined by the position of the peak of the spectral line on the analyzer screen. "A" was measured in the channels (Fig. 4). In addition, after ultrasonic processing of Si-receivers, the charge pulses began to have a sharp leading edge and the signal rise time τ decreased by an average of 10÷15%.

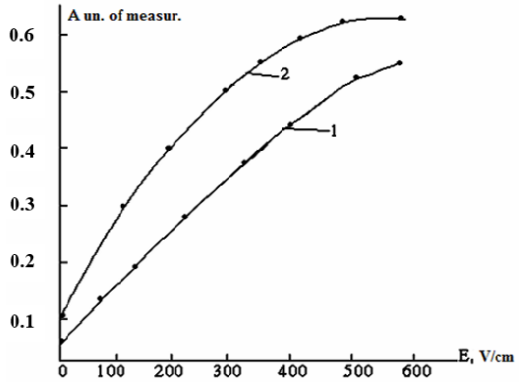

Figure 4. The amplitude of the signal of Si-n-p-detector no. 12 depending on the magnitude of the electric field strength. T = 300 K. Curve 1 - before irradiation with ultrasonic waves. Curve 2 - after irradiation with ultrasonic waves I* = 0.4 W/cm^2, f = 15 MHz, irradiation time t = 40 min

All these experimental data directly indicate that the potential relief in the active region of Si detectors became smoother after ultrasonic wave treatment, i.e. local clusters of impurity atoms began to exert less influence on the processes of carrier capture drift. Polarization effects in Si- SDD-W type detectors disappeared completely, and in Si-SDD -R detectors they significantly decreased. Figure 5 shows the temperature dependences of the signal amplitude for a Si-n-p detector containing local clusters containing Au atoms in the sensitive region, before and after ultrasonic waves passed through it (curves 1 and 2, respectively).

The appearance of a “hump” in the temperature range T = 148 K–168 K is clearly visible, which indicates the presence of a “large-scale” trap. Such “humps” were absent in gold-free silicon detectors. In the same temperature range, the spectral line is a doublet (see Fig. 5, spectrum 1). Therefore, it can be stated that gold, being a rapidly diffusing

impurity in silicon and in the presence of dislocations and stacking faults in it, can be deposited on them, forming Au clusters. At elevated Au concentrations in such microvolumes of the sensitive region of the Si receiver, strong capture of charge carriers begins to occur, reducing the mobility and lifetime of the latter [14]. This leads to a sharp increase in charge losses (a drop in the signal amplitude) and the appearance of a polarization effect. Around the formed clusters of such impurity atoms, there is a zone of mechanical stresses in which strong absorption of ultrasound occurs, leading to the disintegration of clusters and a noticeable improvement in the characteristics of the Si-n-p receiver (Fig. 5, spectrum 2 demonstrates the disappearance of the doublet). Curve 2 shows the disappearance of local clusters after the action of ultrasonic waves on the receiver.

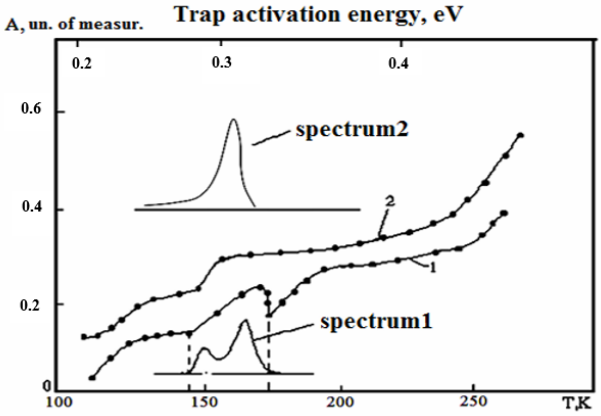

Figure 5. Temperature dependence of the amplitude of the α-spectrum signal from the ^{241}Am isotope of the Si-n-p-detector before (curve 1 and spectrum 1) and after irradiation with ultrasonic waves (curve 2 and spectrum 2) at T=300 K, I* =0.4 W/cm^2, f =15 MHz, t=40 min.

CONCLUSIONS

As a result of the conducted research, the features of diffusion Si-n-p-receivers, their electrophysical and spectrometric characteristics, as well as the influence of various types of trapping centers on them were identified and studied in detail. The obtained results are of significant importance both for the fundamental understanding of physical processes in semiconductor structures and for practical application in the development and optimization of silicon receivers.

It was established that diffusion Si-n-p-receivers are characterized by the presence of two types of defects: single trapping centers and so-called "large-scale" traps of charge carriers. It is the presence of "large-scale" traps that has a decisive effect on the functional characteristics of the studied receivers. These traps are local clusters of impurity atoms that form inhomogeneities in the semiconductor structure and significantly change its electrophysical properties.

The most striking manifestation of the influence of "large-scale" traps is the appearance of anomalous spectral lines in the form of doublets. This effect is observed precisely in those Si-n-p-receivers that contain local clusters of impurity atoms. In addition, pronounced polarization effects are observed in such receivers, indicating a violation of the electric-field homogeneity in the device's sensitive region.

A detailed analysis of the experimental data allowed us to establish the physical mechanism underlying the observed anomalies. The appearance of doublets in the spectral lines and characteristic "humps" on the temperature dependences of the signal amplitude is due to the formation of a space charge in the sensitive region of the receiver. The electric field of this space charge creates a counteraction to the normal drift of charge carriers to the contacts of the receiver, which leads to distortion of the recorded signal and the appearance of the above anomalies.

The conducted studies showed that local impurity accumulations within the Si-n-p receiver's structure actually form built-in n-p microjunctions in its sensitive region. These microjunctions create a complex potential relief, which significantly affects charge-transfer processes and, consequently, the device's spectrometric characteristics. The heterogeneity of the potential relief leads to charge carriers generated in different areas of the receiver moving at various speeds and along different trajectories, resulting in doublets in the spectral lines.

An important practical result of the study was the discovery of an effective method for eliminating the identified anomalies. It was experimentally established that ultrasonic treatment of Si-receivers with pronounced potential relief and polarization effects completely eliminates these undesirable phenomena. Ultrasonic action promotes the redistribution of impurity atoms and a decrease in the concentration of local impurity clusters, which leads to smoothing of the potential relief and normalization of the electrophysical characteristics of the receiver.

The conducted study of polarization effects in Si-n-p radiation detectors allowed to significantly expand the understanding of the physical processes underlying this phenomenon and to develop effective methods for minimizing the negative impact of polarization effects on the characteristics of semiconductor detectors. In the course of the work, the mechanisms of polarization occurrence associated with the capture and accumulation of charge carriers at localized centers in the volume of the semiconductor were studied in detail, which leads to a distortion of the internal electric field and, as a consequence, to the degradation of the spectrometric characteristics of the detectors. Particular attention was

paid to the study of the role of "large-scale" traps - local clusters of impurity atoms that form inhomogeneities of the potential relief in the silicon structure and contribute to the appearance of anomalous spectral characteristics.

Experimental studies of the current characteristics of Si-n-p receivers in various operating modes allowed us to establish a correlation between the parameters of reverse currents and the degree of polarization effect manifestation. It was shown that the temperature dependence of reverse currents is complex and determined by a set of mechanisms for charge-carrier generation, including thermal generation in the space-charge region, tunneling through potential barriers, and generation on surface states. Analysis of the current-voltage characteristics of receivers before and after exposure to ionizing radiation revealed significant changes in the current structure, driven by charge redistribution at localized centers and the formation of additional conductivity channels.

An important result of the work was the discovery and detailed study of the effect of a peak doublet in the energy spectra of Si-n-p-receivers, which manifests itself when registering monoenergetic radiation. It was found that this effect is associated with the inhomogeneity of the electric field within the detector's sensitive volume, caused by the localization of charge on impurity centers. A physical model is proposed that explains the mechanism of doublet peak formation and allows predicting their parameters based on the operating conditions of the receivers. It is experimentally confirmed that the degree of manifestation of the doublet effect depends significantly on the irradiation intensity, temperature and applied bias voltage, which is consistent with theoretical ideas about the nature of this phenomenon.

One of the key achievements of the study was the development and experimental testing of the method of ultrasonic processing of Si-n-p-receivers aimed at minimizing polarization effects. It was shown that the effect of ultrasound of a certain frequency and intensity leads to the redistribution of impurity atoms in the semiconductor structure, smoothing of the potential relief and, as a result, to a significant reduction in polarization effects. The parameters of ultrasonic processing were optimized, providing maximum improvement in the characteristics of the receivers with a minimum risk of mechanical damage to the structure. Long-term tests of ultrasonic-treated detectors confirmed the stability of the achieved improvements and the absence of degradation of the parameters during operation.

A comprehensive study of the influence of various factors on the manifestation of polarization effects allowed us to develop recommendations for optimizing the operating modes of Si-n-p radiation detectors. It was found that increasing the operating temperature of detectors in a certain range helps to reduce the lifetime of charge carriers at localized centers and, accordingly, to reduce the degree of polarization. Optimum values of bias voltage were determined, providing a compromise between the efficiency of charge collection and minimization of polarization effects. Algorithms for compensating for the effect of polarization on the results of spectrometric measurements by introducing appropriate corrections when processing experimental data were proposed.

Theoretical analysis of the experimental results allowed us to develop a refined physical model of polarization effects in Si-n-p detectors, taking into account the spatial distribution of impurity centers, their energy spectrum and the kinetics of the processes of capture and release of charge carriers. The model successfully describes the observed experimental patterns and allows us to predict the behavior of detectors under various operating conditions. Based on this model, a software package for numerical simulation of processes in Si-n-p detectors was developed, which can be used to optimize the design and manufacturing technology of semiconductor detectors.

The successful implementation of the developed methods and recommendations in the production of Si-n-p radiation detectors confirms the practical significance of the obtained results. Detectors manufactured with the proposed modifications to the technological process and subjected to ultrasonic treatment demonstrate significantly improved characteristics: increased temporal stability, improved energy resolution, and reduced sensitivity to changes in operating conditions. This opens new opportunities for the application of Si-n-p receivers across various fields of science and technology, including nuclear physics, space research, medical diagnostics, and radiation monitoring systems.

Thus, the conducted research makes a significant contribution to the development of the physics of semiconductor detectors and the technology of their production. The obtained results not only expand fundamental understanding of processes in semiconductor structures but also have direct practical significance for improving the characteristics of Si-n-p radiation detectors. Further research in this direction can focus on a more detailed study of the microscopic mechanisms underlying ultrasound's effect on semiconductor structure, the development of new methods to modify the properties of silicon detectors, and the expansion of their application scope.

ORCID

Abdumalik G. Gaibov, https://orcid.org/0000-0002-8990-7957

REFERENCES

[1] L. Pan, I.R. Pandey, Z. Liu, John A. Peters, D.Y. Chung, C. Hansson; B.W. Wessels, *et al.* "Study of perovskite $CsPbBr_3$ detector polarization and its mitigation with ultrahigh X-ray flux," J. Appl. Phys. **133**(19), 194502 (2023). https://doi.org/10.1063/5.0151902

[2] P.G. Kasherininov, "Optical recording media based on semiconductor M(TI)S structures with a tunnel-thin dielectric (TI)" Doc. dissertations. St. Petersburg Physicotechnical Institute of the Russian Academy of Sciences, 2011.

[3] K. Ridzonova, E. Belas, R. Grill, J. Pekárek, and P. Praus, "Space-Charge-Limited Photocurrents and Transient Currents in CdZnTe Radiation Detectors," Phys. Rev. Applied, **13**(6), 064054 (2020). https://doi.org/10.1103/PhysRevApplied.13.064054

[4] V.K. Eremin, and E.M. Verbitskaya, "Silicon detectors of relativistic particles in modern high-energy physics," in: *"SILICON-2012"*, (St. Petersburg, 2012). pp. 50.

[5] S.S. Ostapenko**,** N.E. Korsunskaya, and M.K. Sheinkman, "Ultrasound Stimulated Defect Reactions in Semiconductors," Solid State Phenomena*,* **85–86**, 317–336 (2001). https://doi.org/10.4028/www.scientific.net/SSP.85-86.317
[6] K.I. Vakhobov, "Acoustostimulated diffusion of gold atoms in silic," JournalNX — A Multidisciplinary Peer Reviewed Journal*,* **8**(11), 375–380 (2022). https://doi.org/10.17605/OSF.IO/H69YD
[7] A. Saymbetov, R. Muminov, J. Zhang, *et al*. "Equivalent circuit of a silicon–lithium p–i–n nuclear radiation detector," Scientific Reports, **13**, 12525 (2023). https://doi.org/10.1038/s41598-023-39710-5
[8] S.A. Radzhapov, B.S. Radzhapov, and R.Kh. Rakhimov, "Features of the technology for manufacturing silicon surface-barrier detectors with a large sensitive working area for measuring the activity of natural isotopes," Computational Nanotechnology, **1**, 151-154 (2018).
[9] B.N. Zaveryukhin, E.B. Zaveryukhina, R.A. Muminov, *et al*. "Drift of Li atoms in p-Si stimulated by USW," in: *Conf. "Fundamental and applied issues of physics"*, dedicated. 60 years old. Academy of Sciences and Physicotechnical Institute of the Academy of Sciences of the Republic of Uzbekistan, November 27-28, (Tashkent, 2003).
[10] J. Zhang, and N. Japashov, "Investigation and optimisation of a lithium-drift silicon detector using Si–Li structure and bidirectional diffusion and drift techniques," Reviews in Inorganic Chemistry, **44**(1), 65–72 (2024). https://doi.org/10.1515/revic-2023-0034
[11] H. Kim, C.S. Park, and S.J. Yu, "Generalized Electron Emission Theory for One-Dimensional Conducting Materials," Applied Sciences (MDPI), 14(7), (2024). https://doi.org/10.3390/app14072993
[12] M. Kozai, H. Fuke, *et al.* "Statistical investigation of the large-area Si(Li) detectors mass-produced for the GAPS experiment," arXiv:2111.06100 [physics.ins-det (2021). https://doi.org/10.48550/arXiv.2111.06100
[13] R.M. Zedric, C.M. Marianno, S.S. Chirayath, Y. Diawara, and I. Darby, "The Effect of Radiation Damage on the Charge Collection Efficiency of Silicon Avalanche Photodiodes," IEEE Transactions on Nuclear Science, **69**(2), 152–159 (2022). https://doi.org/10.1109/TNS.2021.3137476
[14] A.G. Gaibov, K.I. Vakhobov, B.V. Ibragimova, U.E. Zhuraev, and D.T. Rasulova, "Influence of ultrasonic waves on current-voltage characteristics and polarization effects of si-n-p radiation receivers." Materials Science Forum, **1049**, 317-324 (2022). https://doi.org/10.4028/www.scientific.net/MSF.1049.317

ЕФЕКТИ ПОЛЯРИЗАЦІЇ В ПРИЙМАЧАХ Si-n-p ВИПРОМІНЮВАННЯ

Абдумалік Г. Гаїбов, Кудбіддін І. Вахабов, Маргуба С. Міркомілова, Уткір Е. Джураєв
Ташкентський державний технічний університет, Узбекистан

У цій статті представлено комплексний аналіз струмів n-p переходу та ефектів поляризації в дифузійних Si-детекторах (приймачах) випромінювання. Досліджено механізми поляризації, індукованої захопленням носіїв заряду в локалізованих центрах та формуванням об'ємного заряду в чутливій області детектора. Встановлено зв'язок між наявністю "великомасштабних" пасток, які є локальними кластерами домішкових атомів, та появою аномальних спектральних характеристик у вигляді дублетів. Експериментально показано, що ультразвукова обробка Si-n-p детекторів призводить до значного зменшення ефектів поляризації завдяки перерозподілу домішкових атомів та згладженню потенційного рельєфу в напівпровідниковій структурі. Запропоновано фізичну модель для пояснення механізму, за допомогою якого ультразвуковий вплив впливає на електрофізичні та спектрометричні характеристики кремнієвих детекторів. Отримані результати мають практичне значення для оптимізації технології виробництва та покращення робочих параметрів Si n-p детекторів випромінювання.

Ключові слова: *кремнієві детектори; n-p переходи; ефекти поляризації; центри захоплення; ультразвукова обробка; спектрометричні характеристики; просторовий заряд; потенціальний рельєф; дифузійні детектори; локальні домішкові кластери*

East European Journal of Physics. 4. 675-681 (2025)
DOI:10.26565/2312-4334-2025-4-73 ISSN 2312-4334

SIMULATION OF TUNNEL DIODE I–V CHARACTERISTICS WITH PHOTOCURRENT AND PHONON-ASSISTED PROCESSES

Mukhammadjon G. Dadamirzaev[1], Munirakhon K. Uktamova[1,2], Shirin Rakhmanova[3], Gayrat A. Ibadullayev[4]
[1]*Namangan State Technical University,160103 Namangan, Uzbekistan*
[2]*University of Business and Science, Uzbekistan*
[3]*Urgench State University, Uzbekistan*
[4]*Urgench State Pedagogical Institute, Uzbekistan*
**Corresponding author: umk9391@gmail.com*
Received September 2, 2025; accepted November 23, 2025

In this paper, a unified current model for tunnel diodes has been developed. The model incorporates not only the tunneling, diffusion, and excess currents but also the photocurrent generated under illumination. In addition, phonon-assisted tunneling processes, namely phonon absorption and phonon emission, arising from electron–phonon interactions, have been included. The calculated current–voltage characteristics indicate that the total current shifts downward under illumination. It is demonstrated that the photocurrent increases proportionally with the optical intensity and wavelength. In the case of phonon absorption, electrons gain additional energy, the tunneling channel broadens, and the peak current increases by approximately 15–20%. Conversely, during phonon emission, part of the electron energy is lost, reducing the tunneling probability, and the peak current decreases by about 10–12%. The obtained results indicate that accounting for phonon and photon processes significantly extends the application potential of tunnel diodes in optoelectronic and photodetector devices. The proposed model provides a theoretical basis for the development of tunnel diodes as high-frequency, light-sensitive, and energy-efficient devices.
Keywords. *Tunnel diode; Photocurrent; Diffusion current; Excess current; Semiconductor modeling; Phonon-assisted tunneling; Optoelectronic devices*
PACS: 42.66

INTRODUCTION

Researchers have developed a wide range of models to describe the current–voltage (I–V) characteristics of tunnel diodes. Regardless of their diversity, a reliable tunneling model must accurately reproduce three essential features: (i) the peak current regime, where tunneling dominates; (ii) the valley current regime, where the tunneling probability decreases, and drift mechanisms begin to prevail; and (iii) the diode regime, where carrier drift and diffusion dominate [1]. In the classical Tsu–Esaki model, several of these phenomena are captured, but excess and diffusion currents are not fully incorporated. Later, O. Kan demonstrated that the tunneling current strongly depends on the density of states and on the Wenzel–Kramers–Brillouin (WKB) approximation applied to parabolic and non-parabolic electron transitions [2]. The model proposed by Karlovsky, based on the Franz–Keldysh effect, offered a more straightforward approach for evaluating the current in tunnel diodes but considered only the band bending in the semiconductor's *n*-region [3,4]. Yajima and Esaki discussed the concept of excess current, while Chynoweth [5] proposed a more complete description. Subsequent studies extended these foundations by including additional mechanisms such as generation–recombination processes, illumination-induced photocurrents, and phonon-assisted tunneling (PAT). Under classical tunneling conditions, electron energies must coincide exactly. However, as Tien and Gordon established, phonon interactions significantly modify tunneling, especially in the presence of external electromagnetic fields. Phonon absorption and emission create *satellite tunneling channels*, enriching the I–V characteristics and producing complex behavior under illumination [6]. Recent investigations have further advanced the theoretical and experimental understanding of these effects. Liu et al. proposed an analytical framework that refines tunneling current density calculations by incorporating nonparabolic band structures [9]. Février et al. demonstrated the influence of photon-assisted transport and coherent tunneling in nanoscale junctions, linking optical excitation with negative differential resistance phenomena [10]. Mendez et al. provided detailed *ab initio* simulations of phonon coupling under high-field and quantum confinement conditions, emphasizing the interplay between lattice vibrations and electron tunneling [11]. Similarly, Sugiura et al. investigated tunnel mechanisms in semiconductor devices designed for renewable energy applications, revealing how energy-band engineering can enhance tunneling efficiency [12]. Additionally, Moulin revisited the I–V characteristics of *p–n* tunnel junctions and proposed a revised semi-empirical model that aligns well with experimental data for homojunctions [13]. These studies collectively highlight the growing attention to photon- and phonon-assisted processes and their critical roles in shaping the nonlinear response of tunnel junctions. Nevertheless, existing models still treat these mechanisms separately and rarely unify all contributions—including direct tunneling, diffusion, excess, phonon-assisted, and photo-induced currents—within a single analytical framework.

Cite as: M.G. Dadamirzaev, M.K. Uktamova, S. Rakhmanova, G.A. Ibadullayev, East Eur. J. Phys. 4, 675 (2025), https://doi.org/10.26565/2312-4334-2025-4-73

Therefore, in this work, we present a comprehensive current model for tunnel diodes that explicitly includes photocurrent generation and phonon-assisted tunneling, providing a unified description of the total current in illuminated and non-illuminated conditions. This approach aims to bridge the gap between earlier theoretical models and recent experimental findings, contributing to a deeper understanding of quantum transport in nonlinear semiconductor structures.

METHODS

The hole and electron energies at the p–n junction in tunnel diodes $f_1(\varepsilon_1)$ and $f_2(\varepsilon_2)$ are the Fermi–Dirac distribution functions for holes and electrons in the p and n-regions of the semiconductor, and their difference takes the form: $f_1(\varepsilon_1) - f_2(\varepsilon_2) = \frac{1}{exp\left(\frac{\varepsilon-\mu_n}{kT}\right)+1} - \frac{1}{exp\left(\frac{\varepsilon-\mu_n+qV}{kT}\right)+1}$. The Wentzel–Kramers–Brillouin (WKB) approximation provides an analytical framework for describing quantum tunneling through a slowly varying potential barrier. In this method, the stationary one-dimensional Schrödinger equation for an electron of energy E moving in a potential $V(x)$ is written as

$$\frac{d^2\psi(x)}{dx^2} + \frac{2m}{\hbar^2}[E - V(x)]\psi(x) = 0 \tag{1}$$

Introducing the local wave number $k(x) = \sqrt{\frac{2m}{\hbar^2}|E - V(x)|}$ the WKB solution can be expanded as an $\hbar^2$ -series of the exponential form

$$\psi(x) = exp\left[\frac{i}{\hbar}S(x)\right] \; S(x) = S_0(x) + \frac{\hbar}{i}S_1(x) + \left(\frac{\hbar}{i}\right)^2 S_2(x) + \cdots. \tag{2}$$

Substituting this into the Schrödinger equation and collecting terms of equal powers of $\hbar^2 -$ gives recursive equations for the coefficients $S_n(x)$. The standard applicability condition of the WKB approximation requires that each subsequent term in this expansion be much smaller than the preceding one, i.e.,

$$\left|\frac{\hbar S_{n+1}(x)}{S_n(x)}\right| \ll 1. \tag{3}$$

For practical tunneling problems, this condition is equivalent to the requirement that the potential $V(x)$ varies slowly on the scale of the electron wavelength, namely,

$$\left|\frac{\hbar k'(x)}{k^2(x)}\right| \ll 1. \tag{4}$$

Equation (1) ensures that the semiclassical wave function varies smoothly, and quantum interference between adjacent turning points is negligible. Under this condition, the first-order WKB term dominates, and higher-order corrections can safely be ignored.

In tunnel diodes, the potential barrier is formed by the built-in electric field $F(x)$ arising from heavy doping. The potential variation near the depletion region can be expressed as

$$V(x) = qF(x)x + V_0 \tag{5}$$

so that

$$k(x) = \sqrt{\frac{2m^*}{\hbar^2}[E - qF(x)x - V_0]}. \tag{6}$$

For typical heavily doped GaN or GaAs tunnel diodes, the field gradient $F'(x)$ is moderate and the characteristic spatial scale $L = |V(x)/(dV/dx)|$ exceeds the de Broglie wavelength $\lambda = 2\pi/k(x)$ satisfying Eq. (1) Therefore, the WKB approximation remains valid for calculating tunneling probabilities in such devices. This justification is consistent with the standard analysis presented by Karnakov and Krainov [14] and more recent works extending WKB theory to Dirac-like materials and two-dimensional tunneling systems [15,16].

Consequently, in the modeling of tunnel diodes presented in this paper, the first-order WKB term provides an accurate estimation of the transmission coefficient:

$$T(E) \approx \exp\left[-2\int_{x_1}^{x_2} k(x)dx\right] \tag{7}$$

Where $k(x) = \sqrt{\frac{2m^*}{\hbar^2}[V(x) - E]}$ is the imaginary wave number in the classically forbidden region. This formulation ensures that the WKB approximation is applied within its validity domain and that higher-order $\hbar^2$-corrections contribute negligibly to the total tunneling current. For the transmission coefficient, the following [14-16]:

$$P = \exp\left(-\frac{\alpha E_t^{\frac{3}{2}}}{F}\right) \tag{8}$$

For the transfer (tunneling) coefficient, we use the following formula, where $F-$ is the internal electric field strength, $E_t = E_g - qV + \mu_n + \mu_p$; $\alpha = \theta \frac{4\sqrt{2m_e}}{3Fqh}$; $\theta \approx 1$ (θ - by employing these relations with the constant parameter of the Chynoweth model), we arrive at the following expression[1]. We assume that the internal electric field $F-$is constant in the range $F \approx 10^3 - 10^4 \frac{V}{m}$.

$$I_T = APT \left(\int_0^{\mu_n + \mu_p - qV} \left(\left(\frac{1}{\exp\left(\frac{\varepsilon - \mu_n}{kT} \right) + 1} - \frac{1}{\exp\left(\frac{\varepsilon - \mu_n + qV}{kT} \right) + 1} \right) \sqrt{\varepsilon \left(qV_K - E_g - qV - \varepsilon \right)} \right) \right) d\varepsilon \tag{9}$$

Now, using this expression and taking into account the diffusion current, we obtain the following expression for the I–V characteristic of the tunnel diode:

$$I = APT \left(\int_0^{\mu_n + \mu_p - qV} \left(\left(\frac{1}{\exp\left(\frac{\varepsilon - \mu_n}{kT} \right) + 1} - \frac{1}{\exp\left(\frac{\varepsilon - \mu_n + qV}{kT} \right) + 1} \right) \sqrt{\varepsilon \left(qV_K - E_g - qV - \varepsilon \right)} \right) \right) d\varepsilon + I_0 \left(\exp\left(\frac{-qV}{kT} \right) - 1 \right) \tag{10}$$

Based on the model presented by Chynoweth, the excess current in a tunnel diode can be expressed as follows [17,18]:

$$I_{CH} = D \cdot P = \int \frac{1}{exp\left(\frac{\varepsilon - \mu_n}{kT}\right) + 1} - \frac{1}{exp\left(\frac{\varepsilon - \mu_n + qV}{kT}\right) + 1} \left(1 - \exp\left(-\frac{E_1}{E_g - qV + \mu_n + \mu_p}\right)\right)\left(1 - \exp\left(-\frac{E_2}{E_g - qV + \mu_n + \mu_p}\right)\right) d\varepsilon \cdot \exp\left(-\frac{\theta \frac{4\sqrt{2m_e}}{3qh} (E_g - qV + \mu_n + \mu_p)^{\frac{3}{2}}}{F}\right) \tag{11}$$

Here, for the density of states D, we used the model proposed by Kan. Tunnel diodes are required to withstand large currents and, in some cases, high temperatures. To achieve this, it is advisable to employ either heavy doping of the semiconductor material or heterojunctions. As a result of these methods, numerous discrete energy levels are formed within the forbidden band. To simplify the calculations, we assumed the density of states to be unity. In this case, electrons from the conduction band of the n-type semiconductor can tunnel into the forbidden band of the p-type semiconductor, where they may first occupy the impurity energy levels, then emit a phonon and transition to other impurity states, and finally fall into the valence band. Alternatively, electrons may first emit a phonon, then be captured by impurity levels before transitioning into the valence band of the p-type semiconductor. This process leads to an increase in the minimum current observed in the I–V characteristics of tunnel diodes, i.e., the excess current. When light is absorbed in a semiconductor diode, electron–hole pairs (EHPs) are generated. Their flow contributes to the external circuit, producing a photocurrent denoted as $-I_{ph}$. When the diode is illuminated, each absorbed photon generates one electron–hole pair. If these carriers reach the contacts before recombining, they contribute to the current [19-21]. The incident light intensity on the diode is denoted by P_{in}. The energy of each photon is given by:

$$E = \frac{hc}{\lambda} \tag{12}$$

Photocurrent in a tunnel diode arises due to photon absorption and is proportional to the incident optical power. By relating the photon flux to the optical power and introducing the external quantum efficiency η, the photocurrent expression is derived as:

$$I_{ph} = q\eta \frac{P_{in}\lambda}{hc} \tag{13}$$

η – external quantum efficiency ($0 \le \eta \le 1$), that is, how many photons are converted into carriers, h — Planck's constant, c— the speed of light.

Phonon absorption ($E_g - \hbar\omega$):

An electron absorbs phonon energy and thereby gains additional energy. As a result, even an electron that would typically be unable to overcome the barrier may participate in the tunneling process. This opens a new tunneling channel,

increasing the total current. In the band diagram, this corresponds to an electron originating from a lower-energy level, which, with the assistance of a phonon, is elevated to a higher state and then undergoes tunneling.

RESULTS AND DISCUSSION

The expression for the total current of the tunnel diode, accounting for the photocurrent, is given by the following formula:

$$I = I_{\mathrm{T}} + I_{\mathrm{X}} + I_{dif} + I_{ph} \tag{14}$$

Phonon emission ($E_g + \hbar\omega$):

During tunneling, an electron emits a phonon, thereby losing part of its energy. As a result, the initial energy required for tunneling becomes higher. In this case, the number of electrons capable of tunneling decreases, and consequently, the total current is reduced. In the band diagram, an electron originating from a higher-energy state undergoes tunneling and, by emitting a phonon, transitions to a lower energy level [11-13,20-23]. If we supplement expression (7) given above with the corresponding additional terms, we obtain

$$I = APT\left(\int_0^{\mu_n+\mu_p-qV}\left(\left(\frac{1}{\exp\left(\frac{\varepsilon-\mu_n}{kT}\right)+1}-\frac{1}{\exp\left(\frac{\varepsilon-\mu_n+qV}{kT}\right)+1}\right)\sqrt{\varepsilon\left(qV_K-E_g-qV-\varepsilon\right)}\right)d\varepsilon + I_0\left(\exp\left(\frac{-qV}{kT}\right)-1\right)\right.$$
$$+\int \frac{1}{exp\left(\frac{\varepsilon-\mu_n}{kT}\right)+1}-\frac{1}{exp\left(\frac{\varepsilon-\mu_n+qV}{kT}\right)+1}\left(1-\exp\left(-\frac{E_1}{E_g-qV+\mu_n+\mu_p}\right)\right)(1--\exp\left(-\frac{E_2}{E_g-qV+\mu_n+\mu_p}\right))d\varepsilon\cdot$$
$$\exp\left(-\frac{\theta\frac{4\sqrt{2m_e}}{3qh}(E_g-qV+\mu_n+\mu_p)^{\frac{3}{2}}}{F}\right)+q\eta\frac{P_{in}\lambda}{hc} \tag{15}$$

The transmission coefficient of the tunnel diode when a phonon is absorbed $P = \exp\left(-\frac{\alpha(E_t+\hbar\omega)^{\frac{3}{2}}}{F}\right)$; when emitting a phonon, it takes the form $P = \exp\left(-\frac{\alpha(E_t-\hbar\omega)^{\frac{3}{2}}}{F}\right)$.

Equation (15) represents the generalized current model of the tunnel diode, incorporating photocurrent contributions [16]. The total current of the tunnel diode is highly sensitive to incident optical flux and wavelength, with the photocurrent leading to a noticeable shift in the current–voltage characteristics. As the incident optical power (Pin) increases, the photocurrent rises proportionally, directly shaping the diode's I–V curve. Figure 1 presents the calculated I–V characteristics for different illumination intensities (Pin) and wavelengths (λ). The plots illustrate the effects of incident optical power (P_{in} = 100-500 W/m²) and illumination wavelength (λ = 650 -850 nm) on the total current, including cases where both tunneling and photocurrent contributions are included. The results indicate that an increase in optical flux enhances the overall current, while shorter wavelengths (corresponding to higher photon energies) improve the efficiency of the tunneling process.

The calculated three-dimensional I–V–P_{in} characteristic of the tunnel diode is shown in Figure 2. The plots demonstrate that increasing optical intensity increases the photocurrent, shifting the total current surface.

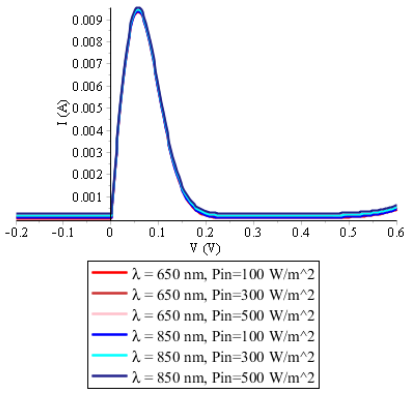

Figure 1. Calculated current–voltage characteristics of the tunnel diode under different optical excitation conditions.

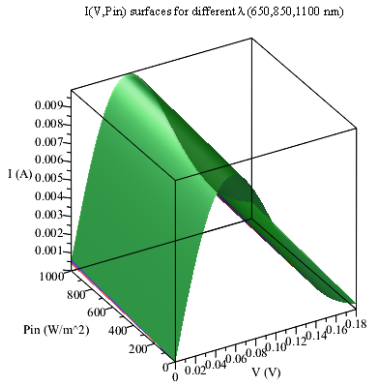

Figure 2. Three-dimensional current–voltage–optical power (I-V-P_{in}) surface characteristics of the tunnel diode for different wavelengths (λ = 650, 850, 1100 nm).

The graph represents the sum of tunneling, diffusion, and photocurrent contributions for different wavelengths. As light intensity increases, the photocurrent rises, shifting the overall characteristic vertically. These findings confirm the strong optical sensitivity of tunnel diodes and highlight their potential for photodetection and advanced optoelectronic devices.

The current–voltage (I–V) characteristics of the p–n tunnel diode were measured both in complete darkness and under controlled optical illumination. In the absence of light, the dark current I_{dark} is dominated by direct band-to-band tunneling, enabled by the extremely high doping levels and the narrow depletion region characteristic of tunnel diodes.

Under illumination, the total current increases to

$$I_{\text{light}} = I_{\text{dark}} + I_{\text{ph}}$$

where $I_{\text{ph}}$is the optically generated photocurrent. At low and moderate biases, the illuminated I–V curve exhibits an approximately constant upward shift relative to the dark curve, corresponding to the bias-independent I_{ph}. At higher electric fields, especially near the resonant tunneling region, photocurrent alters both the peak and valley currents because the internal electric field distribution is modified. This effect is enhanced by field-dependent absorption due to the Franz-Keldysh effect, which changes the tunneling probability and therefore slightly modifies the Peak-to-Valley Ratio (PVR).

The photocurrent under monochromatic illumination of power P_{opt} −and photon energy $-h\nu$ is given

$$I_{ph} = q\eta \frac{P_{in}}{h\nu}$$

where q is the electron charge and η is the external quantum efficiency (EQE) of the device (fraction of incident photons producing collected carriers). Photosensitivity (responsivity) is defined as

$$S(\lambda) = \frac{I_{light} - I_{dark}}{P_{opt}}$$

In structures operating near the band edge, the Franz–Keldysh effect becomes significant. The enhanced electroabsorption leads to sub-bandgap optical response and shifts the spectral sensitivity curve toward longer wavelengths. As the bias increases, the absorption tail broadens, and oscillatory structures may appear due to modulation of the joint density of states [24-28].

To experimentally obtain the spectral response:

-The incident optical power $P_{\text{opt}}(\lambda)$is calibrated at each wavelength using a reference photodiode.

-The diode current is measured in darkness (I_{dark}) and under monochromatic illumination ($I_{\text{light}}(\lambda)$).

-The spectral responsivity is computed as

$$S(\lambda) = \frac{(I_{\text{light}}(\lambda) - I_{\text{dark}})}{P_{\text{opt}}(\lambda)}.$$

A plot of S(λ)vs. λ − reveals the Franz–Keldysh absorption tail below the nominal bandgap.

For a shot-noise-limited photodetector, the dominant noise source is the dark current. The noise current over a detection bandwidth Δf −is

$$\sigma_n = \sqrt{2qI_{\text{dark}}\Delta f}$$

The linear signal-to-noise ratio is

$$SRN_{lin} = \frac{I_{ph}}{\sigma_n} = \frac{I_{\text{light}} - I_{\text{dark}}}{\sqrt{2qI_{dark\Delta f}}}$$

In decibels:

$$SRN_{dB} = \frac{I_{\text{light}} - I_{\text{dark}}}{\sqrt{2qI_{dark\Delta f}}}.$$

Because tunnel diodes inherently exhibit high dark current, the corresponding shot noise is considerable. As a result, the signal-to-noise ratio (SNR) decreases with increasing bias voltage, which is consistent with the experimentally obtained SNR–V characteristics shown in Fig. 3 and Fig. 4. Although increasing bias enhances the photocurrent, it simultaneously increases I_{dark}, making an optimal operating bias essential.

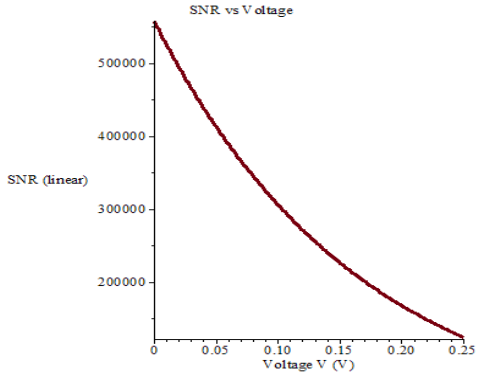

Figure 3. The measured current–voltage characteristic in complete darkness indicates tunneling-dominated conduction.

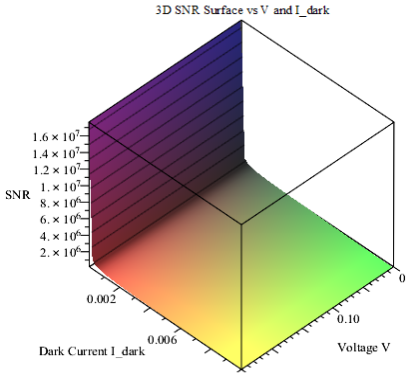

Figure 4. Three-dimensional mapping of the signal-to-noise ratio (SNR) dependence on the current–voltage (I_{dark}–V) characteristics.

CONCLUSIONS

In this study, a unified theoretical model for the total current of a tunnel diode was developed. The model incorporates tunneling current, diffusion current, photocurrent, and the contribution of additional carriers generated through phonon interactions. This comprehensive formulation enables a clearer understanding of how optical excitation and phonon-assisted processes influence the tunneling mechanism.

The measured dark and illuminated I–V characteristics support the validity of the proposed model. In darkness, the current is governed by direct band-to-band tunneling, while under illumination the I–V curve exhibits a consistent upward shift due to the photocurrent. At higher electric fields, variations in the peak and valley currents arise from redistribution of the internal electric field and Franz–Keldysh-enhanced electroabsorption, leading to observable changes in the Peak-to-Valley Ratio (PVR). These graphical results confirm the strong interplay between tunneling, illumination, and internal field modulation.

Numerical simulations further demonstrate that changes in light intensity and phonon energy significantly affect the I–V behavior of tunnel diodes, particularly near the resonant tunneling region. These findings provide a solid theoretical basis for optimizing tunnel-diode-based photodetectors, high-speed optical switches, and low-power optoelectronic components.

Future work may extend the model by incorporating the Tien–Gordon framework and the effects of high-frequency electromagnetic fields, enabling a more detailed description of photon-assisted and RF-assisted tunneling phenomena.

ORCID

Mukhammadjon G. Dadamirzaev, https://orcid.org/0000-0001-8258-4617
Munirakhon K. Uktamova, https://orcid.org/0009-0005-7562-2677

REFERENCES

[1] S.M. Sze, and K.K. Ng, *Physics of Semiconductor Devices*, (John Wiley & Sons, Inc., Hoboken, New Jersey, 2007). 3, 418 https://onlinelibrary.wiley.com/doi/pdf/10.1002/9780470068328.fmatter
[2] E.O. Kane, "Zener tunneling in semiconductors," Journal of Physics and Chemistry of Solids **12**, 181188 (1960). https://doi.org/10.1016/0022-3697(60)90035-4
[3] I. Shalish, "Franz-Keldysh effect in semiconductor built-in fields: Doping concentration and space charge region characterization," Journal of applied physics, **124**, 075102 (2018). https://doi.org/10.1063/1.5038800
[4] J.S. Karlovsky, "Simple Method for Calculating the Tunneling Current of an Esaki Diode," Phys. Rev. **127**, 419 (1962). https://doi.org/10.1103/PhysRev.127.419
[5] A.G. Chynoweth, W.L. Feldman, and R.A. Logan, "Excess Tunnel Current in Silicon Esaki Junctions," Phys. Rev. **121**, 684 (1961). https://doi.org/10.1103/PhysRev.121.684
[6] P.K. Tien, and J.P. Gordon, "Multiphoton Process Observed in the Interaction of Microwave Fields with the Tunneling between Superconductor Films," Physical Review, **129**(2), 647–651 (1963). https://doi.org/10.1103/PhysRev.129.647
[7] J.R. Tucker, "Quantum tunneling in electron devices," IEEE Journal of Quantum Electronics, **15**(11), 1234-1252 (1979). https://doi.org/10.1109/jqe.1979.1069931
[8] G. Gulyamov, and G. N. Majidova, "Influence of electron and phonon heating on the characteristics of solar photocells," Romanian Journal of Physics, **68**(3–4), 607 (2023).
[9] X. Liu, Q. Wang, L. Zhang, *et al*., "Analytical evaluation of tunneling current density in nonparabolic semiconductors," Physica Scripta, 100(4), 045503 (2025). https://doi.org/10.1088/1402-4896/adeb06
[10] P. Février, M. Gabelli, *et al*., "Photon-assisted coherent transport in nanoscale tunnel junctions," Communications Physics, **6**, 92 (2023). https://doi.org/10.1038/s42005-023-01149-5
[11] J.P. Mendez, A. Torres, and D.F. de Lima, "Phonon-coupled tunneling in high-field quantum nanostructures," arXiv preprint, arXiv:2410.17408, (2025). https://arxiv.org/pdf/2410.17408
[12] T. Sugiura, Y. Morita, *et al*., "Analysis of tunneling mechanisms in renewable-energy semiconductor devices," Energy Science & Engineering, **11**(10), 3888-3906 (2024). https://doi.org/10.1002/ese3.1523
[13] B.M. Karnakov, and V.P. Krainov, *WKB Approximation in Atomic Physics*, (Springer, 2012). https://doi.org/10.1007/978-3-031-60065-4
[14] V.A. Mishchenko, *et al*., "Generalized WKB theory for electron tunneling in gapped α-$\mathcal{B}$ lattices," Low Temperature Physics, **51**, 588–595 (2025). https://doi.org/10.1103/PhysRevB.103.165429
[15] G. Gulyamov, Sh.B. Utamuradova, M.G. Dadamirzaev, N.A. Turgunov, M.K. Uktamova, K.M. Fayzullaev, A.I. Khudayberdiyeva, *et al*., "Calculation of the Total Current Generated in a Tunnel Diode Under the Action of Microwave and Magnetic Fields," East European Journal of Physics, (2), 221-227 (2023). https://doi.org/10.26565/2312-4334-2023-2-24
[16] P.R. Berger, G. Gulyamov, M.G. Dadamirzaev, M.K. Uktamova, and S.R. Boidedaev, Romanian Journal of Physics, **69**, 609 (2024). https://doi.org/10.59277/RomJPhys.2024.69.609
[17] A.G. Chynoweth, W.L. Feldman, and R.A. Logan, "Excess Tunnel Current in Silicon Esaki Junctions," Phys. Rev. **121**, 684 (1961). https://doi.org/10.1103/PhysRev.121.684
[18] T.A. Growden, M. Evan, D.F. Storm, P.R. Berger et al., 930 kA/cm2 peak tunneling current density in GaN/AlN resonant tunneling diodes grown on MOCVD GaN-on-sapphire template, Appl. Phys. Lett. 114, 203503 (2019).
[19] I. Fistul, and N.Z. Shvarts, Uspekhi Fizicheskikh Nauk, **77**, 109–160 (1962).
[20] M.W. Dashiell, J. Kolodzey, P. Crozat, F. Aniel, and J.M. Lourtioz, "Microwave properties of silicon junction tunnel diodes grown by molecular beam epitaxy," IEEE Electron Device Letters, **23**, 357–359 (2002). https://doi.org/10.1109/led.2002.1004234
[21] M. Lotfi, and D. Zohir, "International Journal of Control and Automation, **9**(4), 9-50 (2016). http://dx.doi.org/10.14257/ijca.2016.9.4.05

[22] Y. Yan, "Silicon-based tunnel diode technology," Doctoral Thesis, University of Notre Dame, 2008.
[23] P.R. Berger, in: *Comprehensive Semiconductor Science and Technology*, (2011), pp. 176-241. https://doi.org/10.1016/B978-0-44-453153 7.00013-4
[24] Y. Turkulets, and I. Shalish, "Franz-Keldysh effect in semiconductor built-in fields: Doping concentration and space charge region characterization," Journal of Applied Physics, **124**(7), 075102 (2018). https://doi.org/10.1063/1.5038800
[25] Y.Wang, *et al*. "The influence of the Franz-Keldysh effect on the electron diffusion length in p-type GaN determined using the spectral photocurrent technique," Journal of Applied Physics, **112**(4), 045401 (2012). https://doi.org/10.1063/1.4746740
[26] C.Wang, *et al*. "Investigation of Franz–Keldysh effect in GaN-based structures by electroabsorption spectroscopy," Journal of Applied Physics, **124**(3), 035703 (2018). https://doi.org/10.1063/1.5031854
[27] R. Kudritzki, C. Zimmermann, and D. Feiler, "Illumination-induced modifications of tunneling current in heavily doped semiconductor junctions," Journal of Applied Physics, **115**, 083704 (2014). http://dx.doi.org/10.1063/1.4866852
[28] H.L. Hartnagel, and A. Pavlidis, "Bias-dependent photocurrent generation and tunneling enhancement in pn-junction-based photodetectors," Semiconductor Science and Technology, **29**, 045007 (2014). https://doi.org/10.1088/0268-1242/29/4/045007

МОДЕЛЮВАННЯ ВАХ-ХАРАКТЕРИСТИК ТУНЕЛЬНИХ ДІОДІВ З УРАХУВАННЯМ ФОТОСТРУМУ ТА ФОНОННИХ ПРОЦЕСІВ

Мухаммаджон Г. Дадамірзаєв[1], Мунірахон К. Уктамова[1,2], Ширін Рахманова[3], Гайрат А. Ібадуллаєв[4]
[1]Наманганський державний технічний університет, 160103 Наманган, Узбекистан
[2]Університет бізнесу та науки, Узбекистан
[3]Ургенчський державний університет, Узбекистан
[4]Ургенчський державний педагогічний інститут, Узбекистан

У цій статті розроблено єдину модель струму для тунельних діодів. Модель враховує не лише тунельний, дифузійний та надлишковий струми, але й фотострум, що генерується під час освітлення. Крім того, включено процеси тунелювання за допомогою фононів, а саме поглинання фононів та емісію фононів, що виникають внаслідок електрон-фононної взаємодії. Розраховані вольт-амперні характеристики показують, що загальний струм зміщується вниз під впливом освітлення. Показано, що фотострум зростає пропорційно оптичній інтенсивності та довжині хвилі. У випадку поглинання фононів електрони отримують додаткову енергію, тунельний канал розширюється, а піковий струм збільшується приблизно на 15–20%. І навпаки, під час емісії фононів частина енергії електронів втрачається, що зменшує ймовірність тунелювання, а піковий струм зменшується приблизно на 10–12%. Отримані результати показують, що врахування фононних та фотонних процесів значно розширює потенціал застосування тунельних діодів в оптоелектронних та фотодетекторних пристроях. Запропонована модель забезпечує теоретичну основу для розробки тунельних діодів як високочастотних, світлочутливих та енергоефективних пристроїв.

Ключові слова. *тунельний діод; фотострум; дифузійний струм; надлишковий струм; моделювання напівпровідників; тунелювання за допомогою фононів; оптоелектронні пристрої*

East European Journal of Physics. 4. 682–695 (2025)
DOI: 10.26565/2312-4334-2025-4-74 ISSN 2312-4334

ANALYSIS OF RADIATION METHODS FOR EXPLOSIVE MATERIALS DETECTION

G. Onyshchenko[1*], **I. Yakymenko**[1], **O. Sidletskiy**[1,2], **P. Kuznietsov**[1], **O. Tarasenko**[1,4], **O. Shchus**[1], **I. Tolkunov**[3], **O. Kudin**[5], **O. Kuzin**[1], **A. Dobrozhan**[1], **S. Lytovchenko**[6]

[1]*O.I. Akhiezer Department for Nuclear Physics and High Energy Physics, V.N. Karazin Kharkiv National University, Kharkiv, Ukraine*
[2]*Crystal Growth Technology Department, Institute for Scintillation Materials NAS of Ukraine, Kharkiv, Ukraine*
[3]*Department of Mine Action and Special Training of the Educational and Scientific Institute of Engineering and Special Training, National University of Civil Defense of Ukraine, Cherkasy, Ukraine*
[4]*Heterostructured Materials Department, Institute for Scintillation Materials NAS of Ukraine, Kharkiv, Ukraine*
[5]*Department of physics and mathematics, National University of Civil Defence of Ukraine, Kharkiv, Ukraine*
[6]*Department of Reactor Engineering Materials and Physical Technologies, V.N. Karazin Kharkiv National University, Kharkiv, Ukraine*
[*]*Corresponding Author e-mail: gennadiy.m.onyshchenko@karazin.ua*

Received August 25, 2025; revised October 15, 2025; accepted November 10, 2025

The paper examines the physical aspects of some landmine detection methods based on fast neutron backscattering. An analysis of the reaction products of the interaction of fast, slow, and thermal neutrons with H, C, N, O nuclei, which are part of explosive substances, was carried out. Mainly, to make it clear how to use secondary instantaneous and delayed gamma quanta emitted by the nuclei of explosive substances to achieve an increased detection efficiency. Discussed the physical features of some well-known methods of detecting explosive materials, exploiting elastic and inelastic scattering of fast neutrons. The reaction products of the interaction of fast, slow, and thermal neutrons with H, C, N, O nuclei included in explosives were analyzed. The goal was to simultaneously use both scattered fast and intermediate-energy neutrons emitted by the nuclei of explosives from elastic and inelastic scattering reactions (backscattering), as well as secondary instantaneous and delayed gamma quanta. The most suitable candidate for this role may be gamma-neutron detectors based on oxide scintillators of the *ZWO* type, which are simultaneously sensitive to both fast, slowed, and resonant neutrons, as well as to gamma quanta in a wide range of energies from tens of MeV to hundreds of eV. The using of a low-threshold single-photoelectron mode of photon registration makes it possible to significantly increases the sensitivity of the detection systems.

Keywords: *Neutron backscattering; Landmine detection; Neutron detector; Detection efficiency*

PACS: 29; 29.40.Mc; 29.40.-n

1. INTRODUCTION

Over the past decade, significant efforts have been made to develop neutron-based methods for the detection of hidden explosives (EXP), and other contraband materials. None of the well-known landmine detection technologies are capable of detecting mines in all applications. Therefore, a combination of several technologies is required. Among a large number of different instrumental analytical detection methods, some nuclear technologies have retained leading positions in solving special problems. For example, the high penetrating ability of fast neutrons and the characteristic gamma rays generated in reactions (n, γ), $(n, n'\gamma)$ and $(n, x\gamma)$ make it possible to carry out multi-element analysis of bulk samples [1]-[10], [37]. Currently, the requirements for technologies that could provide a successful solution to the task of search and identification (EXP) have been developed. Such requirements include: - permeability, i.e. the detection method must ensure the detection and identification of explosives at a great distance from the surface of the object or behind thick barriers; - sensitivity, i.e. the need to ensure the minimum volume and mass of detectable explosives, since modern explosives can be dangerous even in small quantities; - selectivity, since hidden explosives are often found in a large volume of harmless objects and substances; - reliability, as the level of false positives should not be high.

The chemical composition of the substance under investigation. Explosives consist mainly of elements of low and medium atomic mass: hydrogen H, carbon C, nitrogen N, oxygen O, they have a relatively high ratio of nitrogen and oxygen content to the total mass compared to carbon and hydrogen. Therefore, mine identification technology must detect the nitrogen content along with the oxygen content.

When developing explosive detection methods, the assumed chemical composition of both the explosive and the surrounding soil is taken into account. Chemical composition and density of some explosives: trinitrotoluene (TNT), $C_7H_5N_3O_6$, mol. mass = 227.132 g/mol, density up to 1.65 g/cm^3; hexogen (RDX), $C_3H_6N_6O_6$; minor mass = 222.117 g/mol, density up to 1.80 g/cm^3; C-4, composition: RDX, 91%; plasticizer $C_{26}H_{50}O_4$ 5.3%; binder C_4H_8 2.1%; oil $C_{20}H_{42}$ 1.6%, density up to 1.60 g/cm^3; octogen (HMX), $O_8N_8C_4H_8$, mol. mass = 296.156 g/mol, density up to 1.90 g/cm^3 [11].

Cite as: G. Onyshchenko, I. Yakymenko, O. Sidletskiy, V., P. Kuznietsov, O. Tarasenko, O. Shchus, I. Tolkunov, O. Kudin, O. Kuzin, A. Dobrozhan, S. Lytovchenko, East Eur. J. Phys. 4, 682 (2025), https://doi.org/10.26565/2312-4334-2025-4-74

Table 1. Mass fractions (in %) of elements H, C, N, O in some substances [11]

	H	C	N	O	Si	N/H	N/C
TNT ($C_7H_5N_3O_6$)	2.22	37.02	18.05	42.26	-	8.34	0.50
RDX ($C_3H_6N_6O_6$)	2.72	16.22	37.84	43.22	-	13.90	2.33
C4 ($C_3H_6N_6O_6$)	3.64	21.75	34.43	40.13	-	9.46	1.58
Saltpeter ($N_2H_4O_3$)	5.04	-	35.00	59.97	-	6.94	-
Urea $(NH_2)_2CO$	6.71	20.00	46.65	26.65	-	6.95	2.33
Polyethylene (C_2H_4)	14	86	-	-	-	-	-
Sand (SiO_2)	-	-	-	53.3	46.7	-	-

When analyzing and developing explosive detection methods, it is also necessary to take into account the chemical composition and density of dry soil in which explosives can be found: O (51.4%), Na (0.614%), Mg (1.31%), Al (6.87%), Si (27.06%), K (1.43%), Ca (5.11%), Ti (0.46%), Mn (0.072%), Fe (5.64%), density up to 2.70 g/cm^3.

The composition of the soil may include the following components: Al_2O_3 - 20%, SiO_2 - 57.2%, K_2O -2.5%, CaO - 2.6%, TiO_2- 1.3%, Mn - 0.08%, Fe_2O_3 - 16.2%, Rb_2O - 0.04%, SrO - 0.05%, ZrO_2 - 0.07%. In addition, data on the composition of dry sand are required: SiO_2 - 90–98%, Al_2O_3 - 1–5%, Fe_2O_3 -0.2–2%, CaO - 0.1–1%, MgO -0.1–0.5%, K_2O -0.1–1%, Na_2O - 0.1–0.5%, grain density 2.60 – 2.65 g/cm^3, bulk density 1.60–1.85 g/cm^3.

When experimentally modeling the processes of interaction of neutrons with explosives, it is possible to use ammonium nitrate, $N_2H_4O_3$, mol. mass = 80.0434 g/mol, density 1.72 g/cm^3, urea $(NH_2)_2CO$, mol. mass = 60.056 g/mol. density 1.32 g/cm^3. To obtain experimental data on the response of fast neutrons, as close as possible to the response of neutrons from TNT, it is possible to use the above-mentioned substances with carbon additives (graphite) as a dummy explosive.

The technology of registering gamma radiation emitted during neutron activation was first described as a process for identifying useful materials in the 1970s.

Nuclear composition of the substance under investigation. The essence of neutron analysis methods is to probe the area of interest with a beam of fast or thermal neutrons, which, due to their neutrality, penetrate quite deeply into the volume of the substance, and then interact with the nuclei of certain atoms (for explosives, this is usually hydrogen (^1H), carbon (^{12}C), nitrogen (^{14}N), oxygen (^{16}O), some soil elements - silicon (^{28}Si), etc., and measure the response value - scattered fast and thermal neutrons, instantaneous and delayed gamma quanta that arise in the substance as a result of the interaction of neutrons with the nuclei of its atoms [12].

Neutron analysis methods. Neutron analysis methods differ:
- by the energy of neutrons in the beam (thermal or fast neutrons, mono energy neutrons or neutrons with a continuous spectrum);
- by type of response (scattered thermal neutrons, backscattered thermal neutrons (shadow method), scattered fast neutrons, gamma radiation from nuclear reactions (radiation capture), gamma radiation from inelastic scattering);
- by to the type of neutron source (impulsive or continuous flow of neutrons, continuous neutron spectrum or mono energy).

Interaction mechanisms. During the process of interaction of neutrons with matter, atomic nuclei are excited and emit gamma radiation and secondary neutrons. It should be noted that neutrons, both instantaneous scattered and delayed secondary ones, can also interact repeatedly both in the substance of the sample and in the substance of the detector and makes a useful contribution to the response of the detector in the form of gamma quanta with energy from approximately 8 - 10 MeV to hundreds of electron volts at the points of neutron scattering from the target nuclei due to inelastic collisions and reactions of resonance and radiation capture.

Registration of gamma radiation in the form of a spectrum or registration of the flow of gamma quanta as a whole, in the counting mode, allows you to detect either the corresponding element or the anomaly of the chemical composition, and the radiation intensity correlates with the amount of the substance present. The key components of this technique are a neutron source, a gamma detector, a spectrum analysis, and a decision-making algorithm.

Types of neutron sources. Neutrons can be obtained in synthesis reactions, for example (d,t), (d,d), reactions using radioisotope sources, for example $^{238.9}Pu-Be$, $^{241}Am-Be$ from $Pu(\alpha,n)^9Be$ reactions, in spontaneous fission reactions (^{252}Cf). In addition, by now, compact accelerators have been created that consume about 100 W of power and generate acceptable flows of fast neutrons.

Types of detectors. As detectors, sensitive gamma-quantum scintillation detectors such as $NaI(Tl)$, BGO, ZWO, $LaBr_3$, $NE-213$, $stilbene$ are used, which allows obtaining reliable results and unambiguously identifying target materials at distances of 0.5 m within 5 minutes. The use of methods of visualization of associated particles simultaneously with the method of labeled neutrons makes it possible to mark the time and direction of neutron movement, which significantly improves the signal/background ratio. If the neutron generator is located within 20-30 cm from the target, the materials can be identified in a few seconds [13, 14, 15].

Limitations of the neutron method. These include the fact that in many work scenarios, the number of sensors covering a small corner of the body is limited, so the speed of the identification process increases to several minutes [12]. It should also be noted that neutrons are emitted isotropically from neutron sources, and gamma quanta are emitted isotropically

from atomic nuclei. Consequently, useful signals (gamma quanta) decrease as $1/r^4$. So, if the neutron source and the gamma detector are moved to double the distance from the target, the signal will drop 16 times. Another characteristic that can increase the time of identification of materials is the mass of the object of interest. As the mass increases, the detection time decreases linearly.

Therefore, the limitations of the methods are the proximity of the target and the system, as well as the detection sensitivity. Despite certain shortcomings and limitations of neutron methods, this method proved to be useful for detecting organic materials hidden from the eyes. The fact is that the general approach to the search for hidden explosives (explosives) at the present time consists in the simultaneous use of several methods of identification, for example, $X-ray$ radiation, electromagnetic radiation, etc. Therefore, the neutron method, due to its high sensitivity, can provide significant help in clarifying both the localization of the object of interest and its chemical composition.

2. INTERACTION OF NEUTRONS WITH MATTER

Neutrons can be obtained in reactions using radioactive sources, for example $Pu(\alpha,n)^9Be$, $Am(\alpha,n)^9Be$, in reactions of spontaneous fission (^{252}Cf). Neutrons are also obtained in synthesis reactions, for example (d,t), (d,d), in electro-nuclear reactions (e,n) using electron accelerators. Neutrons interact with nuclides in different ways, depending on the neutron energy (E_n) and, to some extent, the atomic number (Z). The neutron's lack of charge distinguishes the way it interacts with matter compared to other particles. Scattering (elastic and inelastic), absorption, and neutron and proton emission reactions are important mechanisms that reduce the flow of neutrons when they pass through matter. Neutrons, having reached resonance and thermal energy, are usually absorbed by the nucleus, creating at the same time secondary radiation, which usually consists of gamma quanta and recoil nuclei. In addition, as a result of nuclear reactions caused by neutrons, instantaneous gamma quanta emitted by a composite (compound) nucleus, or delayed gamma quanta from beta decay by an excited finite nucleus, and also, as a rule, electrons of internal conversion appear. The interaction of neutrons with nuclei depends on the energy: slow ($E_n < 0.5eV$) and resonant neutrons ($E_n \sim 0.5eV$–$100keV$), fast neutrons ($E_n \sim 100keV$–$1-20MeV$ and higher) [16, 17]. The forms of interaction of neutrons with matter are as follows:
- elastic scattering (n,n). This reaction leads to the slowing down of fast neutrons;
- inelastic scattering $(n,n'\gamma)$. Threshold reaction, neutron energy is spent on the excitation of nuclei, leads to the appearance of "$sloweddown$" fast neutrons, instantaneous and delayed gamma quanta and electrons of internal conversion;
- absorption with emission of gamma radiation (n,γ) - radiation and resonance capture. The reaction is thresholdless. The neutron binding energy is spent on the excitation of compound nuclei and is released through gamma quanta and conversion electrons;
- absorption with proton emission (n,p);
- absorption with nuclear splitting, leaving various fragments (n,r).

In elastic scattering $X(n,n)X$, the loss of kinetic energy during a collision strongly depends on the mass of the target nucleus: if the nucleus is massive, then the incoming neutron practically does not lose energy. Therefore, a hydrogen-rich material such as polyethylene is often used to slow down fast neutrons. In the case of a head-on collision with a proton, the entire momentum of the neutron is transferred to the target nucleus, so the neutron cannot scatter back. Elastic scattering dominates for fast neutrons. Elastic scattering on light nuclei, such as hydrogen nuclei, which form ionization tracks, is usually used to detect fast neutrons. Elastic scattering on the light nuclei of the moderator leads to reactions on thermal neutrons. Heavy nuclei absorb only a small part of the neutron energy.

Inelastic scattering $X(n,n'\gamma)X$ dominates for fast neutrons when the incident (primary) neutron has sufficient kinetic energy (usually more than 100 keV for heavy nuclei and more than several MeV for light nuclei) to excite the target nucleus.

If the reaction proceeds through an intermediate (compound) nucleus ($E < 20-50MeV$), then in a very short time it can decay to the ground state ($\tau < 10-12s$), releasing all the excitation energy in the form of instantaneous ("$fast$") gamma quanta. But a more likely case is when the neutron energy, without taking into account the reaction threshold, goes to the partial excitation of the nucleus and the formation of a secondary neutron with reduced energy (up to 2-3 MeV).

Inelastic scattering on heavy nuclei leaves, as a rule, finite nuclei in an excited state. Its energy is released in the form of a cascade of instantaneous (fast) and, possibly, delayed gamma rays from final nuclei from the reaction (n, n'g) and electrons of internal conversion. It should be noted that the probability of emission of internal conversion electrons (EC) can be comparable to the probability of emission of gamma quanta, therefore, when modeling the energy response of the detector to fast neutrons, it is important to take EC into account. The secondary fast neutron with reduced kinetic energy continues to interact with the surrounding nuclei, generating additional gamma quanta in the capture reaction. Compound nuclei (intermediate) emit instantaneous gamma rays. The total energy of these instantaneous gamma quanta can be comparable to the excitation energy of the nucleus and, in the case of a slow detector path, can be recorded by hardware as one high-energy pulse. Final nuclei, in turn, also emit both instantaneous and delayed gamma rays, which have different energies and are useful in the identification process.

Radiation capture of neutrons by nuclei $A(n,\gamma)A+1$, i.e. the formation of radionuclides (isotopes) mainly occurs when the neutron has resonant or sufficiently low energy. Neutron capture is an exponential process that indicates the inelastic nature of scattering as the dominant mechanism. When a neutron is captured, both instantaneous and delayed gamma quanta arise from the excited nucleus. It is also possible that, as a result of beta-decay of the final nucleus,

additional delayed and isomeric gamma quanta from excited compounds of the daughter final nucleus may occur.

The reaction of radiation capture of a neutron by a proton ($n + p- >^2 H + \gamma$), despite the absence of excited states in the deuteron, occurs with the emission of a high-energy photon with energy $E_\gamma = 2.225\ MeV$, equal to the binding energy of the deuteron and the formation of a bound neutron-proton system (deuteron) in the final state. It is also useful for identifying slow neutrons. That is, hydrogen acts as a moderator and absorber of neutrons. Note that the effect of neutron-proton momentum transfer during s-scattering is used in the shadow method of detecting explosives, when there is a complete absence of thermal neutron scattering at an angle of 180° [8].

Direct detection of neutrons is complicated by the fact that these interactions are most often measured in more complex environments (methods), which include reactions with the emission of gamma quanta and alpha particles.

3. NUCLEAR REACTIONS USED IN THE DETECTION OF EXPLOSIVES

The following reactions are used to detect slow (thermal) neutrons [3, 12, 13, 18, 19, 20, 21, 22]:

$$^1H(n,\gamma)^2H,\ Q = 2.225MeV; E_\gamma = 2.225MeV; \tag{1}$$

$$^3H(n,p)^3H, Q = 0.764MeV, \sigma_{tot} = 5.328kb; \tag{2}$$

$$^6Li(n,\alpha)^3H, Q = 4.783MeV, \sigma_{tot} = 0.9404kb; \tag{3}$$

$$^{10}B(n,\alpha)^7Li, Q = 2.789MeV; E_\gamma = 478keV; \sigma_{tot} = 3.837kb, Q = 2.31; \alpha - thread; \sigma(1eV) = 1kb; \sigma(10MeV) = 2b; \tag{4}$$

$$^{12}H(n,\gamma)^{13}C_*, E_\gamma = \ 1 - 5MeV; \tag{5}$$

$$^{14}H(n,\gamma)^{15}N_*, E_\gamma = \ 1 - 10MeV; \tag{6}$$

The following reactions are used to detect fast neutrons [3, 12, 13, 18, 19, 20, 21, 22]:

$$^1H(n,p)^1H, \sigma_{tot} = (4.5MeV) = 3.85b. \quad \sigma_{tot}(14MeV) = 3.9b; \tag{7}$$

$$^1H(n,\gamma)^2H, \sigma_\gamma = (4.5MeV) = 25ub. \quad \sigma_\gamma(4.5MeV) = 14ub; \tag{8}$$

$$^6Li(n,\alpha)^3H, Q = 4.783MeV; E_thr = 0MeV; \sigma_{tot}(4.5MeV)\ 0.0975b; \sigma_{tot}(14MeV) = \ 0.06–0.08b \tag{9}$$

$$^{12}C(n,n'\gamma)^{12}C^*, E_thr = 4.8130MeV; E_\gamma = 4.438MeV; \sigma_{tot}(4.5MeV)\ 0.1b; \sigma_{tot}(14MeV) = 0.421b \tag{10}$$

$$^{14}N(n,n'\gamma)^{14}N^*, E_\gamma = \ 5.1MeV; \sigma_\gamma = 0.103b; \sigma_{tot}(14MeV) = 0.3664b \tag{11}$$

$$^{16}O(n,n'\gamma)^{16}O^*, E_\gamma = 6.129MeV; \sigma_\gamma = 2.785b; \sigma_{tot}(14MeV) = 0.5084b \tag{12}$$

4. PARAMETERS OF NEUTRONS AND SECONDARY GAMMA QUANTA USED IN THE DETECTION OF EXPLOSIVES

The interaction of fast neutrons with hydrogen, oxygen, carbon and nitrogen, which are part of most explosives, creates gamma-neutron responses (signatures), which are registered with the help of separate gamma- and neutron detectors [19, 20, 21, 22, 23, 24]. The quality of identification depends on the intensity of the signal from the explosive substance compared to the background signal, that is, on the signal/background ratio. The signal/background ratio depends on such parameters as the distance, the mass of the explosive, as well as the sensitivity (efficiency and size) of the detector.

In addition to recording neutrons and gamma quanta with separate detectors, it is possible to use oxide scintillators as a universal gamma-neutron detecting device that combines the properties of a neutron detector and a gamma detector [15]. Neutrons in this approach are registered due to their conversion into secondary cascades of gamma quanta from the reactions of inelastic scattering and resonance capture. At the same time, the high efficiency of registration is achieved due to the absence of an intermediate moderator, which is used in traditional devices for registration of fast neutrons. The effectiveness of the deceleration, as a rule, does not exceed $\sim 5 - 6\%$.

A further significant increase in the calculated efficiency of fast neutron registration is possible when using the single-electron registration mode of the detecting photomultiplier (PMT). This PMT mode makes it possible to significantly reduce the threshold of registration of low-energy secondary gamma quanta, which arise during the interaction of secondary resonant and slowed down neutrons in the scintillator substance.

In Tab. 2 shows the parameters of nuclear reactions with neutrons on the most relevant elements of explosives hidden in the ground and of interest for the detection/identification of explosives [19, 20, 21, 22, 23, 24]. The energies of secondary gamma quanta arising in nuclear reactions with fast and thermal neutrons are also given.

Table 2. Parameters of the products of nuclear reactions with neutrons

Element	Reaction	E_γ, keV	σ_γ, b, [23, 24]	$\sigma_{\gamma,tot}$,b,[23]	σ_n,b,[22]	Neutron
H	1H(n, n)1H				0.6876	Elast(14 MeV)
	1H(n, γ)2H	2223.248	0.3326	0.3326	0.332	Thermal
					0.1495	Resonance
					2.956E-5	Fast (14MeV)
C	12C(n, n)12C				0.8192	Elast(14MeV)
	12C(n, γ)13C*			0.00351	0.00386	Thermal
	-//-				0.00177	Resonance
	-//-				1.1567E-4	Fast (14MeV)
	-//-	1261.765	0.00124			Thermal
	-//-	3683.920	0.00122			-
	-//-	4945.301	0.00261			-
	12C($n, n'\gamma$)12C*	4438.03	0.1847 (5MeV)			
0.31(10MeV)		0.4207	Fast (14MeV)			
	-//-	3214.83	0.0009			-
N	14N(n, n)14N				0.9697	Elast (14MeV)
	14N(n, γ)15N*			0.0795	0.0750	Thermal
	-//-				0.03368	Resonance
	-//-				1.7140E-5	Fast (14MeV)
	-//-	1884.821	0.0147			Thermal
	-//-	3531.981	0.0071			-
	-//-	3677.732	0.0115			-
	-//-	5269.159	0.0236			-
	-//-	5297.821	0,0168			-
	-//-	5533.395	0.0155			-
	-//-	5562.057	0.0084			-
	-//-	6322.428	0.0145			-
	-//-	8310.16	0.0033			-
	-//-	10318	-			-
	-//-	10829.12	0.0113			-
	14N(n,n'γ)14N*				0.3664	Fast (14MeV)
	-//-	729.6	0.0562			-
	-//-	1634.6	0.3136			-
	-//-	2312.8	0.468			-
	-//-	2792.5	0.02668			-
	-//-	3384	0.05148			-
	-//-	3949.9	0.01685			-
	-//-	5104.6	0.10296			-
O	16O(n, n)16O				0.9566	Elast(14MeV)
	16O(n, g)17O*			1.90E-4	1.6991E-4	Thermal
	-//-				1.5829E-4	Resonance
	-//-				2.8349E-5	Fast (14MeV)
	-//-	870.68	1.77E-4			Thermal
	-//-	1087.75	1.58E-4			-
	-//-	2184.42	1.64E-4			-
	16O($n, n'\gamma$)16O*				0.5084	Fast (14MeV)
	-//-	1983.0	0.468		-	-
	-//-	5618	-		-	-
	-//-	6129.3	2.785		-	-
	16O(n, p)16N*	7̃120	-		0.0421	-
Si	28Si(n, n)28Si				0.6619	Elast (14MeV)
	28Si(n, γ)29Si*			0.172	0.169	Thermal
	-//-				0.0818	Resonance
	-//-				6.631E-4	Fast (14MeV)
	-//-	1273.349	0.0289			Thermal
	-//-	2092.902	0.0331			-
	-//-	3538.966	0.1190			-
	-//-	4933.889	0.1120			-
	-//-	6379.801	0.0207			-
	-//-	7199.199	0.0125			-
	28Si($n, n'\gamma$)28Si*	1778.8	0.468		0.5224	Fast (14MeV)
	-//-	2837.9	0.01264			-
	-//-	3199.9	0.00468			-
	-//-	4496.3	0.00393			-

5. NEUTRON METHODS USED IN THE DETECTION OF EXPLOSIVES

To date, a significant number of techniques using neutron methods have been developed for the search and identification of explosives in the environment of bulk soil [1]-[10], [37]. These include the following:

- TNA - thermalized neutron analysis [1, 2, 5, 6, 7, 9, 10, 18, 26, 27, 28, 37, 38, 39];
- FNA, (NRA) - fast neutron analysis [1, 2, 4, 5, 7, 9, 10, 12, 18, 26, 37, 38, 39];
- PGNAA, (PGAA)- Prompt Gamma-Neutron Activation Analysis [3, 4, 7, 9, 10, 12, 18, 25, 31, 34, 39];

- PFTNA - Pulsed Fast-Thermal Neutron Analysis [1, 2, 3, 4, 6, 7, 12, 31, 38, 39];
- PFNTS - Pulsed Fast Neutron Transmission Spectroscopy [1, 3, 12, 38];
- PFNA- Pulsed Fast Neutron Analysis [1, 2, 3, 4, 6, 12, 29, 36, 37, 38];
- FNSA - fast neutron scattering analysis [4, 29, 32, 33, 35, 38];
- MNBRP - Monoenergetic Neutron Backscattering with Resonance Penetration [7, 8, 33, 39];
- API - Associated Particle Imaging [1, 2, 3, 4, 37];
- EBS – elastically backscattered spectrometry [31, 35];
- NBS (FNBS, FNB, FNS) - Neutron Back Scattering [32, 33, 34];
- NRA - Neutron Resonance Absorption [1, 2, 4, 7, 32, 37].

In Table 3 shows the characteristics of the main methods of material analysis using neutron radiation [1].

1. TNA - *Thermalized Neutron Analysis*. [1, 2, 5, 6, 7, 9, 10]. The main mechanism of interaction is the radiation capture reaction (n, γ), which uses instantaneous gamma quanta that arise when activated by slowed down $(< 0.025eV)$ neutrons. Thermal neutrons fall on the inspected object, and the gamma radiation obtained as a result of capture provides information for detection. The measured spectra of gamma rays are related to the number of incident neutrons and known capture cross sections (velocities) for the corresponding nuclides, which allows determining the concentration of elements in the irradiated sample. The use of TNA for the detection of explosives is mainly based on the identification of nitrogen (N) and hydrogen (H) contained in most explosives [1]. Two reactions of delight:

$$^{14}N + n_{thermal} \sim^{15} N + \gamma\,(5.27MeV, 10.83MeV) \tag{13}$$

$$^{1}H + n_{thermal} \sim^{2} H + \gamma\,(2.223MeV) \tag{14}$$

generate energetic (”fast”) γ-rays, which are registered by detectors and analyzed tomographically to obtain the spatial distribution of nitrogen (N) and hydrogen (H) density. A typical TNA spectrum of a metal land mine in sand is shown in Fig.1. The full energy peak, the first and second peaks of the 10.835 MeV nitrogen gamma radiation leakage (N) are not fully resolved, and an exponential slope due to the summation of events with lower energy is observed in the lower part of the region of interest (ROI) window [18, 26, 27, 28, 37, 38, 39].

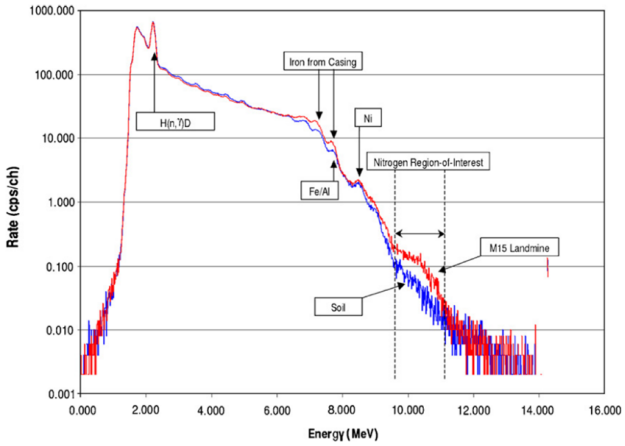

Figure 1. Gamma spectrum of an anti-tank mine in the soil (red upper curve). The mine has a steel case and contains approximately 3.6 kg of nitrogen equivalent. Also shown is the spectrum without the mine (blue lower curve) [27].

2. FNA - *Fast neutron analysis* [1, 2, 4, 5, 7, 9, 10]. The main mechanism of interaction is the reaction of inelastic scattering (n, n’γ). This method approach is very similar to TNA, but it involves bombarding the object under inspection with a collimated beam of continuous fast neutrons, usually from a neutron generator. Nuclei in the sample are excited as a result of inelastic collisions to certain low-level nuclear states, which decay with the emission of discrete gamma rays. Strong gamma transitions, which can be excited by fast neutrons $(E_n \sim 8MeV)$ in nuclides, are important for the detection of ^{1}H, ^{12}C, ^{14}N, ^{16}O nuclei. Particular attention should be paid to the absence of low-lying levels $(< 5MeV)$ in ^{16}O. The attenuation of fast neutrons inside the object is much less than the attenuation of thermal neutrons, which allows obtaining a better image reconstruction than when using the TNA method. Limitations of the fast neutron scattering (FNA) method include a high background and relatively low visualization capabilities of large objects [12, 18, 26, 37, 38, 39].

3. PFNA - *Pulsed Fast Neutron Analysis*. The method was developed with the aim of removing restrictions on the possibility of visualization of large objects. The main mechanism of interaction is the reaction of inelastic scattering $(n, n'\gamma)$. The nanosecond pulse generation method of incident neutrons and the neutron time-of-flight method are used. The deuteron accelerator with an energy of 5.5 MeV generates nanosecond $(\tau \sim 1-2\,ns, f\ 10MHz)$ neutron beams with an energy of about 8 MeV, which are collimated and directed to the scan. Neutrons produced in inelastic scattering processes

Table 3. The main characteristics of some methods of analysis of explosive materials using neutron radiation [1]
[1]ENG: Electronic Neutron Generator – can be based on neutron production processes such as $(d,D),(d,T),(d,Be),(p,Li)),(p,Be)$.
[2]SNM: Special Nuclear Materials – e.g., fissile isotopes ^{235}U, ^{239}Pu.
[3]TOF: Neutron Time of Flight method.

#	Technique Name	Probing Radiation	Main Nuclear Reaction	Detected Radiation	Sources	Primary and Secondary Detected Elements
1	TNA, Thermalized neutron analysis	Thermalized neutron	(n,γ)	Neutron capture γ-rays/promt and delayed neutrons, γ-rays for SNM^2	^{252}Cf, also accelerator based sources (ENG^1)	Cl, N, SNM^2, H, Metals, P, S
2	FNA, Fast neutron analysis	Fast (high energy, usually 14 MeV) neutrons	$(n,n'\gamma)$	γ-rays produced from inelastically scattered neutrons	ENG^1 based on (d,T)	O, C(N), (H)Cl, P
3	FNA/TNA	Pulsed neutron source, fast neutrons during the pulse, thermal neutrons between pulses	$(n,n'\gamma)$ + (n,γ)	During pulse (FNA), after pulse (TNA)	us pulsed ENG based on (d,T)	N, CL, SNM, H, C, O, P, S
4	PFNA (ns Pulsed fast neutron analysis)	Nanosecond pulses of fast neutrons	$(n,n'\gamma)$	Like FNA w / TOF^3 / prompt and delayed neutrons, γ-rays from SNM	ns pulsed (d,D) accelerator with E_d 6 MeV	O, C, N, Cl, Others, SNM
5	API (Associated particles inspection)	14 MeV neutrons in coincident with the associated α-particles	$(n,n'\gamma)$	Like FNA in delayed coincidence with α	(d,T)	H, Metals, Si, P, S, Others
6	NRA (Neutron resonance absorbtion)	Nanoseconds pulsed fast neutrons (0.5-4 MeV), broad energy spectrum	(n,n)	Elastically and resonantly scattered neutrons	Accelerator based ns pulsed (d,Be) or (d,D) w/angular correlation, with $E_d \geq 4$ MeV	O, C, N, Metals

are recorded in an array of $NaI(Tl)$ crystals and sorted by energy and time of registration relative to the neutron pulse, resulting in a spectrum of neutron energies. Gamma rays produced in the process of inelastic scattering are registered by an array of $NaI(Tl)$ crystals and sorted by energy and time of registration relative to the neutron pulse, resulting in a

three-dimensional image of the object under study, Fig.2.

The PFNA technique is used to detect explosives and drugs in passengers luggage, as well as to determine the characteristics of hazardous and nuclear materials transported in containers. On Fig.3 shows the gamma radiation spectrum of PFNA, measured with the NaI(Tl) detector for a sample of the $C-4$ type explosive simulator. Characteristic peaks associated with inelastic gamma rays such as ^{12}C, ^{14}N, ^{16}O are clearly visible. Intense lines of nitrogen and oxygen indicate the presence of an explosive substance. The content of hydrogen (H) in the object under study is not directly measured using this technique [1, 2, 3, 4, 6, 12, 29, 36, 37, 38].

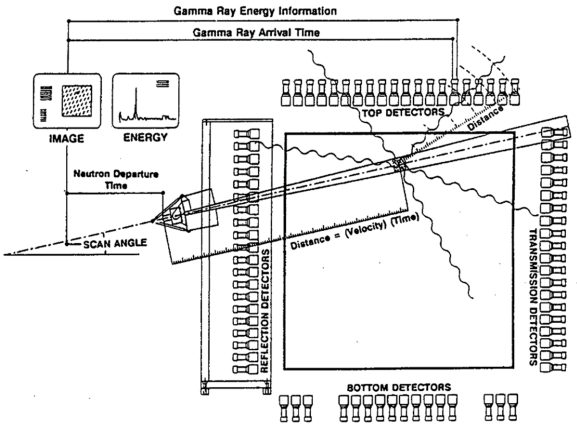

Figure 2. Schematic representation of cargo inspection system based on fast neutron pulse analysis (PFNA) [1].

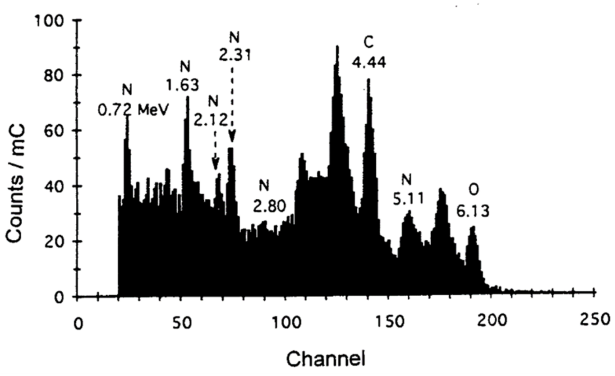

Figure 3. The energy spectrum of gamma radiation measured by the PFNA method with the help of a NaI(Tl) detector for a sample of a $C-4$ explosive simulator. The gamma lines indicated are ^{16}O (6.13 MeV), ^{12}C (4.44 MeV), and ^{14}N (0.72, 1.63, 212, and 2.31 MeV). A weak line of 2.80 MeV associated with ^{14}N is also indicated. The 5.11 MeV ^{14}N line merges with the second leakage peak of the 6.13 MeV ^{16}O line.

4. PGNAA - *Prompt Gamma-Neutron Activation Analysis*, often called thermal neutron analysis, is an isotopic or elemental radioanalytical method. PGNAA is based on the reaction of radiation capture of neutrons (n, γ) - a fundamental nuclear reaction that occurs on every isotope except ^4He. PGNAA is an effective method of non-destructive multi-element analysis of samples such as metals, coal (minerals), cement and radioactive materials, as well as explosives, chemical warfare agents, various drugs, land mines, etc. This method can be used in the laboratory or for on-site analysis of various samples. Thanks to this nuclear reaction, PGNAA stands out among other analytical methods due to several special advantages. This is not only a non-destructive multi-element analysis, which simultaneously analyzes all elements, but also allows for instant measurements, regardless of the state of the sample substance and without any sample preparation. In addition, it is possible to analyze entire arrays of samples, and the measurement results are not limited to the surface of the sample. The method has a wide dynamic range and is characterized by the ability to measure light elements, especially hydrogen (H). PGNAA is a unique method that allows you to determine even trace amounts of H [3, 4, 7, 9].

PGNAA, which has a wide range of applications, has shown great potential in detecting plastic mines. The detection of buried mines using the PGNAA method consists in irradiating the ground with neutrons to activate the elements. Then the sample emits gamma rays by means of (1) instantaneous emission of gamma rays as a result of de-excitation of nuclei, (2) emission of gamma rays as a result of short-lived beta decay, or (3) instantaneous emission of gamma rays as a result of exoenergetic nuclear reactions. On Fig. 4 The schematic diagram of the PGNAA system [Im] is presented.

The detection of instantaneous gamma rays produced in (n, γ) and ($n, n'\gamma$) reactions in hydrogen ^1H (E_γ=2.223 MeV), oxygen ^{16}O (E_γ=6.129 MeV), carbon ^{12}C (E_γ=4.438 MeV) and nitrogen ^{14}N, which is much greater in mines than in soil (E_γ=10.8 MeV), shows the probability of the presence of buried mines in this area. Since the neutron capture cross section (n, γ) on ^{14}N increases with decreasing neutron energy, the optimal geometry of the moderator, which leads to the maximum flow of thermal neutrons, certainly increases the efficiency of this method. In most cases, activation systems are not considered portable and are usually installed at customs terminals.

Several types of neutron sources can be used for PGNAA: nuclear reactors, radioisotope neutron sources such as ^{252}Cf or $^{241}Am-Be$, 14 MeV neutron generators, or accelerators. Pulsed neutron sources can be used in PGNAA systems. The development of small-sized neutron generators made it possible and expanded the scope of application, since a stationary nuclear reactor is no longer an indispensable element in PGNAA. However, the use of pulsed neutron generators without the advantages of a pulsed mechanism is ineffective. Since the nuclear reactor (including the moderator system) produces the highest flux among these sources, it provides the highest analytical sensitivity and is the preferred source.

The most noticeable advantages of using PGNAA methods are non-destructive and direct measurement, since neutrons and γ-rays have high penetrating properties. This radioanalytical method also allows for rapid and simultaneous

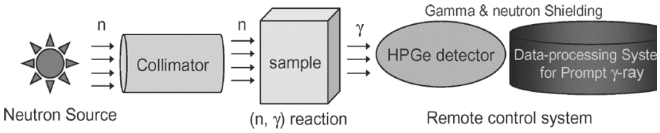

Figure 4. Schematic diagram of the PGNAA system [Im]

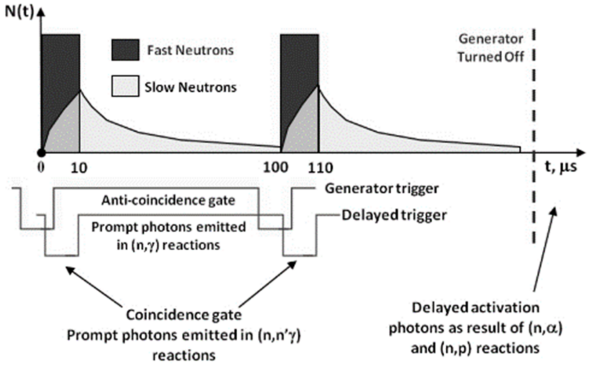

Figure 5. Schematic diagram of the PFTNA system[Im]

analysis of a large number of different elements. In addition, the entire detection system can be built as a mobile system due to the use of small neutron generators. In PGNAA, hydrogen has one fast gamma peak at 2.223 MeV. Therefore, determining the hydrogen content in various materials is quite simple [10, 12, 18, 25, 31, 34, 39].

5. PFTNA (TNA/FNA) - *Pulsed Fast-Thermal Neutron Analysis*. This is a combined method that combines the measurement of γ-radiation and the interaction of fast and thermal neutrons with substance nuclei [1, 2, 3, 4, 6, 7, 12, 31, 38, 39]. The main mechanisms of interaction are reactions of radiation capture and inelastic scattering (n, γ) + $(n, n'\gamma)$. PFTNA is used in conjunction with portable neutron generators. Unlike PFNA, which has a pulse duration of about 2 ns, PFTNA uses pulses with a minimum duration of $\tau_{min} \sim 5 - 10us$. Long pulse duration significantly reduces the cost of PFTNA systems. The PFNA system can be used in the "macropulse" mode, in which the neutron beam is turned off for a period of 100 us. This "macropulse" mode imitates the mode of the PFTNA system.

The advantage of PFTNA systems is the ability to separate the gamma radiation spectrum of inelastic scattering reactions $(n, n'\gamma)$ from the gamma radiation spectra of thermal neutron capture reactions (n, γ) and activation reactions (for example, (n, p)). The data acquisition system collects data during a neutron pulse at one memory address, and then switches to another memory address to collect data between pulses. The data collected during the pulse mainly refer to the $(n, n'\gamma)$ reactions, and the data collected between the pulses mainly refer to the (n, γ) reactions. PFTNA pulses usually have a duration of 10 us with a pulse frequency of 10 kHz. The scheme of the PFTNA with the temporal structure of the neutron pulse is shown in Fig.5.

6. PFNTS - *Pulsed Fast Neutron Transmission Spectroscopy* - (neutron spectroscopy), the same pulsed transmission spectroscopy with fast neutrons — a technique that examines the resulting spectrum of neutrons, not the spectrum of gamma radiation [1, 3, 38]. In this technique, a wide energy beam of neutrons is directed at the array neutron detectors. The investigated object passes through the beam, and the resulting the attenuated spectrum of neutrons is measured with the help of neutron detectors. This method is similar to the method that researchers use to measure cross sections of neutrons. The pulsed nature of PFTNS allows the system to perform time measurements a flight of neutrons. These time-of-flight measurements are used to determine energy of neutrons with a flight path from 4 to 10 m. The resulting spectrum of neutrons is used to estimate the attenuation of neutrons as a function of energy. Light elements such as H, C, N and O have high cross sections for attenuation of neutrons at these energies. Thus, it is possible to determine relative quantities of H, C, N and O, and it becomes possible to "visualize" elements Due to high neutron fluences and the need for accurate timing for PFTNS, this system requires an accelerator similar to that used in PFNA. PFTNS was proposed as a security inspection system airlines.

7. API - *Associated Particle Imaging*. Field analysis methods of neutrons scattered in certain directions, visualization of associated particles by the method of labeled neutrons are also being developed [1, 2, 3, 4, 37]. The main mechanism of interaction is the reaction of inelastic scattering $(n, n'\gamma)$. In associated particle imaging (API), the final nucleus, such as an alpha particle from a d-t reaction, is used to determine the time of flight and direction of the neutrons. In addition, the signal-to-noise ratio for gamma spectra from the $(n, n'\gamma)$ reaction can be significantly improved by measuring the gamma signals emitted only from the selected volume. However, the application of this technique will not affect the signal-to-noise ratio (SNR) of gamma radiation spectra (n, γ) or gamma radiation spectra with an activation delay. The scheme of the API technique is shown in Fig.6 The $d - t$ fusion reaction produces an alpha particle and a fast neutron of 14.1 MeV, which are emitted in opposite directions due to conservation of linear momentum.

A segmented alpha detector, installed inside the hermetic tube of the neutron generator, is used to detect the position and time of the alpha particle event to "mark" the direction of the 14.1 MeV neutron. The geometry of the segments of the alpha detector and the time of flight of neutrons determine the geometry of "voxels" for three-dimensional analysis. A $ZnO(Ga)$ detector was used as an alpha detector. Flashing time $\sim 3.3ns$. The data collection system is configured to generate a logic signal when both events (detection of an alpha particle and a photon) are registered within a short time interval - a "coincidence window". This logic signal is used to select those gamma radiation signals in the energy spectrum that come from the marked voxel. The width of the coincidence window and the neutron flux are interrelated:

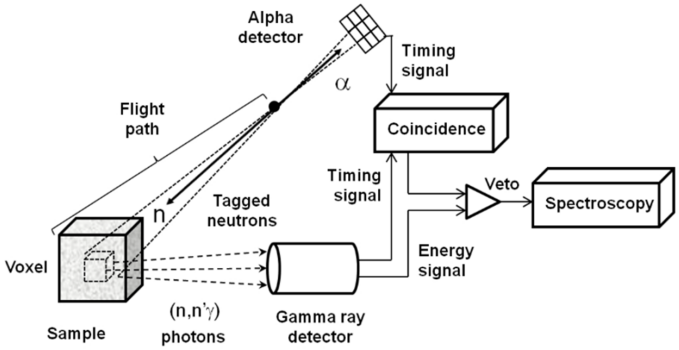

Figure 6. Method of visualization of bound particles [3]

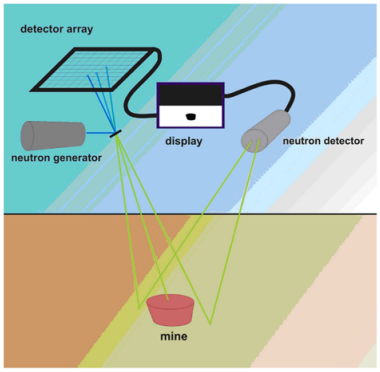

Figure 7. Schematic representation of the device for detecting mines using MNBRP

the frequency of random coincidences increases with the growth of the neutron flux, which limits the neutron output of the generator [3].

8. The MNBRP - *Monoenergetic Neutron Backscattering with Resonance Penetration* method is based on the kinematic property of ^1H not to scatter neutrons in the opposite direction [7, 8, 33, 39]. The method allows detection of hydrogen anomalies in the soil by irradiating the soil with a neutron beam and analyzing the quality of backscattered neutrons. The method uses monoenergetic neutrons. To obtain a shadow image of a buried object containing hydrogen, the following components are required: – monoenergetic neutrons; – backscattering; – the time-of-flight method (split by time) to suppress the background; – method of bound particles to facilitate the visualization of an object containing hydrogen; – resonant penetration for deeper scanning. Figure 7 shows the scheme of the proposed device for detecting mines. It consists of a neutron generator, an array of detectors for the detection of bound charged particles, detector shielding and collimation (not shown), a neutron detector and a visual display of the shadow image. The sensitivity of the method is due to the fact that neutrons are not backscattered from ^1H, an important component of all explosive substances. Thus, when hydrogen is present in an object surrounded by backscattering material, the backscattered monoenergetic neutron flux is suppressed. Thus, it is possible to obtain a shadow image of an object containing hydrogen.

The displacement of the soil by the mine leads to the formation of a volume that does not contain the components of the soil, but contains the components of the mine. The elastic backscattering of neutrons from the volume of a mine is very different from the scattering from a volume of soil of the same size, both in terms of neutron intensity and energy. The components of explosives have low mass numbers, which leads either to the complete absence of backscattering of neutrons (hydrogen), or to the backscattering of neutrons with very low energy (carbon, nitrogen, oxygen in a high energy range). The components of explosives have low mass numbers, which leads either to the complete absence of backscattering of neutrons (hydrogen), or to a noticeable weakening of the energy of backscattered neutrons (Table 4) [7, 39]. Thus, the number of backscattered neutrons with higher energy less in the presence of an explosive substance,

Table 4. Properties of neutrons with an energy of 2.35 MeV scattered at 150° from some isotopes [8]

Isotope	Energy fraction	Energy, MeV
1H	0	
12C	0.730	1.715
14N	0.764	1.795
16O	0.790	1.857
28Si	0.874	2.054
41Ca	0.912	2.143
56Fe	0.935	2.197
	1.00	2.350

which leads to the formation of a "shadow" for backscattered neutron radiation with higher energy. Since the shadow arises due to the difference in scattering from two spaces of the same volume (determined by the collimation of the source and selected in the time domain), the magnitude of the measured effect does not depend on the depth of the mine, i.e., on the thickness of the soil cover above this volume. The depth limitation lies only in the relative intensity of detected neutrons, which decreases exponentially with depth.

9. NRA - *Neutron Resonance Absorption method*. One of the obvious ways to use neutrons is to analyze their energy and scattering angles after interaction in the region of interest [1, 2, 4, 7, 32, 37]. The main mechanism of interaction is the reaction of elastic scattering (n, n). Neutron resonance analysis (NRA) is another method of analysis that requires neutrons of variable energy (white spectrum). Neutron energy is measured using short (ns) pulses to distinguish the time

between pulses. To carry out this analysis of the (n, n) reaction, a powerful source of neutrons is required.

To date, two methods of using neutron scattering to detect mines have been developed. Both methods are based on a sufficiently high content of hydrogen in almost all known explosives. Thermalization of neutrons with hydrogen is used in HYDAD (HYdrogen Density Anomaly Detection) systems, developed for the detection of small (less then 300 g) anti-personnel mines (APM) of plastic construction. Explosive substances contain low-mass elements for which neutrons have a high interaction cross section. The main component of explosives is hydrogen, ^1H. Therefore, the detection of a hydrogen anomaly in some soils is a reliable indicator of the presence of buried explosives. Examination of the soil with the help of a neutron beam and analysis of the quality of backscattered neutrons gives information about the anomalies of hydrogen in the soil. For this, two main properties of ^1H are used:
1. The energy loss of elastically scattered fast neutrons is maximal when neutrons are scattered by ^1H nuclei gives information about hydrogen anomalies in the ground;
2. At the same time, multiple scattering leads to the fact that neutrons acquire thermal energy, resulting in the formation of (backscattered) thermal neutrons that are easy to detect and identify. Using a "white" source of neutrons, thermalization of neutrons by multiple elastic scattering in hydrogen can be measured using a neutron detector, which is insensitive to fast neutrons, but very sensitive to low-energy neutrons (thermal neutrons). This method is usually called the neutron backscattering method.

Single elastic scattering from ^1H occurs with a maximum scattering angle of 87° [8], since the mass of a proton is less than the mass of a neutron. Thus, fewer fast neutrons are backscattered from the soil if an object containing hydrogen is buried in it. It is possible to measure the decrease in the flow of neutrons with the highest energy of backscattering, emanating from the soil components. In principle, backscattering from other light components of explosives, such as nitrogen and carbon, can also be measured. Oxygen is not suitable, since there is a lot of it in typical soil.

When the neutron energy is chosen in such a way that attenuation in the soil is minimal, this method is called MNBRP (monoenergy backscattering of neutrons with resonant penetration).

10. FNSA - *Fast neutron scattering analysis* is an approach that detects neutrons scattered from the material under study. The main mechanism of interaction is the reaction of elastic (n, n) and inelastic $(n, n'\gamma)$ scattering. The nuclides responsible for scattering are determined by measuring the dependence of the intensity and energy of the scattered neutrons on the scattering angle and energy of the incident neutrons. The FNSA method [4, 29, 32, 33, 35, 38], consists in the fact that the processed material sample is bombarded with a beam of monoenergetic neutrons, the energy of the incident neutrons alternates between two carefully selected values, and two detectors are used to observe the scattered neutrons: one detector is positioned at a forward angle (45°), and the other at a backward angle (150°). The pulse height resolution of neutron detectors should ideally, but not necessarily, be sufficient to resolve small energy differences (4%) between neutrons backscattered by elements C, N, and O. Time-of-flight can also be used to resolve large energy differences, for example, to separate elastically and inelastically scattered neutrons. Measurements obtained with the help of two detectors at two different energies of incident neutrons are combined to form a "scattering signature". The FNSA method is based on the assumption that the relative intensities of the H, C, N, and O signatures will be proportional to the atomic shares of the corresponding elements in the scatterer. It was shown that with the help of the FNSA method, atomic fates of elements in a small sample (0.2±0.8 kg) of $HCNO$ material can be measured with an accuracy of several percent and that explosive substances can be reliably identified based on these measurements. An important feature of the FNSA method is that it measures elements that are important for mine detection (H, C, N and O) with equal sensitivity. This guarantees that the atomic proportions of these different elements in the sample are determined with the same accuracy, which leads to a more reliable identification of the investigated material.

11. The EBS *Elastically Backscattered Spectrometry* method. The main components of drugs and explosives are H, C, N and O, which can be identified by various interactions with neutrons [31, 35]. For explosives, the atomic fates of these elements, in particular the C/O and C/N ratios, are significantly different from those present in other materials used for their concealment. The sensitivity and spatial resolution of the methods of neutron transmission, elastic scattering, inelastic scattering, and reactions depend on the size and composition of the sample being studied. Both neutron leakage spectrometry and neutron reaction analysis, used for the analysis of bulk media, require knowledge of the neutron flux density spectrum at a given point inside the sample or averaged over an extended area of the survey. Neutron leakage spectra depend on the interaction cross section, as well as on the integral density of elements between the neutron source and the detector. The energy of elastically backscattered neutrons depends on the mass of the scattering nucleus at a given source-sample-detector geometry. In experiments related to elastic backscattering spectrometry (EBS), the neutron spectrum of the Pu-Be source covers a large energy interval (1.5 - 10 MeV) of the elastic scattering cross sections of C, N and O, which allows the use of various methods for determining the energy of neutrons. In the work [35] the spectral outputs of elastically backscattered PuBe neutrons from C (graphite), H_2O, SiO_2, liquid nitrogen, polyethylene, paraffin oil, Al, Fe, and Pb were investigated the measured dependences of the outputs on the thickness. The net spectral yield was derived as the difference between the data measured with and without the samples. Some of the measured typical spectra of EBS neutrons together with the calculated energy dependence of the reaction rate $R(E_n)$ are shown in Fig.8.

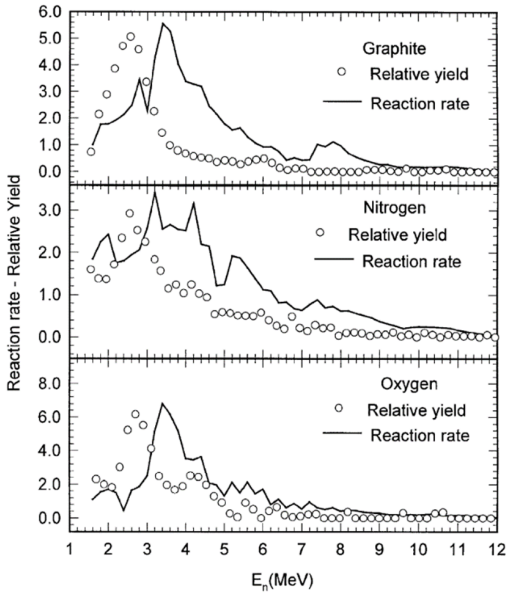

Figure 8. Backscattered spectra of PuBe neutrons for 4 cm slabs of graphite, water and 5.6 cm thick liquid nitrogen as compared to the calculated reaction rates.

6. CONCLUSIONS

The analysis of the products of the interaction of fast and thermal neutrons with nuclei of low atomic number, which are the primary components of explosives, combined with their ability to penetrate the soil, makes neutrons a preferable choice for detecting buried land mines that also have a plastic shell.

The composition of the reaction products of the interaction of fast, slowed, and thermal neutrons with H, C, N, O nuclei, which are part of explosive substances, indicates the presence of a significant number of secondary instantaneous and delayed multiple gamma quanta from both inelastic scattering reactions and resonance and radiation capture reactions. In addition, it is possible to note the high value of the flight cross section of secondary fast neutrons in the reactions of elastic scattering, "slowed down" secondary neutrons from the reaction of inelastic scattering from the investigated explosive samples.

As a rule, the existing neutron detection methods for explosives focus mainly on one type of secondary radiation, which occurs in the interaction of neutrons with matter - these are either secondary instantaneous gamma quanta flying out of target nuclei, or fast or thermal neutrons scattered in the matter of the target. The use of effective oxide scintillation gamma-neutron detectors, for example ZWO, which are simultaneously sensitive to the fast and slow resonance energies of neutrons arising in the samples, as well as gamma quanta in a wide range of energies from tens of MeV to hundreds of eV, in combination with the corresponding high-speed low-threshold single-electron photon detection methods, can contribute to increasing the detection efficiency of detection, and hence the sensitivity of explosives.

Declaration of competing interest

The authors declare that they have no known competing financial interests or personal relationships that could have appeared to influence the work reported in this paper.

Acknowledgments

This work was supported by the Ministry of Education and Science of Ukraine (0124U000837). Partly supported by the U.S. National Academy of Sciences (NAS) and the Office of Naval Research (ONRG) through the Science and Technology Center in Ukraine (STCU) under STCU contract number [7120] in the framework of the International Multilateral Partnerships for Resilient Education and Science System in Ukraine (IMPRESS-U).

ORCID

G. Onyshchenko, https://orcid.org/0000-0001-6945-8413; **I. Yakymenko**, https://orcid.org/0000-0002-0194-8376;
O. Sidletskiy, https://orcid.org/0000-0003-0865-6517; **P. Kuznietsov**, https://orcid.org/0000-0001-8477-1395;
O. Tarasenko, https://orcid.org/0000-0002-8152-2198; **O. Shchus**, https://orcid.org/0000-0001-6063-197X;
I. Tolkunov, https://orcid.org/0000-0001-5129-3120; **O. Kudin**, https://orcid.org/0000-0003-4788-6665;
O. Kuzin, https://orcid.org/0009-0004-3159-1680; **A. Dobrozhan**, https://orcid.org/0000-0002-8830-0942;
S. Lytovchenko, https://orcid.org/0000-0002-3292-5468

REFERENCES

[1] A. Buffler, "Fast neutron scattering analysis," Doctoral Thesis, University of Cape Town, 1998. https://open.uct.ac.za/items/5161f2a2-f3a8-4f5a-a92f-8305a9875f4e

[2] M. Litz, C. Waits, and J. Mullins, *Neutron-Activated Gamma-Emission: Technology review*, (2012). https://doi.org/10.21236/ada554870

[3] A.P. Barzilov, I.S. Novikov, and P.C. Womble, "Material Analysis Using Characteristic Gamma Rays Induced by Neutrons," in: *Gamma Radiation*, edited by F. Adrovic, (InTech. 2012). https://www.perlego.com/book/2014964/gamma-radiation-pdf

[4] T.U. Munchen, *Advanced Lab Course in Physics at FRM II. Prompt Gamma Activation Analysis, (PGAA)*, (2004). https://wiki.mlz-garching.de/_media/fopra:pgaa_praktikum_2015.pdf

[5] E. Hussein, and E. Waller, "Landmine detection: the problem and the challenge. Applied Radiation and Isotopes," **53**(4–5), 557–563 (2000). https://doi.org/10.1016/s0969-8043(00)00218-9

[6] A. Buffler, F. Brooks, M. Allie, K. Bharuth-Ram, and M. Nchodu, "Material classification by fast neutron scattering," Nuclear Instruments and Methods in Physics Research Section B Beam Interactions With Materials and Atoms, **173**(4), 483–502 (2001). https://doi.org/10.1016/s0168-583x(00)00425-0

[7] F. Brooks, M. Drosg, A. Buffler, and M. Allie, "Detection of anti-personnel landmines by neutron scattering and attenuation," Applied Radiation and Isotopes, **61**(1), 27–34 (2004). https://doi.org/10.1016/j.apradiso.2004.02.013

[8] M. Drosg, and F.D. Brooks, "Detection of antipersonnel landmines by measuring backscattered neutrons. P. II: Monoenergetic backscattering," in: International Atomic Energy Agency, Division of Physical and Chemical Sciences, Physics Section, (IAEA, Vienna, Austria, 2007). https://www.osti.gov/etdeweb/biblio/20977099

[9] F. Rahmani, N. Ghal-Eh, and S.V. Bedenko, "Landmine-identification system based on the detection of scattered neutrons: A feasibility study," Radiation Physics and Chemistry, **199**, 110264 (2022). https://doi.org/10.1016/j.radphyschem.2022.110264

[10] R.M. Megahid, *Landmine Detection By Nuclear Techniques*, in: *2nd Conference on Nuclear and Particle Physics*, (Cairo, Egypt, 1999). pp. 564-570. https://www.osti.gov/etdeweb/servlets/purl/20818385

[11] R. Weinheimer, *Properties of Selected High Explosives*, in: *27th International Pyrotechnics Seminar*, (Grand Junction, CO, 2000). https://psemc.com/resources/pyrotechnic-white-papers/properties-of-selected-high-explosives-rev/

[12] V.Y. Plahotnik, and G.A. Poliakov, "Neutrom methods," Visnyk KDPU, 2, (2007). (**43**). p.2. https://visnikkrnu.kdu.edu.ua/statti/2007-2-2(43)/97.pdf (in Ukraine)

[13] H. Klein, and F.D. Brooks, "Neutron detectors," in: *International Workshop on Fast Neutron Detectors*, (University of Cape Town, South Africa, 2006). https://pos.sissa.it/025/097/pdf

[14] R. Novotny, "Inorganic scintillators—a basic material for instrumentation in physics," Nuclear Instruments and Methods in Physics Research Section a Accelerators Spectrometers Detectors and Associated Equipment, **537**(1–2), 1–5 (2004). https://doi.org/10.1016/j.nima.2004.07.221

[15] G.M. Onyshchenko, B.V. Grynyov, I.I. Yakymenko, S.V. Naydenov, P.E. Kuznietsov, and O.P. Shchus, "The contributions to registration efficiency of the fast neutron reactions on the nuclei of the heavy oxide scintillators," East European Journal of Physics, **4**, 355–370 (2023). https://doi.org/10.26565/2312-4334-2023-4-46

[16] K.H. Beckurts, and K. Wirtz, *Neutron physics*, (Springer-Verlag New York Inc., 1964).

[17] J.B. Marion, and J.L. Fowler. *Neutron physics*, (New York, Interscience Publishers, 1960-63). P.1, P.2.

[18] H. Im, and K. Song, "Applications of prompt gamma ray neutron activation Analysis: Detection of illicit materials," Applied Spectroscopy Reviews, **44**(4), 317–334 (2009). https://doi.org/10.1080/05704920902852125

[19] Nuclear Energy Agency. Data Bank. (JANIS). https://www.oecd-nea.org/jcms/pl_39910/janis

[20] Evaluated Nuclear Data File (NDS) (ENDF). Ver. 2025-08-26 https://www-nds.iaea.org/exfor//endf.htm

[21] Brookhaven National Laboratory (BNL). National Nuclear Data Center. Evaluated Nuclear Data File (ENDF) https://www.nndc.bnl.gov/endf/advanced.html

[22] Japan Atomic Agency (JAEA). https://wwwndc.jaea.go.jp/jendl/j40/j40.html

[23] R. Firestone, H. Choi, R. Lindstrom, G. Molnar, S. Mughabghab, R. Paviotti-Corcuera, Z. Revay, *et al*., "Database of prompt gamma rays from slow neutron capture forelemental analysis," (IAEA, Vienna, 2006). https://doi.org/10.2172/882898

[24] A.M. Hurst, L.A. Bernstein, T. Kawano, A.M. Lewis, and K. Song, "The Baghdad Atlas: A relational database of inelastic neutron-scattering $(n, n'\gamma)$ data," Nucl. Instrum. Methods Phys. Res. Sect. A, **995**, 165095 (2021). https://doi.org/10.1016/j.nima.2021.165095

[25] H. Miri-Hakimab, H. Panjeh, and A. Vejdaninoghreiyan, "Experimental optimization of a landmine detection facility using PGNAA method," Nuclear Science and Techniques, **19**(2), 109–112 (2008). https://doi.org/10.1016/s1001-8042(08)60033-0

[26] W. Uchai, S. Changkian, L. Zhu, and H. Sun. "Experiment on the performance of of the neutronbased explosives detection system using 252cf and 241am / 9be," Suranaree J. Sci. Technol. **15**(2), (2008). https://www.thaiscience.info/Journals/Article/SJST/10890604.pdf

[27] E. Clifford, J. McFee, H. Ing, H. Andrews, D. Tennant, E. Harper, and A. Faust, "A militarily fielded thermal neutron activation sensor for landmine detection," Nuclear Instruments and Methods in Physics Research Section a Accelerators Spectrometers Detectors and Associated Equipment, **579**(1), 418–425 (2007). https://doi.org/10.1016/j.nima.2007.04.091

[28] W. Lee, D. Mahood, P. Ryge, P. Shea, and T. Gozani, "Thermal neutron analysis (TNA) explosive detection based on electronic neutron generators," Nuclear Instruments and Methods in Physics Research Section B Beam Interactions With Materials and Atoms, **99**(1–4), 739–742 (1995). https://doi.org/10.1016/0168-583x(95)00221-9

[29] F. Brooks, A. Buffler, M. Allie, K. Bharuth-Ram, M. Nchodu, and B. Simpson, "Determination of HCNO concentrations by fast neutron scattering analysis," Nuclear Instruments and Methods in Physics Research Section a Accelerators Spectrometers Detectors and Associated Equipment, **410**(2), 319–328 (1998). https://doi.org/10.1016/s0168-9002(98)00264-2

[30] A. Berlizov, and J. Magill, "Dose rate and sh4ielding calculations for an IBN-12 Pu-Be neutron source," European Communities, 2007 Report -No: JRC-ITU-TN-2007/78, (2007). https://studylib.net/doc/7376726/pu-bei---nucleonica

[31] J. Csikai, R. Dóczi, and B. Király, "Investigations on landmine detection by neutron-based techniques," Applied Radiation and Isotopes, **61**(1), 11–20 (2004). https://doi.org/10.1016/j.apradiso.2004.02.011

[32] F. Brooks, and M. Drosg, "The HYDAD-D antipersonnel landmine detector," Applied Radiation and Isotopes, **63**(5–6), 565–574 (2005). https://doi.org/10.1016/j.apradiso.2005.05.006

[33] F.D. Brooks, and M. Drosg, "Detection of antipersonnel landmines by measuring backscattered neutrons. Part I: Detection of Thermal Neutrons," in: *International Atomic Energy Agency, Division of Physical and Chemical Sciences, Physics Section*, (IAEA, Vienna, Austria, 1999-2005). https://www.researchgate.net/search/publication?q=brooks%20Detection%20of%20Antipersonnel%20Landmines%20by%20Measuring%20Backscattered%20Neutrons

[34] K. Yoshikawa, K. Masuda, T. Takamatsu, Y. Yamamoto, H. Toku, T. Fujimoto, E. Hotta, *et al.*, "Research and development of the humanitarian landmine detection System by a compact fusion neutron source," IEEE Transactions on Nuclear Science, **56**(3), 1193–1202 (2009). https://doi.org/10.1109/tns.2008.2009118

[35] J. Csikai, and I. ElAgib, "Bulk media assay using backscattered Pu–Be neutrons," Nuclear Instruments and Methods in Physics Research Section a Accelerators Spectrometers Detectors and Associated Equipment, **432**(2–3), 410–414 (1999). https://doi.org/10.1016/s0168-9002(99)00521-5

[36] T. Gozani, "Understanding the physics limitations of PFNA — the nanosecond pulsed fast neutron analysis," Nuclear Instruments and Methods in Physics Research Section B Beam Interactions With Materials and Atoms, **99**(1–4), 743–747 (1995). https://doi.org/10.1016/0168-583x(94)00675-x

[37] T. Gozani, "Detection of Explosives and Other Threats Using Accelerator-Based Neutron Techniques," in: *Electrostatic Accelerators*, edited by R. Hellborg, (Springer Berlin, Heidelberg, 2005). https://link.springer.com/book/10.1007/b138596

[38] I. Mor, "Energy-resolved fast-neutron imaging via time resolved optical readout," M.Sc. Thesis, Ben-Gurion University, Beer-Sheva, Israel, 2006. https://jinst.sissa.it/jinst/theses/2006_JINST_TH_002.pdf?utm_source=chatgpt.com

[39] F. Brooks, A. Buffler, and M. Allie, "Detection of anti-personnel landmines using neutrons and gamma-rays," Radiation Physics and Chemistry, **71**(3–4), 749–757 (2004). https://doi.org/10.1016/j.radphyschem.2004.04.087

НЕЙТРОННІ МЕТОДИ ДЕТЕКТУВАННЯ ВИБУХОВИХ РЕЧОВИН

Г. Онищенко[1], **І. Якименко**[1], **О. Сідлецький**[1,2], **П. Кузнєцов**[1], **О. Тарасенко**[1,4], **О. Щусь**[1], **І. Толкунов**[3], **О. Кудін**[5], **О. Кузін**[1], **А. Доброжан**[1], **С. Литовченко**[6]

[1]*Кафедра фізики ядра та високих енергій імені О.І. Ахієзера, Харківський національний університет імені В.Н. Каразіна, Харків, Україна*

[2]*Відділ технології вирощування кристалів, Інститут сцинтиляційних матеріалів, НАН України, Харків, Україна*

[3]*Кафедра протимінної діяльності та спеціальної підготовки навчально-наукового інституту інженерної та спеціальної підготовки, Національний університет цивільного захисту України, Черкаси, Україна*

[4]*Відділ гетероструктурованих матеріалів, Інститут сцинтиляційних матеріалів, НАН України, Харків, Україна*

[5]*Кафедра фізики і математики, Національний університет цивільної оборони України, Харків, Україна*

[6]*Кафедра матеріалів реакторобудування та фізичних технологій, Харківський національний університет імені В.Н. Каразіна, Харків, Україна*

У статті розглядаються фізичні аспекти деяких методів виявлення наземних мін, заснованих на зворотному розсіюванні швидких нейтронів. Було проведено аналіз продуктів реакції взаємодії швидких, повільних та теплових нейтронів з ядрами H, C, N, O, що входять до складу вибухових речовин головним чином для того, щоб з'ясувати, як використовувати вторинні миттєві та затримані гамма-кванти, що випромінюються ядрами вибухових речовин, для досягнення підвищеної ефективності виявлення вибухових речовин. Обговорюються фізичні особливості деяких відомих методів виявлення вибухових матеріалів, що використовують пружне та непружне розсіювання швидких нейтронів. Метою було одночасне використання як розсіяних швидких, так і нейтронів середніх енергій, що випромінюються ядрами вибухових речовин в результаті реакцій пружного та непружного розсіювання (зворотного розсіювання), а також вторинних миттєвих та затриманих гамма-квантів. Найбільш підходящим кандидатом на роль таких детекторів можуть бути детектори гамма-нейтронів на основі оксидних сцинтиляторів типу ZWO, які одночасно чутливі як до швидких, теплових, і особливо, до резонансних нейтронів, а також до гамма-квантів у широкому інтервалі енергій від десятків МеВ до сотень еВ. Використання низькопорогового одноелектронного режиму реєстрації фотонів дозволяє значно підвищити чутливість систем детектування.

Ключові слова: *зворотне розсіювання нейтронів; виявлення наземних мін; детектор нейтронів; ефективність виявлення.*

East European Journal of Physics. 4. 696-700 (2025)
DOI:10.26565/2312-4334-2025-4-75 ISSN 2312-4334

RAMAN SPECTROSCOPY OF GAMMA-IRRADIATED SILICON DOPED WITH RHODIUM

Sharifa B. Utamuradova[1], Shakhrukh Kh. Daliev[1], Dilmurod A. Rakhmanov[1]*, Aysara B. Uteniyazova[1], Afsun S. Abiyev[2]
[1]*Institute of Semiconductor Physics and Microelectronics at the National University of Uzbekistan, 20 Yangi Almazar st., Tashkent, 100057, Uzbekistan*
[2]*Western Caspian University, Baku, AZ1001, Azerbaijan*
**Corresponding Author e-mail: rahmanovdilmurod363@gmail.com*
Received July 3, 2025; accepted November 23, 2025

This research investigates the impact of gamma-ray irradiation and rhodium (Rh) contamination on the crystalline structure of silicon through Raman spectroscopy. The presence of rhodium in silicon single crystals induces slight structural changes and introduces new elements in the Raman spectral profile. Notably, the intensity of the silicon signature peak at 521 cm^{-1} shows a marked increase, while its full width at half maximum (FWHM) remains essentially unchanged. This rise in peak intensity is likely due to enhanced bonding interactions within the silicon lattice resulting from the incorporation of Rh. Additionally, the new Raman signal at 245 cm^{-1} in the Si<Rh> spectra is attributed to elemental rhodium and the formation of RhSi compounds. Furthermore, irradiation of n-Si with 1.25 MeV gamma rays and a dose of 107 rad disrupts and amorphizes the silicon crystal structure and creates radiation-vacancy defects. The irradiation results for the doped samples indicate that the addition of rhodium atoms reduces the amorphous content in silicon and enhances its crystalline structure.
Keywords: *Silicon; Rhodium; Doping; Irradiation; Gamma quantum; Raman spectroscopy*
PACS: 78.30.Am

INTRODUCTION

Silicon (Si) plays a vital role in microelectronics, serving as the foundation for integrated circuits, transistors, and various semiconductor components. Nevertheless, when exposed to radiation – such as in space environments, nuclear reactors, or areas with ionizing radiation – its structural properties can undergo considerable alterations. These changes lead to degradation of its electrical, mechanical, and optical properties, which restrict its use in extreme conditions [1-3].

The study of radiation effects in silicon is essential for the development of radiation-hardened semiconductor devices used in the military, aerospace, and nuclear industries. In addition, radiation exposure is also used in controlled doping of silicon, making it an active subject of scientific research [4,5].

When silicon is irradiated with various types of radiation (gamma rays, X-rays, electrons, neutrons, heavy ions), the crystal structure of the material changes. This is due to the ionization of atoms, the formation of interstitial defects, and vacancy complexes. The main mechanisms of destruction of the silicon structure include: Ionization processes, Dislocation defects and lattice damage, and Amorphization of the structure [6].

One effective way to increase the radiation resistance of silicon is to alloy it with transition elements such as gold (Au), platinum (Pt), rhodium (Rh), iridium (Ir), etc. These elements play a key role in reducing the concentration of radiation defects and minimizing their negative impact on the material's electrical properties [7,8].

The study of the effect of radiation on the structure of silicon has both theoretical and applied significance. Radioprotective technologies and methods for increasing silicon's resistance to radiation exposure are important areas in microelectronics and materials science.

The radiation effects on Si under the influence of γ-quanta have also been well studied. Research shows that high-energy γ-radiation causes the formation of point defects and partial amorphization at high total doses, which is manifested by a decrease in the intensity of the crystalline peak and an enhancement of the phonon continuum in the low-frequency region [9-11].

Considerable attention in the literature has been devoted to the influence of transition metal impurities on defect formation in silicon. Elements such as Ni, Co, Pt, and Pd can interact with radiation defects, form stable metal-silicide phases, and act as recombination centers for vacancies and interstitial atoms [12]. It has been shown that silicide formation increases lattice stability against radiation damage and reduces the degree of amorphization [13].

Platinum-group metals, including rhodium, are strong silicide-forming elements. Although there are significantly fewer studies on the Rh–Si system than on the Pt–Si or Pd–Si systems, existing data indicate that rhodium can form stable compounds with silicon and influence the evolution of defects in the matrix [14,15]. Similar studies have shown that Pt and Pd increase the radiation resistance of silicon by suppressing the accumulation of the amorphous phase [16], suggesting a similar analogy and mechanisms for Rh.

Cite as: Sh.B. Utamuradova, Sh.Kh. Daliev, D.A. Rakhmanov, Aysara B. Uteniyazova, A.S. Abiyev, East Eur. J. Phys. 4, 696 (2025), https://doi.org/10.26565/2312-4334-2025-4-75

This study aims to investigate the defect structure of silicon doped with rhodium and exposed to gamma radiation, utilizing Raman spectroscopy as the primary analytical method.

Raman spectroscopy is an optical method of material analysis based on the inelastic scattering of monochromatic light (usually a laser) by molecules of the material being studied. This method provides information on vibrational, rotational, and other low-energy states of molecules, making it a powerful tool for studying the structure and properties of materials. This article presents results on the change in the structure of rhodium-doped silicon irradiated with gamma quanta.

EXPERIMENTAL PART

The research was conducted on n-type silicon (n-Si) with a specific resistivity of 40 Ω·cm, fabricated using the Czochralski method. The initial doping concentration of phosphorus in the n-Si single crystals ranged from 8×10^{13} to 7×10^{14} cm^{-3}. Rhodium was incorporated into the silicon via diffusion, which entailed placing rhodium atoms on the silicon surface inside evacuated quartz ampoules. This diffusion process was performed at temperatures ranging from 1100 to 1200°C for durations of 3 to 5 hours. Following the diffusion, the samples were subjected to different cooling rates. [17,18].

The original (n-Si) and doped samples (n-Si<Rh>) were irradiated with gamma quanta with an energy of 1.25 MeV, a dose of 10^7 rad using a ^{60}Co gamma source at the INP ASUz.

The samples were examined using Raman spectroscopy with a 785 nm laser, employing an Ocean Optics Raman spectrometer capable of analyzing the spectral range from 0 to 2000 cm^{-1}. All spectral measurements were carried out at room temperature. Additionally, a Carl Zeiss EVO10 scanning electron microscope (Zeiss, Oberkochen, Germany) was used to analyze the elemental composition and obtain micrographs of the samples.

RESULTS AND DISCUSSIONS

Figure 1 displays the Raman spectra of the original silicon, rhodium-doped silicon, and gamma-irradiated samples. In the spectrum of the undoped silicon, prominent peaks are observed at 305 cm^{-1} and 521 cm^{-1}, along with a broad band spanning from 913 to 1039 cm^{-1} – features that are indicative of the cubic crystalline phase of silicon. It is established [19] that silicon with a diamond cubic structure exhibits a primary first-order Raman-active phonon mode near 520 ±1 cm^{-1}, associated with the longitudinal optical (LTO) mode, along with additional weaker features resulting from long-range translational symmetry. The peak near 304 cm^{-1} corresponds to the longitudinal acoustic (LA) phonon mode, as noted in references [20, 21]. The broad band observed in the 913–1039 cm^{-1} range has been experimentally detected in both single-crystalline [22] and nanocrystalline silicon [20, 21, 23], and is associated with the scattering of multiple transverse optical (2TO) phonons and their overtone vibrations [19, 24].

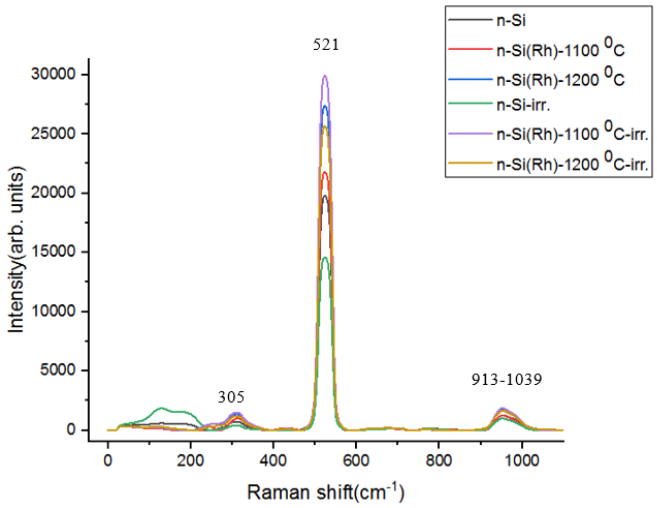

Figure 1. Raman spectra of silicon doped with rhodium and irradiated with gamma quanta

Additional doping of silicon with rhodium results in subtle modifications and the emergence of new vibrational features in the Raman spectra. In the doped samples, the intensity of the primary peak at 521 cm^{-1} increases – by a factor of 1.17 at 1100°C and 1.55 at 1200°C – while the full width at half maximum (FWHM) remains nearly unchanged (Fig.2b). This shows that after doping, rhodium can form complexes with defects in silicon, which reduces inelastic losses of scattered light and increases the scattering yield, strengthens the bonds in the structure of the silicon crystal lattice due to the incorporation of Rh atoms.

In addition, a new peak with low intensity at 245 cm^{-1} Raman shift (Fig. 2a) appears in the Raman spectrum of doped samples. The formation of this peak is due to the introduction of rhodium atoms into the crystal structure of silicon and the formation of rhodium silicide (RhSi) after high-temperature diffusion. Rhodium is recognized as one of the few transition metal impurities in silicon that can induce surface turbidity [25]. This effect is primarily attributed to rhodium's high diffusion coefficient and significant solubility in silicon. Rapid cooling (quenching) of rhodium-doped silicon

samples from high diffusion temperatures down to room temperature results in the formation of electrically active rhodium atoms occupying substitutional positions within the silicon lattice.

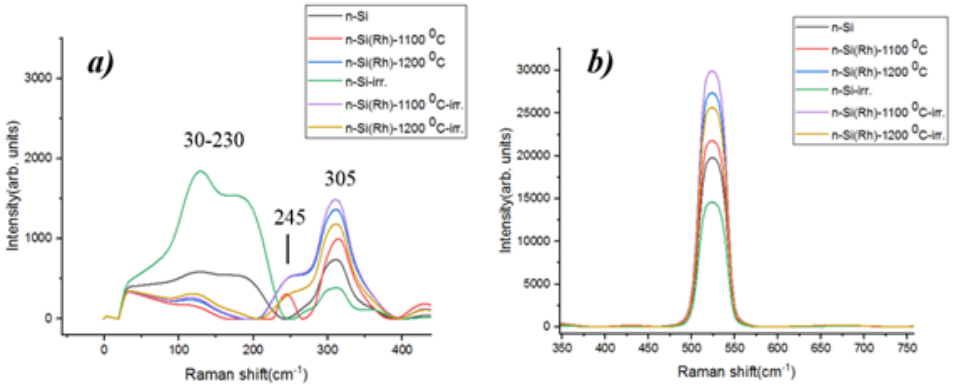

Figure 2. Fragments (a and b) of Raman spectra of single-crystal silicon, doped with rhodium and irradiated with gamma-rays.

Further analysis confirmed the presence of rhodium in the single-crystal samples through X-ray spectral analysis, which revealed a rhodium concentration of 0.68 atomic percent (at.%) or 2.4 weight percent (wt.%). As shown in the energy-dispersive spectra in Figure 3, the samples also contain oxygen and carbon atoms, with concentrations of 1.23 at.% (1.82 wt.%) and 1.84 at.% (1.32 wt.%), respectively, alongside the detected rhodium.

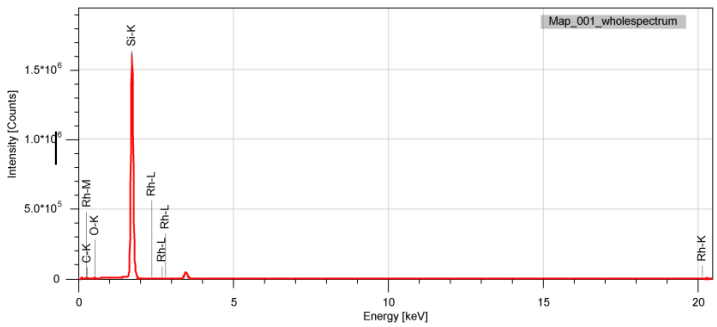

Figure 3. Energy dispersive spectra of a single crystal of silicon doped with rhodium

The change in doping temperature had almost no effect on the concentration of rhodium atoms on the silicon surface. The distribution map (Fig. 4) of impurity atoms in silicon shows that, after high-temperature diffusion, rhodium atoms formed micro- and nanostructures that were uniformly distributed on the silicon surface.

Furthermore, all studied samples were irradiated with 1.25 MeV gamma rays to a dose of 10^7 rad. Some changes in the Raman spectrum of the irradiated samples were determined. After gamma irradiation, the intensity of the main Raman peak at 521 cm^{-1} in the original silicon sample decreases by approximately 1.35 times, indicating a degradation of the crystalline structure. Furthermore, the broad peak observed in the 30–230 cm^{-1} range – associated with the amorphous phase of silicon – becomes more pronounced in the irradiated sample, suggesting an increase in structural disorder.

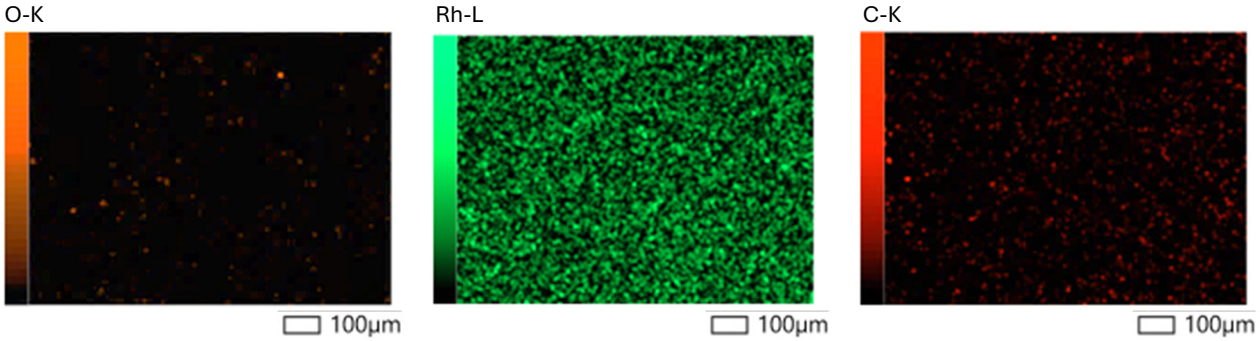

Figure 4. Micrographs of the surface of a Si single crystal after Rh doping with distribution maps

As noted by the authors in [26], exposing silicon to various forms of radiation results in the formation of radiation-induced defects – such as A-centers, divacancies, and E-centers – that introduce deep energy levels within the silicon bandgap. Among these, the vacancy–oxygen complex (A-center or VO) is one of the most prominent defects. This complex creates an acceptor level at approximately Ec – 0.17 eV. When a vacancy forms, it can trap an oxygen atom, which then shifts into the vicinity of the vacancy, residing near the vacant lattice site without wholly occupying a substitutional position [27].

Divacancy is the second most concentrated radiation defect in irradiated silicon. At high irradiation doses, when the accumulation of A-centers is limited, divacancy becomes the dominant radiation defect in concentration [28]. The next radiation defect is considered to be a vacancy-phosphorus complex (E-center), which creates a deep level in the forbidden zone of silicon with an ionization energy of Ec – 0.43 eV. All these radiation-induced defects are considered traps for the main charge carriers in silicon and worsen its electrophysical properties, leading to changes in the crystal structure. Based on [26-28], we can assume that irradiation of silicon leads to the creation of radiation defects, disruption of the crystal structure, and amorphization.

A summary of existing scientific data confirms that introducing transition metals and forming silicide phases can significantly increase silicon's resistance to γ-irradiation, reducing the concentration of structural defects and preventing the destruction of crystalline order. The experimental results obtained for Rh-doped silicon are consistent with the general trend identified in the literature.

The Raman spectra of the rhodium-doped (Si<Rh>) samples subjected to irradiation show an enhanced intensity of the primary silicon peak at 521 cm^{-1}, accompanied by a significant decrease in the broad band within the 30–230 cm^{-1} range. This suggests an improvement in the crystalline structure and a reduction in the amorphous content. This suggests a positive structural effect from the rhodium doping. Transition metals like rhodium are highly chemically active and can interact with radiation-induced defects such as vacancies and interstitials, promoting their recombination and thereby lowering the overall defect concentration [29]. Rhodium atoms can form stable complexes with these defects, effectively preventing them from participating in charge-carrier recombination [30]. Based on these findings, it can be concluded that incorporating rhodium into the silicon lattice reduces radiation-induced defect density and enhances the crystal's structural integrity.

CONCLUSIONS

Raman spectroscopy analysis revealed two distinct peaks at 305 cm^{-1} and 521 cm^{-1}, along with a broad band between 913 and 1039 cm^{-1} – all characteristic of cubic-phase silicon. Additional rhodium doping alters the spectral profile, leading to the appearance of a new peak at 245 cm^{-1}, attributed to the formation of rhodium silicide.

Using a scanning electron microscope, the concentration of impurities on the silicon surface was determined. It was found that, after high-temperature diffusion, rhodium atoms form micro- and nanostructures and are uniformly distributed on the silicon surface.

Further exposure of n-type silicon (n-Si) to gamma radiation with an energy of 1.25 MeV and a total dose of 10^7 rad results in a reduction of the main Raman peak at 521 cm^{-1} and the emergence of a broad feature within the 30–230 cm^{-1} range. These changes indicate damage and partial amorphization of the silicon crystal lattice. However, in irradiated rhodium-doped silicon (n-Si<Rh>), a different behavior is observed: the intensity of the main peak at 521 cm^{-1} increases, while the broad band associated with structural disorder in the 30–230 cm^{-1} region nearly disappears. These results suggest that incorporating rhodium atoms into the silicon matrix mitigates radiation-induced amorphization and enhances the preservation or recovery of the crystalline structure.

Conflict of Interest

The authors declare that there is no conflict of interest regarding the publication of this paper.

ORCID

Sharifa B. Utamuradova, https://orcid.org/0000-0002-1718-1122; **Shakhrukh Kh. Daliev,** https://orcid.org/0000-0001-7853-2777
Dilmurod A. Rakhmanov, https://orcid.org/0000-0003-1275-5999; **Afsun S. Abiyev,** https://orcid.org/0009-0009-9377-7567

REFERENCES

[1] Kh.N. Ahmadova, and S.H. Jabarov, "Obtaining of Al Nanosized Thin Layers and Their Structural Properties," Arabian journal for science and engineering, **48**(6), 8083-8088 (2023). https://doi.org/10.1007/s13369-022-07449-2
[2] Sh.B. Utamuradova, Sh.Kh. Daliev, D.A. Rakhmanov, I.Kh. Khamidjanov, A.S. Doroshkevich, Zh.V. Mezentseva, and A. Tatarinova, "Influence of Gamma Rays on Electrophysical Properties of Silicon Doped with Palladium Atoms," Advanced Physical Research, **7**(3), 166-173 (2025). https://doi.org/10.62476/apr.73166
[3] G. Davies, "The optical properties of radiation damage centres in silicon," Reports on Progress in Physics, **44**(7), 787–830 (1989). https://doi.org/10.1016/0370-1573(89)90064-1
[4] Sh.B. Utamuradova, D.A. Rakhmanov, and A.S. Abiyev, "Investigation of Sensitive Thermal Sensors Based on Si<Pt> and Si<Pd>," East European Journal of Physics, (3), 375-378 (2024). https://doi.org/10.26565/2312-4334-2024-3-45
[5] M.S. Yunusov, M. Karimov, M.N. Alikulov, and K.A. Begmatov, "Radiation Effects and Defects in Solids, **152**(3), 171–180 (2000). https://doi.org/10.1080/10420150008211821
[6] I.S. Tikhonov, "Application of Raman spectroscopy for analysis of the structure of single-crystal silicon," Journal of Technical Physics, **89**(3), 422–428 (2019)/
[7] Sh.B. Utamuradova**,** D.A. Rakhmanov, A.S. Doroshkevich, I.G. Genov, P.L. Tuan, and A. Kirillov, "Processes of Defect Formation in Silicon Diffusionally Doped with Platinum and Irradiated with Protons," Eurasian physical technical journal, **20**(3), 35-42 (2023). https://doi.org/10.31489/2023No3/35-42
[8] Z.T. Azamatov, M.A. Yuldoshev, N.N. Bazarbayev, and A.B. Bakhromov, "Investigation of Optical Characteristics of Photochromic Materials," Physics AUC, **33**, 139-145 (2023).
[9] I. Pintilie, G. Lindström, A. Junkes, and E. Fretwurst, "Radiation-induced point- and cluster-related defects with strong impact on damage properties of silicon detectors," Nuclear Instruments and Methods in Physics Research A, **611**, 52–68 (2009). https://doi.org/10.1016/j.nima.2009.09.065

[10] J.D. Murphy, *et al*. "Transition metals in silicon: fundamental mechanisms and electrical activity," Physica Status Solidi A, **203**(4), 693–704 (2006). https://doi.org/10.1002/pssa.200566153
[11] C. Altana, L. Calcagno, C. Ciampi, F. La Via, G. Lanzalone, A. Muoio, G. Pasquali, *et al*. "Radiation Damage by Heavy Ions in Silicon and Silicon Carbide Detectors," Sensors, **23**(14), 6522 (2023). https://doi.org/10.3390/s23146522
[12] A.A. Lebedev, and V.V. Kozlovskiy, "On comparison of the radiation resistance of silicon and silicon carbide," Semiconductors, **48**(10), 1329–1331 (2014). https://doi.org/10.1134/S1063782614100170
[13] A.W. McCarthy, H.M. Liaw, and T.A. Friedmann, "Properties of rhodium silicide thin films formed by high-temperature annealing," Applied Physics Letters, **63**, 2929–2931 (1993). https://doi.org/10.1063/1.110114
[14] H. Spieler, "Radiation Damage Mechanisms and Effects in Silicon Detectors," in: *Semiconductor Detector Systems*, (Springer, 2017), pp. 151–178. https://doi.org/10.1007/978-3-030-35318-6_5
[15] P. Pellegrino, *et al*. "Structural and electrical characterization of silicide phases formed by transition-metal diffusion into Si," Thin Solid Films, **373**, 56–60 (2000). https://doi.org/10.1016/S0040-6090(00)01057-1
[16] M.A. Mayer, *et al*. "Effects of gamma irradiation on the structure of silicon crystals," Radiation Physics and Chemistry, **79**(3), 221–226 (2010). https://doi.org/10.1016/j.radphyschem.2009.09.002
[17] Sh.B. Utamuradova, D.A. Rakhmanov, and A.S Abiyev, "Influence of Different Types of Radiation on the Crystal Structure of Silicon Monocrystals n-Si," East European Journal of Physics, (2), 380-383 (2024). https://doi.org/10.26565/2312-4334-2024-2-47
[18] M.A. Yuldoshev, Z.T. Azamatov, A.B. Bakhromov, and M.R. Bekchanova, "Investigation of Morphological and Optical Properties of $LiNbO_3$ and $LiNbO_3$:Fe 0.03 wt.% Crystals," East Eur. J. Phys. (4), 250-255 (2024). https://doi.org/10.26565/2312-4334-2024-4-25
[19] I. Iatsunskyi, G. Nowaczyk, S. Jurga, V. Fedorenko, M. Pavlenko, and V. Smyntyna, "One and two-phonon Raman scattering from nanostructured silicon," Optik, **126**(18), 1650–1655 (2015). https://doi.org/10.1016/j.ijleo.2015.05.088
[20] C. Smit, R.A. van Swaaij, H. Donker, A.M. Petit, W.M. Kessels, and M.C. van de Sanden, "Determining the material structure of microcrystalline silicon from Raman spectra," Journal of Applied Physics, **94**(5), 3582–3588 (2003). https://doi.org/10.1063/1.1596364
[21] B. Graczykowski, A. El Sachat, J.S. Reparaz, M. Sledzinska, M.R. Wagner, E. Chavez-Angel, *et al*., "Thermal conductivity and air-mediated losses in periodic porous silicon membranes at high temperatures," Nature Communications, **8**(1), (2017). https://doi.org/10.1038/s41467-017-00115-4
[22] Sh.B. Utamuradova, D.A. Rakhmanov, and A.S Abiyev, "Influence of Palladium Atoms on the Crystal Structure of Silicon (n-Si)," Physics AUC, **34**, 198-203 (2024). https://cis01.central.ucv.ro/pauc/vol/2024_34/16_PAUC_2024_198_203.pdf
[23] A. Wellner, V. Paillard, H. Coffin, N. Cherkashin, and C. Bonafos, "Resonant Raman scattering of a single layer of nanocrystals on a silicon substrate," Journal of Applied Physics, **96**(4), 2403–2405 (2004). https://doi.org/10.1063/1.1765853
[24] K. Uchinokura, T. Sekine, and E. Matsuura, "Critical-point analysis of the two-phonon Raman spectrum of silicon," Journal of Physics and Chemistry of Solids, **35**(2), 171–180 (1974). https://doi.org/10.1016/0022-3697(74)90031-6
[25] D. Tetelbaum, A. Nikolskaya, M. Dorokhin, V. Vasiliev, D. Smolyakov, A. Lukyaenko, F. Baron, *et al*. "Implanted gallium impurity detection in silicon by impedance spectroscopy," Materials Letters, **308**, Part B, 131244 (2022). https://doi.org/10.1016/J.MATLET.2021.131244
[26] M.A. Karimov, and Sh.M. Ismailov, "Study of the influence of γ-irradiation on the structural and optical properties of silicon," Journal of Applied Spectroscopy, **87**(4), 612–618 (2020).
[27] V.A. Kozlov, and V.V Kozlovskiy, "Doping of semiconductors using radiation defects produced by irradiation with protons and alpha particles," Semiconductors, **35**(7), 769-795 (2001). https://doi.org/10.1134/1.1385708
[28] Sh.B. Utamuradova, D.A. Rakhmanov, P.L. Tuan, A.S. Doroshkevich, V.A. Kinev, A. Tatarinova, R.Sh. Isayev, *et al*. "Influence of Alpha Particles on Technological Impurities in Silicon Doped with Platinum," New materials, compounds and applications, **9**(1), 50-57 (2025). https://doi.org/10.62476/nmca.9150
[29] G.P. Gaidar, "Annealing of radiation-induced defects in silicon," Electronic processing of materials, **48**(1), 93–105 (2012). https://doi.org/10.3103/S1068375512010061
[30] A.K. Nabiyeva, S.H. Jabarov, S.V. Trukhanov, A.V. Trukhanov, and N.A. Ismayilova, "XRD and SEM analyses of structural properties of $La_xBa_{1-x}MnO_3$ solid solutions," International Journal of Modern Physics B, **38**(24), 2450327 (2024). https://doi.org/10.1142/S0217979224503272

РАМАНІВСЬКА СПЕКТРОСКОПІЯ ГАММА-ОПРОМІНЕНОГО КРЕМНІЮ, ЛЕГОВАНОГО РОДІЄМ

Шаріфа Б. Утамурадова[1], Шахрух Х. Даліев[1], Ділмурод А. Рахманов[1], Айсара Б. Утеніязова[1], Афсун С. Абієв[2]
[1]Інститут фізики напівпровідників та мікроелектроніки Національного університету Узбекистану, вул. Янги Алмазара, 20, Ташкент, 100057, Узбекистан
[2]Західно-Каспійський університет, Баку, AZ1001, Азербайджан

Це дослідження досліджує вплив гамма-опромінення та забруднення родієм (Rh) на кристалічну структуру кремнію за допомогою раманівської спектроскопії. Присутність родію в монокристалах кремнію викликає незначні структурні зміни та вводить нові елементи в спектральний профіль раманівського розсіювання. Примітно, що інтенсивність піку кремнієвої сигнатури при 521 $см^{-1}$ демонструє помітне збільшення, тоді як його повна ширина на половині висоти (FWHM) залишається практично незмінною. Це збільшення інтенсивності піку, ймовірно, пов'язане з посиленням зв'язків у кремнієвій решітці внаслідок включення Rh. Крім того, новий раманівський сигнал при 245 $см^{-1}$ у спектрах Si<Rh> пояснюється елементарним родієм та утворенням сполук RhSi. Крім того, опромінення n-Si гамма-променями з енергією 1,25 МеВ та дозою 107 рад призводить до порушення та аморфізації кристалічної структури кремнію та до створення радіаційно-вакансійних дефектів. Результати опромінення легованих зразків показують, що додавання атомів родію зменшує вміст аморфного шару в кремнії та покращує його кристалічну структуру.

Ключові слова: *кремній; родій; легування; опромінення; гамма-квант; раманівська спектроскопія*

East European Journal of Physics. 4. 701-708 (2025)
DOI:10.26565/2312-4334-2025-4-76 ISSN 2312-4334

A STUDY OF THE WEAR RESISTANCE OF TiMoN/NbN NANO-MULTILAYER COATINGS DEPOSITED BY CA-PVD TECHNOLOGY UNDER DIFFERENT WORKING PRESSURES

O.V. Maksakova[1,2], V.M. Beresnev[2], S.V. Lytovchenko[2]*, M. Čaplovičova[3], D.V. Horokh[2], B.O. Mazilin[2], M. Sahul[1]

[1]*Institute of Materials Science, Slovak University of Technology in Bratislava, 25, Jána Bottu Str., 917 24 Trnava, Slovakia*
[2]*V.N. Karazin Kharkiv National University, 4, Svoboby Sq., 61000 Kharkiv, Ukraine*
[3]*Centre for Nanodiagnostics of Materials, Slovak University of Technology in Bratislava, Vazovova 5, 812 43 Bratislava, Slovakia*
**Corresponding Author e-mail: s.lytovchenko@karazin.ua*
Received May 1, 2025; revised August 13, 2024; accepted October 21, 2025

This study investigates the wear behaviour of TiMoN/NbN nano-multilayer coatings deposited by cathodic-arc PVD under two nitrogen working pressures (0.52 and 0.13 Pa). Although both coatings exhibit comparable total thicknesses (~10–11 μm) and a similar number of periods (~270), their structural integrity, interface coherence, and elemental distribution differ significantly with deposition pressure. The coating synthesized at 0.52 Pa develops a highly ordered, dense multilayer architecture, characterized by well-defined interfaces and a reduced microdefect density. Conversely, the coating deposited at 0.13 Pa displays pronounced interfacial waviness, disrupted periodicity, and increased defect concentration. Ball-on-disc tribological tests reveal a stable friction coefficient of 0.42–0.48 for the 0.52 Pa coating, whereas the 0.13 Pa coating shows an elevated and unstable friction response (0.60–0.70) with frequent fluctuations. Microstructural and chemical analyses of wear tracks indicate the formation of a robust, adaptive Ti–Nb–Mo–O tribofilm for the high-pressure coating, incorporating lubricious MoO_3 and mechanically strengthening Nb_2O_5 phases. In contrast, the low-pressure coating produces only a thin, brittle TiO_2-rich film lacking self-replenishing capability. These findings demonstrate that optimized nitrogen pressure is essential for achieving structurally coherent nanolaminates capable of forming functional tribofilms, thereby dramatically improving wear resistance in TiMoN/NbN nano-multilayer systems.
Keywords: *PVD; Nitrides; Multilayer coatings; Microstructure; Composition; Wear*
PACS: 68.55.Jk, 68.65.Ac

INTRODUCTION

In modern mechanical engineering, instrument engineering, aviation, and power engineering, materials capable of withstanding extreme operating conditions – high temperatures, abrasive and corrosive wear, and cyclic loading – are playing an increasingly important role [1]. To protect tools, components, and assemblies, hard nitride coatings based on transition metals are widely used, such as CrAlN and TiAlN [2,3], CrMoN and CrTiN [4], ZrNbN [5], TiNbN [6], as well as superhard TiSiN and TiSiN/DLC hybrids [7] and TiN/DLC systems [8]. The classical monolayer nitrides – TiN, MoN, and NbN – which are characterized by high hardness (H ~ 20–30 GPa), low coefficient of friction, and good thermal and corrosion resistance – have been well studied and are widely used [9,10]. For TiN, it has been shown that structural refinement under the action of a substrate bias gradient increases the H/E and H^3/E^2 ratios and ensures high wear resistance [11]. For MoN-containing systems, a combination of increased hardness (up to ~28–30 GPa) and a low friction coefficient is achieved due to the formation of self-lubricating MoO_3 tribo-oxides [12] The NbN films demonstrate high hardness, wear resistance, and corrosion resistance simultaneously [13].

An analysis of modern scientific studies [12–15] in the field of structural materials and the development of the tooling industry indicates that for a long time the main attention has been focused on increasing the durability of protective coatings in order to extend the service life of components and tools. Thus, Chenrayan and co-authors showed that the application of TiAlN, DLC, and TiCN coatings to cutting tools provides an increase in tool life by approximately 5.8 times compared to uncoated tools [16]. In the work of Sonawane et al., it was demonstrated that, during dry turning of DSS2205 steel, a tool with an AlTiCrN coating achieves an operating time of about 124 minutes, which is roughly 3.5 times higher than that of an uncoated tool [17]. Akbar and co-authors established that the use of a multilayer TiAlN/TiN coating on carbide drills makes it possible to increase tool life by approximately six times compared with both uncoated and single-layer variants [18].

The evolution of coating deposition technologies has led to the development of advanced multifunctional and highly wear-resistant materials, thereby creating new opportunities for further optimization of their performance and expansion of their application domains. Xu et al. demonstrated that employing high-power impulse magnetron sputtering (HiPIMS) to fabricate multilayer MoN/TiN coatings results in a dense nanolamellar architecture with significantly enhanced mechanical and tribological properties compared with conventional deposition techniques, making these coatings promising candidates for heavily loaded tribological systems and cutting tools [12].

Zhang et al. developed a superhard high-entropy nitride coating, AlCrNbSiTiN, exhibiting an ultrahigh hardness of approximately 46 GPa and an exceptionally low wear rate of 6.3×10^{-7} $mm^3/N\cdot m$. Such outstanding performance suggests

Cite as: O.V. Maksakova, V.M. Beresnev, S.V. Lytovchenko, M. Čaplovičova, D.V. Horokh, B.O. Mazilin, M. Sahul, East Eur. J. Phys. 4, 701 (2025), https://doi.org/10.26565/2312-4334-2025-4-76

strong potential for applications in components operating under extreme mechanical stresses [19]. Furthermore, Wang and co-authors reported that AlCrNbSiTiN high-entropy nitride coatings deposited by RF magnetron sputtering combine high hardness with markedly improved corrosion resistance in water vapor environments, making them suitable for aggressive and high-temperature service conditions [20].

Recent findings [21] indicate that PEALD processing of Ti–Mo–N systems enables the formation of nitride coatings with excellent adhesion and very low wear, primarily due to precise control of the coating–substrate interface. Van Meter et al. established that the critical factor governing adhesion is the surface condition prior to deposition, specifically the presence of a native oxide layer on the substrate without any adhesion-promoting or buffer interlayers. This native-oxide interface minimized residual stresses in the TiMoN film and provided the strongest adhesion. Conversely, aggressive pre-deposition etch-cleaning increased compressive stresses and degraded interfacial strength. The optimal configuration is TiMoN deposited directly onto a native-oxidized substrate, which resulted in the lowest wear coefficient of ~4×10^{-8} $mm^3/N \cdot m$, underscoring the essential role of controlled interfacial engineering in achieving long-term durability of nitride coatings.

In a recent study, Zhou et al. [22] demonstrated that TiMoN coatings exhibit an atypical deformation behavior compared with conventional TMN hard-coating systems – plastic deformation occurs not through brittle fracture but via intensive dislocation multiplication and grain-boundary-mediated sliding. This dislocation-governed mechanism enables efficient dissipation of contact-induced energy and suppresses crack formation, which typically initiates abrasive or adhesive wear in traditional nitride coatings. Consequently, the intrinsic ability of TiMoN to undergo localized plastic deformation provides a basis for its enhanced wear resistance and improved stability under cyclic and impact loading conditions.

Further investigations of TiMoN-based systems confirm the promising potential of this composition. Zhou et al. reported that Mo-alloyed TiN coatings of the $TiMo_{0.08}N$ type, deposited by multi-arc ion plating, combine high hardness (up to ~34 GPa), strong adhesion (Lc > 65–100 N), and a low friction coefficient (< 0.24) due to the formation of a lubricious MoO_3 tribo-oxide in the wear track. These coatings also markedly reduced the corrosion current compared with WC–Co substrates [23]. Moreover, Wang et al. showed that TiMoN coatings deposited on GCr15 bearing steel by arc ion plating exhibit a minimum friction coefficient (≈ 0.31), a low wear rate of ~1.99×10^{-6} $mm^3/N \cdot m$, and a corrosion current of 3.62×10^{-9} A/cm^2 when an optimal substrate bias of −120 V is applied. These improvements were attributed to a pronounced (111) texture and the formation of a layered MoO_3 tribo-oxide phase, further confirming the potential of TiMoN systems as self-lubricating, wear-resistant coatings [24].

Although monolayer TiMoN coatings already exhibit atypical, dislocation-mediated plasticity and enhanced wear resistance compared with conventional TMN hard-coating systems, a logical next step is to transition to multilayer architectures. Direct examples of multilayer structures based on TiMoN remain limited and are mainly represented by the $TiMoN/Si_3N4$ system, in which the formation of a nanomultilayer configuration leads to increased hardness and reduced wear rates relative to monolithic TiMoN. These improvements arise from the periodic alternation of stiff and more compliant sublayers, as well as the high density of interlayer interfaces [25].

Comprehensive reviews on protective nanomultilayer nitride films indicate that such architectures typically provide higher hardness, improved oxidation stability, and lower wear rates than their corresponding single-layer nitrides. These advantages stem from interfacial dislocation blocking, crack deflection at layer boundaries, and the presence of a controlled stress gradient across the multilayer stack [26]. This behavior is further confirmed by specific examples such as TiN/NbN superlattices, where nanoscale layering periods simultaneously enhance adhesion, fracture resistance, and both corrosion and tribological stability [27].

On the other hand, NbN and multilayer systems incorporating NbN are increasingly regarded as a promising platform for wear-resistant coatings. NbN-based coatings exhibit elevated microhardness, a favorable state of compressive residual stress, and reduced temperature and stress at the cutting edge compared with TiN, which directly translates into extended tool life in machining applications. The transition to multilayer architectures with functional NbN-containing layers further enhances fracture resistance and overall tool performance. In particular, nanoscale WN/NbN coatings deposited by CA-PVD show high hardness values of ~33.6–36.6 GPa and low specific wear rates of $(1.9 – 4.1) \times 10^{-6}$ $mm^3/N \cdot m$, confirming the suitability of NbN as a rigid strengthening constituent in multilayer nitride systems [16].

Considering the low thermal conductivity of NbN and its ability to form protective oxide layers, combining TiMoN with NbN in a multilayer architecture can be expected to deliver a synergistic enhancement in wear resistance through several mechanisms. The hardness and elastic modulus contrast between TiMoN and NbN layers, which impedes crack propagation. The activation of dislocation-mediated plasticity in TiMoN layers, enabling efficient dissipation of contact energy. The formation of beneficial compressive residual stresses and a thermal-barrier effect provided by NbN sublayers. The potential development of “adaptive” tribo-oxides (MoO_3 and Nb_2O_5) that reduce the coefficient of friction. These combined effects position the TiMoN/NbN system as an up-and-coming candidate for the next generation of multilayer wear-resistant coatings.

Our previous investigations of TiMoN/NbN multilayer coatings demonstrated that the microstructure and mechanical response of the system are strongly governed by the combination of working pressure and applied substrate bias. It was established that deposition at −200 V and 0.52 Pa yields the highest layer density, well-defined interfaces, and

minimal microdefect content, which correlates with the maximum hardness of 31.6 GPa and an elastic modulus of 462 GPa. In contrast, deposition at 0.13 Pa results in blurred interfaces, reduced crystallinity, and an elevated density of microdefects, with microstrain nearly doubling from ~1.0×10^{-3} to ~2.1×10^{-3} [28]. These structural differences are expected to play a decisive role in the coating behavior under external loading, particularly in terms of wear resistance.

Given the established dependence of structural and mechanical properties of TiMoN/NbN coatings on nitrogen pressure during deposition, a key open question concerns how these differences manifest under actual sliding contact. It is well known that microstructure and interface quality govern wear behavior ranging from the formation of protective oxide films to localized plastic deformation or brittle fracture. Preliminary results indicate that the coating deposited at 0.52 Pa has a denser, more balanced architecture, whereas the 0.13 Pa coating exhibits greater defectiveness and Ti enrichment. However, the tribological response of these coatings, specifically their chemical evolution, the morphology of worn regions, and the role of possible tribo-oxides, has not yet been systematically examined.

Therefore, in this work, a comparative study was carried out to evaluate the wear resistance and wear mechanisms of TiMoN/NbN nano-multilayer coatings deposited at different nitrogen pressures (0.52 and 0.13 Pa), to identify the optimal deposition regime and gain deeper insight into the tribological processes governing the performance of such multilayer systems.

EXPERIMENTAL DETAILS

Deposition Process

The TiMoN/NbN multilayer coatings were deposited using cathodic-arc PVD, a technique distinguished by its high deposition rate and the substantial ion energies inherent to arc plasmas, which promote the formation of dense, well-adherent nitride layers even on substrates with complex geometries. The arc discharge generates multiply charged metal ions, creating favorable conditions for the growth of compact layers and for the strengthening of the near-surface region of the substrate.

For the experiments, 12X18H9T stainless steel plates with dimensions of 10 × 10 × 2.5 mm were used as substrates. The substrates were ground with 2000-grit abrasive paper and polished using a one micron diamond suspension. The Ti and Mo species were supplied from a sintered composite TiMo cathode with a Ti : Mo ratio of 80:20. At the same time, the NbN layers were deposited from a high-purity (99.8 %) niobium cathode. Nitrogen gas (N_2, 99.6 %) served as the reactive atmosphere. The substrates were ultrasonically cleaned in acetone, ethanol, and deionized water (25 min each) and then mounted on a vertical sample holder inside the chamber. The base pressure was reduced to ~4×10^{-3} Pa to minimize oxygen contamination.

The coatings were deposited for 90 minutes at various working nitrogen pressures (0.13 and 0.52 Pa) and negative substrate bias of –200 V. The cathode currents were set to 110 A for the TiMo target and 90 A for Nb target. The multilayer architecture was achieved by continuous rotation of the substrate holder, ensuring uniform layer growth. The deposition regimes are summarized in Table 1.

Table 1. Deposition parameters of the TiMoN/NbN nano-multilayer coatings

Sample	Arc current, A	Substrate bias, V	N2 pressure, Pa	Deposition time, min
1552(TiMoN/NbN)	110/90	-200	0.52	90
1554(TiMoN/NbN)			0.13	

Characterization

The cross-sectional microstructure at multiple magnifications and the morphology of the worn surfaces were characterized using field-emission scanning electron microscopy (FE-SEM) employing Quanta 600 FEG and FEI Nova NanoSEM 450 microscopes operated at accelerating voltage of 20 kV. The acquired images were used to assess the columnar growth characteristics and to determine the thickness and uniformity of the individual nanolayers. In addition, the wear tracks were examined to evaluate their microstructure and elemental composition.

Ball-on-disc tribological tests were conducted using a Bruker UMT-2 universal tribometer. A 6.3 mm WC–Co ball was employed as the counterbody. The tests were performed under a normal load of 5 N at a rotational speed of 200 rpm for a total sliding duration of 30 min. The sliding radius was maintained constant throughout the experiment, and the corresponding linear sliding speed was adjusted accordingly. The tests were carried out under ambient laboratory conditions (22–24 °C, relative humidity 35–45 %), and no lubrication was applied. The evolution of friction during sliding was continuously recorded to obtain the friction coefficient as a function of time.

RESULTS AND DISCUSSIONS

The TiMoN/NbN nano-multilayer coatings deposited at different working nitrogen pressures (0.52 and 0.13 Pa) will exhibit fundamentally distinct tribological behaviors directly governed by the structural integrity of the nanolayers, the quality of the interfaces, and the chemistry of the tribofilm formed during sliding. Despite having comparable total thicknesses (~10–11 μm) and similar numbers of periods (~270), the sequence of alternating hard NbN and more compliant TiMoN layers and, critically, the defect density at their interfaces determines the mechanical response of the system under cyclic contact loading.

The cross-sectional SEM images of TiMoN/NbN nano-multilayer coatings are shown in Fig. 1. It is evident that both coatings exhibit a well-defined, nearly perfectly parallel multilayer architecture in which the NbN layers act as structural "reinforcement ribs." These layers uniformly distribute the applied load and serve as effective barriers to dislocation propagation.

The cross-sectional SEM images of TiMoN/NbN nano-multilayer coatings are shown in Fig. 1. It is evident that both coatings exhibit a well-defined, nearly perfectly parallel multilayer architecture in which the NbN layers act as structural "reinforcement ribs." These layers are supposed to uniformly distribute the applied load and serve as effective barriers to dislocation propagation. Although both coatings exhibit a clearly developed multilayer architecture, the cross-sectional images reveal subtle but technologically significant differences in the microstructural quality as a function of the nitrogen pressure. The coating deposited at 0.52 Pa (sample 1552) shows a highly compact, slightly columnar morphology with straight, well-defined, and sharply delineated interfaces between adjacent nanolayers. The individual TiMoN/NbN periods maintain a nearly constant thickness across the entire coating cross section, and the interlayer boundaries appear clean and continuous, indicating a stable growth regime with suppressed defect formation. In contrast, the coating grown at 0.13 Pa (sample 1554) also forms a multilayer stack, yet the nanolayers do not exhibit a columnar structure. However, it is evident that there is a higher density of microdroplet-related defects, which is typical of low-pressure arc evaporation. While the periodicity is preserved, the interfaces in sample 1554 appear locally less sharp and occasionally broadened, suggesting less effective kinetic energy dissipation during layer formation and reduced adatom mobility. These microstructural distinctions, namely, the higher layer density, cleaner interfaces, and reduced defect concentration in sample 1552, play a decisive role in its superior mechanical response under sliding contact and correlate directly with the stability of the friction coefficient and the robustness of the tribofilm formed during wear.

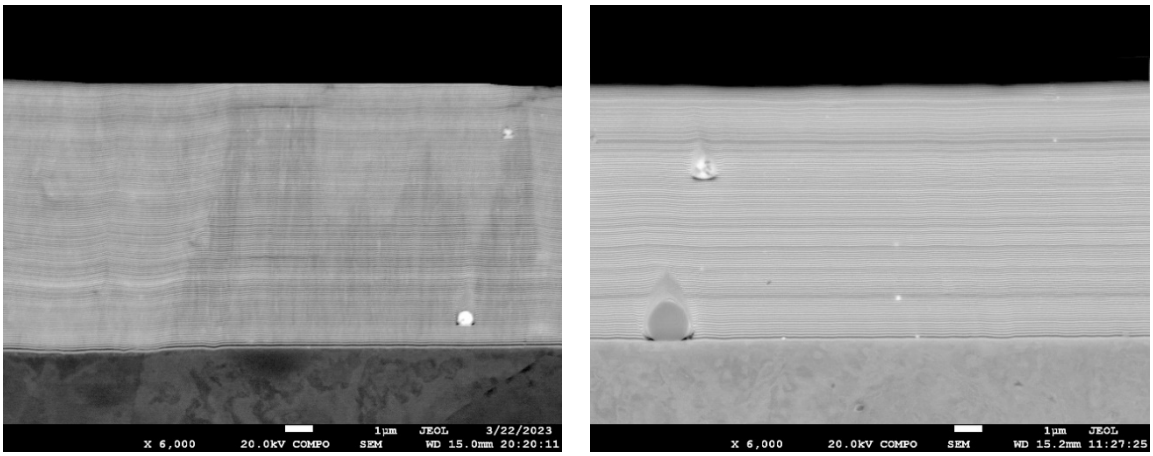

a b

Figure 1. Cross-sectional SEM images of TiMoN/NbN nano-multilayer coatings deposited at different working nitrogen pressures: (a) 0.52 Pa and (b) 0.13 Pa

A comparative analysis of the elemental composition of the as-deposited TiMoN/NbN nano-multilayer coatings (Table 2) reveals pronounced differences that arise already at the deposition stage under different nitrogen pressures. Sample 1552 contains a higher fraction of titanium (36.71 wt. %) and a slightly lower fraction of niobium (42.48 wt. %) compared with sample 1554, which suggests a more uniform growth of the TiMoN sublayers and a better-stabilized superlattice structure at the higher reactive-gas pressure. In contrast, sample 1554 exhibits substantial niobium enrichment (46.92 wt. %) accompanied by a reduction in titanium content to 14.94 wt. %, indicating a change in the layer growth mechanism and a possible dominance of NbN in the nanolayers under low-pressure conditions. The moderately increased molybdenum content in 1554 is also consistent with deposition conditions that promote a local redistribution of metallic constituents toward Nb–Mo enrichment. Such compositional variations directly influence the microstructure, residual stress state, and, ultimately, the tribological performance of the coatings.

Table 2. Elemental composition of the TiMoN/NbN nano-multilayer coatings deposited at different working nitrogen pressures: (a) 0.52 Pa and (b) 0.13 Pa.

Element	1552(TiMoN/NbN)		1554(TiMoN/NbN)	
	wt. %	at. %	wt. %	at. %
N	18.02	48.30	14.94	37.57
Ti	36.71	30.20	32.98	30.45
Nb	42.48	18.02	46.92	24.23
Mo	2.79	3.48	5.16	7.75
Total	100.00	100.00	100.00	100.00

The friction–time curves shown in Fig. 2 demonstrate that sample 1552 maintains a stable sliding response with a COF of approximately 0.42–0.48 throughout nearly the entire test. The initial running-in stage (COF increasing from ~0.20 to

~0.45 within the first 10–20 s) gradually transitions into a regime dominated by the formation of a self-sustaining oxide–nitride tribofilm, which effectively suppresses stress fluctuations and prevents a shift toward abrasive wear.

In contrast, the COF of sample 1554 progressively rises to 0.60–0.70 and exhibits periodic spikes corresponding to repeated cycles of tribofilm breakdown and localized reformation. This behavior indicates the predominance of abrasive–adhesive wear mechanisms and the absence of a stable lubricious phase at the sliding interface.

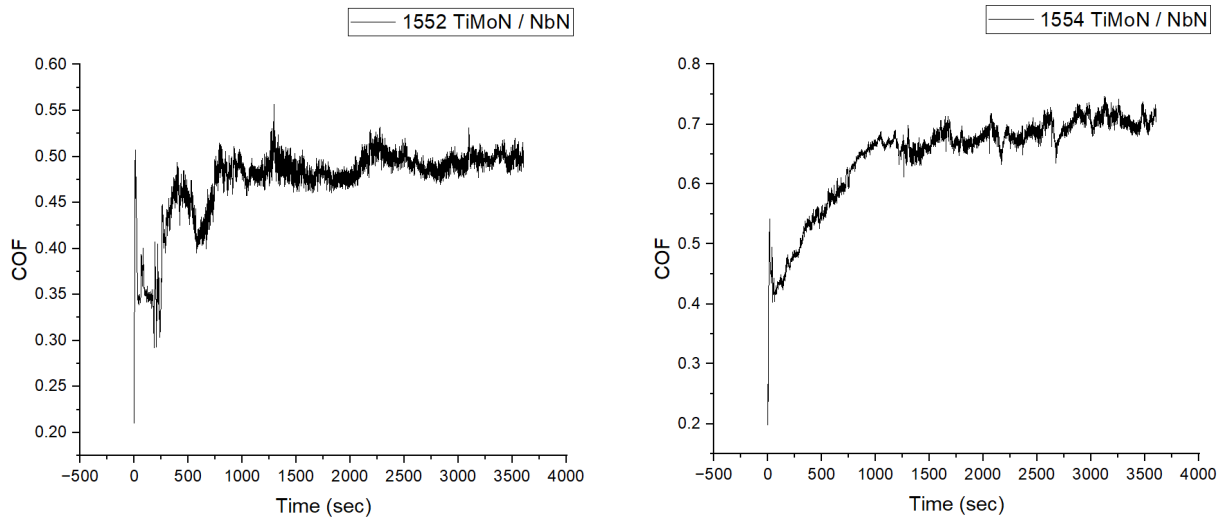

a b

Figure 2. Evolution of the friction coefficient of the TiMoN/NbN nano-multilayer coatings deposited at different working nitrogen pressures: (a) 0.52 Pa and (b) 0.13 Pa.

The morphology of the wear tracks of the TiMoN/NbN nano-multilayer coatings deposited at different working nitrogen pressures is presented in Fig. 3. The results shows a striking contrast between the two deposition regimes. The wear track of sample 1552 exhibits smooth, well-aligned sliding marks with only faint groove formation, indicative of a weak abrasive component in the overall wear process. By contrast, sample 1554 shows deeper grooves, numerous micro-pullouts, and distinct regions of transferred counterbody material (W–Co), confirming a combined abrasive–adhesive wear mechanism. This mode of degradation points to the absence of a stable protective tribofilm and to local coating failure extending down to the sublayer level.

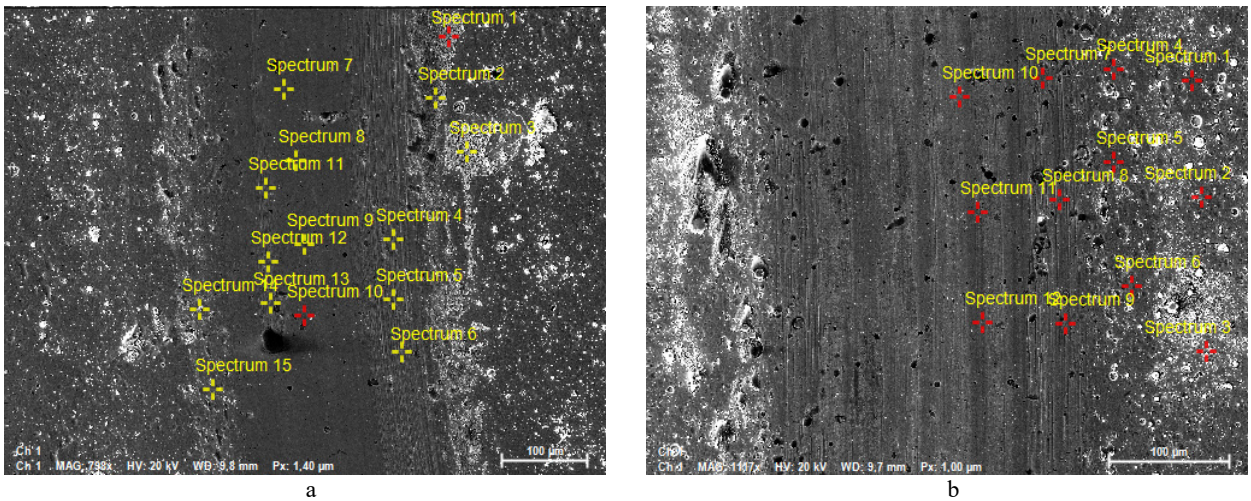

a b

Figure 3. Wear tracks on the surface of the TiMoN/NbN nano-multilayer coatings deposited at different working nitrogen pressures: (a) 0.52 Pa and (b) 0.13 Pa.

The TiMoN layers likely exhibit the dislocation-mediated plasticity characteristic of TiMoN-based systems: intensive dislocation multiplication and grain-boundary sliding enable localized dissipation of frictional energy without the formation of brittle cracks. As a result, the multilayer structure attains an adaptive load-bearing response in which the "rigid" NbN and more "compliant" TiMoN sublayers operate synergistically.

The EDS analysis of the worn surface regions enables a direct correlation between the chemical nature of the tribofilm and the distinct tribological responses of the coatings. Table 3 presents the elemental composition of the wear track obtained at different regions of the sample 1552. Across the width of the wear track, the elemental distribution in sample 1552 exhibits behavior characteristic of stable adaptive tribosystems. The periphery is covered with thick,

predominantly titanium-rich oxides (O = 70–75 wt. %, Ti < 25 wt. %), which play minimal functional roles during sliding. In contrast, the central region develops a thin, compact, and mechanically robust tribofilm with a balanced Ti−Nb−Mo−O composition (O = 13–19 wt %, Ti = 38–42 wt. %, Nb = 37–40 wt. %, Mo = 5–6 wt. %). The elevated fractions of Mo and Nb in the central zone point to the formation of lubricious MoO_3 and strengthening Nb_2O_5 phases, while Ti probably contributes through the formation of stable TiO_2 oxides. This multicomponent adaptive tribofilm is responsible for the low friction coefficient and smooth sliding behavior of sample 1552.

Table 3. Elemental composition of the wear track of the TiMoN/NbN nano-multilayer coating (1552) in wt. %.

Spectrum No	O	Ti	Fe	Nb	Mo	W
Sp. 1	71.99	13.20	0.92	11.29	2.33	0.02
Sp. 2	75.35	11.47	1.04	10.08	1.81	0.01
Sp. 3	46.16	23.93	0.50	24.77	4.00	0.29
Sp. 4	13.37	41.48	0.06	38.55	5.80	0.04
Sp. 5	15.51	40.00	0.04	37.79	5.92	-
Sp. 6	14.19	40.58	0.00	38.64	6.07	-
Sp. 7	16.28	39.96	0.20	37.29	5.63	-
Sp. 8	18.35	39.61	0.13	35.70	5.60	0.07
Sp. 9	13.75	41.00	0.14	38.23	6.09	-
Sp. 10	12.38	41.38	0.05	39.40	6.05	-
Sp. 11	15.21	39.90	0.14	38.28	5.77	0.05
Sp. 12	29.53	32.85	0.20	31.30	5.63	-
Sp. 13	31.65	32.06	0.04	31.04	4.65	-
Sp. 14	69.39	14.02	0.42	13.58	2.33	0.04
Sp. 15	30.44	33.96	0.04	30.16	4.97	-

The elemental composition of the wear track obtained at different regions of the sample 1554 is presented in Table 4. It indicates the absence of a well-developed adaptive tribofilm, in sharp contrast to the behavior observed for sample 1552. Across the entire width of the wear track, the oxygen content remains low (O = 8–14 wt. %), suggesting the formation of only a thin and brittle TiO_2 layer rather than complex Ti–Mo–Nb–O oxides. The high titanium content (Ti = 46–55 wt. %) together with the relatively uniform distribution of niobium (Nb = 27–32 wt. %) implies exposure and progressive degradation of the outer TiMoN layers rather than the formation of the strengthening Nb_2O_5 phase typically associated with stable tribosystems.

Although molybdenum is present at a measurable level (5–6 wt %), the limited degree of oxidation prevents the development of lubricious MoO_3, depriving the coating of an intrinsic friction-reducing mechanism. Consequently, the tribofilm formed on sample 1554 is thin, heterogeneous, and brittle, lacking any self-replenishing capability. This unstable surface layer readily breaks down under load, resulting in a dominant abrasive–adhesive wear mechanism and a correspondingly elevated friction coefficient.

Table 4. Elemental composition of the wear track of the TiMoN/NbN nano-multilayer coating (1554) in wt. %.

Spectrum No	O	Ti	Fe	Nb	Mo	W
Sp. 1	8.17	54.34	0.08	30.50	6.21	-
Sp. 2	11.74	53.47	0.10	27.93	6.11	-
Sp. 3	23.11	46.04	0.05	25.19	5.09	-
Sp. 4	8.48	54.03	-	30.70	6.09	-
Sp. 5	23.71	47.25	-	14.29	13.86	0.01
Sp. 6	12.27	53.04	-	28.39	5.83	-
Sp. 7	5.88	55.03	-	32.11	6.16	0.09
Sp. 8	9.54	54.25	0.10	29.58	5.96	0.02
Sp. 9	9.88	52.97	-	30.43	6.14	-
Sp. 10	9.16	55.06	-	29.30	5.86	-
Sp. 11	13.68	51.93	-	27.94	5.82	0.09
Sp. 12	12.71	52.89	0.04	28.23	5.53	-

Overall, the obtained results clearly demonstrate that the wear resistance of the TiMoN/NbN nano-multilayer coatings is governed not only by the presence of NbN sublayers but, critically, by the degree to which they are structurally integrated into the multilayer architecture. The higher at working nitrogen pressure (0.52 Pa) promotes uniform layer alternation, which facilitates the formation of a stable adaptive tribofilm and enables efficient dissipation of mechanical energy through controlled TiMoN-mediated plasticity. Under lower working nitrogen pressure (0.13 Pa), however, the increased defect density and disrupted periodicity of the nanolayers diminish the stabilizing role of NbN, yielding a tribofilm that is thin, brittle, and spatially heterogeneous.

These microstructural distinctions ultimately dictate whether the TiMoN with NbN layers' sequence operates as an effective nanolaminate capable of crack deflection, adaptive load partitioning, and generating lubricious MoO_3 phases or transitions into an unstable sliding regime dominated by abrasive and adhesive wear processes.

CONCLUSIONS

This work provides a comprehensive assessment of the wear behaviour of TiMoN/NbN nano-multilayer coatings deposited by CA-PVD at two markedly different working nitrogen pressures (0.52 and 0.13 Pa). The combined structural, chemical, and tribological analyses clearly demonstrate that the wear performance of these multilayer systems is governed not simply by their nominal composition or the presence of alternating TiMoN and NbN layers, but critically by the degree of structural order, interface integrity, and the capacity of the coating to generate a functional tribofilm during sliding contact.

Deposition at the higher nitrogen pressure (0.52 Pa) results in a well-organized multilayer architecture with sharply defined and nearly perfectly parallel interfaces. This structural coherence minimizes microstrain, suppresses defect formation, and ensures a more homogeneous distribution of Ti, Nb, and Mo throughout the multilayer stack. Under sliding conditions, these features enable the formation of a robust, multicomponent adaptive tribofilm enriched in TiO_2, Nb_2O_5, and MoO_3 phases. The presence of MoO_3 contributes lubricious properties, while Nb_2O_5 enhances thermal and mechanical stability. As a result, the coating demonstrates a consistently low friction coefficient and limited wear, confirming the synergistic action of stiff NbN layers and plastically accommodating TiMoN layers.

In contrast, deposition under low nitrogen pressure (0.13 Pa) leads to significant structural degradation. The altered metal distribution – particularly the reduced titanium content in the as-deposited state and the inability to generate oxidized Mo- or Nb-rich phases during wear – prevents the formation of a stabilizing tribofilm. Instead, only a thin, brittle TiO_2 film develops, which lacks both mechanical robustness and self-replenishing characteristics. Consequently, the coating is prone to abrasive–adhesive wear, exhibits substantial counterbody transfer, and manifests a high, unstable friction coefficient.

The comparative analysis unequivocally shows that the tribological response of TiMoN/NbN nano-multilayer systems depends on the interplay between: (i) structural periodicity and interface sharpness; (ii) microdefect density and residual stress distribution; and (iii) the chemistry and adaptability of tribofilm formation. Coatings deposited at 0.52 Pa satisfy all three requirements, yielding an optimized nanolaminate capable of crack deflection, controlled energy dissipation through TiMoN-mediated plasticity, and formation of a lubricious, strengthening tribofilm. Those deposited at 0.13 Pa fail to meet these criteria, leading to unstable friction and accelerated wear.

Overall, the study demonstrates that precise control of working nitrogen pressure during CA-PVD deposition is a determining factor for tailoring the structural integrity and tribological performance of TiMoN/NbN nano-multilayer coatings. The findings highlight the strong potential of these materials for advanced wear-critical applications, provided that deposition conditions are optimized to promote coherent multilayer architectures and the formation of effective adaptive tribofilms.

Acknowledgments

Funded by the EU NextGenerationEU through the Recovery and Resilience Plan for Slovakia under project No. 09I03-03-V01-00028. The Ukrainian state budget program under project No. 0124U001127 also supports this research.

ORCID

Olga Maksakova, https://orcid.org/0000-0002-0646-6704; **Vyacheslav Beresnev**, https://orcid.org/0000-0002-4623-3243;
Serhiy Lytovchenko, https://orcid.org/0000-0002-3292-5468; **Mária Čaplovičová**, https://orcid.org/0000-0003-4767-8823;
D.V. Horokh, https://orcid.org/0000-0002-6222-4574; **B.O. Mazilin,** https://orcid.org/0000-0003-1576-0590;
M. Sahul, https://orcid.org/0000-0001-9472-500X

REFERENCES

[1] W. Li, P. Liu, and P.K. Liaw, Mater. Res. Lett. **6**(4), 199 (2018). https://doi.org/10.1080/21663831.2018.1434248
[2] R. Lin, S. Sun, B. You, T. Dong, Y. Sui, and S. Wei, Mater. Res. Express. **11**, 096402 (2024). https://doi.org/10.1088/2053-1591/ad7350
[3] J. Liu, Y. Wang, G. Liu, J. Hua, and X. Deng, Coatings, **13**(7), 1229 (2023), https://doi.org/10.3390/coatings13071229
[4] K. S. Surendra Mohan, S. Gunasekaran, D. Manjubashini, S. Umayal, S. Sivaranjani, and B. Subramanian, J. of Materi Eng and Perform **33**, 10614–10622 (2024). https://doi.org/10.1007/s11665-023-08691-x
[5] S. Zhang, N. Wang, D.J. Li, L. Dong, H.Q. Gu, R.X. Wan, and X. Sun, Nuclear Instruments and Methods in Physics Research Section B: Beam Interactions with Materials and Atoms, **307**, 119-122 (2013). https://doi.org/10.1016/j.nimb.2012.12.067.
[6] H. Dempwolf, M. Proft, A. Baumann, S. Malz, O. Keßler, Coatings, **12**, 935 (2022). https://doi.org/10.3390/coatings12070935
[7] N. Vattanaprateep, N. Panich, and P. Surin, Journal of Southwest Jiaotong University, **58**(6), (2023). https://doi.org/10.35741/issn.0258-2724.58.6.25
[8] Z. Xia, W. Song, H. Yu, X. Li, Y. Yin, and W. Xie, Coatings, **15**(10), 1150 (2025). https://doi.org/10.3390/coatings15101150
[9] J. Chen, S. Zhang, J. Li, Z. Chen, and D. Sun, Surface and Coatings Technology, **497,** 131800 (2025). https://doi.org/10.1016/j.surfcoat.2025.131800
[10] Y. Wang, W. Yuan, W. Han, J. Gao, H. Li, and T. Zhao, Ceramics International, **50**(6), 9460-9468 (2024). https://doi.org/10.1016/j.ceramint.2023.12.263
[11] Y.H. Wang, F. Guo, H. Ren, S.Y. Hu, Y.J. Chen, Y.H. Zhao, F. Gong, and Z.W. Xie, Ceramics International, **48**(6), 8746–8750 (2022). https://doi.org/10.1016/j.ceramint.2022.01.010
[12] J. Xu, P. Zhang, J. Yu, P. Ying, T. Yang, J. Wu, T. Wang, N. Myshkin, and V. Levchenko, Lubricants, **13**(8), 319 (2025). https://doi.org/10.3390/lubricants13080319

[13] Q. Guo, K. Wang, T. Fang, D. Zhang, H. Sun, and Y. Wan, Advanced Engineering Materials, **27**(18), 2500974 (2025). https://doi.org/10.1002/adem.202500974
[14] B. Warcholinski, A. Gilewicz, K. Kminikowska, A.S. Kuprin, G.N. Tolmachova, E.N. Reshetnyak, I.V. Kolodiy, *et, al.,* Wear, **578-579,** 206224 (2025). https://doi.org/10.1016/j.wear.2025.206224
[15] K. Smyrnova, M. Sahul, M. Haršáni, V. Beresnev, M. Truchlý, L. Čaplovič, M. Čaplovičová, *et al.,* ACS Omega, **9** (15), 17247-17265 (2024). https://doi.org/10.1021/acsomega.3c10242
[16] V. Chenrayan, C. Manivannan, K. Shahapurkar, A. Krishna, V. Tirth, A. Algahtani, and I.M. Alarifi, *et al.,* Journal of Nanomaterials, **2022**(1), 9664365 (2022). https://doi.org/10.1155/2022/9664365
[17] G.D. Sonawane, R. Bachhav, and A. Barnwal, JOM, **76**, 313–326 (2024). https://doi.org/10.1007/s11837-023-05991-4
[18] F. Akbar, and M. Arsalan, Proceedings of the Institution of Mechanical Engineers, Part B: Journal of Engineering Manufacture, **238**(1-2), 95-107 (2023). https://doi.org/10.1177/09544054231157247
[19] X. Zhang, Z. Zeng, X. Zeng, V. Pelenovich, Q. Wan, A. Pogrebnjak, L. Xue, *et al.,* Materials Research Letters, **13**(2), 103–112 (2024). https://doi.org/10.1080/21663831.2024.2425167
[20] X. Wang, J. Liu, Y. Liu, W. Li, Y. Chen, and B. Yang, Coatings, **14**(8), 1006 (2024). https://doi.org/10.3390/coatings14081006
[21] K. Van Meter, Md.I. Chowdhury, T. Babuska, Jewel Haik, T. Tanasarnsopaporn, M.J. Sowa, A.C. Kozen, *et al.,* Wear, **570**, 205980 (2025). https://doi.org/10.1016/j.wear.2025.205980
[22] S. Zhou, Z. Qiu, Z. Wang, W. Yang, and A. Wang, Rare Metals, **44**(5), 2845-2852 (2025). https://doi.org/10.1007/s12598-024-03128-3
[23] S. Zhou, W. Zhao, Y. Wu, Z. Qiu, S. Lin, Z. Zheng, and D.C. Zeng, Vacuum, **190**, 110311 (2021). https://doi.org/10.1016/j.vacuum.2021.110311
[24] C. Wang, J. Liu, G. Liu, L. Xue, and K. Zhang, Coatings, **15**(8):956 (2025). https://doi.org/10.3390/coatings15080956
[25] T. Wang, G. Zhang, and B. Jiang, Applied Surface Science, **326**, 162-167 (2015). https://doi.org/10.1016/j.apsusc.2014.11.125
[26] W. Cheng, J. Wang, X. Ma, P. Liu, P.K. Liaw, and W. Li, Journal of Materials Research and Technology, **27,** 2413-2442 (2023). https://doi.org/10.1016/j.jmrt.2023.10.012
[27] AA. Sugumaran, Y. Purandare K. Shukla,I. Khan, A. Ehiasarian, and P. Hovsepian, Coatings, **11**, 867 (2021). https://doi.org/10.3390/coatings11070867
[28] O. Maksakova, V. Beresnev, M. Caplovicova, Z. Zhang, M. Sahul, S. Lytovchenko, and B. Mazilin, in: *IEEE 15th International Conference Nanomaterials: Applications & Properties (NAP)* (Bratislava, Slovakia, 2025), pp. MTFC03-1-MTFC03-5. https://doi.org/10.1109/NAP68437.2025.11216249

ДОСЛІДЖЕННЯ ЗНОСОСТІЙКОСТІ TiMoN/NbN НАНОБАГАТОШАРОВИХ ПОКРИТТІВ, ОСАДЖЕНИХ ВАКУУМНО-ДУГОВОЮ ТЕХНОЛОГІЄЮ ЗА РІЗНИХ РОБОЧИХ ТИСКІВ

О.В. Максакова[1,2], В.М. Береснєв[2], С.В. Литовченко[2], М. Чапловичова[3], Д.В. Горох[2], Б.О. Мазілін[2], М. Сахул[1]
[1]Інститут матеріалознавства, Словацький технологічний університет у Братиславі, вул. Яна Ботту 25, 917 24, Трнава, Словаччина
[2]Харківський національний університет імені В.Н. Каразіна, майд. Свободи, 4, 61000, Харків, Україна
[3]Центр нанодіагностики матеріалів, Словацький технологічний університет у Братиславі, Вазовова 5, 812 43, Братислава, Словаччина

Дане дослідження присвячене аналізу зносостійкості нанобагатошарових покриттів TiMoN/NbN, осаджених методом катодно-дугового PVD за різних робочих тисків азоту (0.52 та 0.13 Па). Хоча обидва покриття мають подібну загальну товщину (~10-11 мкм) і близьку кількість періодів (~270), їх структурна цілісність, якість інтерфейсів та елементний розподіл суттєво відрізняються залежно від тиску під час осадження. Покриття, синтезоване при 0.52 Па, формує високовпорядковану та щільну багатошарову архітектуру з чітко визначеними межами та зниженою концентрацією мікродефектів. Натомість покриття, отримане при 0.13 Па, характеризується вираженою хвилястістю меж, порушенням періодичності та зростанням дефектності. Трибологічні випробування «кулька–диск» показали стабільний коефіцієнт тертя 0.42–0.48 для покриття, отриманого при 0.52 Па, тоді як покриття, синтезоване при 0.13 Па, демонструє підвищений і нестабільний коефіцієнт тертя (0.60–0.70) з частими коливаннями. Мікроструктурний та хімічний аналізи доріжок зношування вказують на формування у покритті, отриманому при високому тиску, міцної адаптивної Ti–Nb–Mo–O трибоплівки, яка містить мастильні фази MoO_3 і зміцнювальні фази Nb_2O_5. У випадку низького тиску на поверхні формується лише тонка, крихка TiO_2-вмісна плівка, що не має здатності до самовідновлення. Отримані результати демонструють, що оптимізація тиску азоту є ключовою умовою для формування структурно узгоджених наноламінатів, здатних утворювати функціональні трибоплівки, що суттєво підвищує зносостійкість нанобагатошарових систем TiMoN/NbN.

Ключові слова: *вакуумно-дугова технологія; нітриди; багатошарові покриття; мікроструктура; склад; зносостійкість*

East European Journal of Physics. **4.** 709-714 (2025)
DOI:10.26565/2312-4334-2025-4-77 ISSN 2312-4334

POLYPHENOL EFFECT ON THE INTERACTIONS BETWEEN FUNCTIONAL PROTEINS AND AMYLOID FIBRILS

U. Malovytsia[1]*, V. Trusova[1], M. Thomsen[2], K. Vus[1], O. Zhytniakivska[1], G. Gorbenko[1]
[1]Department of Medical Physics and Biomedical Nanotechnologies, V.N. Karazin Kharkiv National University
4 Svobody Sq., Kharkiv, 61022, Ukraine
[2]AAU Energy, Aalborg University, Niels Bohrs Vej 8, 6700 Esbjerg, Denmark
**Corresponding Author email: uliana.tarabara@karazin.ua*
Received August 29, 2025, revised October 22, 2025; accepted November 6, 2025

Among a wide variety of protein-protein interactions, the complexation of functionally important proteins with pathogenic protein aggregates (amyloid fibrils) attracts particular interest in view of its possible contribution to amyloid cytotoxicity. In the present study we investigated the interactions between the functional proteins (human serum albumin (HSA), hemoglobin (deoxyHb and oxyHb) and insulin Ins)) and amyloid fibrils from Abeta peptide, islet amyloid polypeptide (IAPP), insulin (InsF), apolipoprotein A-I (apoA-I) and apolipoprotein A-II (apoA-II) with an accent on evaluating the possibility of modulating such interactions by polyphenolic compounds including quercetin, curcumin in keto and enol forms, gallic acid, salicylic acid, sesamin and resveratrol. The analysis of the molecular docking data showed that the binding affinities of amyloid fibrils to functional proteins vary in a wide range depending on the structural peculiarities of the examined systems. The most pronounced destabilizing effects of polyphenols on the complexes between the proteins in native and amyloid states were revealed for the systems HSA + QR / CRketo +ApoA-I, HSA +SES +IAPP, deoxyHb + SES / RES +InsF. Further experimental evaluation of these molecular docking predictions will create prerequisites for extending the range of polyphenol applications as anti-amyloid agents.
Keywords: *Amyloid fibrils; Functional proteins; Polyphenols; Molecular docking*
PACS: 87.14.C++c, 87.16.Dg

INTRODUCTION

Protein-protein interactions (PPI) are known to control a diversity of cellular processes, among which are cell growth, signal transduction, immune response, regulation of metabolic pathways, etc. [1, 2]. Over 80% of proteins have been found to function in complexes with other proteins, forming the complex networks of PPI [3]. Along with the functional interactions between protein molecules, there are aberrant PPI that may lead to multiple pathological conditions [4, 5]. In particular, self-association of specific proteins and peptides into elongated ordered aggregates with a core β-sheet architecture (amyloid fibrils) is thought to provoke a number of human disorders such as Alzheimer's, Parkinson's, Huntington's diseases, systemic amyloidosis, type-II diabetes, cancer, etc. [6, 7]. Several lines of evidence indicate that cytotoxic action of amyloid fibrils is associated with predominantly with disintegration of cell membranes and impairment of their functioning, suppression of proteasomal degradation and generation of reactive oxygen species [8-10]. However, the disruption of PPI networks resulting from the complexation between the fibrillized and native proteins may also contribute to amyloid cytotoxicity. This opens a new line of research focusing on investigation of the interactions between proteins in amyloid and natively-folded states. Such kind of research is worthy of attention in at least two aspects. First, amyloid fibrils can impair the structure and function of endogenous proteins, as was demonstrated, particularly, in our recent study for fibrillized N-terminal (1-83) fragment of apolipoprotein A-I with amyloidogenic mutation G26R interacting with hemoglobin, cytochrome c or serum albumin [11]. Second, functional proteins may act as endogenous inhibitors of amyloid formation [12-14] and disaggregating agents for mature fibrils [15]. In particular, human serum albumin (HSA), the predominant protein in blood plasma, has been found to inhibit aggregation of the amyloid-β (Aβ) peptide involved in pathogenesis of Alzheimer's disease [16, 17]. The in vitro experiments demonstrated the ability of HSA to form complexes with various Aβ amyloid intermediates such as monomers, oligomers, and protofibrils [18-20]. The ability to disassemble the preformed amyloid fibrils has been revealed for proteins belonging to the family of molecular chaperones [21]. To exemplify, the shaperones Hsp70 and Hsp90 brought about the disaggregation of tau fibrils [22, 23], while lipocalin-type prostaglandin D synthase and transthyretin disrupted the preformed Aβ fibrils [24, 25]. Obviously, the interactions between the fibrillized and native proteins can be a potential target for therapeutic intervention with various bioactive compounds. One extensively studied group of such compounds is represented by polyphenols (PF), the secondary plant metabolites with a diversity of beneficial biological properties including anticancer, immunomodulating, antioxidative, anti-inflammatory and antimicrobial properties [26, 27]. In view of the above rationales, the aim of the present study was to ascertain whether the polyphenolic compounds of various classes can destabilize the complexes between amyloid fibrils (AF) and functional proteins (FP). To this end, we employed the molecular docking technique to explore the binding characteristics in the systems FP + AF and FP + PF + AF.

Cite as: U. Malovytsia, V. Trusova, M. Thomsen, K. Vus, O. Zhytniakivska, G. Gorbenko, East Eur. J. Phys. 4, 709 (2025), https://doi.org/10.26565/2312-4334-2025-4-77

METHODS

The examined molecular systems were designed from four functional proteins (human serum albumin, hemoglobin (in deoxy and oxy forms) and insulin), five types of amyloid fibrils formed by Abeta peptide (Abeta), islet amyloid polypeptide (IAPP), insulin (Ins), apolipoprotein A-I (apoA-I) and apolipoprotein A-II (apoA-II), and seven polyphenols (quercetin (QR), curcumin in keto and enol forms (CRketo, CRenol), gallic acid (GA), salicylic acid (SA), sesamin (SES) and resveratrol (RES)). The crystal structures of the functional proteins were taken from the Protein Data Bank (https://www.rcsb.org/) using the following PDB IDs:1AO6 (human serum albumin), 2DN2 (human deoxyhemoglobin, deoxyHb), 1LFQ (human oxyhemoglobin, oxyHb), 5ENA (human insulin). The structures of the amyloid fibrils from Abeta, ApoA-II and IAPP were derived from the Protein Data Bank using the following PDB IDs: 8OT4 (Aβ amyloid fibrils from Alzheimer's brain tissue), 8OQ4 (ApoA-II) and 6Y1A (IAPP)). The structure of insulin fibril was taken from the archive of M. Sawaya (http://people.mbi.ucla.edu/sawaya/jmol/fibrilmodels/). The model amyloid fibrils of apoliporotein A-I were constructed using the CreateFibril tool with the input structures being generated by PatchDock from the β-stranded ApoA-I monomers. The PDB files of polyphenols were prepared with MarvinSketch as a drawing tool and Avogadro 1.1.0 as a geometry optimization tool. The docking of amyloid fibrils (ligand) to proteins or complexes FP + PF was conducted using the web-based server HDOCK [28]. The most energetically favorable docking complexes were visualized with the UCSF Chimera software (version 1.14).

RESULTS AND DISCUSSION

As seen from Table 1, all examined proteins can form complexes with amyloid fibrils, with the binding affinities decreasing in the rows*:* serum albumin: ApoA-II > IAPP > InsF ≥ Abeta > ApoA-I; deoxyhemoglobin: InsF > Abeta > ApoA-II > IAPP > ApoA-I; oxyhemoglobin: Abeta > IAPP > InsF > ApoA-II > ApoA-I; insulin: Abeta ~ ApoA-II > InsF ~ IAPP > ApoA-I. As judged from the values of the best docking score, the highest binding affinities were observed for oxyHb in its complexes with Abeta (the best docking score -317.95), IAPP (-306.20) and InsF (-289.50), while the weakest complexes were formed by HSA with ApoA-II (-167.26), ApoA-I(-181.51) and insulin with ApoA-I (-187.72).

Table 1. The best score values for the complexes of amyloid fibrils with functional proteins

Protein	Amyloid fibrils				
	Abeta	InsF	ApoA-I	ApoA-II	IAPP
HSA	-244.67	-208.32	-181.51	-167.26	-266.13
DeoxyHb	-251.21	-264.10	-213.98	-237.01	-226.21
OxyHb	-317.95	-289.50	-209.58	-272.66	-306.20
Insulin	-250.93	-245.04	-187.72	-250.09	-245.10

Next, it seemed of importance to clarify whether the polyphenols in question are capable of modulating the interactions between functional proteins and amyloid fibrils through altering the binding affinity and the amino acid composition of the binding sites. For this purpose, we performed an extensive docking study of 140 systems FP+PF+AF containing 4 functional proteins, 7 polyphenols and 5 types of amyloid fibrils in different combinations. The analysis of the best score values allowed us to find the complexes in which the presence of polyphenols results in the decreased affinities of amyloid fibrils to proteins.

As can be seen in Fig. 1 and Table 2, there are 11 systems FP+PF+AF in which PF addition results in the pronounced destabilization of the complexes between functional proteins and amyloid fibrils (the decrease in the absolute value of the best docking score exceeds 5%). Of these, five systems, viz. HSA + QR / CRketo +ApoA-I, HSA +SES +IAPP, deoxyHb + SES / RES +InsF appeared to be most promising from the viewpoint of the protective effect of polyphenols against amyloid fibrils.

Table 2. The systems with the strongest destabilizing effect of polyphenols on the affinity of amyloid fibrils for functional proteins

System FP+PF+AF	The changes of the best docking score relative to the system without PF, %
Ins + SA + InsF	-8.7
Ins + GA + InsF	-5.7
HSA + QR + ApoA-I	-10.9
HSA + CRketo + ApoA-I	-11.3
HSA + SES +IAPP	-12.4
DeoxyHb + CRketo + InsF	-7.6
DeoxyHb +SES + InsF	-13.8
DeoxyHb +RES + InsF	-14.4
OxyHb + SA + Abeta	-7.6
OxyHb + QR + InsF	-6.2
OxyHb + RES + InsF	-7.5

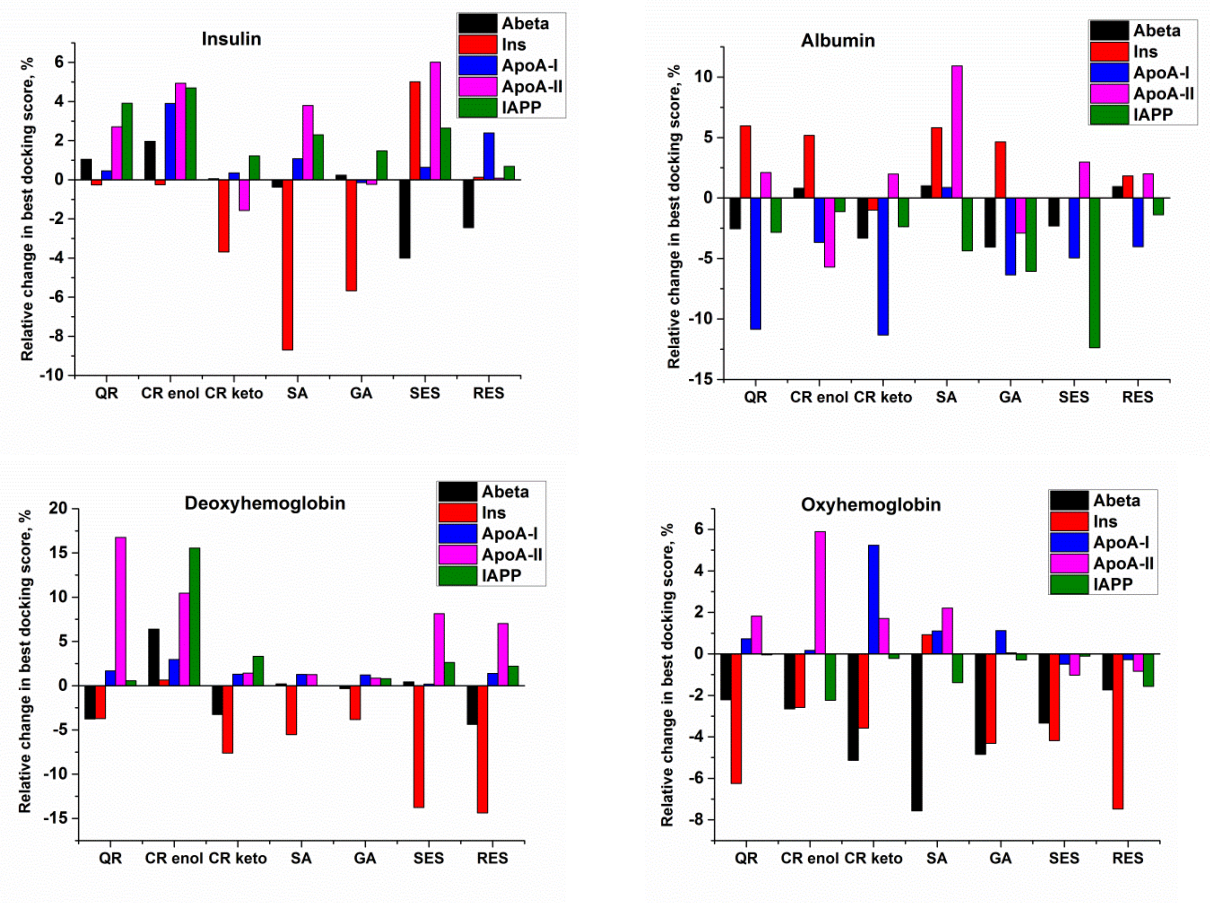

Figure 1. The changes in the best docking score (BDS) values calculated as (BDS (FP+PF+AF) - BDS (FP+AF))·100/BDS (FP+AF)

In the following analysis we compared the amino acid compositions of the binding sites of the functional proteins for polyphenols and amyloid fibrils (in the absence and presence of PF). The insulin binding sites for InsF, SA and GA were found to contain 6 (SA) or 7 (GA) overlapping amino acid residues, all belonging to the protein chain B (marked in gray in Table 3). Therefore, it seems probable that SA and GA can serve as competitive ligands for InsF. Accordingly, the amino acid composition of the insulin binding sites for InsF are essentially different for the systems without and with polyphenols, for SA they contain 5 overlapping residues, while in the interaction of Ins with InsF in the absence and presence of GA occurs through completely different sites.

Table 3. Insulin interface residues in the complexes of insulin with amyloid fibrils in the absence and presence of polyphenols

Ins + InsF	GLN_{5A} CYS_{7A} THR_{8A} SER_{9A} ILE_{10A} CYS_{11A} SER_{12A} LEU_{13A} TYR_{14A} GLN_{15A} PHE_{1B} VAL_{2B} ASN_{3B} GLN_{4B} HIS_{5B} LEU_{6B} CYS_{7B} HIS_{10B} GLU_{13B} ALA_{14B} LEU_{17B}
Ins + SA	PHE_{1B} VAL_{2B} GLN_{4B} LEU_{6B} SER_{9B} HIS_{10B} LEU_{11B} GLU_{13B} ALA_{14B}
Ins + SA + InsF	GLY_{1A} ILE_{2A} GLU_{4A} GLN_{5A} SER_{12A} LEU_{13A} TYR_{14A} GLN_{15A} GLU_{17A} ASN_{18A} TYR_{19A} CYS_{20A} ASN_{21A} GLU_{21B} ARG_{22B} GLY_{23B} PHE_{24B} PHE_{25B} TYR_{26B} THR_{27B} PRO_{28B} LYS_{29B} THR_{30B}
Ins + GA	PHE_{1B} VAL_{2B} GLN_{4B} LEU_{6B} SER_{9B} HIS_{10B} GLU_{13B} ALA_{14B} LEU_{17B}
Ins + GA + InsF	CYS_{20A} ASN_{21A} SER_{9B} VAL_{12B} TYR_{16B} GLY_{20B} GLU_{21B} ARG_{22B} GLY_{23B} PHE_{24B} PHE_{25B} TYR_{26B} THR_{27B} PRO_{28B} LYS_{29B} THR_{30B}

As shown in Table 4, the HSA binding sites for ApoA-I, QR and CRketo possess only two overlapping amino acid residues, LYS_{137A} and GLU_{141A}, so that the competitive interactions between QR / CRketo and ApoA-I seem to be weaker than in the case of insulin and InsF. As a result, the amino acid composition of the HSA binding sites for ApoA-I show significant similarity in the absence and presence of QR / CRketo, differing in five residues in the case of QR and in three residues in the case of CRketo. In contrast to the above albumin-containing systems, the HSA binding sites for IAPP and SES do not have overlapping amino acids, so that HSA-IAPP interactions are mediated by the same amino acid residues, but in the system HSA + IAPP two additional residues, GLU_{376A} and SER_{489A} are involved, compared to the system HSA + SES + IAPP (Table 4).

Table 4. Albumin interface residues in the complexes of insulin with amyloid fibrils in the absence and presence of polyphenols

HSA + ApoA-I	GLN_{33A} CYS_{34A} PRO_{35A} PHE_{36A} GLU_{37A} ASP_{38A} ARG_{81A} GLU_{82A} THR_{83A} TYR_{84A} GLY_{85A} GLU_{86A} ASN_{111A} LEU_{112A} PRO_{113A} VAL_{122A} THR_{125A} ALA_{126A} HSD_{128A} ASP_{129A} LYS_{137A} TYR_{140A} GLU_{141A} ARG_{144A} GLU_{501A} PHE_{502A} ASN_{503A} ALA_{504A} GLU_{505A} THR_{508A} GLU_{565A} ALA_{569A} LYS_{573A} GLN_{580A}
HSA + QR	LEU_{115A} ARG_{117A} PRO_{118A} MET_{123A} PHE_{134A} LYS_{137A} TYR_{138A} GLU_{141A} ILE_{142A} TYR_{161A} LEU_{182A} ASP_{183A} ARG_{186A}
HSA + QR + ApoA-I	GLN_{33A} CYS_{34A} PRO_{35A} PHE_{36A} GLU_{37A} ARG_{81A} GLU_{82A} THR_{83A} TYR_{84A} GLY_{85A} GLU_{86A} ASN_{111A} LEU_{112A} PRO_{113A} PRO_{118A} GLU_{119A} ASP_{121A} VAL_{122A} THR_{125A} ALA_{126A} ASP_{129A} LYS_{137A} TYR_{140A} GLU_{141A} ARG_{144A} ARG_{145A} GLU_{501A} PHE_{502A} ASN_{503A} ALA_{504A} GLU_{505A} THR_{508A} GLU_{565A} ALA_{569A} LYS_{573A} GLN_{580A}
HSA + CRketo	LEU_{115A} VAL_{116A} ARG_{117A} PRO_{118A} PHE_{134A} LYS_{137A} TYR_{138A} GLU_{141A} ILE_{142A} HSD_{146A} PHE_{149A} PHE_{157A} TYR_{161A} LEU_{182A} LEU_{185A} ARG_{186A} GLY_{189A} LYS_{190A}
HSA + CRketo + ApoA-I	GLN_{33A} CYS_{34A} PRO_{35A} PHE_{36A} GLU_{37A} ASP_{38A} ARG_{81A} GLU_{82A} THR_{83A} TYR_{84A} GLY_{85A} GLU_{86A} ASN_{111A} LEU_{112A} PRO_{113A} PRO_{118A} ASP_{121A} VAL_{122A} THR_{125A} ALA_{126A} HSD_{128A} ASP_{129A} LYS_{137A} TYR_{140A} GLU_{141A} ARG_{144A} GLU_{501A} PHE_{502A} ASN_{503A} ALA_{504A} GLU_{505A} THR_{508A} GLU_{565A} ALA_{569A} LYS_{573A} GLN_{580A}
HSA + IAPP	ASP_{375A} GLU_{376A} LYS_{378A} PRO_{379A} GLU_{382A} GLU_{383A} ASN_{386A} LYS_{389A} GLN_{390A} GLU_{393A} LEU_{394A} GLU_{396A} GLN_{397A} LEU_{398A} ASN_{405A} ALA_{406A} LEU_{407A} VAL_{409A} ARG_{410A} LYS_{413A} LYS_{414A} SER_{489A} GLU_{492A} VAL_{493A} GLU_{495A} PRO_{537A} LYS_{538A} THR_{540A} LYS_{541A} GLU_{542A} LYS_{545A}
HSA + SES	LEU_{115A}, ARG_{117A}, PRO_{118A}, MET_{123A}, PHE_{134A}, LYS_{137A}, TYR_{138A}, GLU_{141A}, ILE_{142A}, TYR_{161A}, LEU_{182A}, ASP_{183A}, LEU_{185A}, ARG_{186A}
HSA + SES + IAPP	ASP_{375A} LYS_{378A} PRO_{379A} GLU_{382A} GLU_{383A} ASN_{386A} LYS_{389A} GLN_{390A} GLU_{393A} LEU_{394A} GLU_{396A} GLN_{397A} LEU_{398A} ASN_{405A} ALA_{406A} LEU_{407A} VAL_{409A} ARG_{410A} LYS_{413A} LYS_{414A} GLU_{492A} VAL_{493A} GLU_{495A} PRO_{537A} LYS_{538A} THR_{540A} LYS_{541A} GLU_{542A} LYS_{545A}

In contrast to insulin and albumin, deoxyhemoglobin possesses no overlapping amino acid residues in the binding sites for InsF, CRketo, SES and RES (Table 5), thereby excluding the possibility of competition between InsF and PF for the same HSA sites. As a consequence, the deoxyHb binding sites for InsF without and with PF contain many identical amino acid residues (marked in gray in Table 5), differing in four residues for CRketo, three residues for SES and four residues for RES.

Table 5. Deoxyhemoglobin interface residues in the complexes of insulin with amyloid fibrils in the absence and presence of polyphenols

DeoxyHb + InsF	GLU_{27A} GLU_{30A} PHE_{33A} LEU_{34A} LEU_{48A} SER_{49A} HSD_{50A} GLY_{51A} HSD_{112A} HSD_{2B} THR_{4B} PRO_{5B} GLU_{6B} GLU_{7B} LYS_{8B} SER_{9B} ALA_{10B} THR_{12B} ALA_{13B} TRP_{15B} GLY_{16B} LYS_{17B} LEU_{75B} ALA_{76B} HSD_{77B} ASP_{79B} LYS_{120B} GLU_{121B} PHE_{122B} THR_{123B} PRO_{124B} PRO_{125B} VAL_{126B} GLU_{90D} LEU_{91D} CYS_{93D} ASP_{94D} LYS_{95D} HSD_{97D} HSD_{146D}
DeoxyHb + CRketo	LYS_{99A}, LEU_{100A}, SER_{102A}, HSD_{103A}, LEU_{106A}, PHE_{117A}, HSD_{122A}, ALA_{123A}, ASP_{126A}, LYS_{127A}, LEU_{129A}, ALA_{130A}, VAL_{34B}, TYR_{35B}, TRP_{37B}, GLU_{101B}, LEU_{105B}, ASN_{108B}, VAL_{109B}, CYS_{112B}, ASP_{94C}, PRO_{95C}, ARG_{141C}
DeoxyHb + CRketo + InsF	GLU_{27A} GLU_{30A} ARG_{31A} PHE_{33A} LEU_{34A} LYS_{40A} LEU_{48A} SER_{49A} HSD_{50A} GLY_{51A} HSD_{112A} HSD_{2B} LEU_{3B} THR_{4B} PRO_{5B} GLU_{6B} LYS_{8B} SER_{9B} ALA_{10B} THR_{12B} ALA_{13B} TRP_{15B} GLY_{16B} LYS_{17B} LEU_{75B} ALA_{76B} HSD_{77B} ASP_{79B} LYS_{120B} GLU_{121B} PHE_{122B} THR_{123B} PRO_{124B} PRO_{125B} VAL_{126B} GLU_{90D} LEU_{91D} CYS_{93D} ASP_{94D} LYS_{95D} LEU_{96D} HSD_{97D} HSD_{146D}
DeoxyHb + SES	TYR_{42A}, ASP_{94A}, PRO_{95A}, VAL_{96A}, ARG_{141A}, LYS_{99C}, SER_{102C}, ASP_{126C}, LEU_{129C}, ALA_{130C}, SER_{133C}, TYR_{35D}, TRP_{37D}, THR_{38D}, ASP_{99D}, GLU_{101D}, ASN_{102D}, LEU_{105D}, ASN_{108D}
DeoxyHb + SES + InsF	GLU_{27A} GLU_{30A} LEU_{34A} LEU_{48A} HSD_{50A} HSD_{112A} HSD_{2B} THR_{4B} PRO_{5B} GLU_{6B} GLU_{7B} LYS_{8B} SER_{9B} ALA_{10B} THR_{12B} ALA_{13B} TRP_{15B} GLY_{16B} LYS_{17B} ASP_{73B} LEU_{75B} ALA_{76B} HSD_{77B} LEU_{78B} ASP_{79B} LYS_{120B} GLU_{121B} THR_{123B} PRO_{124B} PRO_{125B} VAL_{126B} GLU_{90D} LEU_{91D} CYS_{93D} ASP_{94D} LYS_{95D} HSD_{97D} HSD_{146D}
DeoxyHb + RES	LYS_{99A}, LEU_{100A}, SER_{102A}, HSD_{103A}, LEU_{106A}, PHE_{117A}, HSD_{122A}, ALA_{123A}, ASP_{126A}, VAL_{34B}, TYR_{35B}, LEU_{105B}, ASN_{108B}, VAL_{109B}, CYS_{112B}, VAL_{113B}
DeoxyHb + RES + InsF	GLU_{27A} GLU_{30A} LEU_{34A} LEU_{48A} SER_{49A} HSD_{50A} HSD_{112A} HSD_{2B} THR_{4B} PRO_{5B} GLU_{6B} GLU_{7B} LYS_{8B} SER_{9B} ALA_{10B} THR_{12B} ALA_{13B} TRP_{15B} GLY_{16B} LYS_{17B} VAL_{18B} ASP_{73B} LEU_{75B} ALA_{76B} HSD_{77B} LEU_{78B} ASP_{79B} LYS_{120B} GLU_{121B} PHE_{122B} THR_{123B} PRO_{124B} PRO_{125B} VAL_{126B} GLU_{90D} LEU_{91D} CYS_{93D} ASP_{94D} LYS_{95D} HSD_{97D} HSD_{146D}

Analogously, there is no overlap between the oxyhemoglobin binding sites for Abeta and SA (Table 6). However, only 12 of 31 (oxyHb + Abeta) or 30 (oxyHb + SA + Abeta) amino acids forming the binding sites for Abeta, are identical for the systems without and with SA.

Table 6. Oxyhemoglobin interface residues in the complexes of insulin with amyloid fibrils in the absence and presence of polyphenols

OxyHb + Abeta	VAL_{1A} LEU_{2A} ARG_{92A} ASP_{94A} PRO_{95A} VAL_{96A} ASN_{97A} LYS_{99A} ASP_{126A} LYS_{127A} ALA_{130A} SER_{131A} THR_{134A} LYS_{139A} TYR_{140A} ARG_{141A} VAL_{34B} TYR_{35B} PRO_{36B} TRP_{37B} ARG_{40B} PHE_{41B} GLU_{43B} CYS_{93B} ASP_{94B} HIS_{97B} ASP_{99B} PRO_{100B} GLU_{101B} TYR_{145B} HIS_{146B}
OxyHb + SA	GLU_{27A}, ARG_{31A}, ALA_{111A}, HIS_{112A}, GLY_{119B}, LYS_{120B}, PHE_{122B}, THR_{123B}, PRO_{124B}
OxyHb + SA +Abeta	SER_{35A} PHE_{36A} PRO_{37A} THR_{38A} THR_{39A} THR_{41A} TYR_{42A} ARG_{92A} ASP_{94A} PRO_{95A} VAL_{96A} ASN_{97A} LYS_{99A} LEU_{100A} LYS_{139A} TYR_{140A} VAL_{1B} HIS_{2B} LEU_{3B} PRO_{100B} GLU_{101B} ARG_{104B} GLN_{131B} LYS_{132B} ALA_{135B} ASN_{139B} ALA_{142B} HIS_{143B} TYR_{145B} HIS_{146B}
OxyHb + InsF	PHE_{36A} THR_{38A} ALA_{88A} HIS_{89A} LYS_{90A} LEU_{91A} ARG_{92A} ASP_{94A} PRO_{95A} VAL_{96A} ASN_{97A} PHE_{98A} LYS_{99A} LEU_{100A} SER_{102A} HIS_{103A} LEU_{106A} HIS_{122A} ALA_{123A} ASP_{126A} LYS_{127A} ALA_{130A} LYS_{139A} TYR_{140A} ARG_{141A} VAL_{34B} TYR_{35B} PRO_{36B} TRP_{37B} CYS_{93B} ASP_{94B} HIS_{97B} ASP_{99B} PRO_{100B} GLU_{101B} ASN_{102B} PHE_{103B} ARG_{104B} LEU_{105B} ASN_{108B} VAL_{109B} CYS_{112B} GLN_{131B} VAL_{134B} ALA_{138B} ASN_{139B} ALA_{142B} LYS_{144B} TYR_{145B} HIS_{146B}
OxyHb + QR	LYS_{99A} SER_{102A} HIS_{103A} LEU_{106A} ASP_{126A} LEU_{129A} ALA_{130A} SER_{133A} TYR_{35B} GLU_{101B} ARG_{104B} LEU_{105B} ASN_{108B}
OxyHb + QR + InsF	VAL_{1A} LYS_{7A} HIS_{72A} ASP_{74A} ASP_{75A} MET_{76A} PRO_{77A} ASN_{78A} SER_{81A} SER_{84A} ASP_{85A} HIS_{89A} ASP_{94A} PRO_{95A} LYS_{99A} LYS_{127A} ALA_{130A} THR_{134A} THR_{137A} SER_{138A} LYS_{139A} TYR_{140A} ARG_{141A} VAL_{34B} TYR_{35B} PRO_{36B} TRP_{37B} GLN_{39B} ARG_{40B} GLU_{43B} LEU_{48B} SER_{49B} ASP_{94B} LYS_{95B} LEU_{96B} HIS_{97B} ASP_{99B} LYS_{144B} TYR_{145B} HIS_{146B}
OxyHb + RES	PHE_{98A}, LYS_{99A}, SER_{102A}, HIS_{103A}, LEU_{106A}, VAL_{107A}, HIS_{122A}, ASP_{126A}, LEU_{129A}, ALA_{130A}, SER_{133A}, TYR_{35B}, LEU_{105B}, ASN_{108B}, VAL_{109B}, CYS_{112B}
OxyHb + RES + InsF	VAL_{1A} ASP_{6A} LYS_{7A} HIS_{72A} ASP_{74A} ASP_{75A} MET_{76A} PRO_{77A} ASN_{78A} SER_{81A} SER_{84A} ASP_{85A} HIS_{89A} ASP_{94A} PRO_{95A} LYS_{99A} LYS_{127A} ALA_{130A} THR_{134A} THR_{137A} SER_{138A} LYS_{139A} TYR_{140A} ARG_{141A} VAL_{34B} TYR_{35B} PRO_{36B} TRP_{37B} GLN_{39B} ARG_{40B} GLU_{43B} LEU_{48B} SER_{49B} CYS_{93B} ASP_{94B} LYS_{95B} LEU_{96B} HIS_{97B} ASP_{99B} LYS_{144B} TYR_{145B} HIS_{146B}

Unlike Abeta fibrils, the binding sites of oxyHb for InsF and QR or RES have multiple overlapping residues (11 for QR and 13 for RES), so that these polyphenols can be regarded as competitive ligands for InsF (Table 6). Likewise, in the absence of PF the binding site for InsF is more extended (is composed of 50 amino acids), while in the presence of QR or RES it reduces to 40 (QR) or 42 (RES) amino acids, with the number of overlapping residues being 18 for QR and 21 for RES. Overall, our findings suggest that the factors such as the competition between PF and AF for the FP binding sites and ii) the changes in the set of interfacial amino acids play significant role in determining the ability of polyphenols to destabilize the aberrant complexes between functional proteins and amyloid fibrils.

CONCLUSIONS

In summary, we performed the molecular docking study of the binary (functional protein + amyloid fibril) and ternary (functional protein + polyphenol + amyloid fibril) systems to evaluate the protective effects of polyphenolic compounds against toxic action of amyloid fibrils of endogenous proteins. The examined systems were composed of human serum albumin, hemoglobin (in deoxy and oxy forms) and insulin as functional proteins, amyloid fibrils from Abeta peptide, islet amyloid polypeptide, insulin, apolipoprotein A-I and apolipoprotein A-II, and a series of polyphenols including quercetin, curcumin in keto and enol forms, gallic acid, salicylic acid, sesamin and resveratrol. It was found that the strongest complexes are formed between oxyHb and amyloid fibrils from Abeta peptide, IAPP and insulin, while the complexes HSA-ApoA-I, HSA-ApoA-II and Ins-ApoA-I are characterized by the lowest binding affinities. The comparison of the binding affinities for the systems FP+AF and FP+PF+AF revealed 11 ternary combinations in which polyphenols can destabilize the complexes between functional complexes and amyloid fibrils. The systems HSA + QR / CRketo +ApoA-I, HSA +SES +IAPP, deoxyHb + SES / RES +InsF can be recommended for further experimental testing. The results obtained may be of interest for the development of polyphenol-based approaches to reducing the amyloid toxicity.

Acknowledgements

This project has received funding through the EURIZON project, which is funded by the European Union under grant agreement No. 3049.

ORCID

Uliana Malovytsia, https://orcid.org/0000-0002-7677-0779; **Valeriya Trusova,** https://orcid.org/0000-0002-7087-071X;
Mette Hedegaard Thomsen, https://orcid.org/0000-0001-6805-7247; **Kateryna Vus,** https://orcid.org/0000-0003-4738-4016
Olga Zhytniakivska, https://orcid.org/0000-0002-2068-5823; **Galyna Gorbenko,** https://orcid.org/0000-0002-0954-5053

REFERENCES

[1] S. Wang, R. Wu, J. Lu, Y. Jiang, T. Huang, and Y. Cai, Proteomics. **22**, 2100190 (2022). https://doi.org/10.1002/pmic.202100190

[2] L. Walport, J. Low, J. Matthews, and J. Mackay, Chem. Soc. Rev. **50**, 12292 (2021). https://doi.org/10.1039/D1CS00548K
[3] T. Berggård, S. Linse, and P. James, Proteomics **7**, 2833 (2007). https://doi.org/10.1002/pmic.200700131
[4] J. Brown, and M. Horrocks, Curr. Opin. Struct. Biol. **15**, 441 (2005). https://doi.org/10.1016/j.sbi.2005.06.001
[5] H. Lu, Q. Zhou, J. He, Z. Jiang, C. Peng, R. Tong, and J. Shi, Signal Transduct. Target. Ther. **5,** 213 (2020). https://doi.org/10.1038/s41392-020-00315-3
[6] J. Brown, and M. Horrocks, Semin. Cell Dev. Biol. **99**, 65 (2020). https://doi.org/10.1016/j.semcdb.2018.05.006
[7] B. Liu, H. Zhang, and X. Qin, Nanomaterials **15**, 255 (2025). https://doi.org/10.3390/nano15040255
[8] M. P. Jackson, and E. W. Hewitt, Essays Biochem. **60**, 173 (2016). https://doi.org/10.1042/EBC20160005
[9] K. F. Winklhofer, and C. Haass, Biochim. Biophys. Acta **1802**, 29-44 (2010).
[10] B. Uttara, A.V. Singh, P. Zamboni, R.T. Mahajan, Curr. Neuropharmacol. 7, 65 (2009). https://doi.org/10.2174/157015909787602823
[11] U.K. Malovytsia, V.M. Trusova, M.H. Thomsen, and G.P. Gorbenko, East Eur. J. Phys. (1), 367 (2025). https://doi.org/10.26565/2312-4334-2025-1-45
[12] B. Bohrmann, I. Tjernberg, P. Kuner, S. Poli, B. Levet-Trafit, J. Näslund, R. Grayson, W. Huber, H. Döbeli, and C. Nordstedt, J. Biol. Chem. **274**, 15990 (1999). https://doi.org/10.1074/jbc.274.23.15990
[13] S. Han, J. Park, and I. Mook-Jung, Prog.Neurobiol. **137**, 17 (2016). https://doi.org/10.1016/j.pneurobio.2015.12.004
[14] H. Xie, and C. Guo, Front. Mol. Biosci. **7**, 629520 (2021). https://doi.org/10.3389/fmolb.2020.629520
[15] K. Jia, Y. Low, A. Venkatraman, J. Mehta, and K. Pervushin, J. Adv. Res. **36**, 113 (2022). https://doi.org/10.1016/j.jare.2021.05.007
[16] A. Ezra, I. Rabinovich-Nikitin, P. Rabinovich-Toidman, and B. Solomon, J. Alzheimers Dis. **50,** 175 (2016). https://doi.org/10.3233/JAD-150694
[17] M. Boada, O. López, J. Olazarán, L. Núñez, M. Pfeffer, M. Paricio, J. Lorites, *et al*. Dement. **16**, 1412 (2020). https://doi.org/10.1002/alz.12137
[18] C. Wang, F. Cheng, L. Xu, and L. Jia, RSC Adv. **6**, 71165 (2016). https://doi.org/10.1039/c6ra14590f
[19] M. Algamal, R. Ahmed, N. Jafari, B. Ahsan, J. Ortega, and G. Melacini, J. Biol. Chem. **292**, 17158 (2017). https://doi.org/10.1074/jbc.M117.792853
[20] D. Bode, H. Stanyon, T. Hirani, M. Baker, J. Nield, and J. Viles, J. Mol. Biol. **430**, 919–934 (2018). https://doi.org/10.1016/j.jmb.2018.01.008
[21] Z. Almeida, and R. Brito, Biomedicines **10**, 3276 (2022). https://doi.org/10.3390/biomedicines10123276
[22] E. Nachman, A. Wentink, K. Madiona, L. Bousset, T. Katsinelos, K. Allinson, H. Kampinga, *et al*., J. Biol. Chem. **295**, 9676 (2020). https://doi.org/10.1074/jbc.RA120.013478
[23] Y. Ali, H. Allen, L. Yu, D. Li-Kroeger, D. Bakhshizadehmahmoudi, A. Hatcher, C. McCabe, *et al*., PLOS Biol. **14,** e1002472. (2016). https://doi.org/10.1371/journal.pbio.1002472
[24] B. Kannaian, B. Sharma, M. Phillips, A. Chowdhury, M. Manimekalai, S. Adav, J. Ng, *et al*., Sci. Rep. **9**, 1 (2019). https://doi.org/10.1038/s41598-019-48819-5
[25] R. Costa, A. Gonçalves, M. Saraiva, and I. Cardoso, FEBS Lett. **582**, 936–942 (2008). https://doi.org/10.1016/j.febslet.2008.02.034
[26] C. Weng, and G. Yen, Canc. Treat. Rev. **38**, 76 (2012). https://doi.org/10.1016/j.ctrv.2011.03.001
[27] T. Ozdal, E. Capanoglu, and F. Altay, Food Res. Int. **51**, 954 (2013). https://doi.org/10.1016/j.foodres.2013.02.009
[28] Y. Yan, H. Tao, J. He, and S-Y. Huang, Nat. Protoc. **15**, 1829 (2020). https://doi.org/10.1038/s41596-020-0312-x

ВПЛИВ ПОЛІФЕНОЛІВ НА ВЗАЄМОДІЇ МІЖ ФУНКЦІОНАЛЬНИМИ БІЛКАМИ ТА АМІЛОЇДНИМИ ФІБРИЛАМИ

Уляна Маловиця[1], Валерія Трусова[1], Метте Томсен[2], Катерина Вус[1], Ольга Житняківська[1], Галина Горбенко[1]
[1]Кафедра медичної фізики та біомедичних нанотехнологій, Харківський національний університет імені В.Н. Каразіна м. Свободи 4, Харків, 61022, Україна
[2]Університет Аалборг, вул. Нільса Бора 8, 6700 Есб'єрг, Данія

Серед великого розмаїття білок-білкових взаємодій, утворення комплексів між функціонально важливими білками та патогенними білковими агрегатами (амілоїдними фібрилами) привертає особливий інтерес з огляду на можливу роль таких комплексів у цитотоксичності амілоїдів. У даній роботі ми дослідили взаємодії між функціональними білками (сироватковим альбуміном людини (HSA), гемоглобіном (deoxyHb та oxyHb) та інсуліном (Ins)) та амілоїдними фібрилами із Абета пептиду (Abeta), амілоїдного поліпептиду (IAPP), інсуліну (InsF), аполіпопротеїну A-I (apoA-I) та аполіпопротеїну A-II (apoA-II). Головний акцент був зроблений на оцінці можливості модуляції таких взаємодій поліфенольними сполуками, включаючи кверцетин, куркумін в кето та єнольній формах, галову та саліцилову кислоти, сесамін та ресвератрол. Аналіз результатів, отриманих методом молекулярного докінгу, показав, що спорідненість амілоїдних фібрил до функціональних білків варіює в широких межах та залежить від структурних особливостей досліджуваних систем. Найбільш виражений дестабілізуючий вплив поліфенолів на комплекси між білками в нативному та амілоїдному станах був виявлений для систем HSA + QR / CRketo +ApoA-I, HSA +SES +IAPP, deoxyHb + SES / RES +InsF. Подальша експериментальна верифікація даних молекулярного докінгу створить передумови для розширення діапазону застосування поліфенолів як антиамілоїних агентів.

Ключові слова: *амілоїдні фібрили; функціональні білки; поліфеноли; молекулярний докінг*

East European Journal of Physics. 4. 715-719 (2025)
DOI:10.26565/2312-4334-2025-4-78 ISSN 2312-4334

ASSESSMENT OF THE SENSITIVITY OF A FLUORESCENT SQUARAINE DYE TO HEAVY METAL IONS

U. Malovytsia*, O. Zhytniakivska, K. Vus, V. Trusova, G. Gorbenko
Department of Medical Physics and Biomedical Nanotechnologies, V.N. Karazin Kharkiv National University
4 Svobody Sq., Kharkiv, 61022, Ukraine
**Corresponding Author E-mail: uliana.tarabara@karazin.ua*
Received August 30, 2025; revised September 16, 2025; accepted October 21, 2025

The contamination of natural water systems with heavy metal ions poses a significant global environmental and public health threat due to their persistence, bioaccumulation, and severe toxicological effects. Consequently, the development of rapid and sensitive detection methods is essential for effective water quality monitoring. Squaraine dyes represent a promising class of chemosensors for heavy metal detection owing to their high molar extinction coefficients, near-infrared fluorescence, and pronounced spectral responsiveness to metal binding. In this study, we evaluate the sensitivity of the symmetric squaraine dye SQ-1 toward four environmentally relevant heavy metal ions – Cu^{2+}, Zn^{2+}, Ni^{2+}, and Pb^{2+} – and explore its applicability within a β-lactoglobulin/SQ-1 nanosystem for metal sensing in aqueous media. Spectroscopic analysis revealed metal-dependent modulation of SQ-1 optical properties, driven largely by alterations in dye aggregation and metal–dye coordination. Ni^{2+} and Pb^{2+} promoted SQ-1 deaggregation and enhanced fluorescence emission, whereas Cu^{2+} induced pronounced quenching consistent with strong coordination. Our results indicate that, SQ-1 retained its responsiveness in the presence of β-lactoglobulin fibrils, exhibiting metal-specific fluorescence changes indicative of combined dye–metal–fibril interactions. Further studies are warranted to assess SQ-1 performance toward additional metal ions and to elucidate the molecular mechanisms underlying metal-induced modulation of its photophysical behavior.
Keywords: *Squaraine dye; Metal detection; Heavy metals*
PACS: 87.14.Cc, 87.16.Dg

The contamination of natural water systems with heavy metal ions remains a critical global environmental and public health issue. Metals such as mercury (Hg^{2+}), lead (Pb^{2+}), cadmium (Cd^{2+}), copper (Cu^{2+}), and iron (Fe^{3+}) persist in aquatic environments due to their non-biodegradable nature and tendency to bioaccumulate in living organisms. Exposure to these metals, even at trace levels, can result in severe toxicological effects, including neurotoxicity, carcinogenicity, kidney dysfunction, and developmental disorders [1-4]. Consequently, the development of rapid, sensitive, and cost-effective analytical methods for heavy metal detection is essential for monitoring water quality and ensuring environmental safety. In this context, organic fluorescent dyes that undergo distinct spectral changes upon interacting with metal ions have emerged as a particularly promising class of chemosensors, offering high sensitivity, fast response times, and the potential for direct visual detection [5-6].

Among the diverse families of fluorescent probes used for heavy metal detection, squaraine dyes have attracted significant attention due to their distinctive optical properties, including intense absorption and emission in the visible to near-infrared (NIR) region [7,8], high molar extinction coefficients [9], and unique donor-acceptor-donor (D-A–D) resonance-stabilized zwitterionic structure [10,11]. Numerous studies have demonstrated their high sensitivity and selectivity toward heavy metal ions, which is largely attributed to their strong electron-accepting core, extended π-conjugation, and ability to form stable complexes with metal species [12-17]. These structural features enable pronounced changes in their optical properties – such as absorption or fluorescence – upon metal binding, allowing for rapid and accurate detection even at low concentrations [12-17]. As a result, squaraine-based sensors have gained significant attention for monitoring toxic metal contaminants in biological systems, industrial wastewater, and environmental samples [12-17]. To exemplify, Chen et al. developed a novel squaraine-based chemosensor for Hg^{2+} ion selective detection, whose sensing mechanism relies on a pronounced colour change resulting from dye disaggregation upon coordination with the heavy metal [14]. A simple 1,2-squaraine derivative has been shown to provide dual colourimetric detection of Fe^{3+} and Hg^{2+} ions, with visible colour change and detection limits of 0.538 μM for Fe^{3+} and 1.689 μM for Hg^{2+} [15]. Similarly, more recently developed NIR-absorbing squaraine dyes (e.g., BBSQ) demonstrate selective response to Fe^{3+}, Cu^{2+} and Hg^{2+} even in the presence of competing metal ions, with observable colour changes and acceptable detection limits ~6 μM for Cu^{2+} [16]. Thapa et al. also developed a near-infrared squaraine-based chemosensor, SQ-68, whose solvent-dependent sensing mechanism enables selective detection of Cu^{2+} Ag^{+} in real water samples with recovery rates ranging from 73–95% for Cu^{2+} to 59–99% for Ag^{+} [17]. Shafeekh et al. reported the highly selective and sensitive colourimetric detection of Hg^{2+} ions by sulphonate group-containing unsymmetrical squaraine dyes [18].

The present study aims to expand the application of squaraine dyes for heavy metal ion detection by evaluating the sensitivity of the squaraine dye SQ-1 (Figure 1) toward Cu^{2+}, Zn^{2+}, Ni^{2+}, and Pb^{2+} ions. Specifically, the study had two main objectives: first, to assess the sensitivity of SQ-1 to these metal ions, and second, to explore the potential development of a β-lactoglobulin/SQ-1 nanosystem for detecting heavy metals in water.

Cite as: U. Malovytsia, O. Zhytniakivska, K. Vus, V. Trusova, G. Gorbenko, East Eur. J. Phys. 4, 715 (2025), https://doi.org/10.26565/2312-4334-2025-4-78

EXPERIMENTAL SECTION

Materials

Bovine β-lactoglobulin (βlg), copper(II) chloride dihydrate, nickel(II) chloride, lead(II) nitrate, zinc chloride and thioflavin T (ThT) were purchased from Sigma, USA. The symmetric squarylium derivative SQ-1 (Figure 1) was synthesized according to previously reported procedures [10] and was kindly provided by Professor A. Vasilev. All other reagents were of analytical grade and used without the further purification.

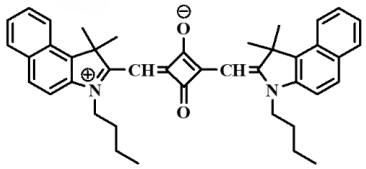

Figure 1. Structural formula of the symmetric squarylium dye SQ-1.

Spectroscopic measurements

SQ-1 stock solution was prepared in ethanol, whereas ThT was dissolved in 10 mM Tris buffer (pH 7.4). The β-lactoglobulin stock solution (10 mg/mL, βlgF) was prepared in distilled water and adjusted to pH 2.0 using HCl. Fibrillization was induced by incubating the protein solution at 90 °C for 2 days. Amyloid formation kinetics were monitored by the Thioflavin T (ThT) assay [19]. Working protein solutions were obtained by diluting the fibrillar β-lactoglobulin stock in distilled water (pH 6.07). All fluorimetric measurements were performed in distilled water at pH 6.07.

The absorption spectra of the examined dyes were recorded with a Shimadzu UV-2600 spectrophotometer (Japan) at 25ºC. The dye concentrations were determined spectrophotometrically using the extinction coefficients $\varepsilon_{663}^{EtOH} = 2.3 \cdot 10^5$ $M^{-1}cm^{-1}$ and $\varepsilon_{412}^{water} = 3.6 \cdot 10^4$ $M^{-1}cm^{-1}$ for SQ-1 and ThT, respectively. Steady-state fluorescence spectra were recorded with an RF-6000 spectrofluorimeter (Shimadzu, Japan). Fluorescence measurements were performed at 25°C using 10 mm pathlength quartz cuvettes. Fluorescence spectra were recorded in the range 620–825 nm with an excitation wavelength of 600 nm. The excitation and emission slit widths were set at 10 nm**.**

RESULTS AND DISCUSSION

Squaraine dye SQ-1 features a symmetric zwitterionic structure, comprising a central squarate core flanked by two butyl-substituted heterocyclic chromophores [10]. This intrinsic electronic symmetry gives rise to a sharp and intense absorption spectrum, characterized by a dominant peak at 662 nm and a secondary shoulder at 614 nm in ethanol [10]. SQ-1 has demonstrated remarkable versatility across a broad range of applications [10,20–24]. Notably, the dye exhibits high sensitivity to protein-induced modifications in the structural and physicochemical properties of lipid bilayers [10], serves as an effective fluorescent probe for detecting reactive oxygen species [9,20], and provides a powerful platform for both detecting and structurally analysing amyloid fibrils [21]. Owing to its near-infrared fluorescence, SQ-1 has proven highly suitable for the development of photoluminescent amyloid-based nanomaterials, achieved by functionalizing insulin nanofibrils with the dye, where SQ-1 acts as a long-lasting fluorescent sensor within the cascade system [22, 23].

In the present study, we extend the application of the squaraine dye SQ-1 by assessing its sensitivity to Cu^{2+}, Zn^{2+}, Ni^{2+}, and Pb^{2+} ions, while also exploring the potential development of a β-lactoglobulin/SQ-1 nanosystem for detecting heavy metals in water. Figure 1 shows the absorption and fluorescence spectra of the fluorophore in aqueous solution and in the presence of these metal ions. The absorption spectrum of SQ-1 in water exhibits two peaks at 614 nm and 660 nm, with the shorter-wavelength component showing higher absorbance than the longer-wavelength peak. Assuming that in ethanol the short-wavelength component appears as a minor spectral shoulder, the dominant 614 nm peak observed in aqueous solution suggests dye aggregation due to π–π stacking interactions. The tendency of squaraine dyes to aggregate in water has been reported in previous studies and is typically dependent on dye concentration [7, 14]. The addition of heavy metal ions led to a pronounced decrease in the absorbance of H-aggregates, with the effect diminishing in the order $Ni^{2+} > Zn^{2+} > Pb^{2+} > Cu^{2+}$. Importantly, the monomer peak (~660 nm) predominated in all systems investigated, except Zn^{2+}, where the absorbance of the monomer and H-aggregates remained comparable, indicating partial retention of aggregation in the presence of this ion. Moreover, as shown in Figure 1, binding with Cu^{2+} and Pb^{2+} induces approximately a 1.6-fold decrease in absorbance at 614 nm, accompanied by a reduction in monomer absorption, a 28 nm red shift of the monomer maximum, and notable band broadening.

In aqueous solution, SQ-1 displays a broad emission spectrum with a prominent peak at 715 nm. The addition of heavy metal ions leads to pronounced changes in the dye's fluorescence intensity, with the magnitude of these effects depending on the specific metal ion. Notably, binding with Ni^{2+} and Pb^{2+} induces an approximately 1.4-fold increase in fluorescence intensity at 715 nm, accompanied by a 3 nm red shift of the emission maximum and an enhanced shoulder at 787 nm, with the effect being most pronounced for Ni^{2+}. In contrast, complexation of SQ-1 with Cu^{2+} leads to a decrease in fluorescence intensity at 715 nm, along with a 2 nm red shift of the emission maximum.

Numerous studies indicate that the sensing mechanism of squaraine dyes presumably relies on coordination between the dye molecule and the metal ion, which can induce significant changes in both the dye's electronic structure and its

aggregation behavior [12-17]. In general, probe molecules exhibit selectivity for specific metal ions based on how effectively ligand atoms with lone-pair electrons, such as nitrogen, oxygen, and sulfur, can coordinate with those ions. Therefore, to interpret the aforementioned changes in the absorption and fluorescence spectra of the dyes, it is necessary to discuss the possible mechanisms underlying the squaraine dye–metal interactions. Numerous studies examining the sensing behavior of squaraine dyes indicate that, upon interaction with a target metal ion, they may (i) form coordination complexes through electron-rich sites on the dye, or (ii) disrupt dye aggregates, which are commonly present in aqueous environments. These processes enable squaraine dyes to function as either "turn-on" or "turn-off" sensors, depending on the specific metal ion and dye structure [12–17].

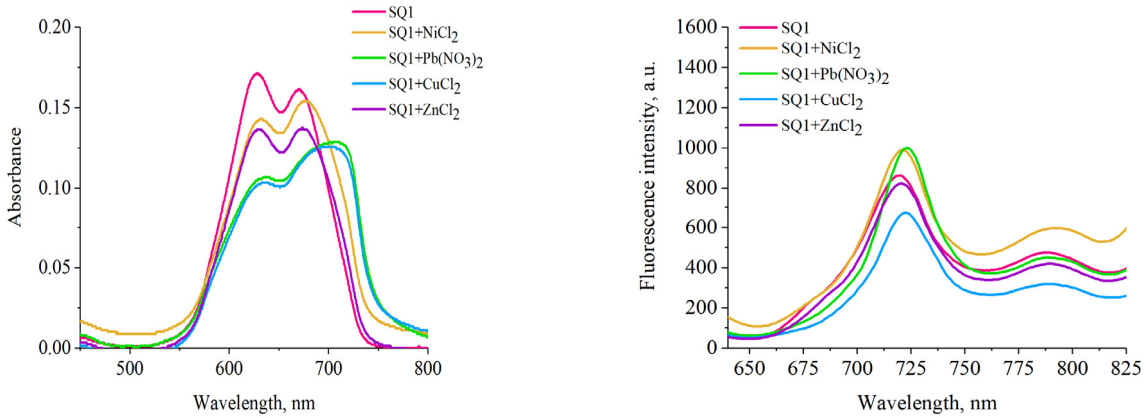

Figure 1. Absorption (left) and emission spectra (right) of SQ-1 in water and in the presence of heavy metal ions. Heavy metal concentration was 423 µM. SQ1 concentration was 2 µM.

One possible explanation for the aforementioned changes in the absorption and fluorescence spectra of the dyes lies in the interplay between metal–dye interactions and the aggregation state of SQ-1. In aqueous solution, the dominant absorption band at 614 nm indicates the presence of H-type aggregates formed through π–π stacking of squaraine molecules. Upon addition of heavy metal ions, these aggregates are disrupted to varying extents, leading to a decrease in aggregate absorbance and a corresponding increase in the monomeric band near 660 nm. The differing degrees of aggregate disruption ($Ni^{2+} > Zn^{2+} > Pb^{2+} > Cu^{2+}$) likely reflect variations in the binding affinity and coordination geometry of each metal ion with the squaraine dye. Zn^{2+} appears to partially preserve the aggregated state, as suggested by the comparable intensities of the monomer and H-aggregate peaks, possibly due to weaker or more sterically hindered interactions. Notably, a study by Chen et al. reported that among multiple tested metal ions, only Hg^{2+} produced a significant sensing response for a related squaraine dye, underscoring the strong dependence of sensing behavior on dye structure and metal-binding characteristics [14].

The fluorescence response of SQ-1 further supports this interpretation. The enhanced emission observed upon interaction with Ni^{2+} and Pb^{2+} may arise from deaggregation, which reduces nonradiative decay pathways and thus promotes more efficient radiative emission. The observed red shifts and increases in shoulder intensity suggest subtle modifications of the dye's electronic environment, potentially caused by metal-induced conformational adjustments or stabilization of specific dye orientations. In contrast, Cu^{2+} induces fluorescence quenching, likely due to stronger coordination with the squaraine core that facilitates nonradiative pathways—such as electron or energy transfer—or promotes structural perturbations that favor aggregation.

In the next phase of our study, we examined the response of SQ-1 to heavy metal ions in the presence of amyloid fibrils. Figure 2 presents the emission spectra of SQ-1 in systems containing β-lgF and various metal ions. In the absence of metals, SQ-1 exhibits a strong emission peak at 660 nm with a weaker shoulder around 760 nm. The addition of heavy metal ions modulates the relative intensities of these bands in a metal-specific manner, reflecting differential interactions among SQ-1, β-lgF, and the metal ions. Specifically, the addition of Zn^{2+}, Ni^{2+}, and Pb^{2+} did not substantially alter the overall shape of the emission spectra but did affect the peak intensities. Compared to the SQ-1–β-lgF system, an enhancement in fluorescence intensity was observed in the presence of these ions, with the effect being most pronounced for Zn^{2+}. In contrast, the addition of Cu^{2+} to the SQ-1–β-lgF system resulted in a 1.4-fold decrease in emission intensity.

A possible explanation for these observations is that metal ions interact with both the dye and the amyloid fibrils, altering the local environment of SQ-1. Zn^{2+}, Ni^{2+}, and Pb^{2+} may weakly bind to the fibrils or interact with the dye in a way that restricts nonradiative relaxation, leading to enhanced fluorescence. On the other hand, Cu^{2+} likely binds more strongly to the fibrils and/or the dye, inducing conformational changes or promoting quenching interactions that decrease emission intensity. These results suggest that the fluorescence response of SQ-1 is determined not only by direct dye–metal interactions but also by how metal ions influence the structural and electronic environment of the fibril-bound dye.The influence of metal ions on aggregation plays a critical role in determining the absorption and emission behavior of SQ-1. However, further studies are needed to evaluate SQ-1's sensitivity to additional metal ions and to elucidate the molecular mechanisms underlying metal–dye and metal–dye–fibril interactions.

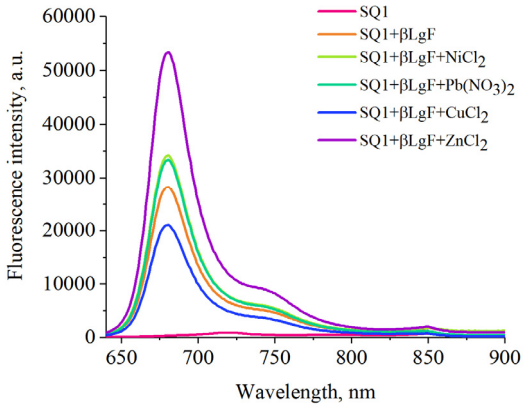

Figure 2. Emission spectra of SQ-1s in water, in the presence of 6.64 μM β-lgF (B), and in the presence of heavy metal ions. Heavy metal concentration was 423 μM. SQ1 concentration was 2 μM

CONCLUSIONS

In the present study, the sensitivity of the fluorescent squaraine dye SQ-1 toward four environmentally relevant heavy metal ions—Cu^{2+}, Zn^{2+}, Ni^{2+}, and Pb^{2+}—was evaluated. The results demonstrated that the dye's optical properties are metal-dependent, primarily influenced by changes in aggregation state and metal–dye coordination. Ni^{2+} and Pb^{2+} promoted SQ-1 deaggregation and enhanced fluorescence emission, whereas Cu^{2+} induced fluorescence quenching, consistent with strong coordination interactions. In the presence of β-lactoglobulin fibrils, SQ-1 retained its responsiveness and exhibited metal-specific fluorescence changes, indicating the potential for developing protein-based nanosystems for heavy metal detection in aqueous media. Further studies are required to assess SQ-1 performance toward additional metal ions and to elucidate the molecular mechanisms underlying metal-induced modulation of its photophysical behaviour.

Acknowledgements

This work was supported by the Ministry of Education and Science of Ukraine (the project "Development of economically affordable nanosystems for rapid identification and purification of water from heavy metal ions based on carbon nanoallotropes and amyloids from organic waste" No. 0124U000968).

ORCID

Uliana Malovytsia, https://orcid.org/0000-0002-7677-0779; **Olga Zhytniakivska,** https://orcid.org/0000-0002-2068-5823;
Kateryna Vus, https://orcid.org/0000-0003-4738-4016; **Valeriya Trusova,** https://orcid.org/0000-0002-7087-071X
Galyna Gorbenko, https://orcid.org/0000-0002-0954-5053

REFERENCES

[1] M.L. Sall, A.K.D. Diaw, D. Gningue-Sall, S. Efremova-Aaron, and J.-J. Aaron, Environ. Sci. Pollut. Res. **27**, 29927 (2020). https://doi.org/10.1007/s11356-020-09354-3
[2] L. Järup, Br. Med. Bull. **68**, 167 (2003). https://doi.org/10.1093/bmb/ldg032
[3] P. Zhang, M. Yang, J. Lan, Y. Huang, J. Zhang, S. Huang, Y. Yang, and J. Ru, Toxics, **11**, 828 (2023). https://doi.org/10.3390/toxics11100828
[4] J. Huff, R. Lunn, M. Waalkes, L. Tomatis, and P. Infante, Int. J. Occup. Environ. Health, **13**, 202 (2007). https://doi.org/10.1179/oeh.2007.13.2.202
[5] J. Khan, J. Fluoresc. **35**, 561 (2025). https://doi.org/10.1007/s10895-023-03559-8
[6] M.A.M. Alhamami, J.S. Algethami, and S. Khan, Critical Reviews in Analytical Chemistry, **54**(8), 2689 (2024). https://doi.org/10.1080/10408347.2023.2197073
[7] K. Illina, W.M. MacCuaig, M. Laramie, J.N. Jeouty, L.R. McNally, and M. Henary, Bioconjugate Chem. **31**, 194 (2020). https://doi.org/10.1021/acs.bioconjchem.9b00482
[8] J. He, Y.J. Jo, X. Sun, W. Qiao, J. Ok, T. Kim, Z. Liet, Advanced functional materials, **31**, 2008201 (2021). https://doi.org/10.1002/adfm.202008201
[9] V.M. Trusova, G.P. Gorbenko, T. Deligeorgiev, N. Gadjev, and A. Vasilev, J. Fluoresc. **19**, 1017 (2009). https://doi.org/10.1007/s10895-009-0501-z
[10] V.M. Ioffe, G.P. Gorbenko, T. Deligeorgiev, N. Gadjev, and A. Vasilev, Biophys. Chem. **128**, 75 (2007). https://doi.org/10.1016/j.bpc.2007.03.007
[11] L.Hu, Z. Yan, and H. Hu, RSC Advances. **3**, 7667 (2013). https://doi.org/10.1039/C3RA23048A
[12] D.D. Ta, and S.V. Dzyuba, Chemosensors, **9**, 302 (2021). https://doi.org/10.3390/chemosensors9110302
[13] X. Liu, N. Li, M.M. Xu, C. Jiang, J. Wang, G. Song, and Y. Wanget, Materials, **2018**, 11 (1998). https://doi.org/10.3390/ma11101998
[14] C. Chen, R. Wang, L. Guo, N. Fu, H. Dong, and Y. Yuanet, Organic Letters**, 13**(5), 1162 (2011). https://doi.org/10.1021/ol200024g
[15] X. Liu, N. Li, MM. Xu, C. Jiang, J. Wang, G. Song, and Y. Wang, Materials (Basel). **11**(10), 1162 (1998). https://doi.org/10.3390/ma11101998

[16] H. Li, Y. Tang, K. Shen, J.Li, Z. Zhang, D. Yi, and N. Hao, RSC Adv. **13**, 17202 (2023). https://doi.org/10.1039/D3RA02419A
[17] S. Thapa, K.R. Singh, and S.S. Pandey, Chemosensors, **13**(8), 288. https://doi.org/10.3390/chemosensors13080288J
[18] KM. Shafeekh, M.K.A. Rahim, M.C. Basheer, C.H. Suresh, and S. Daset, Dyes Pigments, **96**(3), 714 (2013). https://doi.org/10.1016/j.dyepig.2012.11.013
[19] M. Groenning, J. Chem. Biol. **3**, 1 (2010). https://doi.org/10.1007/s12154-009-0027-5
[20] V. Trusova, G. Gorbenko, T. Deligeorgiev, N. Gadjev, East Eur. J. Phys. **3**(3), 25 (2016). https://doi.org/10.26565/2312-4334-2016-3-02
[21] G. Gorbenko, V. Trusova, E. Kirilova, G. Kirilov, I. Kalnina, A. Vasilev, S. Kaloyanova, *et al*. Chem. Phys. Lett. **495**, 275 (2010). https://doi.org/10.1016/j.cplett.2010.07.005
[22] V. Trusova, U. Tarabara, O. Zhytniakivska, K.Vus, and G. Gorbenko, BBA Adv. **2**, 100059 (2022). https://doi.org/10.1016/j.bbadva.2022.100059
[23] G. Gorbenko, U. Tarabara, O. Zhytniakivska, K. Vus, and V. Trusova, Mol. Syst. Des. Eng**. 7**, 1307 (2022). https://doi.org/10.1039/D2ME00063F

ОЦІНЮВАННЯ ЧУТЛИВОСТІ ФЛУОРЕСЦЕНТНОГО СКВАРАЇНОВОГО БАРВНИКА ДО ІОНІВ ВАЖКИХ МЕТАЛІВ

У. Маловиця, О. Житняківська, К. Вус, В. Трусова, Г. Горбенко

Кафедра медичної фізики та біомедичних нанотехнологій, Харківський національний університет імені В.Н. Каразіна м. Свободи 4, Харків, 61022, Україна

Забруднення природних водних систем іонами важких металів становить серйозну глобальну екологічну та медико-біологічну загрозу через їхню стійкість, здатність до біоакумуляції та виражені токсикологічні ефекти. Відповідно, розроблення швидких і чутливих методів детектування є необхідним для ефективного моніторингу якості води. Скваранові барвники є перспективним класом хемосенсорів для виявлення важких металів завдяки їхнім високим молярним коефіцієнтам поглинання, ближньоінфрачервоній флуоресценції та вираженій спектральній чутливості до зв'язування з металами. Дана робота спрямована на дослідження чутливості симетричного скваранового барвника SQ-1 до чотирьох екологічно значущих іонів важких металів - Cu^{2+}, Zn^{2+}, Ni^{2+} та Pb^{2+} — і дослідження можливість його застосування у β-лактоглобулін/SQ-1 наносистемах для сенсингу металів у водному середовищі. Спектроскопічний аналіз виявив модулювання оптичних властивостей SQ-1 залежно від типу металу, зумовлене переважно змінами у ступені агрегації барвника та координації барвник–метал. Іони Ni^{2+} і Pb^{2+} сприяли дезагрегації SQ-1 та підсиленню флуоресценції, тоді як Cu^{2+} викликав виражене гасіння, можливе при координації. Наші результати свідчать, що SQ-1 зберігає свою чутливість і у присутності фібрил β-лактоглобуліну, демонструючи метал-специфічні зміни флуоресценції, характерні для комбінованих взаємодій барвник–метал–фібрила. Подальші дослідження є необхідними для оцінки ефективності SQ-1 щодо інших іонів металів і для з'ясування молекулярних механізмів, що лежать в основі модулювання його фотофізичної поведінки під впливом металів.

Ключові слова: *скваранновий барвник; детектування металів; важкі метали*